3-2022

Manufacturing of a Ceramic Turbine Rotor for a Compact Jet Engine

Bryan T. Leicht

Manufacturing of A Ceramic Turbine Rotor for a Compact Jet Engine

THESIS

Bryan T. Leicht, Captain, USMC

AFIT-ENY-MS-22-M-304

DEPARTMENT OF THE AIR FORCE
AIR UNIVERSITY

AIR FORCE INSTITUTE OF TECHNOLOGY

Wright-Patterson Air Force Base, Ohio

AFIT-ENY-MS-22-M-304

MANUFACTURING OF A CERAMIC TURBINE ROTOR FOR A COMPACT JET ENGINE

THESIS

Presented to the Faculty

Department of Aeronautics and Astronautics

Graduate School of Engineering and Management

Air Force Institute of Technology

Air University

Air Education and Training Command

in Partial Fulfillment of the Requirements for the

Degree of Degree of Masters of Aeronautical Engineering

Bryan T. Leicht, B.S.

Captain, USMC

March 2022

AFIT-ENY-MS-22-M-304

MANUFACTURING OF A CERAMIC TURBINE ROTOR FOR A COMPACT JET ENGINE

Bryan T. Leicht, B.S.
Captain, USMC

Committee Membership:

Lt Col Brian T. Bohan, PhD
Chairman

Frederick R. Schauer, PhD
Member

Maj Ryan A. Kemnitz, PhD
Member

Abstract

Compact engines offer many potential applications for the Air Force, including use in remotely piloted vehicles, but these can be costly and do not have the necessary power required for most missions. To gain the required power output from a compact engine the combustion temperature needs to be increased. The required temperature increase exceeds the limit of current uncooled metal turbine rotors, but can be achieved through turbine rotors made out of ceramics such as silicon nitride. Current ceramic turbine manufacturing methods are costly and time consuming, but recent breakthroughs in ceramic printing and injection molding have allowed for cheaper methods and faster production which is beneficial for research and development. The present research sought to determine a manufacturing process that could produce a drop-in replacement ceramic turbine rotor on the JetCat P400 small-scale engine in a manner that is cost-effective, timely, and scalable for production. This hobby class engine was used to demonstrate that a cost effective ceramic turbine could be manufactured while avoiding the additional expense of purchasing a military grade engine.

To meet this research objective, first a finite element analysis was utilized to determine if a silicon nitride turbine rotor could allow for elevated turbine inlet temperatures of 1,300°C (an increase from 700°C for the stock engine) at 90,000 RPM determined by cycle analysis. The study further tested two low-cost ceramic production methods to identify a successful process to produce turbine rotors; ceramic casting of silicon nitride, and stereolithography based ceramic manufacturing methods using an ADMATEC 3D printer with alumina. For the ceramic production methods, the baseline turbine rotor design was modified to best suit the manufacturing method.

Finite element analysis was also conducted on each design to determine failure criteria under current JetCat P400 operating regimes.

This research determined that a silicon nitride turbine rotor can meet the elevated temperature criteria. Further a low-cost scalable manufacturing process was successfully found for producing turbine rotors utilizing stereolithography based ceramic manufacturing methods. The casting method proved to be inconsistent and defect prone, specifically due to issues with drying. The 3D printing manufacturing process enabled multiple turbine rotor designs made from alumina, which served as a proof of concept, that can be built and tested on a JetCat P400 under idle conditions. The lessons learned for stereolithography based ceramic manufacturing allow for follow-on scaling for turbine rotor production to utilize and test turbine rotors made from zirconia and silicon nitride as more 3D printing material options become available.

Acknowledgements

First and foremost I would like to thank my thesis advisor Lt Col Brian Bohan, whose guidance and expertise was invaluable to this research. A special thanks as well to my committee members, Maj Ryan Kemnitz and Dr. Frederick Schauer, for providing their expertise. Maj. Kemnitz specifically helped with the initial design work for the four point bend apparatus and his materials knowledge helped bridge many gaps. Dr. Schauer's immense expertise on propulsion helped provide further explanation and understanding for dynamics of the turbine rotor.

An additional thanks to my sponsors from AFRL Dr. Mark Fernelius and Dr. Lisa Rueschhoff. Dr. Fernelius provided us with the goals and requirements for the turbine rotor driving the research. Dr. Rueschhoff provided expertise in ceramics and allowed me to continue working off her previous research. Her knowledge and support helped lead to a successful turbine rotor design.

Finally, I want to thank everyone who assisted with various aspects of the project that led to the success of this research. Travis Shelton who helped me with laser scanning microscope. Dr. William Costakis who mentored and guided me through the casting process. Dr. Willie Kemp and 1st Lt Benjamin Lam who were instrumental in the assisting with the ADMATEC printing process. Connor Wyckoff who acted as the utility player and kept the project moving. The AFRL shop team who helped design and create the SiC four point bend structure. Maj John Brewer who mentored and taught me how to effectively utilize FEA through Solidworks.

Bryan T. Leicht

Table of Contents

Page

Page

List of Figures

Figure Page

List of Tables

List of Abbreviations

Abbreviation		Page
RC	Radio-Controlled	1
AFRL	Air Force Research Laboratory	1
BYU	Brigham Young University	2
FEA	Finite Element Analysis	3
CAD	Computer-Aided Design	39
SLS	Selective Laser Sintering	40
SLCM	Stereolithography based Ceramic Manufacturing	42
ASTM	American Society for Testing and Materials	47
FDM	Fused Deposition Modeling	51
TGA	Thermogravimetric Analysis	57
RSa	Areal Roughness	58
FOS	Factor of Safety	86
EDM	Electrical Discharge Machining	148

List of Symbols

MANUFACTURING OF A CERAMIC TURBINE ROTOR FOR A COMPACT JET ENGINE

I. Introduction

1.1 Compact Engines

Compact engines were initially created as small turbine jet engines to go on radio-controlled (RC) aircraft for hobbyists. These compact engines soon began to offer many different utilities and produce thrust outputs that range from 5 lbs in the JetCat P20-SX for small RC aircraft up to 247 lbs seen in the JetCat P1000 Pro to power a human jet pack.[1] The Air Force Research Laboratory (AFRL) has recently become interested in compact engines and their applications in Air Force remotely piloted vehicles. Unfortunately, current compact engines for remotely piloted vehicles are costly and replacement parts are expensive to procure for research and development purposes. Using the JetCat P400 would offer a low-cost research and development test bed at $12,500 per engine [1] with a high power density.

The compact JetCat P90 RXi shown in Figure 1 works similarly to a more traditional large-scale jet engine. Air enters the engine through the inlet towards a single-stage radial compressor which increases the pressure and temperature of the air. The compressor directs air into the combustion chamber where it combines with fuel and is ignited in the combustor. The expansion of gas from combustion leads to an increase in temperature, however, the pressure and density decrease causing velocity to increase prior to entering the turbine section. Then air is directed through the stators towards the single-stage axial turbine. The turbine extracts energy from

the fluid as hot air moves through it, causing a decrease in overall pressure and total temperature. The work extracted by the turbine turns the shaft and powers the compressor. The arrangement of components shown in Figure 1 approximately matches that of the JetCat P400.

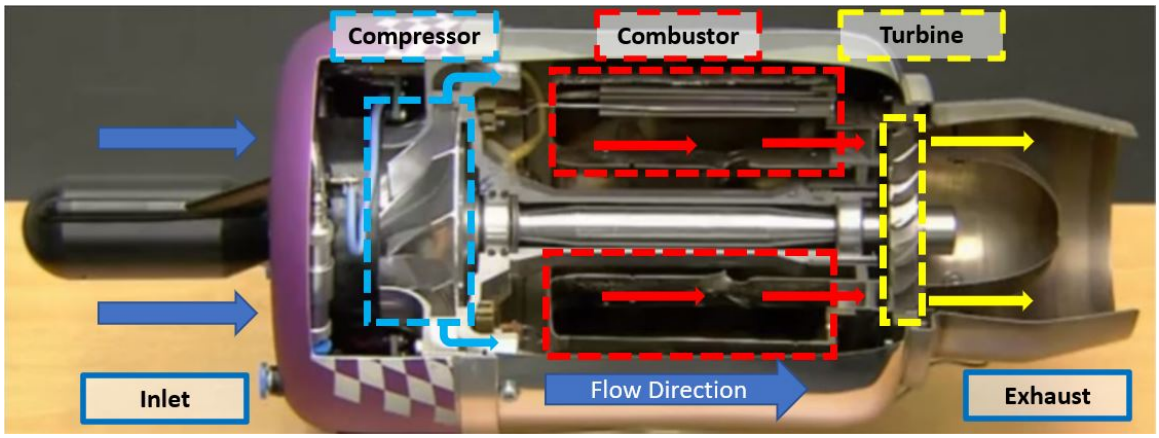

Figure 1. A cutaway of the JetCat P90 RXi showing key components of the engine. [2]

Ceramics offer the ability to maintain similar strength parameters to metals while withstanding much higher temperatures. This allows for the ability to increase power, as more fuel is injected into the combustor increasing the equivalence ratio and causing even higher turbine inlet temperatures (T_4), leading to an increased flow velocity. The increased velocity allows more work to be extracted by the turbine rotor and leads to a higher thrust output. The current inconel turbine rotor has strength degradation at higher temperatures, which limits the power and thrust achievable in the JetCat P400 below what may be necessary to power remotely piloted vehicles. In order to get an increased thrust and power output the metal turbines have to be replaced with a material that can withstand a higher T_4. Ceramic turbine rotors have been manufactured to allow such increase in performance output, but have been complex and costly to produce until recently.

AFRL recently worked with Brigham Young University (BYU) to design and

analyze, through Finite Element Analysis (FEA), a ceramic turbine rotor, as shown in Figure 2, made from Silicon Nitride (Si_3N_4) to replace the current turbine rotor in a JetCat P400. The ceramic turbine rotor had to meet centrifugal loads at 90,000 RPM and a thermal profile of 1315°C (2400 °F) at the blades with 427°C (800 °F) at the shaft. The present research sought to optimize the turbine rotor design analyzed by BYU for manufacturing as well as produce a ceramic turbine capable of being tested in a JetCat P400 engine as a proof of concept for producing cheaper ceramic turbine rotors for testing purposes.

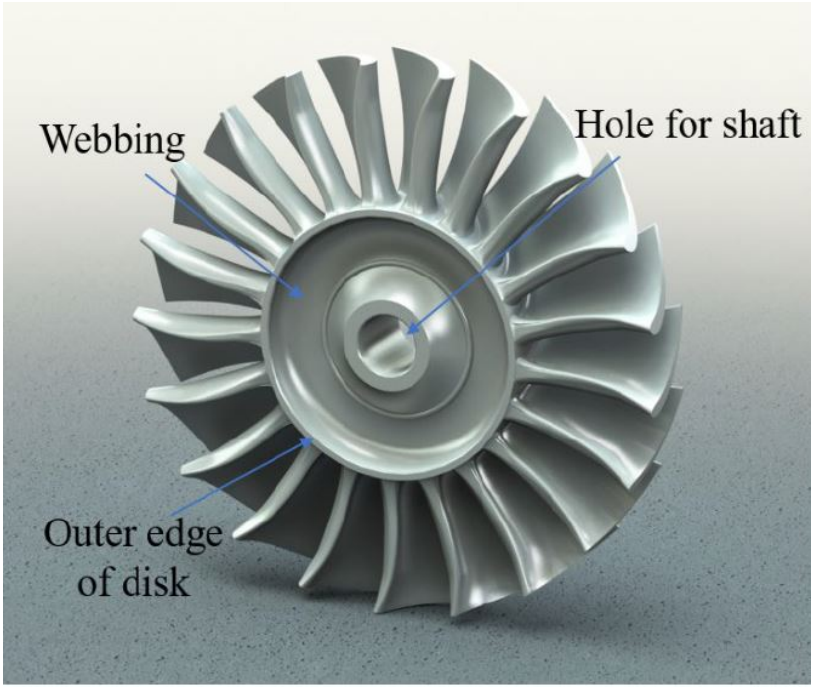

Figure 2. Final BYU turbine rotor design. [3]

1.2 Ceramic Manufacturing

Currently, manufacturing processes of ceramics require high tooling costs, lengthy timelines for ceramic production, and complexities in processing make it difficult for large scale manufacturing of complex ceramic designs, which has prevented ceramic

turbines from being used on a wider scale in engines. Small-scale engines are considered expendable, so any modifications that cause a large increase in cost is a major detracting factor. Traditional methods in ceramic manufacturing, such as investment casting, can take anywhere from 9 to 14 weeks.[4] This is predominantly due to the time it takes to produce a metallic mold for casting purposes which also adds to the high cost of material used.

With the implementation of 3D printers, research in manufacturing complex ceramic designs has shown potential to greatly reduce tooling costs and timelines. The two most researched methods include gelcasting, described by Huang et al.[5] and Wu et al.[6], and injection molding, described by Rueschhoff et al.[7], both of which utilize 3D printed molds that can be filled with a ceramic slurry. These printed molds replace the multi-piece metal molds that were originally utilized cutting down the timeline for mold production from 6 to 14 weeks to 1 to 2 days, and use a much more cost-effective material.[4] Utilizing 3D printed molds along with the gelcasting and injection molding process has shown a lot of promise for large-scale manufacturing.

Along with 3D printing molds for casting and injection molding of ceramics, some 3D printers are now able to print ceramics themselves. This allows for the ability to directly print a complex ceramic shape without concerns of material adhering to the mold surface, and can potentially eliminate defects caused from casting or injection molding. Every processing method poses unique challenges, and each technique will influence the overall outcome and strength parameters of the ceramic. Therefore, knowing the required strength characteristics will be important when determining what method to use, along with trying to eliminate defects incurred during the processing of the ceramic.

1.3 Objectives

The primary goal of this research is to develop a manufacturing method that produces a ceramic turbine that can be tested on a JetCat P400 engine, utilizing the design produced by BYU in conjunction with AFRL as the starting point. This requires four sub-objectives to reach this goal:

1. Use FEA on the preliminary turbine rotor design to determine failure points.
2. Identify a suitable manufacturing process for a turbine rotor employing methods of casting with an aqueous Si_3N_4 slurry and 3D printing with alumina.
3. Analyze the turbine rotor "as manufactured" geometry with FEA, to determine failure criteria in a JetCat P400 relevant environment.
4. Experimentally quantify material properties.

In support of Objective 1, FEA of the turbine rotor design produced by the BYU team will need to be altered to meet the design requirements given by AFRL based on the expected strength parameters from Rueschhoff et al.[7] Further changes to external parameters and design alterations will need to be conducted to ensure requirements for a Si_3N_4 turbine are met.

To produce the turbine to support Objective 2, two manufacturing methods will be tested; casting with an aqueous Si_3N_4 slurry and 3D printing of a ceramic with alumina. This will require testing of mold designs and treatments, casting techniques, and slurry designs to optimize a successful low-cost casting fabrication process. For 3D printing, alumina was utilized for the ceramic as a manufacturing proof of concept. Currently Si_3N_4 is in development for 3D printing but not readily available. The testing of print designs and binder processing techniques are required to optimize the 3D printing process, allowing for the determination if this is a suitable low-cost

method for fabrication using Si_3N_4 in the future. Further analysis will need to be conducted for the turbines used by these manufacturing methods.

The analysis in Objective 3, is necessary to determine the correct design and account for the differences in processing between the multiple ceramic materials. The analysis for the fabricated final turbine rotor designs will be necessary compare to actual testing in the JetCat P400 environment, in order to validate the results experimentally.

For Objective 4, testing of the produced turbines and material characterization of the ceramic material utilized will need to be classified and strength parameters determined. The material requires testing to determine final density, yield strength, and shrinkage.

1.4 Contribution

The ground work for research into multiple low-cost ceramic manufacturing techniques for complex geometry parts has already been conducted through gelcasting[5][6] and injection molding with an aqueous solution[7]. Additionally, research has begun in printing ceramic material to form complex shapes.[8] These processes have been shown as solutions for new manufacturing methods and Wu et al.[6] even produced a very simple turbine design. However, none of the researched methods has been applied to build a properly designed turbine rotor that can work in a compact engine. This research seeks to build on previous research, to find a process that is capable of producing a working turbine rotor design that fits and is testable in a JetCat P400 using a manufacturing process that is cost-effective, timely, and scalable for production.

II. Background

With the objective of developing a manufacturing process of a ceramic turbine to be utilized in a small engine, the possible materials utilized need to be understood as well as a deep dive into possible manufacturing methods. Defining the specific Si_3N_4 characteristics of the slurry used for the ceramic will be critical, since different manufacturing processes affect Si_3N_4 mechanical properties and its behaviors. Due to these considerations, it is useful to gain an understanding of the benefits of technical ceramics over metals, how ceramics are made, and basic design considerations for turbine rotors outlined in Sections 2.1. Considerations for joining two dissimilar materials together between the metal shaft and ceramic turbine are discussed in Section 2.2. Further insight into different manufacturing techniques and considerations are outlined in Section 2.3. The material considerations of Si_3N_4 and how different Si_3N_4 development techniques can affect the mechanical properties are outlined in Section 2.4.

2.1 Turbine Material and Design

2.1.1 Material Selection.

Metal alloy turbines are easier to manufacture for many technical uses, but in areas such as aerospace and engines these metal alloys tend to be more dense leading to increased weight and are limited by operating temperature. Technical ceramics, for aerospace and engine applications have lower densities and the capability to maintain similar strength properties to metal alloys while operating at much higher temperatures. To provide a comparison of different material classes and specific material properties, Michael F. Ashby created multiple plots comparing different material parameters known as Ashby plots.[9] The Ashby plot depicted in Figure 3 compares

various materials' strength and density properties together with technical ceramics, grouped in yellow, and metals grouped together in red. When observing the plot, the higher strength technical ceramics such as Silicon Carbide (SiC), Alumina (Al_2O_3), and Si_3N_4 show similar strength properties, between 500 to 800 MPa, to high strength metals such as tungsten, steels, nickel alloys, and titanium alloys.[9] However, the technical ceramics have lower densities than the metals, which make them beneficial in aerospace application in reducing weight.

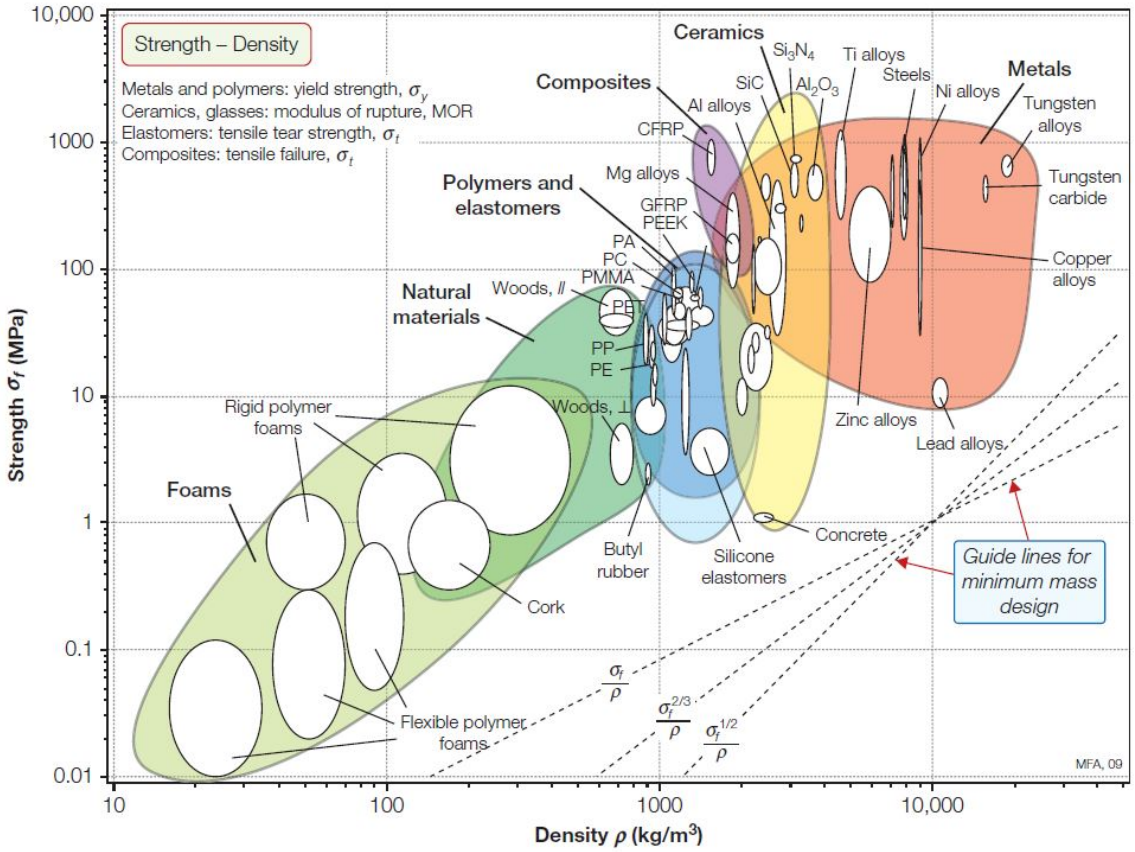

Figure 3. Ashby plot showing materials strength versus density. [9]

The Ashby plot in Figure 4 depicts strength ranges of materials based on their maximum service temperature range with metals highlighted in red, and technical ceramics in yellow.[9] Technical ceramics show a larger maximum temperature capability and little strength degradation compared to metals whose strength profile

varies greatly at maximum service temperature levels.[10] The ability for technical ceramics to maintain similar strength characteristics to metal near maximum operating temperatures allows for increased turbine operating temperatures with limited strength degradation, which increases overall power and thrust output.

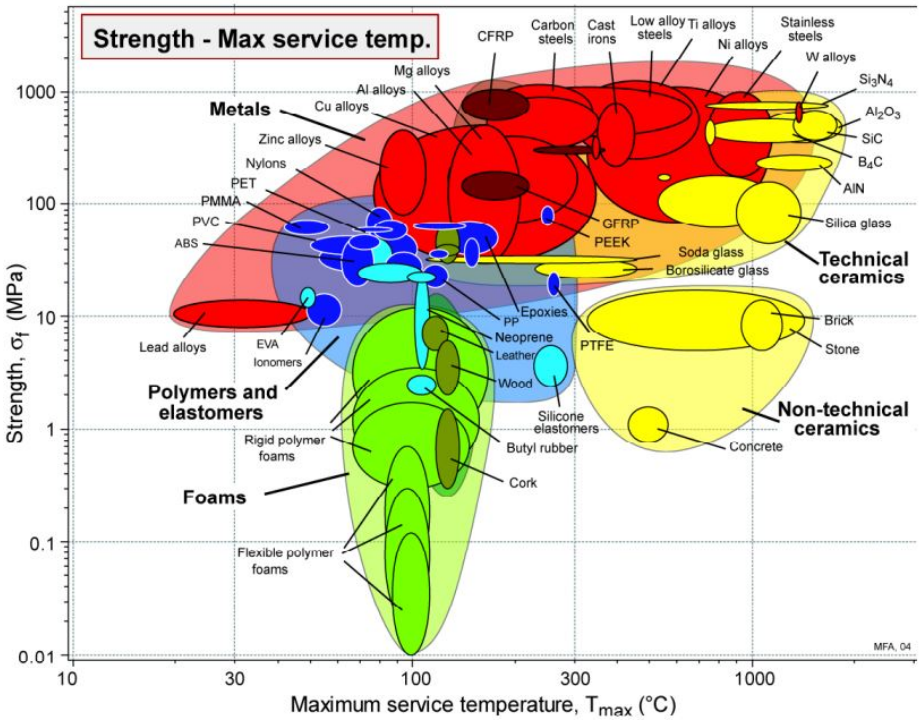

Figure 4. Ashby plot showing material strength vs. maximum service temperature. [9]

A materials specific modulus is compared to the specific strength in Figure 5 by dividing each materials Young's modulus of elasticity and strength by the material's density. The value on the chart presents an idea of the overall "mechanical efficiency" of a material, where the materials higher and to the right on the chart are more efficient.[9] Since technical ceramics are typically stiffer due to their brittle nature and less dense than metals, they have a larger specific modulus and are more efficient for use as a material. While ceramics are more mechanically efficient and maintain better strength properties at higher temperatures, the brittle nature of ceramics combined with complex geometries, such as those of turbine rotors, leads to many manufacturing

complexities that are costly and lengthy. The high costs and prolonged production time for consistently produced complex technical ceramics makes it currently difficult for large-scale manufacturing.

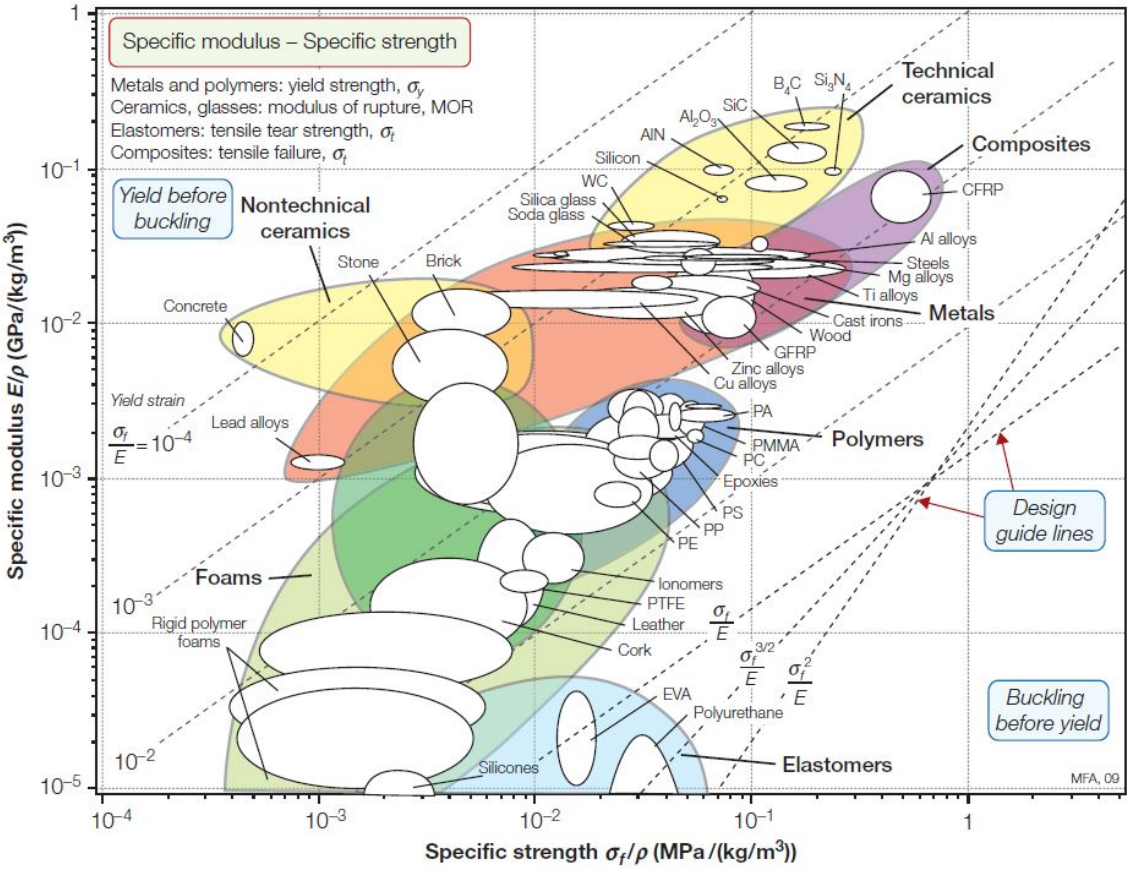

Figure 5. Ashby plot comparing materials specific modulus to specific strength. [9]

To try to make use of the mechanical efficiency of technical ceramics, research in scalable manufacturing has increased in recent years. While metals are formed through metallic bonding and have specific crystalline structures, ceramics are bonded covalently. To form the covalent bonds, all ceramic manufacturing follows the same basic steps akin to baking a cake. Different ingredients and the baking process will affect the overall outcome and properties of the end result. The first step is to mix the required ingredients together, which consist of the raw ceramic material powder

with other sintering aids that will create the bonds when heated to temperature.[11] Additional additives such as Yttrium Oxide (Y_2O_3) or Magnesium Oxide(MgO) are included based on the processing technique or to enhance the material properties of the ceramic. Dry powder ingredients can be mixed together or mixed with liquid to form a wet slurry depending on the forming process, which is the second step. Forming methods such as pressing would typically utilize a mixed powder and press them together into shape, whereas molding would use the slurry to pour into a mold and harden.[12] Once the ceramic is formed into shape it is known as a green body, which is the ceramics state before the final sintering stage. Once the green body is formed it is then baked or sintered in the final stage. The sintering stage causes the covalent bonds to form as the sintering aids react with the raw ceramic material to form the dense grain boundaries of the ceramic.

During sintering, the ceramic is heated above its melting temperature and the powders begin to melt together forming covalent bonds. These bond structures compact into grains through a process called glassification.[7][10][13][14] Upon glassification the material becomes more dense as the grain structure forms a glassy matrix which can be seen in Figure 6 from Zeng et al.[13] The images show the grain structures from the fracture surfaces of two different Si_3N_4 samples. The top two images depict the grain structure of a green body, while the bottom two images depict the densified grain structure after sintering. The sintered images show a more compact grain structure and a smoother glassy surface when looking at the post-sintered sample compared to the coarser green body samples. Additionally, the left photos are of a 45% solid loading sample and the right photos are based on a 52% solid loading sample. Solid loading is based on the percentage of the initial raw ceramic material in the overall powder or slurry of the ceramic. When comparing the different solid loading post sintered images, the higher solid loading sample of 52% has fewer voids,

shown in the white circles. These voids, referred to as porosity, form between grains and are reduced in more densified ceramics.

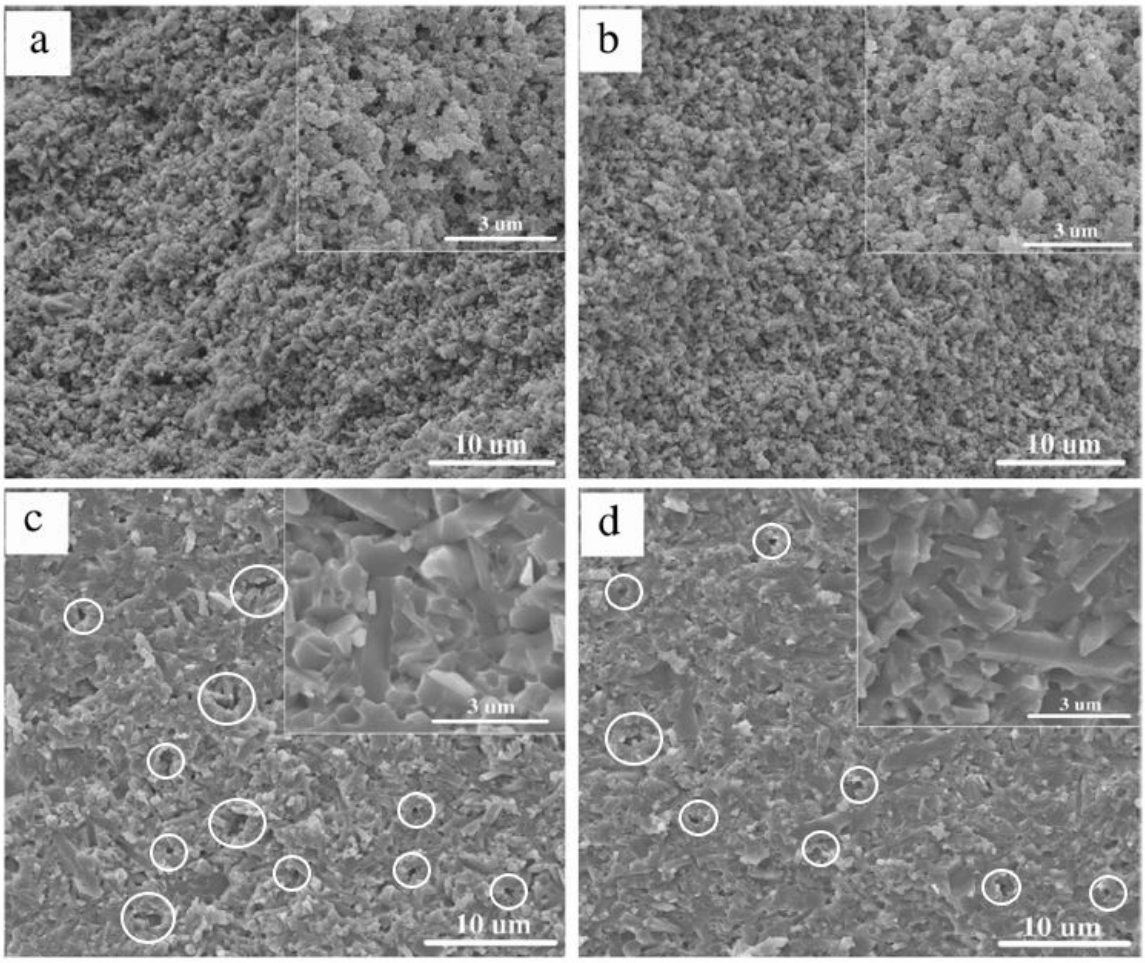

Figure 6. SEM micrographs of the fracture surfaces of the Si_3N_4 green bodies (a and b) and sintered ceramics (c and d): solids loading 45% (a and c) and 52% (b and d) adapted from Zeng et al. [13].

The amount of porosity in a ceramic is based on the number of voids formed between the grain structures in the post-sintered ceramic during densification. Increasing the solid loading, increases densification of the material and decreases the voids incorporated on the molecular level.[5][13] Zeng et al. shows how density and flexural strength are affected by different solids loading in Figure 7. The relative densities of the green body in black and sintered Si_3N_4 ceramic in red at different

solid loadings of 45 vol%, 48 vol%, 50 vol%, and 52 vol% were plotted.[13] The green body has much lower relative densities than the final sintered sample, due to the densification of the covalent bonds during sintering. The plot further shows in both the green body and sintered ceramic, the density increases due to more raw ceramic powder being implemented for bonding purposes. The blue line represents the flexural strength of each solid loading sample. As solid loading increases so does the flexural strength due to the increased densification and reduction of microvoids.[5][6][7][14]

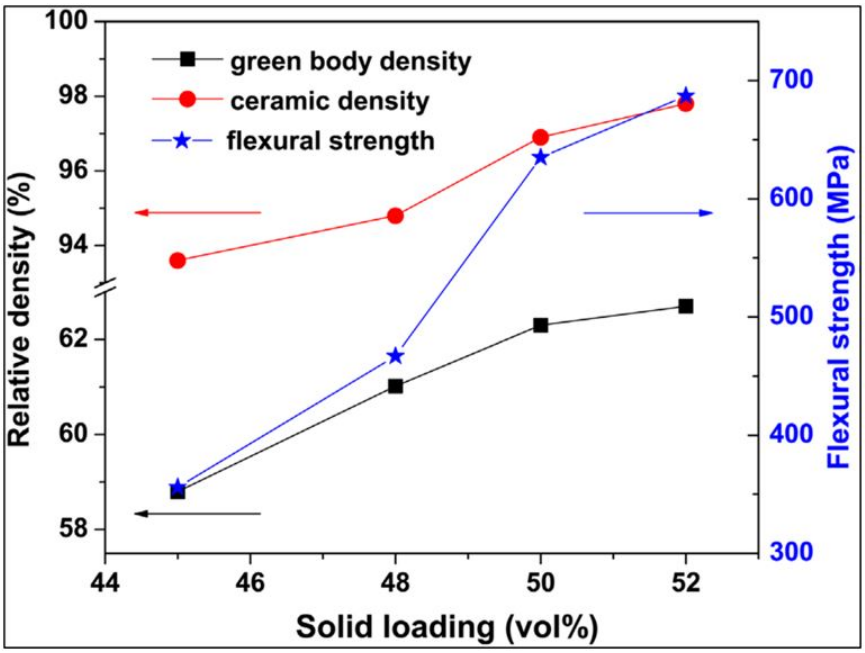

Figure 7. Plot depicting slurry loading effects on density and flexural strength of sintered Si_3N_4 ceramic from Zang et al. [13]

As the ceramic material densifies during sintering it also decreases the overall volume in the material, known as shrinkage. As shown in Figure 8[7] , Rueschhoff et al. shows the difference in size between a Si_3N_4 green body on the left and Si_3N_4 sintered ceramic on the right after shrinkage.The amount of shrinkage that occurs in a ceramic depends on the materials in the ceramic the processing technique.

For the technical ceramic to achieve the strength and higher temperature require-

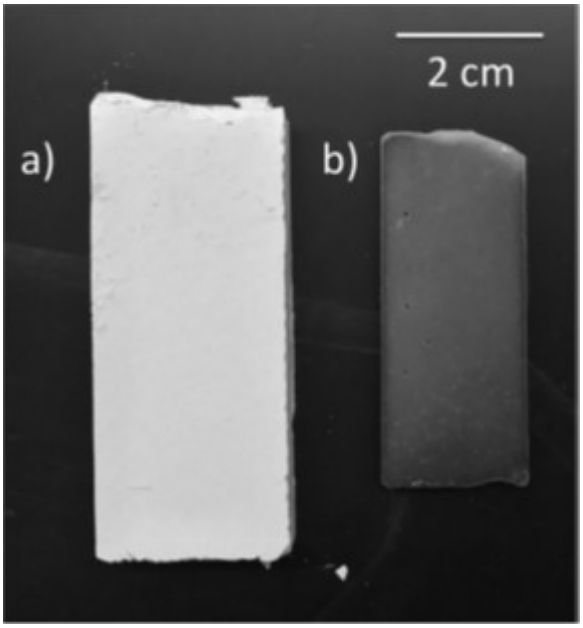

Figure 8. Shows the shrinkage of Si_3N_4 from (a) a green body to (b) post sintering sample from Rueschhoff et al. [7]

ments to replace metal alloys, the manufacturing process must be carefully tailored to handle the complex geometry of a turbine rotor. The manufacturing process must maintain the ceramic strength characteristics by decreasing porosity and accounting for shrinkage on the microscopic level at a consistent mass producible scale. Ceramic production must also be balanced with the complex design of turbine rotors and how the ceramics' brittle nature effects the process on a macroscopic level.

2.1.2 Turbine Rotor Design.

While ceramics higher temperature and strength characteristics allow for an increased power output, their stiff-brittle nature requires careful consideration to the geometric design of the turbine rotor. For the design of the turbine rotor efficiency goals, turbine operating conditions, life and reliability requirements, assembly requirements, cost, and fabrication considerations all must be balanced to achieve a successful design.[15]

Small gas-turbine engines utilize a single-stage turbine configuration with a stator and turbine rotor to translate the high-pressure and temperature from the combustion chamber into extracted power and thrust to drive the engines compressor and move the vehicle. To do this the stator vanes and turbine rotor blades are designed with twist in order to direct airflow in the most efficient manner to produce torque on the rotor. The design of stator and turbine rotor blades are done with velocity triangles shown in Figure 9.[16] As air moves through the stator vanes the flow is directed in a tangential direction (V2) against the turbine rotor blades. The static pressure decreases causing an increase in the tangential velocity (V2) of the airflow as it approaches the turbine rotor. As the air flows through the turbine rotor the exit velocity is decreased (V3) and forces are exerted on the rotor blades which translate into torque due to the change in the direction of the flow. Relative to the moving rotor blades there is an acceleration of airflow (V3R) due to the decrease in static pressure across the turbine stage. Total values are also decreased as energy is removed from the flow in the form of work.[16]

Since there is a favorable pressure gradient across the turbine, stator and rotor blades are able to be designed with high angular changes to create larger pressure and temperature changes to achieve more work extraction in fewer stages.[16]

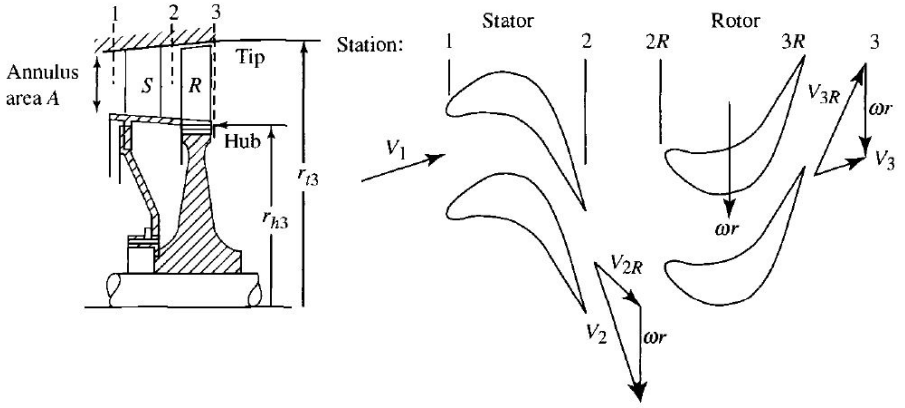

Figure 9. Diagram of single stage turbine and velocity diagram from Mattingly. [16]

Classic turbine designs usually place the material in tension due to centrifugal force, but ceramics are much stronger in compression than tension leading some researchers to design ceramic turbines in compression.[12][17][18] Tradeoffs need to be considered when designing a turbine in tension or compression. Assembly requirements can drive a decision towards what type of turbine will be developed. If a turbine is being developed as a replacement for an existing engine part, then a turbine under tension may be the only option. However, if the requirements allow for more redesign of the turbine stage, then a ceramic turbine in compression may present more opportunities. Choosing to design a turbine in tension or compression will drive different considerations for blade orientation and hub design in order to mitigate effects from the thermal and rotational stresses. Additionally, the more complex a design, the higher the chances defects get introduced during the fabrication process.

2.1.2.1 Turbine in compression.

To take advantage of ceramic's higher compressive strength, Landry et al.[18] developed a turbine in compression known as an inside-out turbine. As shown in Figure 10, an inside out turbine consists of a flexible hub, ceramic blades, metal rim insulation layer, and composite rim. The flexible hub assists with radial displacement incurred by the expansion of the composite rim from rotational forces.[18] The ceramic blades are placed in compression and fixed between the flexible hub and cooling rings. The cooling rings have air channels that drives cool air through them to prevent the composite rim from exceeding transition temperature and delaminating.[18]

Utilizing FEA, Landry et al.[18] showed the stress distribution throughout the flexible hub to the composite rim. This stress distribution, shown in Figure 11, shows a smaller distribution of 350 to 566 MPa in the flexible hub, 350 MPa at the turbine blades, and 665 MPa in the cooling rings all in blue when compared to 845 MPa

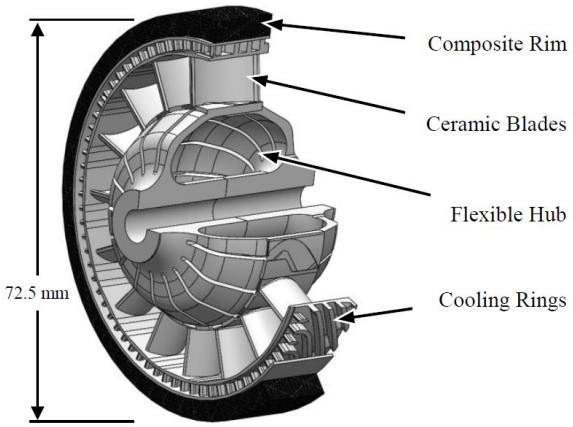

Figure 10. Section view of a turbine in compression from Landry et al. [18]

in the composite rim.[18] Since the blades are in compression, the centrifugal loads are translated into hoop stresses imparted on the composite rim. But, as the rim is composite it has much higher stiffness and tensile strength to resist the forces imparted on it.[18]

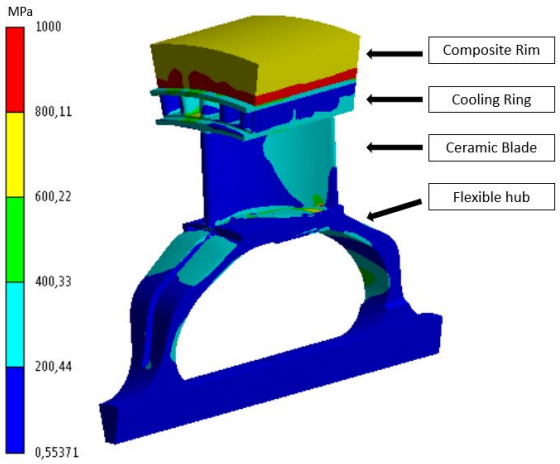

Figure 11. FEA image of stresses on the turbine blade on a rotor in compression adapted from Landry et al. [18]

Landry et al.'s turbine was designed to operate at speeds of 115,000 RPM and a max turbine inlet temperature of 920°C due to a limitation of the metal hub. With more freedom in engine design, inside out turbines offer the ability to handle

much higher stresses in compression than tension. Unfortunately, the metal hub's temperature limits restrict the output potential that could be increased with an entirely ceramic turbine rotor. Furthermore, the complex design of the flexible hub also presents unique fabrication challenges for ceramics. Turbine development in compression is still in its infancy: as they progress, inside out turbines could offer unique opportunities for thrust increase in engines.

2.1.2.2 Turbine in tension.

The turbine rotor for this study shown in Figure 12, is a typical turbine design commonly observed for small aircraft engines. Smaller engines typically consist of a turbine rotor that is a single piece, while for larger engine applications individual blades are produced to connect to a single hub. The turbine rotor consists of the turbine blades which surround the hub, which in turn slides onto the shaft and is balanced by shaving down part of the balance ring. Turbines designed in this manner are typically under tensorial loads from the rotational and thermal stresses imparted on the rotor.

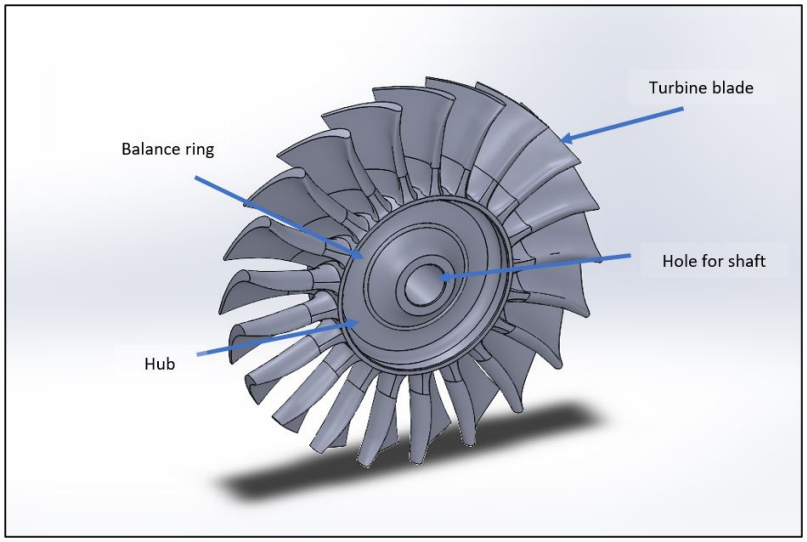

Figure 12. Image of turbine rotor in tension designed by AFRL.

For high-speed turbines similar to this study, the turbine blade loads are typically dominated by the centrifugal forces in the blade root.[3][19] Unlike metals which tend to be ductile, ceramic material is often brittle which requires turbine blades to be thicker to handle the stresses.[15] Thickening the blades may be necessary to strengthen them, but could potentially cause more stress on the hub from the centrifugal forces and increase in mass on the rotors, for this reason the number of blades in a ceramic rotor is typically reduced.[3][15][19] Other techniques can help offset some of the stresses without thickening the blades. Boyle et al.[19] ran FEA on composite turbine blades at high pressure and under centrifugal loading to come up with general design considerations for ceramic blade improvements. Upon initial investigation the stresses in a regular blade, shown in Figure 13a, were found to dominate in the blade root, where the blade attaches to the hub, and on the leading and trailing edge annotated in red. In the analysis, Boyle et al. offset the position of the blade tip from the blade root by varying distances creating a slight side angle in the blade. By offsetting the tip of the blade, the stresses became more evenly distributed, Figure 13b, and reduced the overall stress by 76%.[17] In this study, an offset of 0.3 inches proved to be the optimized position, since further offset began to increase the stresses along the side of the blade.

Since most of the blade stress is carried in the blade root, adding a fillet and increasing the fillet size has also shown to decrease the stress in that region as shown in Figure 14. A larger concentration of stresses at the blade root is seen on the side, that is reduced and more evenly distributed when the fillet is added. Boyd et al. found a 20% decrease in tensile stress when increasing the fillet size to 10% of the span around the blade root. While this is a smaller impact, it still provides a reduction in stresses by reducing the stress concentration at the root. However, as the fillet increases the total number of blades around the hub will be reduced.[3][19]

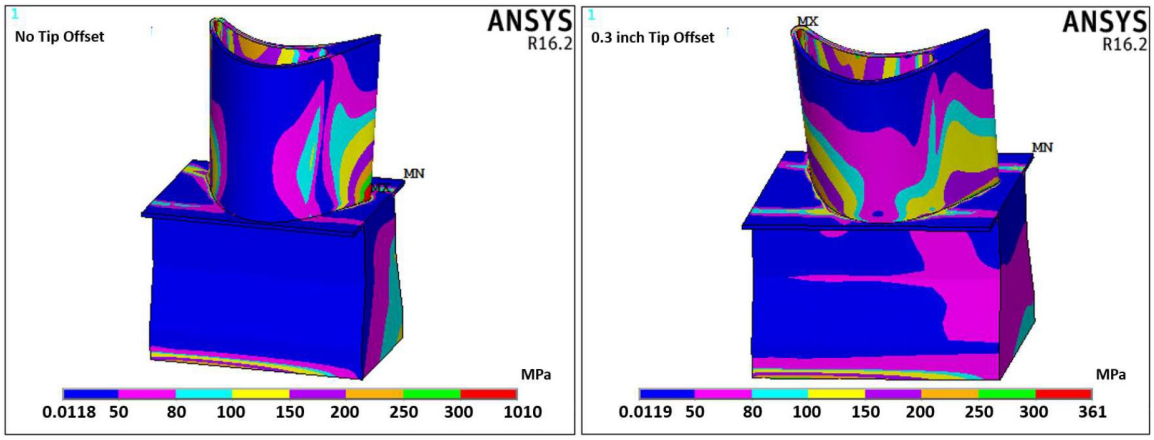

(a) No tip offset. (b) 0.3 inch tip offset.

Figure 13. Turbine blade stress tip offset analysis by Boyle et al. [19]

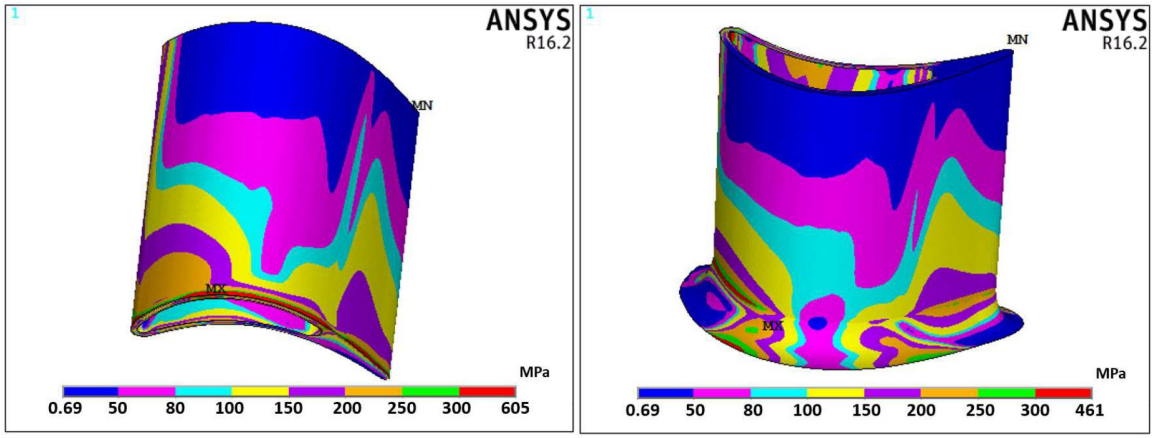

(a) Blade without a fillet. (b) Blade with a fillet.

Figure 14. Turbine blade stress fillet analysis by Boyle et al. [19]

Stresses in the hub of the turbine rotor also have to be taken into account. The BYU turbine design team analyzed the initial ceramic turbine this study is based on. For the blade stresses, they had similar findings to Boyle et al.[3][19] When analyzing the entire turbine rotor, the middle of the hub and the bore had the highest stresses due to the combination of thermal and centrifugal loads.[3] To reduce stress in the middle of the hub an asymmetric U shape was added in the webbing denoted in red in Figure 15. Decreasing the webbing area near the outer edge while thickening the

webbing area near the shaft region showed a decrease in stress around the bore. To decrease stress in the shaft region the team found that by increasing the axial thickness of the webbing in the middle of the hub, the hub stress would decrease, but the shaft stress increased.[3] After evaluating the tradeoffs, this led to their recommendation of an optimized solution of 3.81 mm web thickness in the center shown in Figure 15.

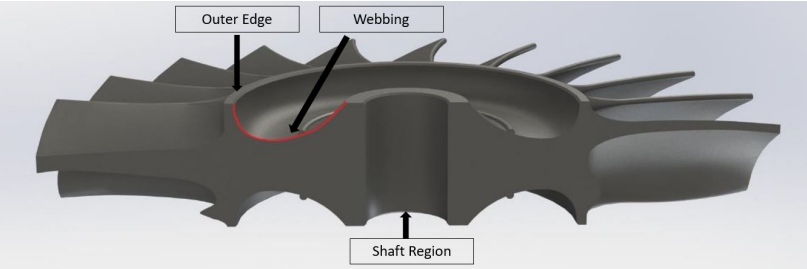

Figure 15. Cutaway image of the turbine rotor showing varying hub thickness. [3]

Another consideration in engine design is tip clearance between the turbine blade and casing. Engine efficiency increases as the tip clearance decreases. While a turbine in compression does not have a tip space loss, a turbine in tension does. It is beneficial to reduce that tip gap as much as possible, but the material still needs room to expand due to thermal growth and blade contact with the engine casing would be catastrophic, causing the blades to break. Research has been conducted to try to eliminate that space by adding a shroud on the top of the blade.[19][20] Boyle et al.[19] looked to utilize a three-finger shroud on thin material to help eliminate this tip space as shown in Figure 16. Their analysis found that maximum stress was located on the top of the turbine blade near the front edge where it met the shroud by the front finger seal caused by bending from the centrifugal forces.[19] The maximum stress can be seen in the left finger seal in red where the shroud rests on the blade. Efforts to thicken the shroud would impart more forces onto the blade.[19] While a shroud may offer the ability to remove tip clearance, careful consideration must be taken to the additional centrifugal forces imparted on the blades, and increase in design complexity.

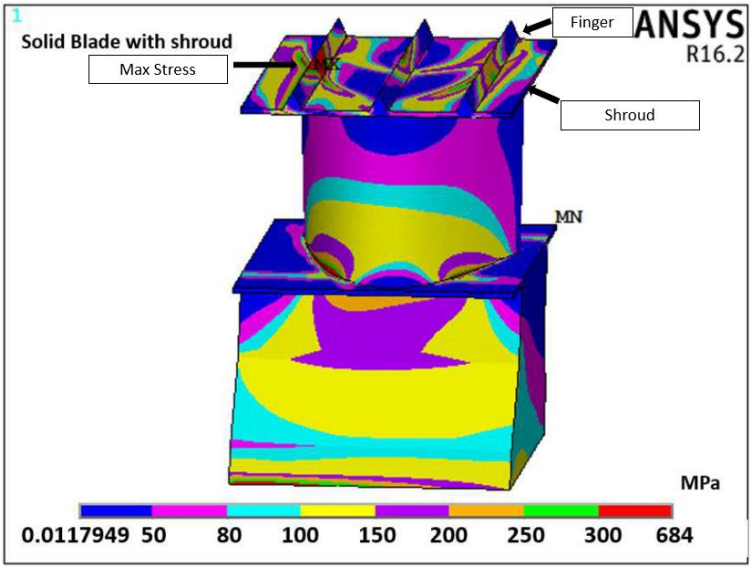

Figure 16. Turbine blade FEA with three finger shroud adapted from Boyle et al. [19]

2.1.2.3 BYU Team Results.

The turbine design that was utilized by this research was developed by John Clark from AFRL in conjunction with BYU who analyzed the design. The team worked through multiple redesigns to optimize stress performance of the turbine rotor. This ceramic turbine was a replacement for stock hardware in the JetCat P400 and was planned to be made of Si_3N_4, operate at 1,200°C, 450°C above the stock turbine operating temperature, and spin at a rate of 90,000 RPM. Additionally, the turbine had to be of similar size to the turbine it was replacing in the JetCat P400 engine to ensure fit. The stress analysis for the combined thermal and centrifugal stresses for the final design was presented as a factor of safety plot and is shown below in Figure 17. The plot shows the failure regions, represented in orange, located in the center of the hub and shaft region, based on a yield criteria of 206 MPa (29,900 psi).[3] The yield criteria utilized is low for Si_3N_4 which is typically 2.5 to 4 times the value used depending on how it is processed. The yield strength used for the present study is based on the work of Rueschhoff et al. and selected as 600 MPa (87,000 psi).[7]

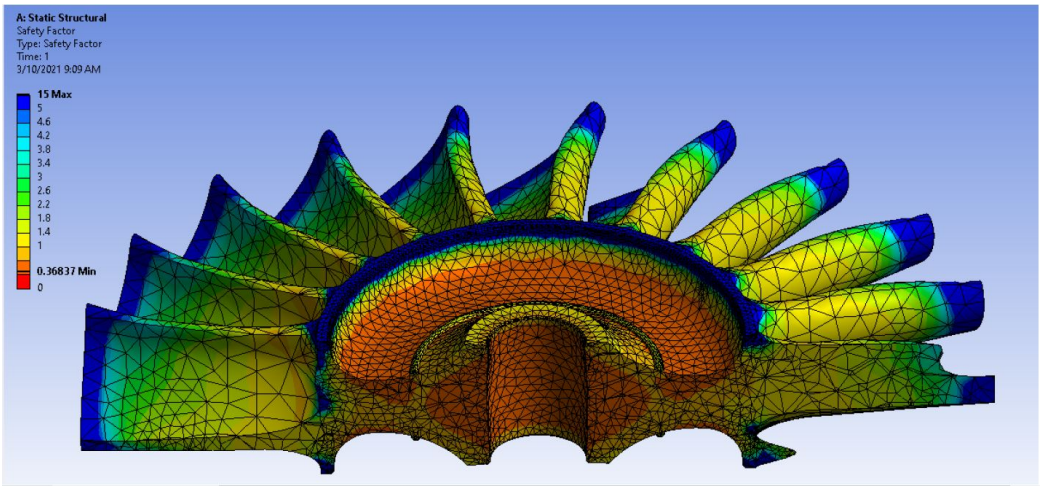

Figure 17. Factor of Safety analysis of the turbine with combined thermal and centrifugal forces by the BYU team. [3]

The BYU team additionally ran simulations for centrifugal and thermal forces separately. The centrifugal force simulation, denoted in Figure 18, showed maximum stresses ranged from 344 MPa (50,000 psi) to 541 MPa (78,564 psi) in both the shaft and hub region. However, the analysis does not specify where exactly the maximum stress takes place. While the thermal stress analysis, denoted in Figure 19, showed a maximum stress range in the shaft from 169 MPa (24,581 psi) to 204 MPa (29,595 psi). Based on the principle of superposition, this means the maximum stress would be expected in the shaft region and, would range from within limits at 514 MPa (74,581 psi) to failure at 745 MPa (108,159 psi).[3]

Upon completion of the stress analysis, the team recommended further design improvements for the turbine. For the hub, potentially varying thickness in certain areas in the middle of the hub could offset stresses, as well as altering the radius of curvature throughout the webbing. Within the blades, it was recommended to increase the hub to blade fillet size again, but cautioned blade number would need to be reduced further. This reduction in blade count could force a change in the blade geometry to extract the same work with less blades. Instead, potentially thickening

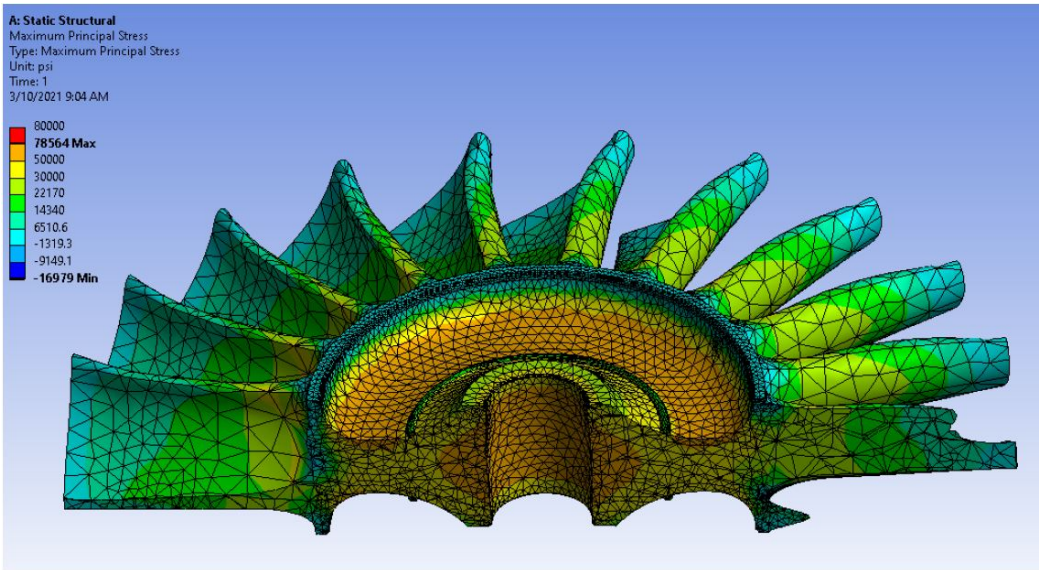

Figure 18. Centrifugal analysis at 90,000 RPM of the turbine rotor by BYU. [3]

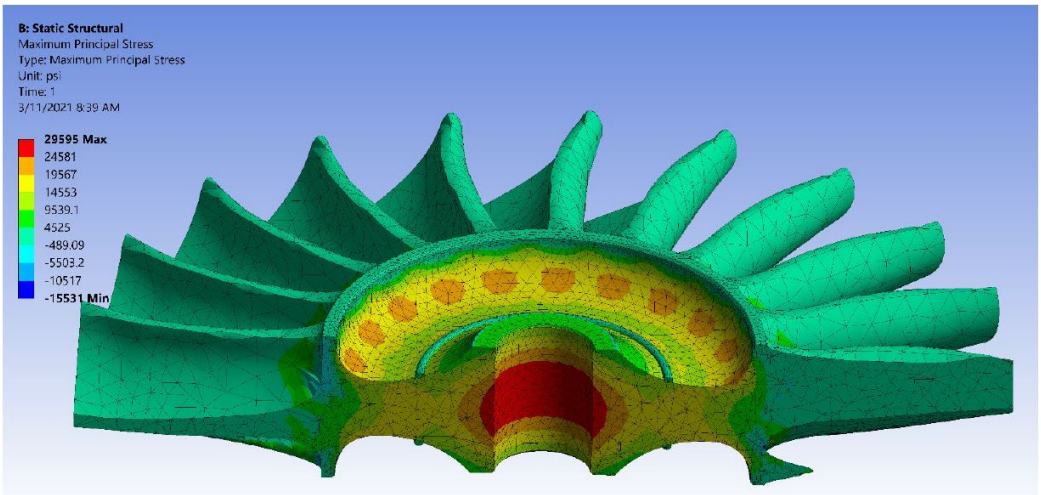

Figure 19. Thermal analysis at 1,200°C of the turbine rotor by BYU. [3]

the trailing edge of each blade, which is the thinnest part of the blade, could have better effects.[3]

The work of the BYU team was useful in providing a starting point for the present research. The stress analysis shows that this turbine design is potentially within the material capabilities of Si_3N_4 when using the larger values of strength parameters.

Further analysis is required to determine if the rotor design meets criteria or if redesign in the hub may be necessary to reduce stress in the shaft region and allow flexibility for strength reduction from potential defects incurred during the manufacturing process. Also, the BYU analysis did not consider the thermal stresses induced on the ceramic components from the thermal expansion of a steel shaft. Understanding the forces imparted from the shaft's expansion will also lead to design considerations of an interference for coupling the ceramic turbine to the shaft, while ensuring concentricity after thermal cycling.

2.2 Ceramic Metal Interfacing

Coupling a ceramic turbine to a steel shaft requires further design considerations, due to the difference in coefficients of thermal expansion. The Ashby plot in Figure 20 shows how metal thermal coefficient of expansions compare to technical ceramics. It can be seen that steels and titanium alloy's, which are metals that typically make up shafts in engines, expand much greater than ceramics made of SiC or Si_3N_4 leading to thermal residual stresses in the interface between the shaft and turbine rotor. These residual thermal stresses occur due to a change in volume from expansion and shrinkage from the heating and cooling, difference in coefficient of thermal expansions, and stresses from thermal differential rates induced by a temperature gradient.[21]

As the engine shaft temperature heats up, the metal expands and compresses the ceramic. Since the ceramic expands at a slower rate than the metal, the ceramic begins to crack at the joint.[22][23] Figure 21 shows how the faster expansion of the metal when heated places a compressive force on the ceramic. The cracks form a permanent residual stress after heating is removed, weakening the overall joint leading to plastic deformation of the metal and further fracture of the ceramic, greatly reducing the overall strength of the ceramic.[21]

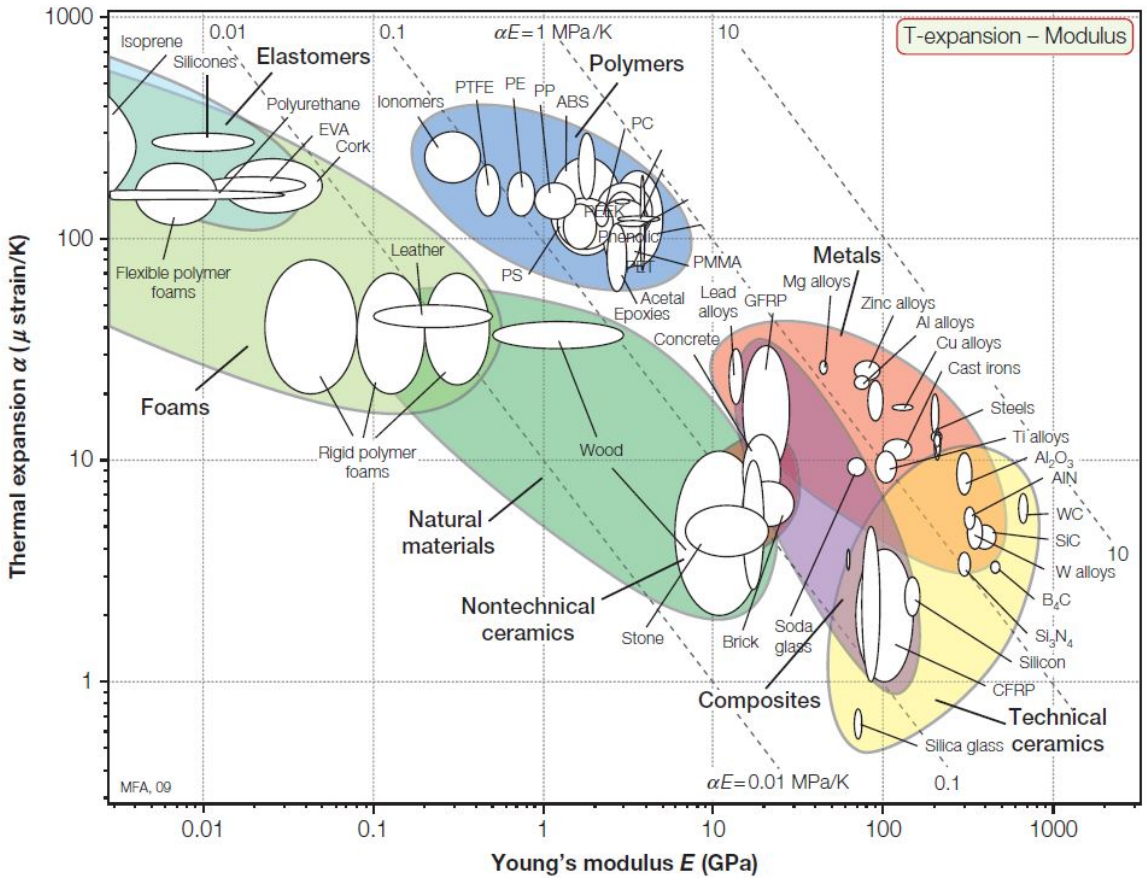

Figure 20. Ashby plot comparing materials thermal expansion coefficient to Young's modulus. [9]

Lemus and Drew[22] recommended three ways to help relieve thermal stress between ceramics and metals: 1) utilize a metal with similar thermal coefficients to reduce the magnitude of stress, 2) use a ductile metal that develops more plastic deformation under thermal stress, or 3) utilize a combination of both. Additionally, Zhou et al.[23] recommended multiple solutions to account for the thermal differences between materials: 1) utilize a soft filler metal with low yield strength, 2) utilize a soft interlayer that is elastic and will plastically deform, 3) reduce residual stress, or 4) use a composite interlayer of hard and soft metals. Both recommendations are utilized when considering the two most common techniques: brazing and shrink fitting.

Brazing is a common technique utilized to join ceramics to metals. The process

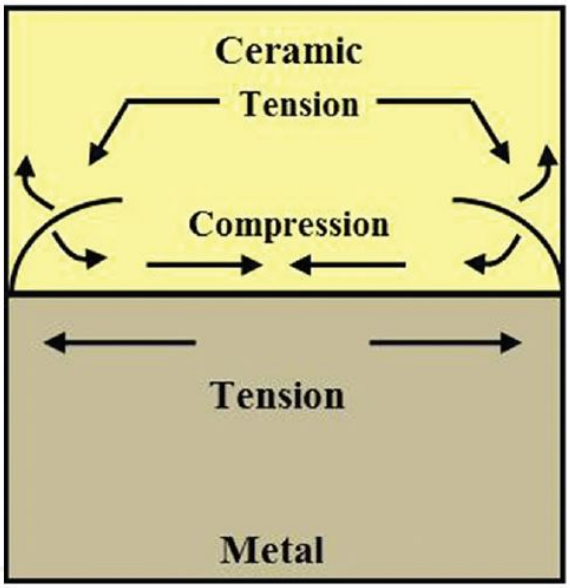

Figure 21. Image of stress caused by larger coefficient of thermal expansion in metal than a ceramic. [21]

joins two types of materials utilizing a filler material. The filler material is placed between the two different materials, then heated just above its melting point so it fills in between the two surfaces forming the composite, shown in Figure 22. The joint is then cooled back to room temperature creating a permanent bond between the materials. This technique is beneficial as a cost effective method and effective for larger scale manufacturing.[21] Some downsides to brazing are that it forms a permanent bond, induces residual stresses if not incorporated correctly, and brazed joints usually can only withstand material temperatures up to 590°C.[15][21] Some of the residual stresses potentially induced through brazing can be overcome utilizing heat treatment, lower joining temperatures, or changing the type of filler metal to bridge the gap between the mismatch of coefficients of thermal expansion.[23]

Another joining technique of ceramics to metals utilizes a shrink fitter, as shown in Figure 23, which keeps contact pressure between the different material at the joint interface through a large temperature range compensating for the difference in

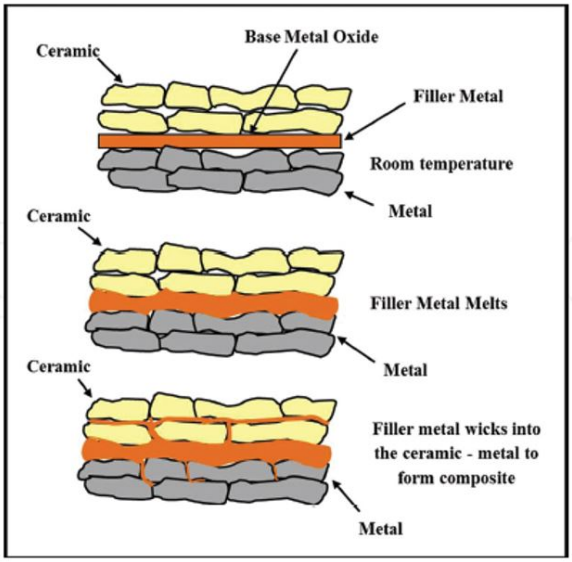

Figure 22. Diagram outlining the brazing process. [21]

coefficients of thermal expansion. An added benefit is the shrink fitter imparts a compressive load on the ceramic where material properties are favorable instead of a tensorial load. Heinrich et al.[24] designed a shrink fitter that utilized a metal outer sleeve, slitted shrink-fitter in the middle, and a ceramic stub in the center connected to the turbine. The outer metal sleeve has a low coefficient of thermal expansion, while the inner shrink fitter has a higher coefficient of thermal expansion. As the device is heated, the axial slits cut down the hoop stresses as the shrink fitter expands, which imparts a compressive force on the stub.[24] Shrink fitters are beneficial because they utilize the compressive benefits of ceramics and they have the ability to operate at higher temperatures unlike the filler material in the brazing techniques.

The difference in coefficient of thermal expansion between the Si_3N_4 turbine and steel shaft needed to be accounted for in this study. Since brazing is permanent and could debond at temperatures near 1,200°C, it is not a technique that can be utilized. Additionally, using a shrink fitter would require designing a new shaft and would not allow for a drop in turbine rotor replacement for the JetCat P400 engine. For

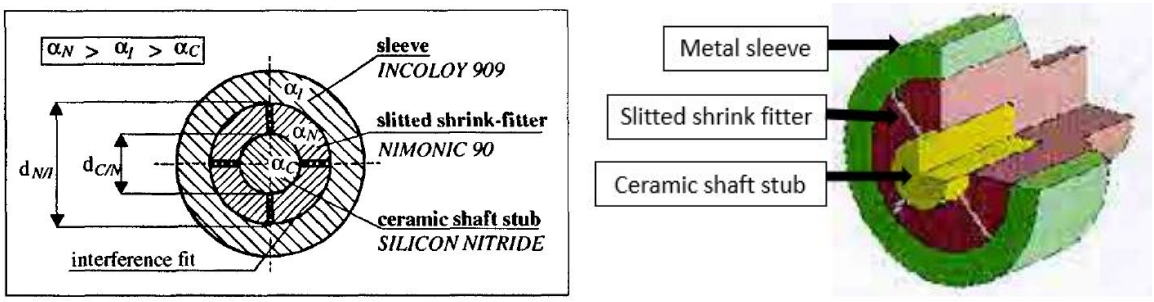

(a) 2D schematic (b) 3D drawing

Figure 23. Image of a shrink fitter with 2D schematic adapted from Heinrich et al. [24]

this study, the shaft is required to fit through the turbine. To join them together, utilizing the techniques of Lemus-Ruiz[22] and Zhou[23], a ductile metal or Teflon could be used as a soft interlayer with elastic properties that can plastically deform under thermal stress. Utilizing this material to act similar to a spring, referred to as a tolerance ring, could help dampen the residual stresses due to the thermal expansion from the steel shaft.

2.3 Ceramic Fabrication Methods

Similar to baking, the manufacturing process and ingredients utilized greatly affect the final characteristics and design of the ceramic.[12] The method of forming the ceramic dictates whether a dry mix of powders will be utilized or if a wet slurry is needed. Forming methods are typically broken down into three categories: pressing, casting, and plastic forming. Some of these methods are denoted below in Figure 24. For large-scale manufacturing and simpler geometries, pressing and extrusion methods are predominately utilized. For manufacturing complex geometries, casting and injection molding are more commonly used.

Pressing consists of uniaxial (die) pressing or isostatic (rubber mold) pressing and are typically utilized for mass producing simpler geometric shapes. Pressing is accomplished by placing the ingredients into the appropriate die or mold and applying

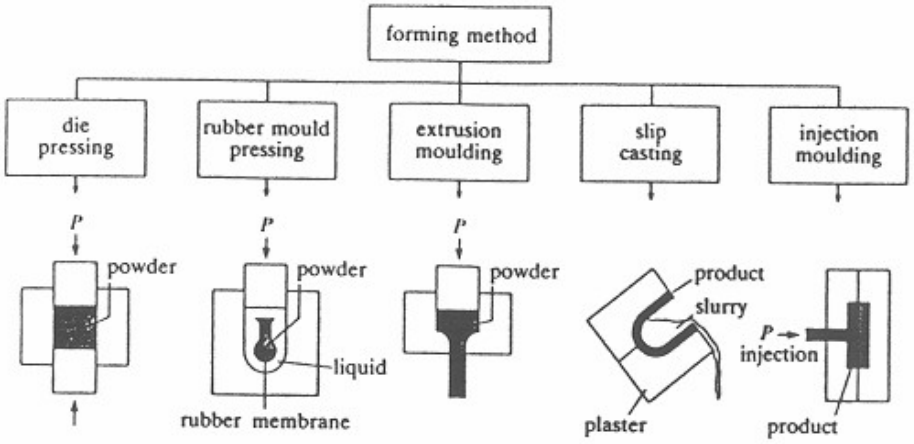

Figure 24. Forming methods from Wasson et al. [25]

pressure to compact ceramic powders into shape. Uniaxial pressing imparts a force on the die to compact the particles, while isostatic pressure systems use hydrostatic pressure to form simple 3-dimensional shapes.[12] Since isostatic pressing is capable of applying pressure in multiple directions, this leads to a more evenly distributed density in the ceramic which tends to be an issue in uniaxial loading.[12] An example of isostatic pressing of a spark plug insulator is depicted in Figure 25. The fluid is pressed into the die around the rubber molding imparting even pressure around the powder. This pressure compacts the powder into shape creating a more uniform density around the spark plug.

Casting is utilized to build both simple and complex shapes using a slurry that is poured into a porous mold at room temperature to form and dry into the final shape.[12] Initially casting methods were costly due to tooling and manufacturing the dye. With the ability to 3D print molds, two more recently researched techniques, gelcasting and soluble-mold casting, have shown the ability to reduce the cost of tooling and material.[5][6][7] Both casting methods follow similar steps forming the ceramic but vary in order to compensate for the different slurry compositions. Gel-

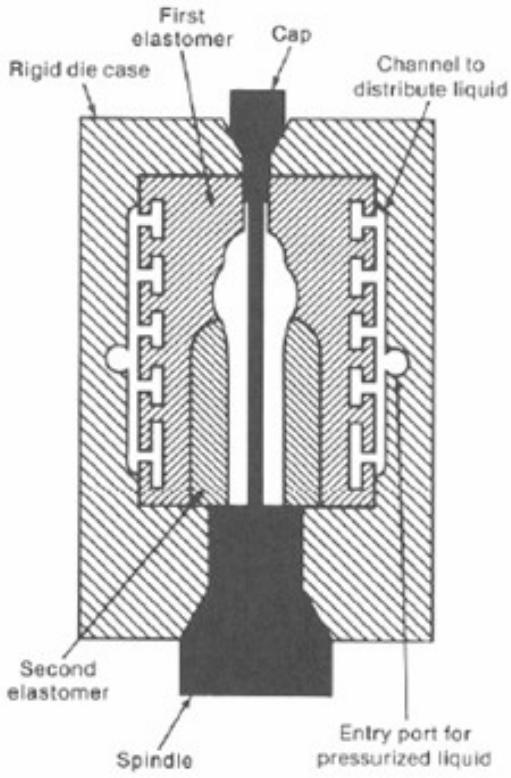

Figure 25. Isostatic pressing of a spark plug insulator. [12]

casting utilizes a more gel based slurry, while soluble mold casting utilizes a more aqueous based slurry.[5][6][7] Both processes for gelcasting and soluble mold casting are shown in Figure 26. For both methods a slurry is mixed and degassed, followed by pouring into a mold to form into shape. Once formed, the green body is dried and demolded through varying processes. The differences between the two methods is the composition of the slurry, which dictates how they are de-aired and dried to prevent defects in the material. Gelcasting requires an initiator to be input prior to casting, and then has the added step of gelation of the slurry while in the mold prior to demolding.

The slurry consists of raw powder, binder material, sintering aids, a wetting agent, and potentially other additives based on material property objectives. The type of wetting agent is dependent on producing an aqueous or gel type slurry, and the ratio of

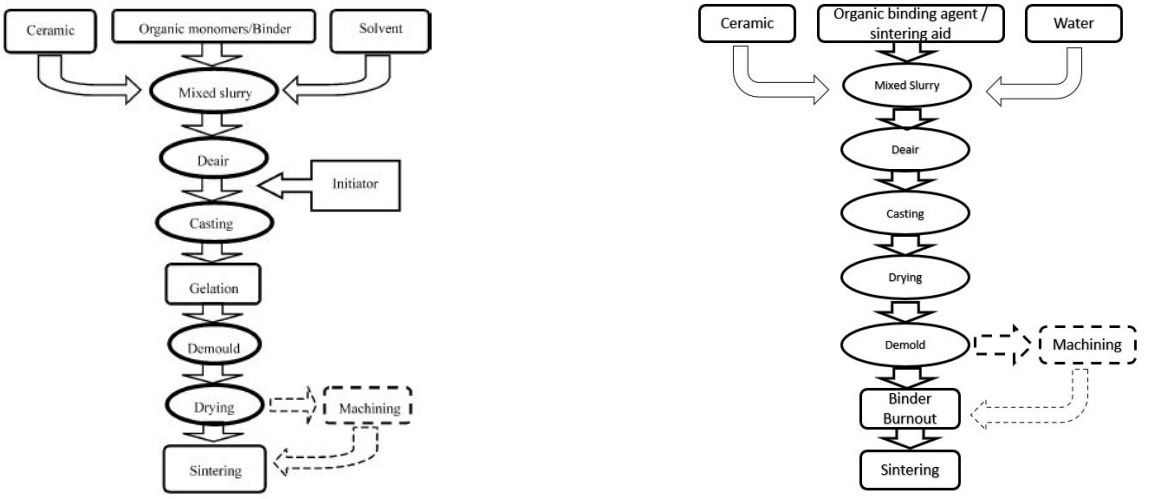

(a) Gelcasting forming process.

(b) Soluble mold casting forming process.

Figure 26. Different casting forming process adapted from Cai et al. [26]

wetting agent to the other material effects the overall rheology, or flow characteristics, of the slurry. The overall solid loading of the material controls the viscosity of the slurry.[12]

The viscosity of the slurry is affected by the solid loading and particle interactions of the raw powders as well as the temperature of the slurry. Huang et al. demonstrated the solid loading and temperature effects by plotting the viscosity against shear rate of an alumina slurry in Figure 27.[5] The left plot shows solid loading at 54%, 56%, and 58% and compare the viscosity to shear rate of the slurries. When comparing the three solid loadings it can be seen the higher the solid loading the higher the viscosity of the slurry. While a higher solid loading increases the strength properties, particles also get closer together and come into contact more often. This contact increases the interlayer forces thus increasing the viscosity making the slurry thicker and harder to pour.[5] The plot on the right side of Figure 27 shows how different temperature profiles effect the viscosity of a slurry at 58% solid loading. The increase in temperature reduces the interlayer forces of particles thus decreasing the viscosity

of the slurry and making it easier to pour.[5] The study found that between 50°C and 60°C, annotated by the blue and light blue lines, the viscous effects were similar. However, once the slurry was at 60°C solvent evaporation began to accelerate, leading to a poorer rheology. Therefore, 50°C was determined to be the optimal solution. When determining the correct solid loading of a material for casting it is important to consider the rheology of the slurry to balance strength properties with pourability effects to ensure the slurry fills the entire mold.[5]

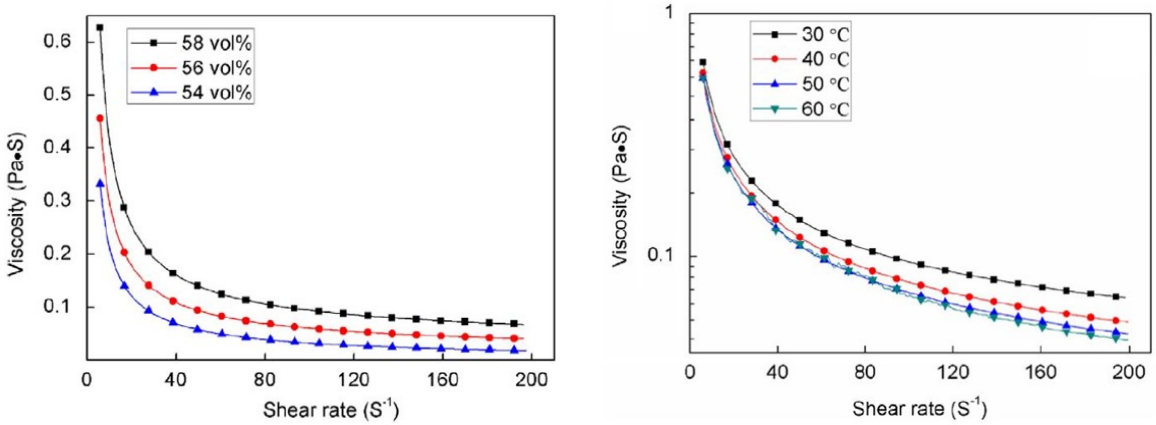

(a) Viscosity plot depicting solid loading effects. (b) Viscosity plot depicting temperature effects.

Figure 27. Plots depicting how solids loading and temperature effect viscosity of the slurry by Huang et al. [5]

Once mixed, the slurry is typically ball milled, shown in Figure 28. Ball milling utilizes milling media, usually ceramic balls, placed in a cylindrical container with the slurry. The container is rotated on rollers and the media grinds the powders into the smaller size. Smaller particles provide a better densification of the overall ceramic.[12]

Once ball milled, the slurry is then de-aired prior to pouring. Gelcasting typically utilizes a vacuum to de-air the slurry.[5][6] For the aqueous slurry de-airing occurs during pouring, since a vacuum would remove some of the water from the solution ruining the overall solution.[7] Once the slurry is ready it is then poured into a porous mold. The porosity in the mold allows the fluid to be removed from either by vacuum

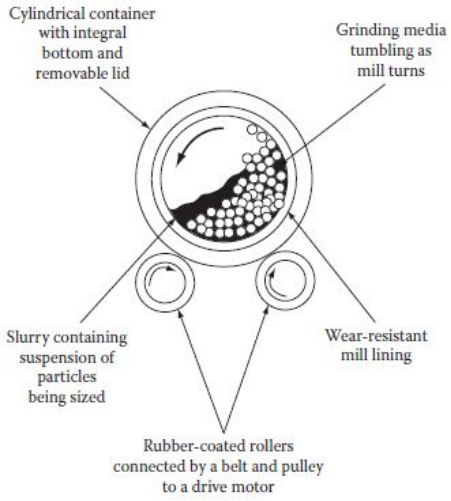

Figure 28. A depiction of ball milling a slurry. [12]

for gelcasting or through evaporation for aqueous slurries. As the slurry dries and materials form into the green body.[5][6][7] This step is heavily controlled to prevent cracking of the ceramic by drying out too quickly. Huang et al. shows effects of different drying conditions for a gelcasting process in Figure 29.[5] Three different turbine rotors were poured and dried under different conditions: room temperature, in air at 60°C, and vacuum at 60°C. The turbine rotors that were dried and formed in air both showed signs of spalling due to oxidation leading to deformation of the blades and hubs. The turbine rotors dried under vacuum in the mold help their shape and were ready for the sintering process.[5] Due to the water that is in the aqueous slurry a slower dryout is required to evaporate the water and allow the green body to harden. Deformation and cracking will also result if the evaporation rate is not controlled during the process.[7] Once the slurry has dried into the green body the mold can then be removed through various means. At this state the ceramic is fragile but is easiest to machine since it has yet to be hardened by the sintering process.[12] Once the green body is machined, if necessary, it is ready for sintering.

The final common forming method is through plastic forming by extrusion and

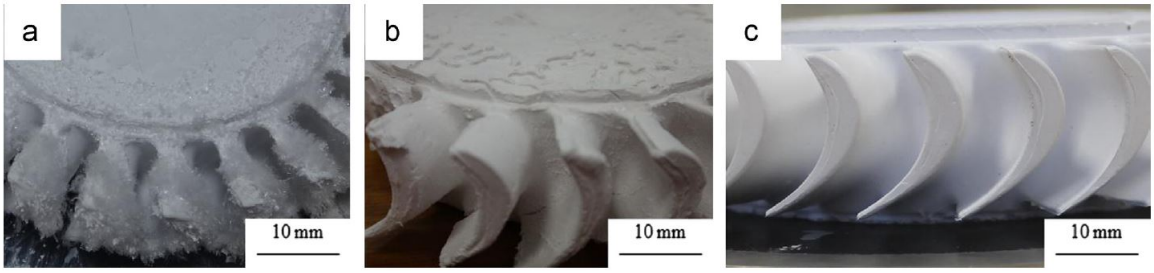

Figure 29. Green body rotors with different drying conditions from Huang et al. study: a) at room temperature, b) in air at 60°C, and c) in vacuum at 60°C. [5]

injection molding. This method utilizes a mixture of powder and additives that deform under pressure to produce various shapes. The goal of the slurry mixture is to have enough plasticity to form the desired shape and is typically a thicker slurry than casting.[12] Extrusion methods are utilized for more simple parts and consistent cross section such as pipes, tile, bricks, and heat exchangers. Similar to pressing, the extrusion process forces a high viscosity clay-like mixture through a shaped die. Instead of compressing a powder into form, extrusion presses the ceramic mixture through a die to form the shape. Figure 30 shows how a piston forces the slurry material through a die forming the extruded product.

Injection molding follows a similar process to casting methods. The main differences lie in the rheology of the slurry and how the slurry is introduced into the mold. For injection molding, the slurry is injected into the mold under pressure instead of being poured into the mold by casting.[7] Since it is under pressure, a thicker, higher solid loaded slurry can be introduced into the mold leading to stronger ceramics. However, rheology effects still must be controlled to ensure there is no clumping in the injector and the mold is completely filled.[7] The drying considerations for an injection molded ceramic are the same as cast ceramics. Once the green body is formed it is ready to be sintered.

Sintering is the stage where the ceramic is formed into its final state by heating

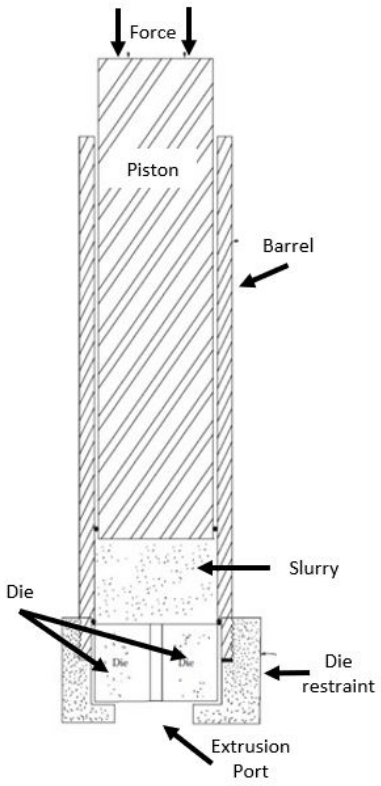

Figure 30. Extrusion process pushing slurry through a die. [12]

it in a furnace and allowing the covalent bonds to form between the ceramic material and sintering aids. Sintering methods are broken down into either pressure sintering or pressureless sintering. Pressure sintering utilizes a furnace at temperature as well as an elevated pressure to help hold the ceramic in shape as it sinters. This is known as hot pressing or hot isostatic pressing depending on the press method for forming utilized. While the powder is being pressed into shape the ceramic is sintered in the furnace under pressure. This typically is a more expensive process due to the cost of tooling and running the furnace. Benefits of combining these methods include potential for minimizing porosity and grain growth and leading to higher strengths when compared to pressureless sintering. It can also reduce the amount of sintering aids required.[12] Pressureless sintering occurs in a furnace at lower temperatures and ambient pressure. The ceramics are able to densify at lower temperatures based on

sintering aids added to the mixture.[12] This method typically is useful and much lower cost due to the more simplistic furnace and is utilized primarily for casting and injection molded methods.[5][6][7] For powder material, pressure sintering by hot pressing or hot isostatic pressing can utilize a one-step sintering process. Since pressure is already being applied and there is no wetting agent, there is no need for the dryout process necessary for a slurry.

When a slurry is utilized, it is crucial that the sintering process is broken into a two-step process: binder burnout to remove the binding agent at a lower temperature and final sintering to form the covalent bonds. This requirement is due to the addition of binder material to form the green body in the slurry, which must be removed prior to the final sintering stage so that it does not affect the covalent bonds between the raw ceramic powder and sintering aids. Huang et al. studied what happened to an alumina rotor when the binder burnout stage and final sintering stage were combined into one continuous process.[5] For a slurry tested with the one-step process binder burnout was conducted up to 600°C for 1 hour then continued immediately to the sintering stage of 1600°C with a 4 hour dwell time. Since the sintering stage was continued after the binder burnout the rotor was not able to utilize a powder bed for sintering while the two-step process could utilize it. The comparison of the normal two-step process and the one-step process are shown in Figure 31. The results showed major cracking and deformation in the turbine rotor created in the one-step method on the left image while the two-step sintered turbine was intact. Sintering is a very controlled process similar to drying out. If done too fast it can cause cracking due to evaporation and gas elimination or uneven heating. To help prevent this, pressureless sintering typically utilizes a powder bed to assist with controlling the heating, evaporation, and gas elimination of the ceramic.[5][6][7] The lack of a powder bed in the one-step method further led to less control of the overall process.

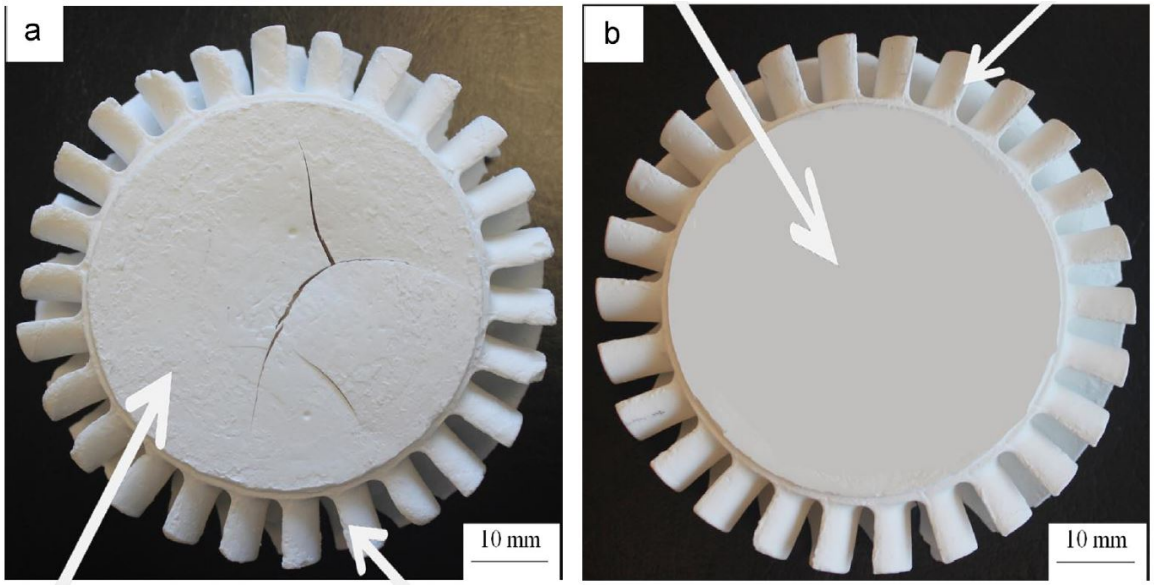

(a) One-step method (b) Two-step method

Figure 31. Sintered turbine rotors by Huang et al. [5]

During sintering, when the ceramic densifies, shrinkage of the material will occur. The amount of shrinkage is dependent on the ceramic, processing method, and additives in the powder. Wu et al.[6], were able to reduce drying shrinkage by freeze drying the ceramic and reduce sintering shrinkage by increasing the amount of MgO powder in the slurry combined with reducing the sintering temperature. These changes worked well in reducing the drying and sintering shrinking percentages to 0.25% and 1.12%, respectively. The results of the study are shown in Figure 32, where the failed sample with no magnesium oxide is on the left and successful sample with magnesium oxide is on the right. This study shows the importance of carefully controlling the additives and gelcasting process during drying and sintering. Through those controls the study was successfully able to reduce the sintering stresses from excessive shrinkage as the ceramic formed to shape leading to minimal defects in the final sample.

Creating complex geometric parts through casting and mold methods originated from conventional investment casting methods for metal parts. As stated previously,

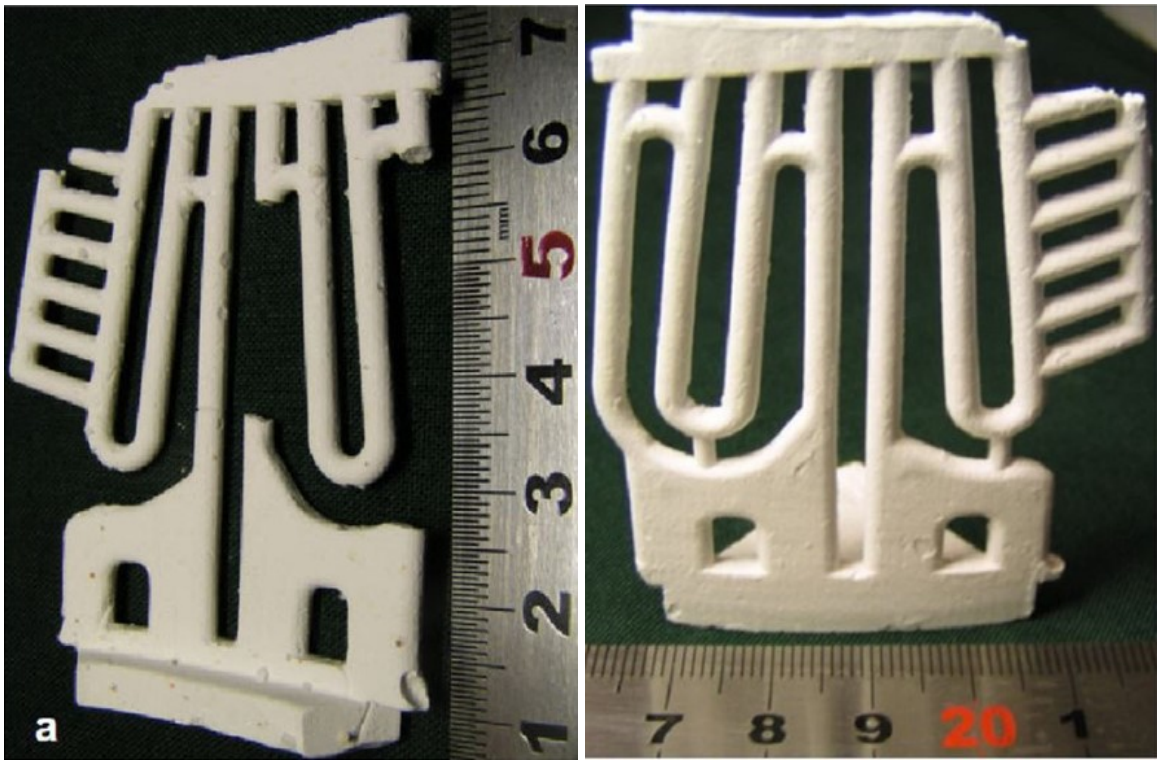

(a) Sample with no MgO (b) Sample with 4% MgO

Figure 32. Sintered defects of a complex shape by Wu et al. [6]

these methods usually required high cost due to tooling and took a lengthy amount of time. While able to cast complex shapes, this method was not useful for large-scale manufacturing techniques. Figure 33 denotes the timeline and process for traditional investment casting. In manufacturing, the computer-aided design (CAD) would be produced and the mold would be machined typically out of aluminum. Next, wax would be introduced into the mold and removed. Then a ceramic shell would be poured around the wax to form a shell and allowed to harden. The ceramic shell, once processed, would then be cast with the liquid metal until cooled into shape. The final product would be knocked out of the mold to be finished, destroying the mold in the process. This process would take 13-21 weeks to produce a metal component.[4]

For ceramics, the process of investment casting was adapted so the ceramic could fill the wax mold to create the final geometric shape instead of the metal. When the

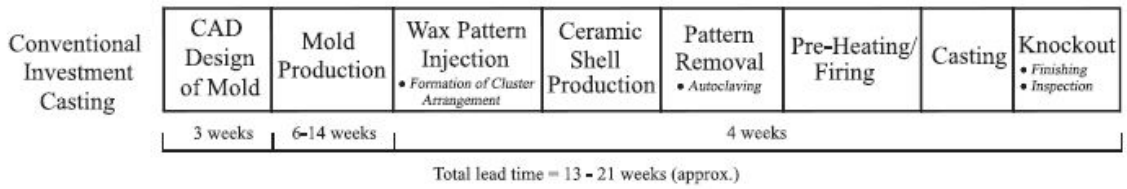

Figure 33. Process of investment casting for a complex geometric metal part. [4]

ceramic was sintered, the wax would melt away leaving just the ceramic as it densified into its final shape in the furnace. However, this process was still costly and lengthy due to initial tooling for mold production and the timeline to develop those tools, making it unfit for mass production.[4] As 3D printing evolved, the utilization of 3D printed molds have shown the ability to decrease molding cost and speed up the timeline for mass production for ceramic materials.[4][5][6][7] Utilizing 3D printing for the mold reduces the 6-14 week mold production from the timeline to 1-2 days as outlined in Figure 34. Once the mold is printed, the remaining time depends on the processing of the ceramic through dry time and sintering until the final part is made.

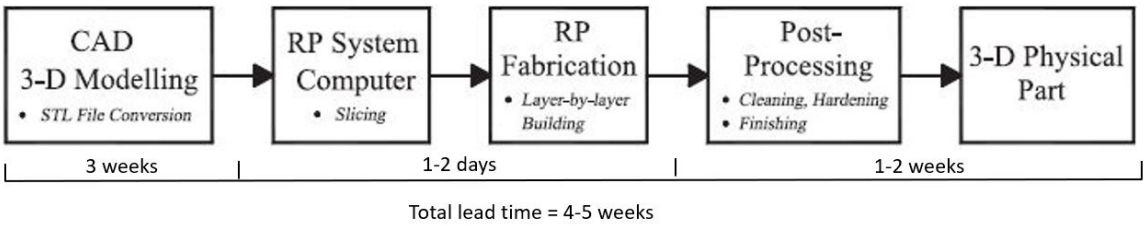

Figure 34. Process of fabricating a part from a 3D printed mold adapted from Cheah et al. [4]

Different types of 3D molds can be utilized based on the ceramic production method. Figure 35 showcases two examples of molds, with the one on the left utilized for a lost mold burnaway method and a multi-part mold on the right designed for pressure injection.[6][7] The mold on the left was built utilizing selective laser sintering (SLS) methods by Wu et al. and designed to burn away during the binder burnout

stage utilizing a lost mold approach.[6] The mold on the right was created more robustly as a 3 part mold by Rueschhoff et al. to combine together, with ports created for injection of the ceramic into the mold.[7] The ability to create a 3D printed mold allows for lower cost and more flexibility in the processing method of the forming stage. Three dimensional printed molds allow for cheaper methods and greater flexibility in design when utilizing different forming methods for a ceramic.

(a) Single piece burn away mold

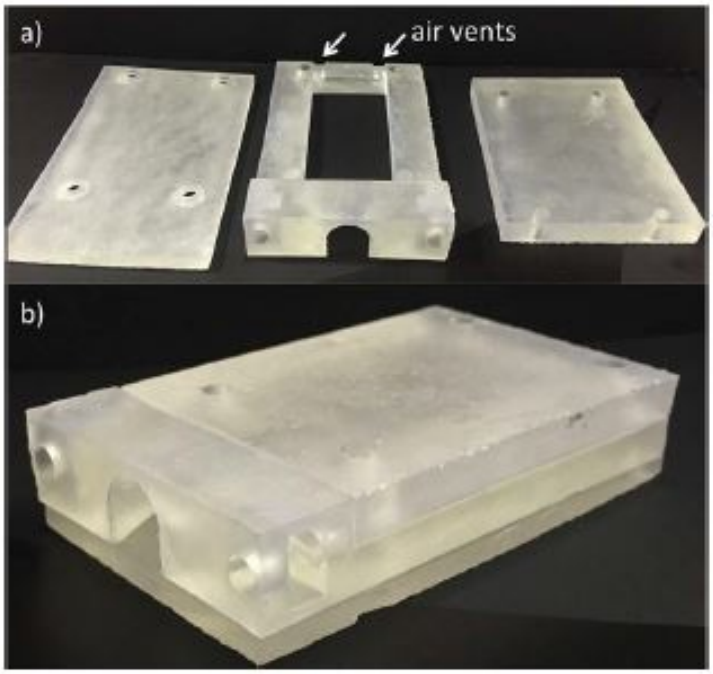

(b) Three part injection mold

Figure 35. 3D printed molds for forming ceramics. [6][7]

Three dimensional printing has evolved past polymers and is now being utilized to research printing complex ceramic shapes directly. Similar to printing the molds with deposition modeling, ceramic 3D printing deposits a controlled flow of an aqueous slurry layer by layer to build the complex shape utilizing a CAD file.[8] Rueschhoff et al. conducted a study on 3D printing evaluating how solid loading utilizing alumina affected the printing of the layers as depicted in Figure 36. The study used a slurry extruded from a computer controlled syringe and evaluated effects on the printed

layers based on solids loading of 51%, 53%, 55%, 56%, and 58% volume. What was found was too little solid loading led to slumping shown in the 51% sample due to an inability to support the structure. However, too high of solid loading led to clumping and uneven heights in the deposited layers.[8] Finding the right viscosity due to solid loading is a key consideration to creating a sample with limited defects. Once the shape is printed, the dryout, binder burnout, and sintering process is similar to the soluble mold casting process discussed previously.[8]

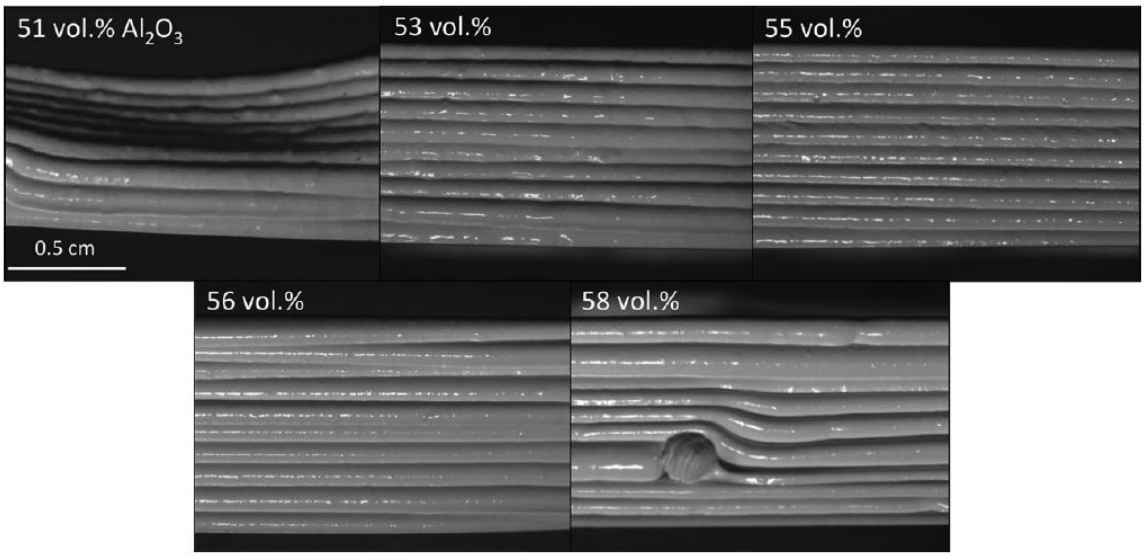

Figure 36. 3D ceramic printed samples at different solid levels by Rueschhoff et al. [8]

Recently, a new large-scale ceramic printing technique was developed called digital light processing, also known as stereolithography based ceramic manufacturing (SLCM), by ADMATEC.[27] The SLCM process utilizes a photosensitive liquid ceramic polymer cured by an image flashed by a high definition projector screen for each print layer. As shown in Figure 37, for each print layer, new material is replaced on the film and cured with the projected layers image, building upon each layer until the ceramic design is built.[27] Once printed, the ceramic part is placed in a water tank to remove the water-soluble binding agent and then undergoes binder burnout to burn

off any remaining polymer. The ceramic is then sintered to fully densify the ceramic. One drawback to SLCM is the potential for delamination of the layers, requiring a careful consideration of design requirements to ensure a successful part. The benefit of utilizing 3D printing is that it removes the mold process entirely and allows the ceramic to hold its shape and dry more evenly over time. This method speeds up the dry time and reduces potential defects that could be integrated by incomplete fill of a mold due to casting or pressure injection. Additionally, printing a ceramic allows for large-scale manufacturing that can further reduce cost and timeline.

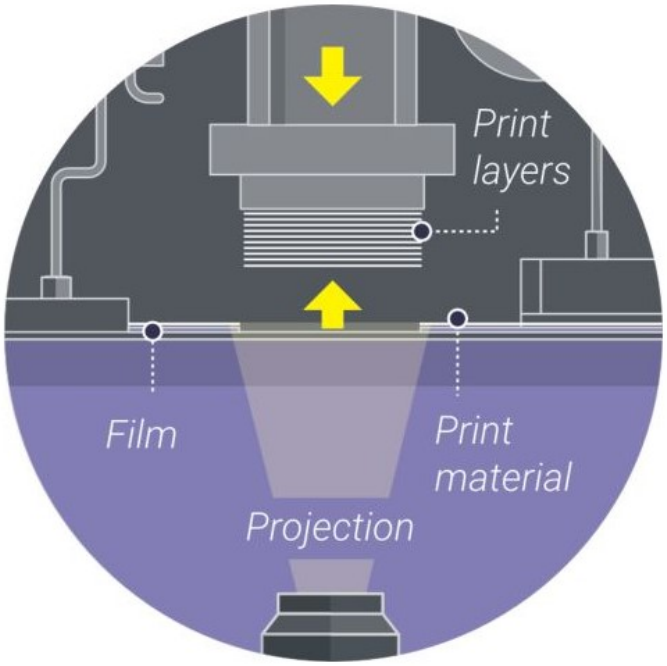

Figure 37. Rendering by ADMATEC of the SLCM printing process. [27]

Understanding how to eliminate defects during ceramics processing is critical in affecting the overall flexural strength of the ceramic material. This includes issues at the microscale level due to porosity as well as the macroscale level due to cracks or deformation introduced throughout the manufacturing. Since there are many steps in the fabrication of ceramic materials, multiple controls must be implemented to elim-

inate these defects. This requires reducing porosity on the microscale level, and controlling the manufacturing process through reducing powder impurities, de-gassing, controlled drying, and sintering processes. Understanding the different fabrications methods, mold builds, and each stage defects can occur helps to build a good ceramic fabrication process.

2.4 Material Characteristics

For design in engine applications, Silicon Nitride has shown desirable characteristics for use in turbine rotors. When compared to metals utilized for engine turbines, such as nickel-based alloys, Si_3N_4 has similar strength characteristics around 500 to 700 MPa and fracture toughness from 4.0 to 8.5 $MPa \cdot (m^{\frac{1}{2}})$.[10] In addition to high strength, Si_3N_4 has high creep resistance up to 1350°C surpassing that of metals.[10][28] Thus Si_3N_4 is capable of operating at the strength of metals, while operating at much higher temperatures.[7]

While ceramics have a relatively high fracture toughness, they do not exhibit the same elastic qualities of metals due to their brittle nature, leading to them being stiffer. As shown in the Ashby plot of Figure 38[9], ceramics have a much lower fracture toughness than metals. Therefore it is important to find ways to enhance the fracture toughness of ceramics to make them more robust, typically implemented at the grain boundary level.

Fracture toughness is the materials ability to resist crack growth which directly correlates to the size of the Si_3N_4 grain. The strength and hardness of Si_3N_4 is dependent on the grain boundaries formed during the final sintering stage. A more fine-grained structure leads to higher strength qualities, while a coarse-grained structure will lead to higher fracture toughness. A larger grain structure forces the crack to have to propagate around the grain boundary because it does not have the en-

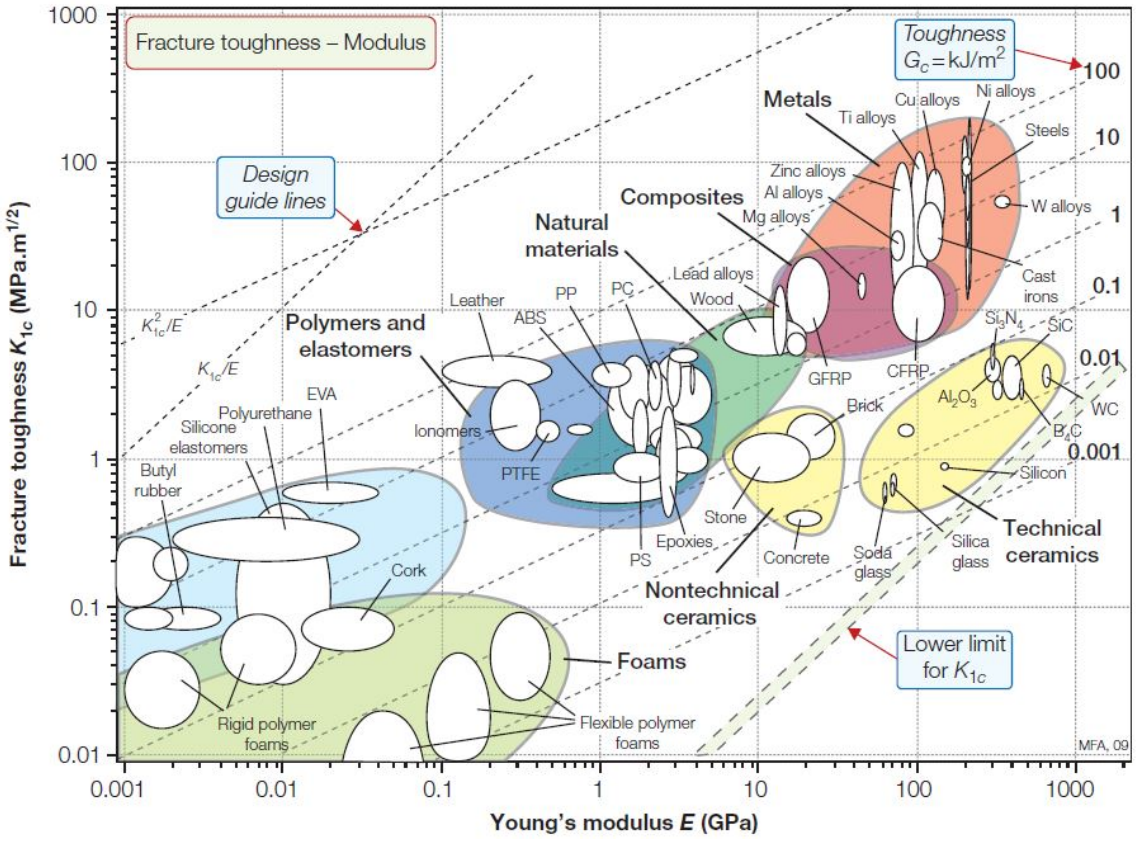

Figure 38. Ashby plot showing materials Fracture toughness versus strength. [9]

ergy to break through the grain. However, if the grain gets too large the crack will require less energy to break through the grain which limits how much the crack is deflected.[10] Therefore there is a limit on how high of a fracture toughness that can be achieved.

Bocanegra-Bernal and Matovic[10] compiled multiple studies of additives to Si_3N_4 for various processes to characterize how Si_3N_4 strength and fracture toughness are affected based on different chemical makeups.[10] The sintering aids typically consist of metal and rare-earth oxides.[10] Two common oxide additives utilized for slurries are Y_2O_3 and Aluminum Oxide (Al_2O_3). Zheng et al. found utilizing Y_2O_3 assisted in increasing fracture toughness through increased crack deflection, grain pull-out similar to fiber material, and bridging.[29] When Y_2O_3 is used in conjunction with

Al_2O_3 results have shown, together the two sintering additives help the Si_3N_4 densify at lower sintering temperatures increasing strength characteristics.[30] Due to these benefits, Y_2O_3 and Al_2O_3 are commonly utilized additives during pressureless sintering techniques.

As Si_3N_4 operates at elevated temperatures above 1000°C the strength characteristics begin to degrade due to phases in the grain boundary, additives, and processing procedures.[10][31] Kobayashi et al.[31] evaluated strength parameters for different Si_3N_4 at elevated temperatures and noted the deterioration in strength after 1000°C as shown in Figure 39. Similar to this research, Kobayashi et al.'s Si_3N_4, SN-88, was formed using injection molding of the blades with pressureless sintering. At room temperature the strength was 790 MPa and only degraded to 770 MPA by 1200°C.[31]

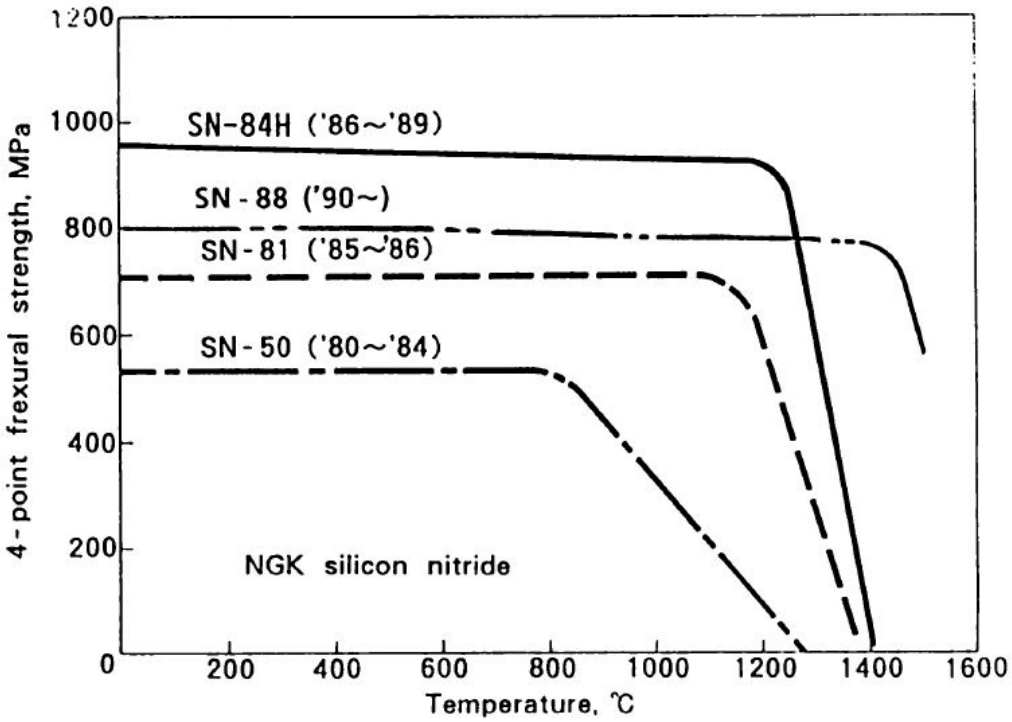

Figure 39. Strength parameters of different Si_3N_4 with increasing temperature by Kobayashi et al. [31]

The degradation of strength at temperatures is due to the glassy phases developed after processing softening at the elevated temperatures. Utilizing the sintering aid Y_2O_3 creates a higher softening temperature than MgO, allowing for strength degradation to begin at more elevated temperatures.[10]

To determine the overall strengths for ceramics, Weibull statistical analysis, developed by Waloddi Weibull, is commonly conducted.[32] Weibull analysis provides a probabilistic failure analysis to determine the likelihood a ceramic material will yield under given conditions. Since ceramics are brittle materials, they tend to display linear stress-strain behavior upon failure. This linear behavior along with varying flaws between samples produces varying failure strengths when testing.[7][33] Weibull analysis allows for the ability to determine the reliability of final ceramic parts based on varying processing techniques through the Weibull modulus (m). The Weibull analysis process is standardized through the American Society for Testing and Materials (ASTM) C1239-13 based on the Weibull equation, shown in Equation 1.[32][33]

$$F = 1 - exp(\frac{-\sigma_f}{\sigma_o})^m \tag{1}$$

In Equation 1, the probability of failure is (F), failure strength is (σ_f), and the characteristic strength is (σ_o). A higher Weibull modulus leads to a narrower distribution of data and is indicative of a more reliable process.[7][33] The precision required for reporting parameters will determine how many samples are required to be tested.

2.4.1 Summary.

Current ceramic manufacturing processes are expensive, timely, and complicated. Recent breakthroughs in ceramic manufacturing through pressureless sintering after casting or injection molding have shown promise in manufacturing ceramics out of Si_3N_4 into complex geometries that is both affordable and easily scalable in industry.[5][6][7]

When forming Si_3N_4 slurry the additives must be tailored to account for the manufacturing process while eliminating defects to achieve the best material strength and fracture toughness characteristics of the Si_3N_4. Understanding the different procedures for manufacturing ceramics and how defects are introduced allows for the ability to tailor the Si_3N_4 to best suit the specific manufacturing process and design the Si_3N_4 to meet the specified qualities necessary for the turbine rotor application.

III. Methodology

To meet the objectives for this research, this study focused on three main areas. The first focus was on comparing two fabrication methods: casting with a Si_3N_4 aqueous slurry solution, and printing a ceramic turbine utilizing stereolithography based ceramic manufacturing (SLCM). The second area of research focused on using FEA to adapt the turbine design from the original BYU design to meet the design criteria necessary for each fabrication method. The final area of research focused on testing of the actual turbine and classification of the material produced.

3.1 Fabrication Process

For the fabrication process, pour casting and ceramic printing were compared to determine the most consistent, cost effective, and scalable manufacturing process to produce a turbine. The manufactured turbine rotors would then be placed in a spin test rig or JetCat P400 engine and tested to compare to the FEA for their specific design parameters.

3.1.1 Pour Casting.

The pour casting process followed similar steps used in the injection molding process by Rueschhoff et al.[7] The steps and timelines that were followed for this study are shown in Figure 40. The slurry and mold preparation were conducted simultaneously, and each took three days, see Section 3.1.1.1 and 3.1.1.2, respectively. Once the mold and slurry were ready, the slurry was cast into the turbine mold and dried in a humidity chamber set at 99% humidity for 42 days to ensure adequate drying for the entire sample. This time could be reduced to approximately three weeks but was extended to ensure the best chance at drying without cracks. Once

drying was complete, the turbine went through binder burnout to remove the binder material from the turbine, which took two days. After binder burnout the turbine was prepped and sintered through a pressureless sintering process lasting two days. As shown in Figure 40 the entire process took 28 to 49 days from slurry prep through final ceramic turbine production.

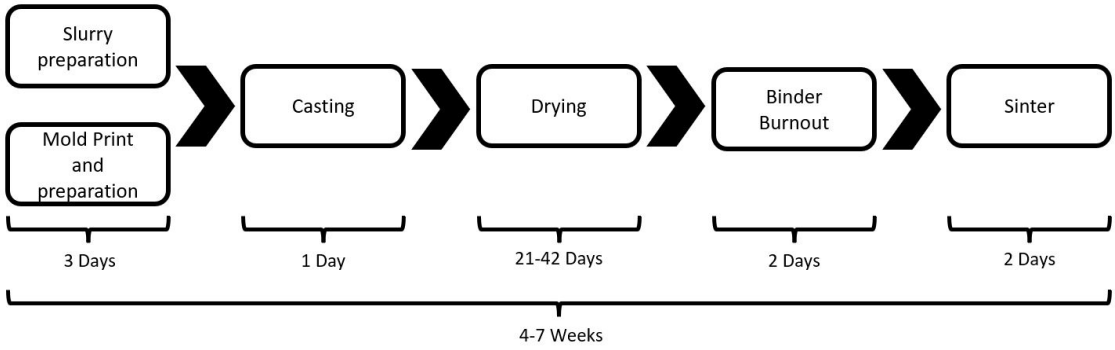

Figure 40. Pour casting process and timeline.

3.1.1.1 Slurry preparation.

For the pour casting portion of this study, a 43% Si_3N_4 slurry was utilized based on the 45% slurry used by Rueschhoff et al.[7] The slurry was prepared in 50 mL batches utilizing a gradual mixing process. It consisted of 18.125 g of distilled water and 10.5 g of Glenium 7500 aqueous solution. Followed by an addition of dry powders of 3.51 g of Al_2O_3 AA-03, 3.51 g of Y_2O_3, and 63.12 g of Si_3N_4. To mix the compounds together a FlackTek Speed Mixer was used, as shown in Figure 41a.

First, the distilled water and Glenium were added together and then mixed in the mixer at 850 RPM for 1.5 minutes. Then the alumina (Al_2O_3) , yttrium oxide (Y_2O_3), and 15 g of the Si_3N_4 were added. The slurry was then mixed through a four-step program of 850 RPM for 1.5 minutes, 5500 RPM for one min, 1050 RPM for one minute, and 550 RPM for one minute. Once mixed an additional 15 g of

Si_3N_4 was added along with two alumina milling media. This was then mixed with the same previous program. Next an additional 10 g of Si_3N_4 was added and mixed with the same program. Finally, the remaining 13.12 g of Si_3N_4 was added and the slurry was mixed for ten minutes at 650 RPM, due to the thickness of the slurry. Once mixing was complete, the slurry was left to ball mill overnight using the setup shown in Figure 41b. The next day, the slurry was mixed one more time utilizing the four-step program to ensure a complete mix of the components. Once complete it was placed back on the ball mill overnight until ready to pour.

(a) Flak Tek mixer (b) Slurry on the ball mill awaiting casting

Figure 41. Mixing mechanisms.

3.1.1.2 Mold Printing and Preparation.

The final turbine rotor mold was printed utilizing a PolyCast material in an Ultimaker printer shown in Figure 42. PolyCast was design for Fused Deposition Modeling (FDM) extrusion printing to allow for clean burnaway of printed parts. The print utilized 0.1mm layers, 20% infill, external supports, and 17% unilateral scaling for printing. The entire print time for the mold took 24 hours. Once the mold was

printed, the inside layers were smoothed utilizing an alcohol bath by pouring isopropyl alcohol in the mold cavity for two minutes and then draining the alcohol. The mold was then left to dry for two days.

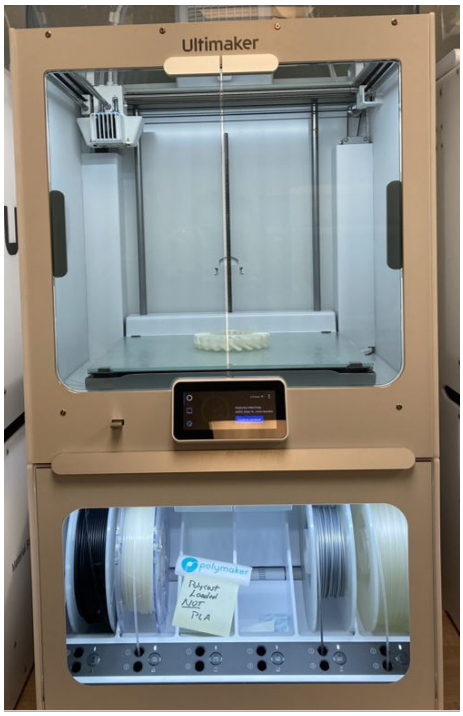

(a) Ultimaker printing the turbine mold

(b) Final turbine printed turbine mold

Figure 42. Ultimaker printer printing the final turbine mold design.

3.1.1.3 Casting.

When casting the slurry into the mold, the turbine mold was first prepped with a mold release agent to keep the slurry from sticking to the mold while it dried. A liquid form of Smooth On Universal Mold Release was first poured into the turbine mold to coat the inner surface of the entire mold. After 30 seconds, the mold release was poured out and the mold was left upside down to drain and dry for five minutes. After drying, the liquid mold release was again poured into the mold for 30 seconds coating the entire surface. The mold was drained and again allowed to dry for 20

minutes, at this point the mold was ready for casting.

To prepare the slurry for casting, it was first placed in the FlackTek mixer and run on the four-step program used for mixing to warm it up. The slurry was then poured into a 50 mL syringe, using a vibrating table to help remove air bubbles as the slurry settled into the syringe. Once filled, the syringe plunger was inserted and flipped upside down and mixed at 700 RPM for one minute to allow the air to move to the end of the syringe. Once done mixing, the air was pushed out of the syringe, and then mixed right side up at 1000 RPM for one minute.

Once prepared, a wide gauge needle was attached to the end of the syringe to release any remaining trapped air bubbles from the slurry during pouring. The mold was placed on a vibrating table while the slurry was slowly distributed into the turbine mold as shown in Figure 43. While the mold was being cast a humidifier was used to keep the slurry from drying and allow it to continually settle together. The vibration table helped assist with the slurry distribution throughout the turbine blade cavities to ensure complete fill as well as help remove other air trapped from pouring into the mold.

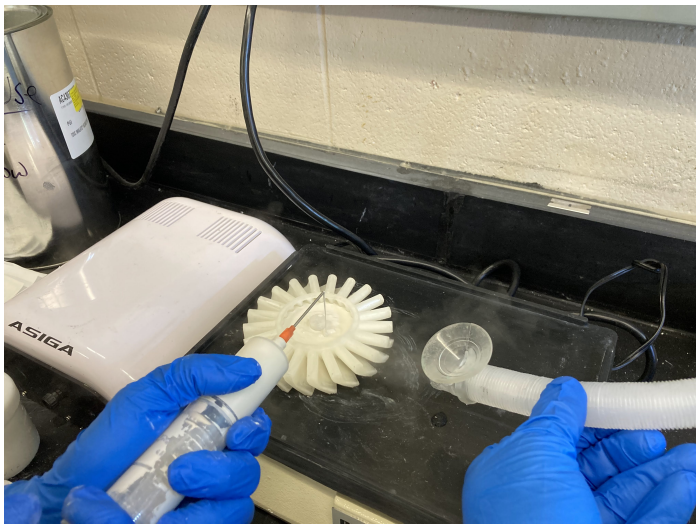

Figure 43. Casting of the turbine mold utilizing a syringe, vibrating table, and humidifier.

3.1.1.4 Drying.

Once the sample was cast it was placed inside a humidity chamber set at 99% humidity shown in Figure 44. The humidity chamber was prepared using sulfuric acid mixed with distilled water to maintain 99% humidity in the chamber. The high humidity rate allowed the turbine rotor to dry slowly for 42 days as the water evaporated out of the ceramic.

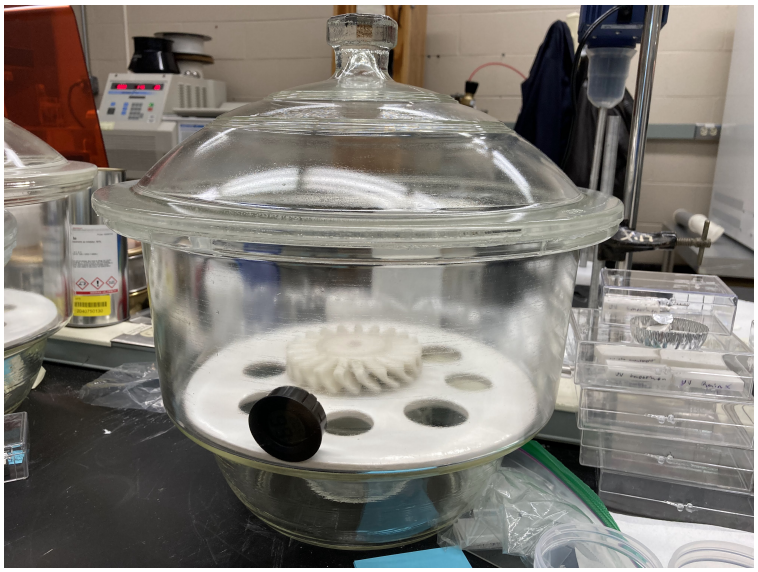

Figure 44. The cast turbine rotor drying in the humidity chamber at 99% humidity.

3.1.1.5 Binder Burnout.

To remove the dispersant and any leftover water from the ceramic, the turbine rotor and mold were placed in a crucible and inserted into an ash furnace for binder burnout. The furnace was heated at a rate of 0.5°C per minute up to 525°C. The furnace then dwelled at 525°C for six hours burning away the Polycast mold material and removing the binding agent. Once cooled to room temperature the turbine rotor was removed and prepped for sintering. The ash furnace with the turbine mold is pictured in Figure 45.

Figure 45. The quarter turbine rotor sample in the Ash Furnace for binder burnout.

3.1.1.6 Sintering.

To prepare the Si_3N_4 turbine rotor for sintering, it was placed in a Boron Nitride (BN) crucible surrounded by a powder bed. The powder was made up of 50 wt% Si_3N_4, 45 wt% BN, 2.5 wt% Al_2O_3, and 2.5 wt% Y_2O_3. The powder was placed a minimum of 0.5 inches under the turbine rotor and packed around the entire turbine rotor until fully covered.

Once prepared, the crucible was placed in a graphite furnace to be pressurelessly sintered. The furnace first pulled vacuum to purge air from the furnace in order to create an inert Nitrogen atmosphere. Once the Nitrogen atmosphere was created, the furnace was heated to 1750°C at a rate of 20°C per minute. Once at 1750°C the turbine rotor sintered for 1 hour and was then cooled back down to room temperature at a rate of 40°C per minute. Once at room temperature the turbine rotor would be ready to be removed from the furnace. Once sintered the turbine rotor was ready for machining utilizing diamond tools.

3.1.2 Mold design.

For the pour casting method, the mold development in this study was a critical part of the process. Mold considerations for porosity, type of material, and a burnaway temperatures were all necessary as shown by Cai et al.[26] Additionally, since the molds are printed, Zhoe et al.[34] discussed the importance of reducing the surface roughness to prevent the ceramic slurry from sticking to the mold as it dried. For this study, two materials and printing methods were compared: a photopolymer material, VeroClear, was printed on a Stratasys Objet 260 Connex 3 PolyJet 3D printer, and a burnaway polymer material, Polycast, printed on an Ultimaker FDM 3D printer, shown in Figure 46.

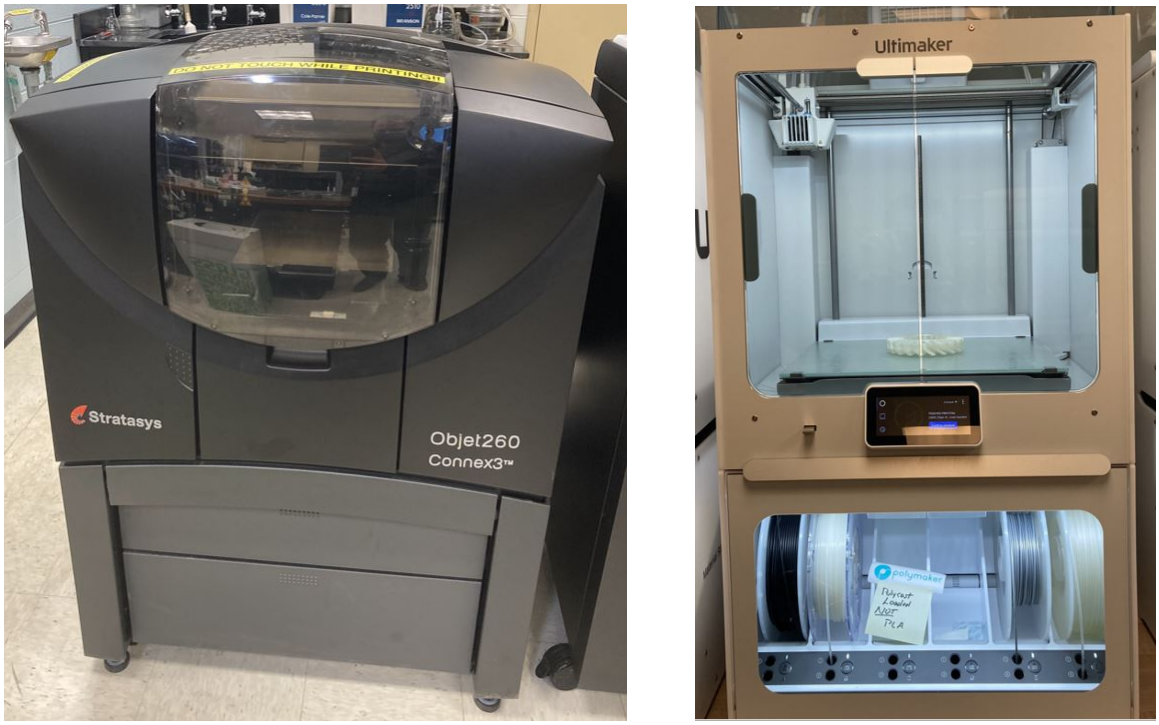

(a) Objet 260 Connex 3 printer (b) Ultimaker 3D printer

Figure 46. 3D printers utilized for molds.

To compare the two materials, burnaway temperature, surface roughness, and mold release considerations had to be considered to determine the mold material that

would give the best chance at success. Additionally, a final mold design had to be created to allow for complete filling of the slurry into the mold

3.1.2.1 Thermogravimetric Analysis.

When the slurry was cast into the mold it remained in the mold through drying. This required the sacrificial mold to burn away from the turbine rotor before the binder burnout dwell temperature was reached. Therefore, thermogravimetric analysis (TGA) was utilized to determine when the 3D printer material completely burned away. To do this a sample of Polycast and VeroClear was burned in the furnace simulating binder burnout conditions. The burnout of each material was conducted in air at a rate of 5°C per minute to a final temperature of 1,000°C. The final analysis produced results showing how much material remained over time and at what temperature it is completely removed, shown in Figure 47.

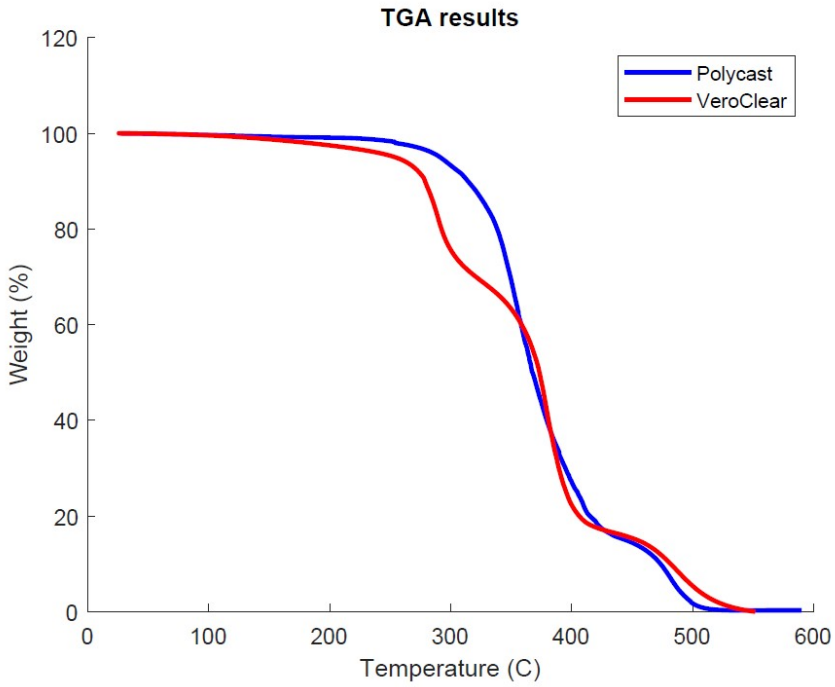

Figure 47. TGA of the Polcast and VeroClear material.

The results show both the Polycast (in blue) and VeroClear (in red) have mostly burned away by 450°C and completely burned away by 550°C. This results indicates the mold material will be completely removed from the turbine rotor during binder burnout by the time it begins to dwell at 550°C, which helps prevent any issues with burnout.

3.1.2.2 Surface Roughness Testing.

For the molds, the surface roughness needed to be measured to see how smooth each layer transition was from each printer. To do this, sample pieces from each 3D printer were scanned using a Zeiss LSM 700 Laser scanning microscope. The microscope image was analyzed utilizing Zen software at 10x zoom to create a topographical map and output a surface roughness value for each sample, with an example output shown in Figure 48. The image shows the distinct ridges from the 3D printed layers made by the Ultimaker in yellow. The computer also measures a relative roughness as an areal roughness (RSa) value. The software calculates the average of surface heights and depths across the area that is scanned to produce the RSa value.

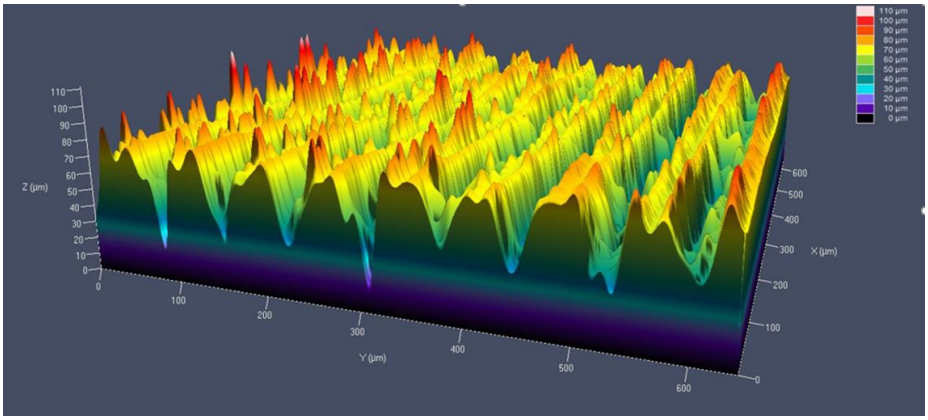

Figure 48. Scanned image of the Polycast material with no surface treatments.

Since the Polycast was printed with 0.1 mm thick layers, a surface finisher was utilized to provide a smoother finish. This process made use of a Polymaker Polysher

post-processing device, shown in Figure 49. The Polysher atomizes isopropyl alcohol and distributes the vapor in the chamber to coat the surfaces of the mold. The alcohol dissolves the outer surface of the mold material causing the layers to fuse, thus creating a smoother surface. Once finished in the alcohol bath, the samples had to dry for 5 minutes in air until they could be carefully removed from the tray to another surface to finish drying. After they were moved to a separate surface, they continued to dry for two days. Rectangular mold samples were collected after 20 minutes and 30 minutes in the chamber to determine the best finish quality. These samples were compared to rectangular samples prepared in the Objet printer with no post-processing.

(a) Samples being processed (b) Samples post-processing

Figure 49. PolyMaker Polysher.

Since the turbine mold has smaller internal cavities for the turbine blades, an isopropyl alcohol mist risked not coating the entire inner surface. Therefore, further research was conducted to determine if pouring isopropyl alcohol into a mold would produce similar post-processing results. Since Rain X was being tested as a potential mold release it was determined that it might function like the isopropyl alcohol and

needed to be evaluated. Rectangular Polycast samples were also tested in three separate batches utilizing isopropyl alcohol, Rain X, and then both liquids in sequence. The solutions were each poured into the mold for tests at one, two, and three minute intervals. These nine samples were also then analyzed to see the affects of surface roughness for each test.

3.1.2.3 Mold Release Testing.

As the Si_3N_4 slurry dries in the mold, it shrinks approximately 1.5% in each direction as the water evaporates. As the ceramic begins to shrink, there is potential for it to dry unevenly as parts stick to a pourous mold leading to stress cracks and a failed material as it forms into its green state as demonstrated in Figure 50. The sample on the left developed a stress crack as it failed to release from the mold while drying. However, the sample on the right seperated from the mold with no issues as it dried. Utilizing a mold release helps allow for the Si_3N_4 slurry to separate from the mold more evenly, while allowing for the water to evaporate through the porous mold and into the drying chamber.

Figure 50. Si_3N_4 samples showing stress cracking due to adherence to the mold (left) and release from the mold (right).

To determine the appropriate mold release to use, four mold releases were tested for both the VeroClear and Polycast using 45 x 20 x 6 mm rectangular mold samples, as shown in Figure 51. The Polycast molds were first treated for 20 minutes in the Polysher for post-processing. The molds were then treated with an aerosol Teflon

spray, dry Teflon, Smooth-On Universal mold release aerosol, and Rain-X. Earlier research at AFRL in mold releases showed potential of Rain-X for 15 minutes after UV cure to show the ability to be a potential releasing agent. A total of 14 samples were prepared with seven being treated under UV light for 3 minutes and seven untreated by UV light. As shown in Figure 51, mold release samples for UV and non-UV treated molds were then applied with no treatment, aerosol Teflon, dry Teflon, Smooth-on, and Rain-X. The Rain-X was tested at time intervals of 5, 10, and 15 minutes.

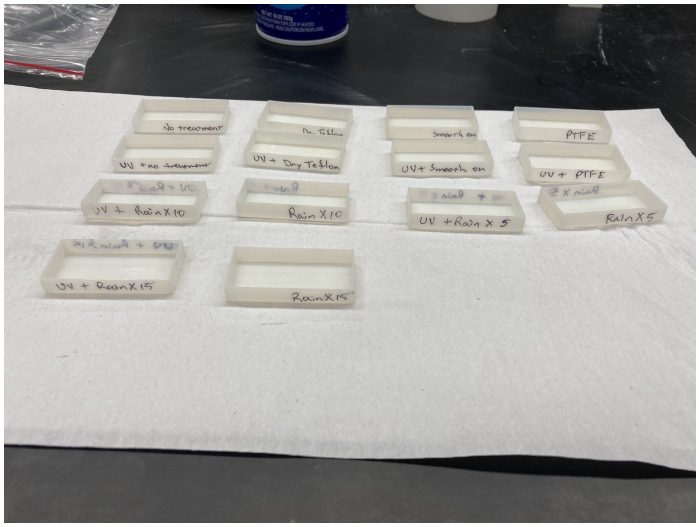

Figure 51. Objet mold release samples after treatment prior to filling.

The samples were left to dry for two days. After drying, slurry was cast into each with a 43% Si_3N_4 solid loading using the same process used for the turbine. Unlike the turbine, these smaller samples were dry and ready for binder burnout in two weeks. The samples were evaluated for cracks and then moved into the binder burnout stage. After burnout the samples that survived were then measured and sintered to determine the shrinkage of the material covered further in Section 3.3.

3.1.2.4 Mold Design and Testing.

Additional consideration had to be given to designing the mold to best suit pour casting for a complete turbine rotor. Three printers and material were tested: the Objet printer with VeroClear material, the Ultimaker printer using Polycast material, and a Formlabs stereolithography printer with a UV standad clear resin. To determine the best printer to produce the turbine rotor mold for this study, quartered turbine molds were created initially so as not to waste material and to reduce the amount of Si_3N_4 slurry used. The mold was created using Solidworks and transferred into a .STL file format for printing. The first mold was initially a rounded mold with a negative of the turbine rotor utilizing the core feature in Solidworks, shown in Figure 52a. The slurry was cast following the same casting method as the turbine with a 43% Si_3N_4 slurry and only a 2.5 week dry time since they were quarter molds.

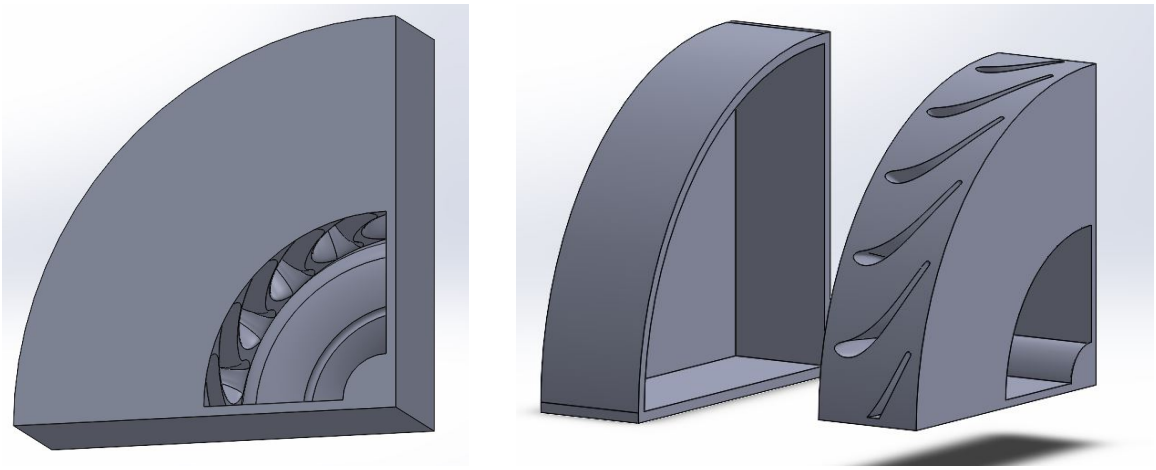

(a) Rounded mold for pour casting formed into quarter molds for testing.

(b) Turbine mold with the blade tips exposed and the sleeve.

Figure 52. Quarter turbine mold designs for testing.

During printing, the Objet had to put internal gel supports in the blade regions. Those were removed with a water jet, however, removing all the gel from the surface proved difficult. A quarter mold with open ends at the turbine blade tips was made

with an outer section cover the opening for casting, shown in Figure 52b. This allowed for easier access to remove the support from the Objet mold. This was then cast with a 43% Si_3N_4 slurry and evaluated.

Concern also came due to the amount of material that would need to burn out as well as excess mold material hindering drying. While the Ultimaker was able to the produce a partial infill within the walls of the mold the Objet and Formlabs printers were not. This led to material being removed between the blades and air holes being added to the top of the blade portion of the mold to allow for release of air to achieve a complete fill of the blades as the rotor was being cast. The final mold design is shown in Figure 53. After selection of the final printer and material was made, this mold was printed utilizing the Ultimaker printer out of Polycast.

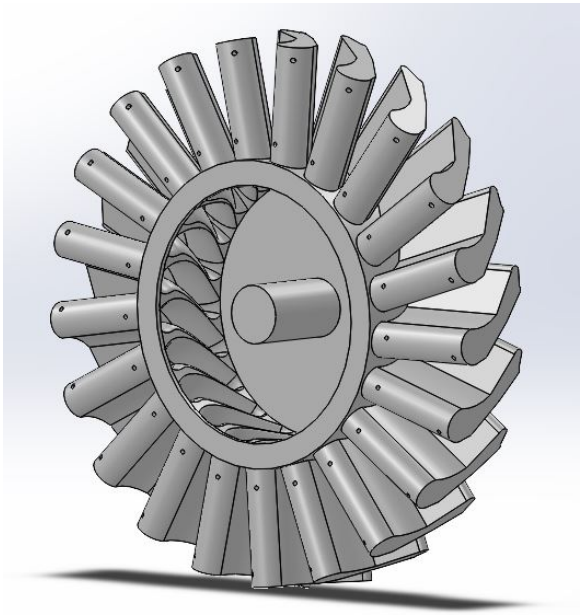

Figure 53. Final turbine mold design utilized to cast the mold.

An additional three-part mold was also created for follow-on research that could be utilized for injection molding using the same final mold design. In this configuration, shown in Figure 54, the mold would fit into the bottom support at the keyhole and the

mold cover would be placed over the mold and screwed to the bottom support. The slurry could then be injected through the injection port located on the top portion of the mold cover. The slats in the top mold would allow for the air to still escape from the rotor blades to allow for a full fill of the mold. This would be injection molded on a vibrating table to help with distribution into the mold. This mold was manufactured but not tested with injection molding.

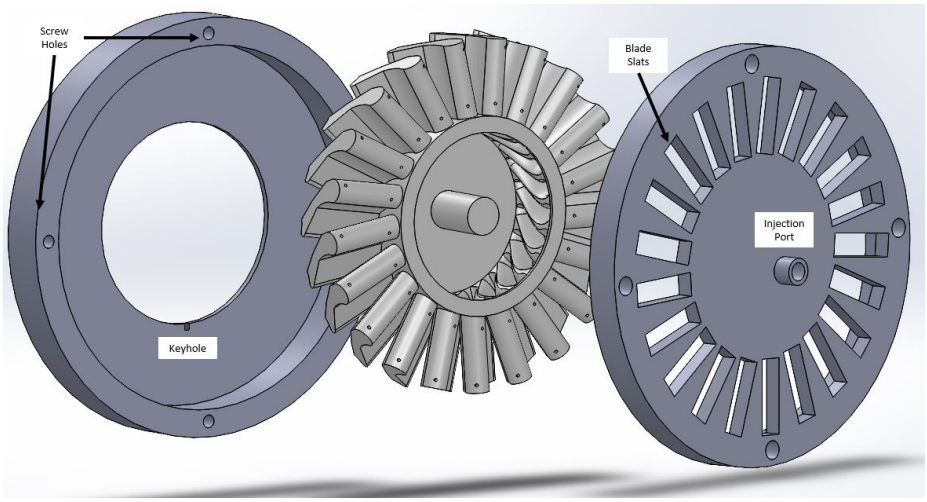

Figure 54. Three part mold created for injection molding.

3.1.3 Stereolithography based Ceramic Manufacturing.

The second manufacturing process evaluated was SLCM. This was done utilizing an ADMATEC Admaflex 300 printer shown in Figure 55a. The printer utilizes a polymer based ceramic slurry and a light processing to print the ceramic directly into the desired shape. For this process, the turbine CAD models were scaled 30% in the turbine rotor plane direction, shown in Figure 56, and 10% in the turbine rotor through thickness direction to account for shrinkage, according to ADMATEC literature, and were uploaded via an .SLC or .STL file format. The print parameters were set to 0.05 mm layer thickness and a light setting based on the literature according

to the remaining volume of slurry. For the printing process shown in Figure 55b, The printer lays down a 0.05 mm layer of slurry then selectively cures it by laser light. The build plate is then raised a layer heigher as more slurry is placed below the plate. This process is repeated until the part is complete. The material used for this study was an alumina slurry purchased through ADMATEC with material properties shown in Table 1 below. In addition to alumina, a zirconia slurry was evaluated for use and determined suitable for follow-on research. Silicon nitride slurry is currently still in development and was not available for use at this time.

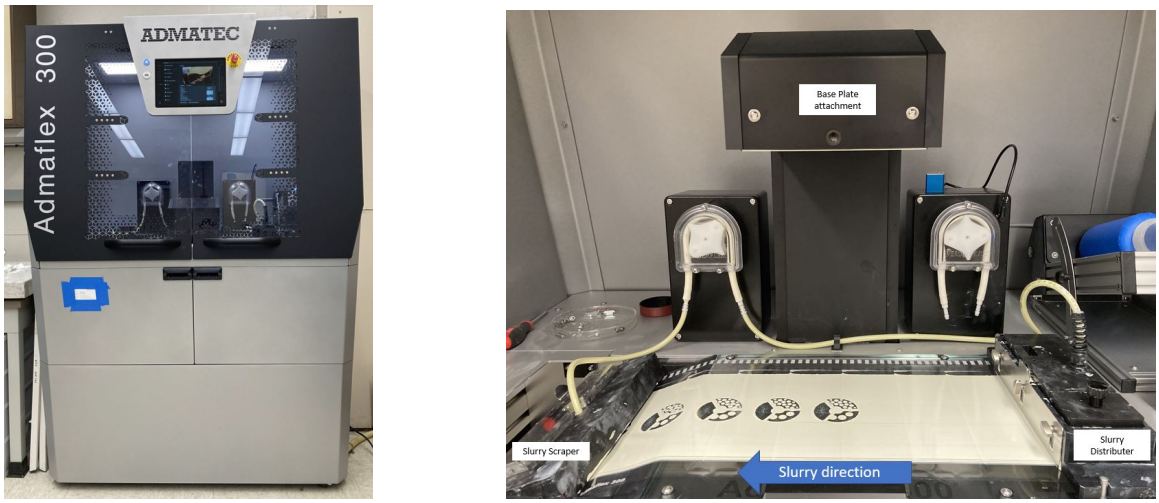

(a) ADMATEC Admaflex 300 SLCM printer.

(b) samples post-processing.

Figure 55. ADMATEC Admaflex 300 SLCM printer and process.

Once the ceramic is printed, it is then moved to a tank of water to begin water debinding as shown in Figure 57. The binding agent in the slurry is water-soluble, so after printing it is removed by soaking in water for 2-3 days depending on the size of the build. Once removed from the water the part is dried in air for 24 hours before binder burnout.

To remove any leftover binder from the ceramic, the turbine rotor was inserted into an ash furnace for binder burnout for two days. The furnace was heated at a

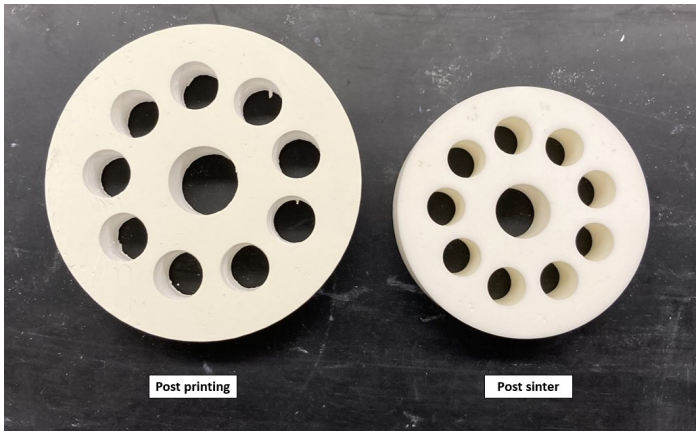

Figure 56. Shrinkage of an alumina hub in the turbine rotor plane direction.

Table 1. ADMATEC Polymer Ceramic Slurry Properties

Material properties	alumina	zirconia
Young's Modulus (E_c) (GPa)	360	210
Poisson's ratio (ν)	0.21	0.22
Density (ρ) (kg/m^3)	3900	6060
Tensile strength(MPa)	415	800
Compressive strength(MPa)	4150	8000
Yield strength(MPa)	415	800
Coefficient of Thermal Expansion(α) ($1/K$)	7.5E-6	1E-5
Thermal Conductivity ($W/(mK)$)	30	10

rate of 1°C per minute up to 150°C and held for 30 minutes. Then the temperature was increased at a rate of 0.2°C per minute to 500°C. The furnace then dwelled at 500°C for 9.2 hours. Upon dwell time completion the furnace was cooled down to room temperature at a rate of 1.6°C per minute. Once cooled, the turbine rotor was removed and prepped for sintering.

Sintering was conducted in a Thermolyne Type 46200 high temperature pressure-less ceramic furnace in air. The temperature was increased from room temperature to 1,000°C at a rate of 3.3°C per minute with a dwell time of 30 minutes. The furnace was then heated to 1,450°C at a rate of 1.7°C per minute. Once at 1,450°C the rate of temperature increase was reduced to 1.25°C per minute until reaching 1,500°C. The

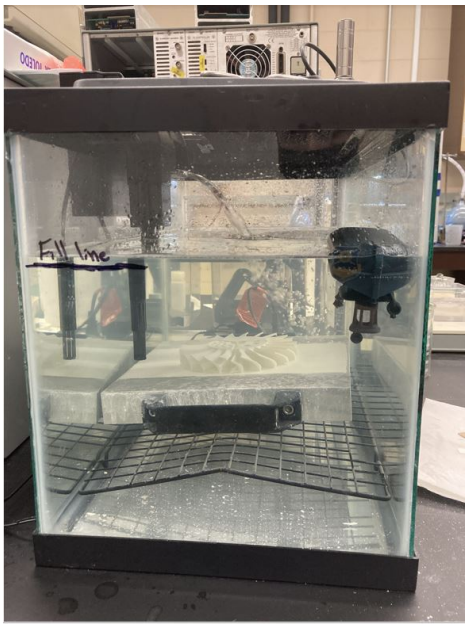

Figure 57. Turbine rotor in the water tank for water debinding.

temperature was held at 1,500°C for two hours. Once complete, the temperature was reduced to room temperature at a rate of 5°C per minute. The entire process from print to sintering takes a total of 1.5 weeks as outlined in Figure 58, which is 2.5-4.5 times faster than the casting process timeline.

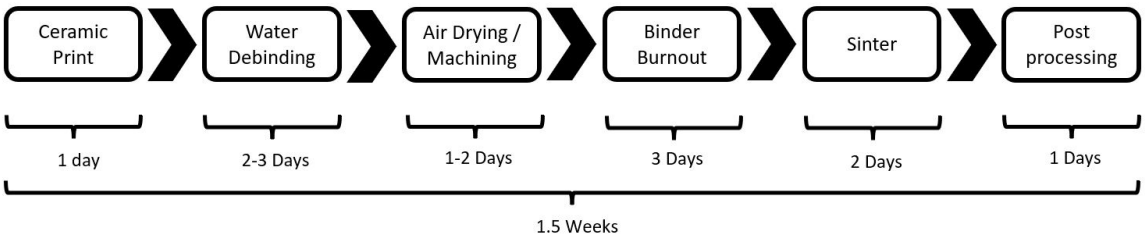

Figure 58. Timeline utilizing SLCM process.

3.1.3.1 SLCM Turbine Design.

For the alumina slurry, ADMATEC cautioned against having sections that were thicker than 10mm in two directions. Exceeding these thicknesses would cause de-

lamination during binder burnout due to the inability to remove all the binding agent during water debinding. The result of having dimensions exceeding 10 mm can be seen in Figure 59. The printed turbine rotor shown was based on the solid hub design from casting. While it printed well with no defects, the turbine rotor broke apart with the layers delaminating during binder burnout. The delamination was due to the design being too thick and exceeded the 10 mm thickness limitations for the alumina slurry. This dimensional limitation required altering the hub design so there were no areas larger than 10 mm in two directions to print alumina, and 5 mm in either direction for zirconia.

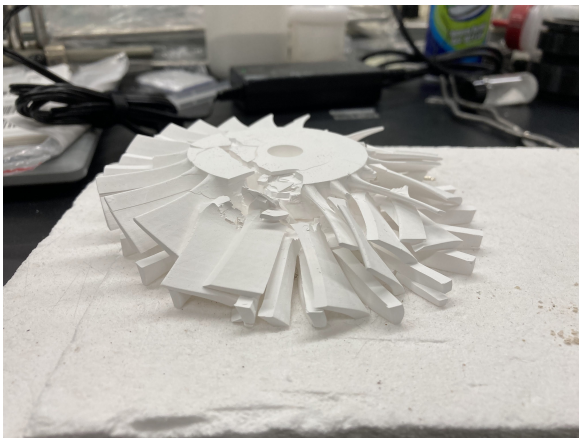

Figure 59. Turbine rotor sample delaminated due the hub being to thick.

Three designs were created for testing, with their cross sections shown in Figure 60. The designs used circles to act similar to reduced infill to decrease the amount of mass in the hub, and avoid sharp corners for lower stress concentrations. The first design, Figure 60a, extruded a set of 11 circles from the back of the hub to the last 7mm of the front of the hub. The second design, Figure 60b, utilized 4 sections of circles around the hub allowing no more than 4 mm of thickness between the circles, to account for the zirconia thickness limitations. These holes were extruded from the back of the hub to 4mm from the front of the hub. The final design, Figure 60c, used

the same pattern as the second design, but was filled in with 4 mm thick walls on the back of the hub to act as a cap. The cap design was done to see if there would be any issues from off gassing causing failure during water debinding and binder burnout. Scaled partial samples of each design were printed and processed according to the ceramic printing process outlined above using alumina.

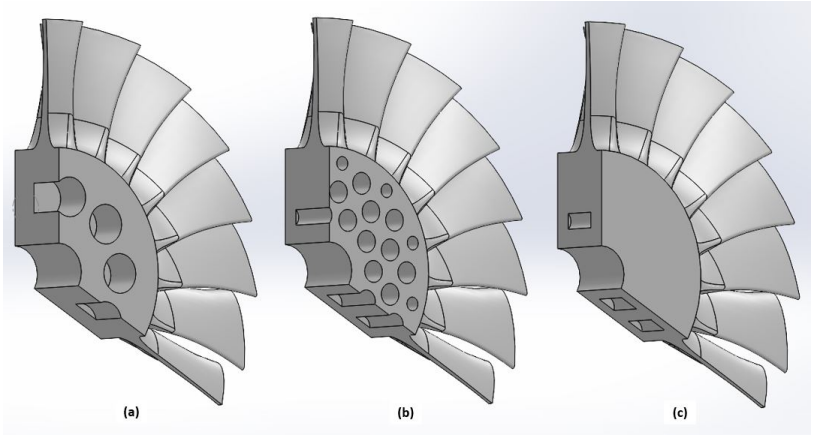

Figure 60. Three cross sections designed for the SLCM printed turbine: alumina infill design 1(a), zirconia infill design 2(b), Capped design 3(c).

In addition to the partial turbine rotor sections, six varying hub designs, shown in Figure 61, were created to test varying thickness options in order to eliminate cracking in the hub. Hubs A and D, increased the extrusion of the holes to allow for only 2.5 mm of wall thickness on the leading edge side of the hub. Hub A had a fillet added to the bottom of the extrusion. This was done to attempt to eliminate any cracking or larger separation at the bottom of the hole due to stress concentrations during drying and sintering. Hub C, was the original tapered design produced by BYU. This hub met the thickness criteria, and provided further insight into whether or not supports are needed for printing due to the tapered design.The remaining hubs, (B,E, and F), all have varying honeycomb structures that are through holes to completely eliminate any cracking due to stress concentrations at the layers where the holes meet an end wall. These three designs feature a full hub for the alumina and zirconia infill design

from the partial turbines and an additional oval design to remove more mass. The six hub designs were processed utilizing alumina through the printing process outlined above.

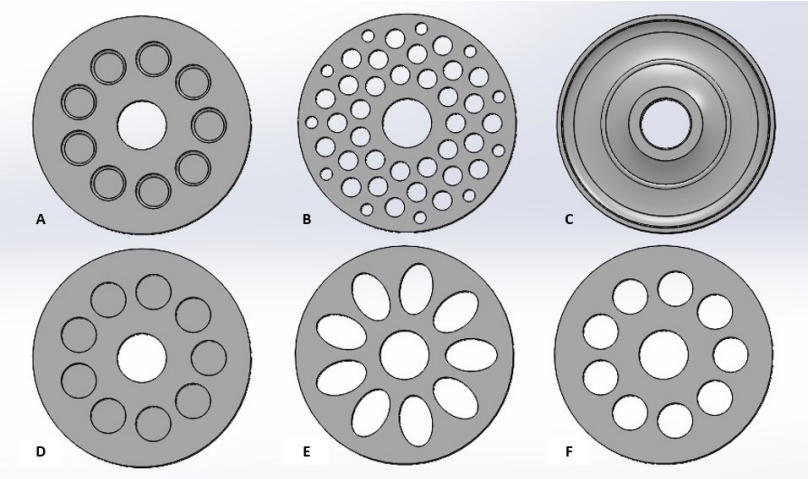

Figure 61. Six hub designs created to alleviate cracking in the hub.

The successful hub designs were sent to the AFIT shop to test fit the hubs to the tolerance rings in order to join the turbine rotor to an engine shaft. The tolerance rings, shown in Figure 62, were produced by USA Tolerance Rings, utilizing 0.2032 mm thick Hastelloy 276-C material. The wavelengths had a pitch of 2.5 mm with a nominal reference wave height of 0.5 mm and nominal wave width of 12.7 mm. The tolerance ring design was made based on design criteria of a thermal range of 20°C to 427°C with a torque hold of 8.5 ft-lbs. The given shaft diameter was 9.9822 mm which led to a required turbine rotor bore size of 10.8966 ± 0.0254 mm. Twenty tolerance rings were purchased for initial testing.

In order to attach the tolerance ring, the turbine rotor bore had to be milled out to the required bore size within the given tolerance. This required the printed bore size to be 10.16 mm to allow for excess material to be removed to meet tolerance requirements. It was recommended that the turbine rotor be heated to expand the bore to assist with installing the tolerance ring on the turbine rotor. Based on test

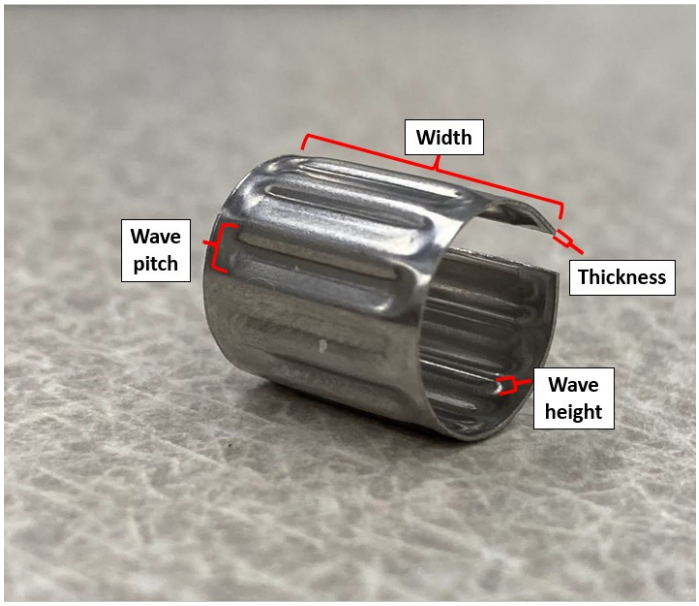

Figure 62. Final produced tolerance ring.

results in spin testing and the JetCat P400 it is recommended to change the nominal diameter in 0.0254 mm increments to obtain optimum perfomance.

The FEA for the successful designs and the test sample results were compared to choose a single final turbine rotor design. The final design, shown in Figure 63, was printed and post-processed to be fitted on a JetCat P400 shaft. This final turbine rotor allowed for the ability for spin testing and to test in the JetCat P400 to see how well it met the operating parameters according to FEA results from the simulation described in Section 3.2.

3.2 Turbine Rotor Design Optimization

The second part of this study focused on FEA of multiple designs of the turbine rotor. First, the BYU turbine rotor had to be analyzed and redesigned to meet the criteria set out by AFRL utilizing the Si_3N_4 strength parameters of 600 MPa from Rueschhoff et al.[7] as an estimate for the slurry cast in this study. Further analysis

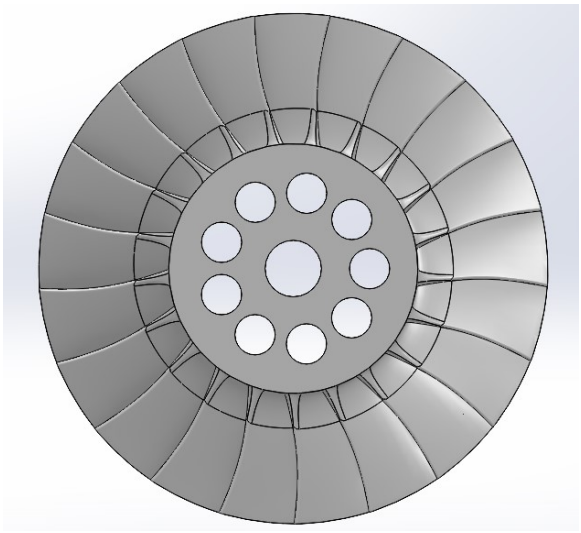

Figure 63. Final turbine rotor design produced.

was run to determine the stress at the bore with a shaft inserted and no tolerance ring to see how much stress would result from thermal expansion. A third analysis was run to confirm the design for the cast Si_3N_4 turbine rotor design, to see if it would be able to do a full run up in a JetCat P400 as a proof of concept. Finally, a fourth analysis of was run to develop a design that allowed the Al_2O_3 ceramic printed turbine rotor to run in the JetCat P400. The FEA for all of the analysis was run utilizing Solidworks simulations. Steps can be found in Appendix 1.

3.2.1 Turbine Rotor Initial AFRL Operating Conditions Analysis.

The first FEA study evaluated the AFRL operating conditions on the BYU turbine design specifically quantifying the difference in coefficient of thermal expansion between the shaft and the turbine depicted in Figure 64a. This was followed by analysis on the turbine rotor at the AFRL thermal and centrifugal profile without the shaft, shown in Figure 64b.

For the shaft and turbine rotor analysis, the rotor was fixed on the shaft which simulated being held mechanically in place by a nut. The FEA was run based on the

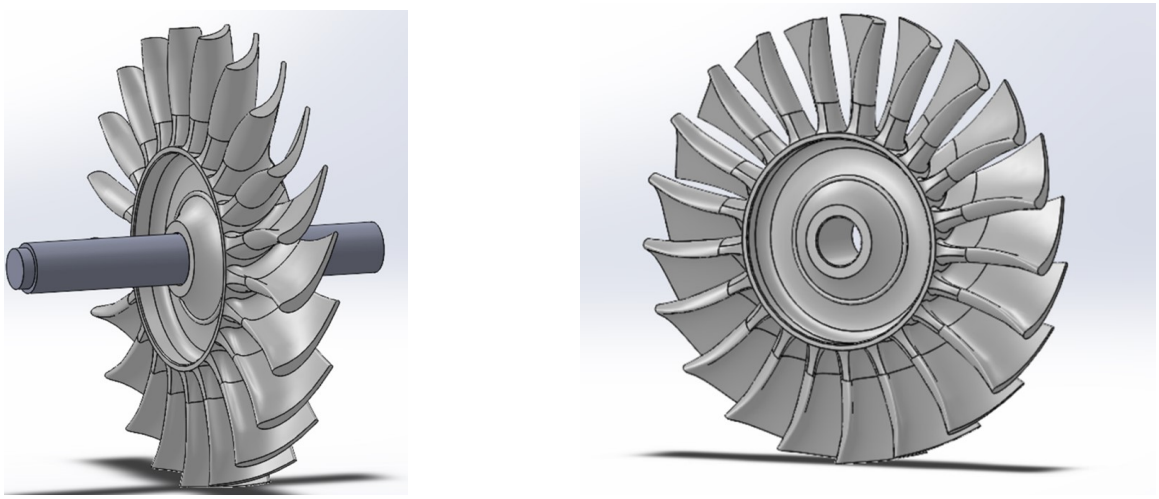

(a) Assembly of the shaft and turbine rotor.

(b) Turbine rotor with the shaft removed.

Figure 64. AFRL turbine analysis designs.

material properties listed in Table 2 for the Si_3N_4 turbine rotor and 2507 stainless steel shaft. The simulation was a thermal static study based on the given AFRL thermal profile, shown in Figure 65. The highest temperature was 1300°C in the middle of the blade region denoted in red. The tips and roots of the blades see a temperature of 1200°C. From the roots of the blade a temperature gradient moves through the hub until a temperature of 426°C is reached at the shaft, shown in blue.

Table 2. Solidworks Simulation Material Properties

Material properties	**Silicon Nitride**	**2507 Stainless Steel**
Young's Modulus (E_c) (GPa)	310	200
Poisson's ratio (ν)	0.25	0.3
Density (ρ) (kg/m^3)	3188	7806
Tensile strength (MPa)	600	800
Compressive strength (MPa)	6000	NA
Yield strength (MPa)	600	552
Coefficient of Thermal Expansion (α) ($1/K$)	2.50E-6	1.30E-5
Thermal Conductivity ($W/(mK)$)	20	15

The second portion of this study evaluated three different hub designs in the

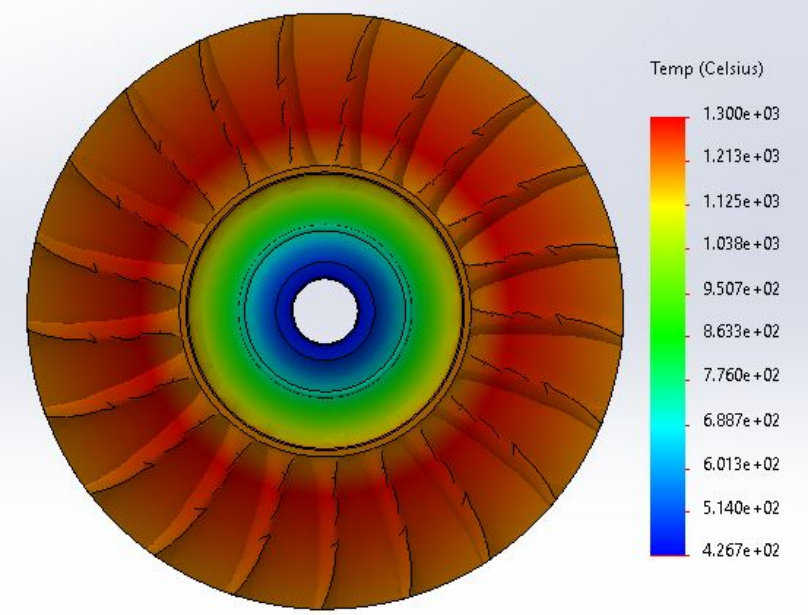

Figure 65. AFRL Thermal profile of the turbine rotor for analysis

turbine rotor. The shaft was removed from the study, assuming that a tolerance ring was used to remove the forces resulting from different coefficients of thermal expansion. The cross section of the turbine rotor designs can be seen in Figure 66. The first design, Figure 66a, is the original BYU design with a tapered hub on both sides. The second design, Figure 66b, incorporated a flat hub on the leading-edge side to begin simplifying the design to assist with better distribution of Si_3N_4 slurry during pour casting. The final turbine rotor design has a filled in hub on both sides, shown in Figure 66c, to evaluate the effects of an even more simplified geometry.

Each of the three profiles utilized the same combined loading conditions: a centrifugal load of 90,000 RPM and the same thermal profile shown in Figure 65. The simulations were all run as static simulations, with no inertia, and used the standard mesh profile produced in Solidworks. For each turbine design an individual simulation was run for the centrifugal case and thermal case. After the individual case, a combined thermal and centrifugal load was performed. These results were then analyzed

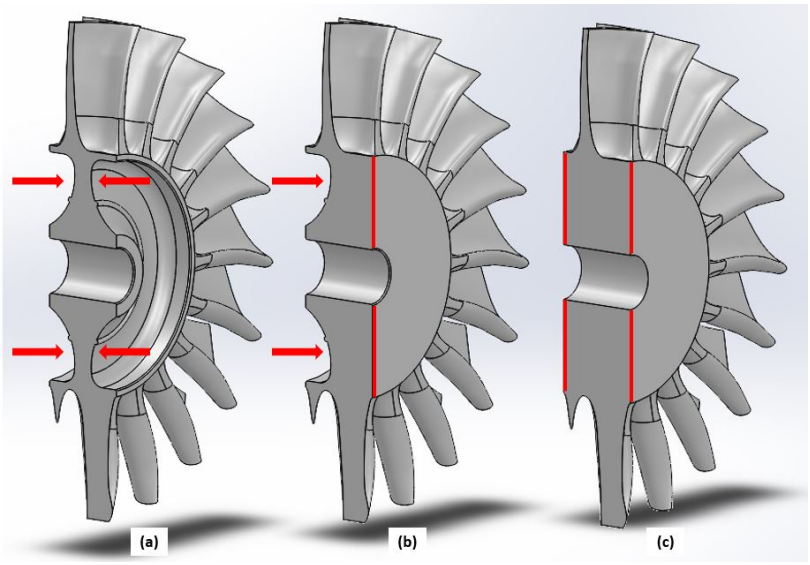

Figure 66. Three different tested turbine rotor designs BYU design (a), partially filled in hub (b) and completely filled in hub (c).

to see where the highest stresses or potential failure occurred within the material.

An additional study was run to try to decrease the stress at the bore by increasing the temperature in the shaft. Maintaining the same centrifugal forces and temperatures at the blade roots, new temperature profiles were created increasing the bore temperature from 427°C to 927°C in 100°C increments. A simulation was run at each of these temperatures for the BYU turbine in Figure 66a and solid hub design in Figure 66c and the results were then plotted showing the stress in the bore. These simulations were run to determine the best way to meet the requirements for AFRL.

3.2.2 Cast Si_3N_4 turbine design Analysis.

The next set of simulations were created to determine what regimes of the JetCat P400 engine the cast turbine rotor designs could operate in to be used for the pour casting method in Section 3.1. The simulations consisted of combined centrifugal force and thermal profile based on three stages for the JetCat P400: idle, half power, and full power. The rotational speed and temperature used for the thermal profiles are

shown in Table 3. These thermal profiles produce color distributions based on their specific temperature distributions similar to what is shown in Figure 65. Appendix 1 shows how the thermal profiles were built.

Table 3. JetCat P400 regime centrifugal and thermal profiles.

JetCat Profiles	Rotational velocity (RPM)	Blade tip Temp (C)	Blade root Temp (C)	Middle blade Temp (C)	Bore Temp (C)
Idle	30,000	342	377	537	427
Half Power	80,000	632	485	827	427
Full Power	98,000	700	627	1,005	427

3.2.3 Printed turbine design analysis.

Since alumina and zirconia do not have the strength properties of Si_3N_4, simulations were run to see if there was an engine operating regime these weaker printed turbine designs could still be used in. The two initial design configurations for simulation, shown in Figure 67, were designed with holes to meet the initial material thickness criteria for each material. The alumina turbine, Figure 67a, had a single row of nine 7.25 mm diameter holes placed into the middle of the hub. The holes were 8.85 mm in depth allowing for 7 mm wall thickness on the leading edge side. The zirconia turbine design, Figure 67b, had four rows of holes at a depth of 11.85 mm of depth to allow for a 4 mm thick wall on the leading edge. The larger holes are set at 4 mm in diameter and the smaller outer holes are 2.5 mm in diameter. The printed turbine rotor design for alumina and zirconia, from Section 3.1.3.1 was run using the same combined thermal and centrifugal profiles for idle and half power as outlined in Table 3 for the casting simulations.

Once testing with the ceramic printer was complete, an analysis was conducted on the successful designs to determine the final selected design. This last analysis

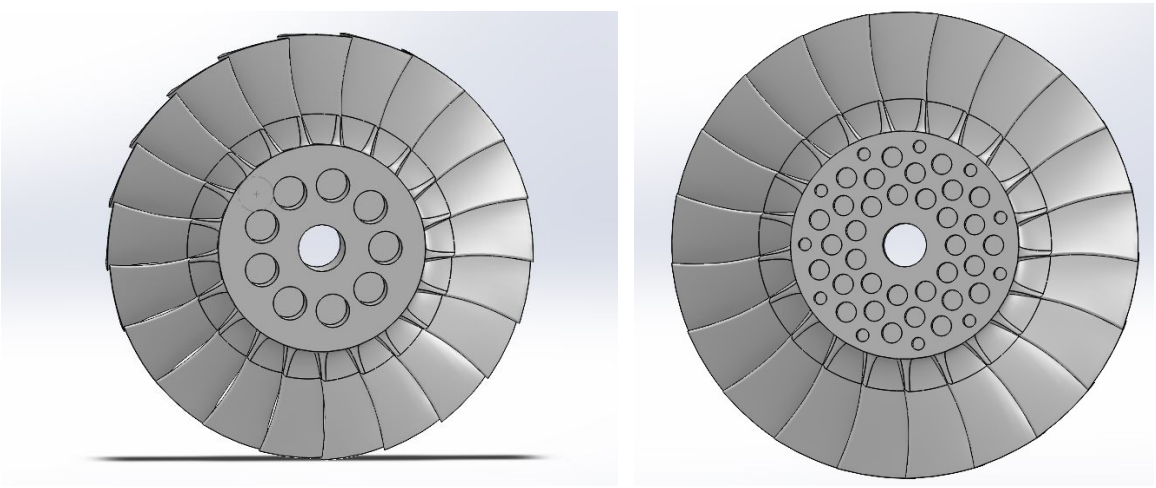

(a) Initial alumina turbine rotor design. (b) Initial zirconium turbine rotor design.

Figure 67. Initial turbine rotor Admatec printed designs.

determined what regime the final design could operate in for testing in the JetCat P400 and the maximum expected load for a room temperature spin test. This analysis would then be compared to the experimental test results conducted on the final design.

3.3 Testing and material characterization

3.3.1 Cast Si_3N_4 characterization.

The Si_3N_4 slurry for the cast rotor was based on the 45% Si_3N_4 slurry used by Rueschhoff et al. [7] for injection molding. Since the Si_3N_4 turbine rotor for this study used the casting method, a 43% Si_3N_4 slurry was utilized to allow the slurry to distribute more easily throughout the mold. Since this study used a reduced solid loading from Dr. Rueschhoff's study, the actual material properties needed to be determined to evaluate if the reduced solid loading would still meet the expected strength. This required determining the strength of the material, overall shrinkage, and full density. Additional consideration could be given to find the hardness and fracture toughness for further classification of the material.

3.3.1.1 Strength testing.

For ceramics strength testing, a three- or four-point bend test is most commonly used to determine the flexural strength of the material. The standards and specifications are dictated through the ASTM C1161-18. The three-point bend test typically leads to larger values when strength testing than the four-point bend test. This is due to the fact that there is only a single point load on the top of the sample, so it has less of a chance of finding the weaker point in a sample.[35] While the three-point bend test is acceptable, ASTM recommends the four-point bend test for more accuracy. The set up for three-point and four-point fixture spacing is shown in Figure 68. The length between the articulating load points are based on configuration tested. This study utilized the ASTM Configuration B parameters which required a length (L) of 40 mm. This determines where the test fixture points must be located to meet the standards.

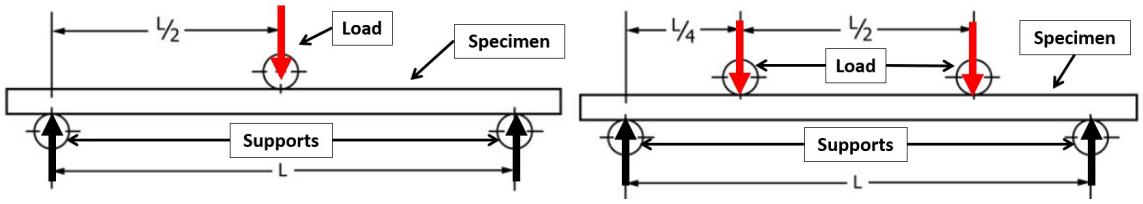

(a) Three-point bend fixture. (b) Four-point bend fixture.

Figure 68. ASTM standards for fixture configuration.[35]

Since the strength would need to be determined for the ceramic material in this study, a four-point flexural test fixture was needed to be used with an MTS load machine. This required designing a device based on ASTM Configuration B where specimen sample sizes were required to be 4 x 3 x 45 mm. Typically, at least 10 samples would be tested, which is the minimum required for an uncertainty distribution using a Weibull analysis. Initial samples would be tested at room temperature to determine the flexural strength of the material. However, since Si_3N_4 strength

properties change above 1000°C, the strength properties needed to be determined at elevated temperatures also. Testing was planned to be conducted at 1000°C, 1100°C, and 1200°C using samples for each temperature level. In order to meet the elevated temperature criteria a four-point flexural bend fixture had to be created that could operate at room temperature and elevated temperatures up to 1200°C and fit within the confines of the MTS furnace for testing.

This led to a design for a top and bottom fixture made of SiC, shown in Figure 69. The top fixture, Figure 69a, has three cylindrical grooves that hold 2 mm diameter ceramic rods which act as the point loads of the fixture. The two outer grooves would be used for four-point testing and the middle groove for three-point testing. The upper slot is for alignment of the push rod that extends out of the furnace. The bottom fixture, Figure 69b, has two cylindrical grooves, for the SiC rods, that act as the outer points for the bottom fixture matching the requirements for the ASTM standard. A groove is also on the bottom for the fixture to rest on a second push rod. The specimen is lowered through the side grooves on the bottom piece, which aligns the specimen onto the articulating ceramic rods ensuring proper placement. A basket was designed under the specimen in the bottom fixture to catch any part of the samples that may fall after testing.

Each push rod is connected to the MTS load machine through a stainless steel grip and held in place by set screws on four sides. Once the specimen is set up on the bottom fixture, the top fixture is lowered just on top of the specimen with the top push rod lowered into the groove on the top fixture. Once in place, the furnace is closed and heated to the desired temperature. Once at temperature the test can be run. The entire setup is shown in Figure 70.

To create the samples, rectangular molds were made with 5 individual sample slots for each specimen, shown in Figure 71. Each slot in the mold was 4 x 3 x 45 mm and

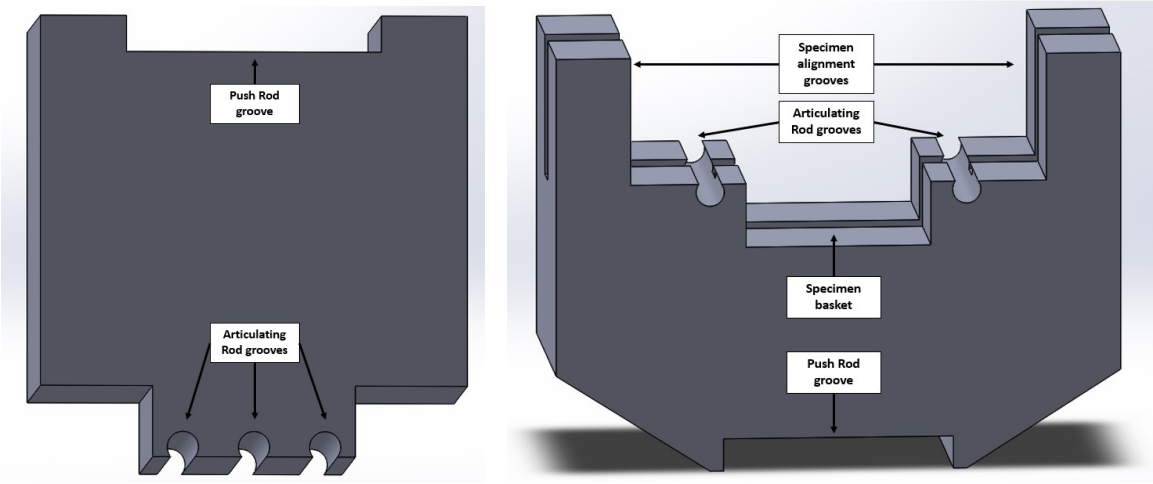

(a) Top four point bend fixture. (b) Bottom four point bend fixture.

Figure 69. Initial SiC bend fixture designed for strength testing.

the entire mold was scaled up 20% uniformly to account for shrinkage. The Si_3N_4 was cast into the molds to create samples but developed stress cracks during the drying process. This was due to the mold slots being too small, and as the slurry began shrinking during dryout, it cracked across the walls, which can be seen in Figure 71.

To alleviate the cracking from the ridges, a rectangular mold was created that was 28 x 3 x 45 mm and scaled 20% uniformly. The 28 mm wide mold would allow for approximately five specimens to be produced. The 43% Si_3N_4 slurry was then cast into eight molds, depicted in Figure 72a, utilizing the casting process in Section 3.1.1. After sintering, the specimens were to be shipped off to BOMAS to be machined and polished to ASTM specifications for testing. Of the eight specimens created, four survived through sintering without any cracks, as shown in Figure 72b. Unfortunately, they were measured just under the 3 mm requirements and were not able to be machined for testing.

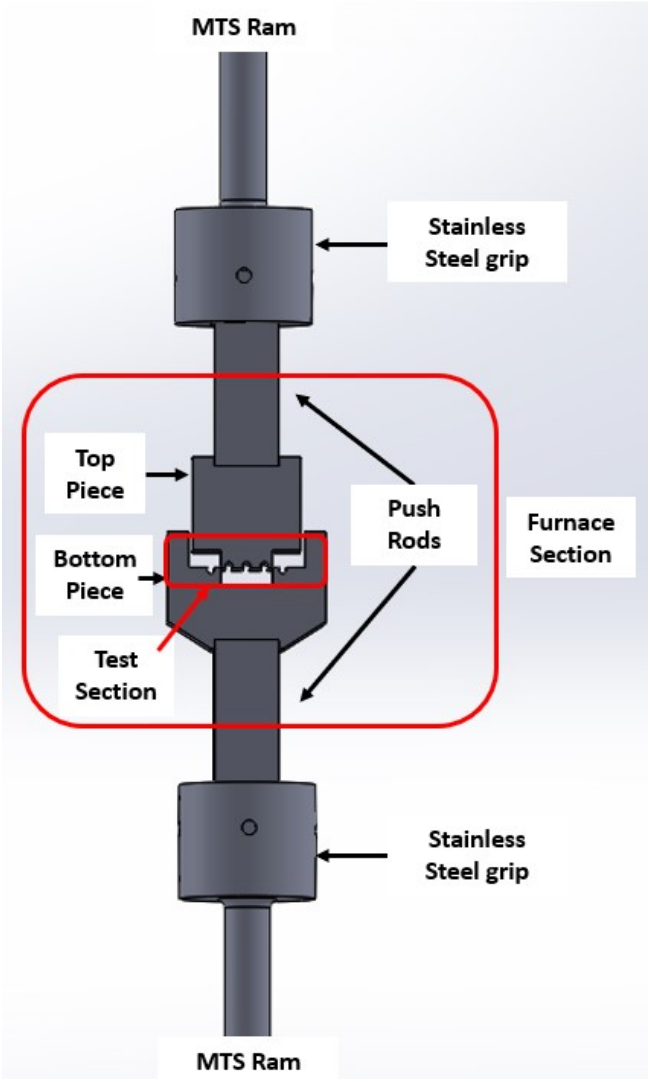

Figure 70. Complete four point bend structure device.

Figure 71. Si_3N_4 specimens cracked in the mold.

(a) cast specimens prior to binder burnout.

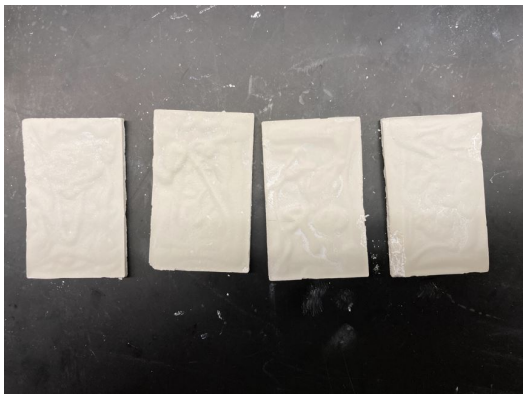

(b) Sintered specimens.

Figure 72. Si_3N_4 specimens casting.

3.3.1.2 Shrinkage characterization.

To determine the 43% Si_3N_4 slurry shrinkage, average measurements from two samples were taken in the width, depth, and length direction, after binder burnout and after sintering, utilizing a caliper. The dimensions were compared between the original fill of the mold, assuming complete fill, and after binder burnout to determine how much the material shrunk during the process. Additionally, the dimensions between binder burnout and sintering were compared to determine how much shrinkage occurred when the material densified. Finally, an overall shrinkage was determined for the sample. Knowing this information allows for the ability to appropriately scale the mold to allow the final turbine rotor design to shrink to the appropriate dimensions. Figure 73 show a comparison of a sample before binder burnout and after sintering.

3.3.1.3 Density evaluation.

Archimedes density testing was performed to determine the overall density of the Si_3N_4 after densification according to the standards laid out in ASTM C693-93.[36] To prepare for testing the sample had to first be cleaned. This was done by placing the sample in de-ionized water in a beaker. The beaker was then put in a sonicator

Figure 73. Comparison of Si_3N_4 sample specimens showing pre-binder burnout and post sintering

which helped remove excess powder bed material from the samples. The water was continuously swapped out until the material was cleaned.

Once cleaned, de-ionized water was again replaced in the beaker. The beaker with the samples was then placed on a heat plate. The heat plate was increased 120°C every ten minutes until reaching 400°C. Once at 400°C the sample boiled for 30 min and was then taken of the heat plate and allowed to cool to room temperature while still in the water. Once the water returned to room temperature, the de-ionized water was changed with fresh de-ionized water.

The Archimedes density testing was performed utilizing a Cole-Parmer scale. The first measurement recorded the weight of the samples suspended in water. For set up, shown in Figure 74a, a beaker of water was placed on the scale with a thermometer to read the temperature of the water. A basket was suspended in the water. Then the scale was zeroed out. To record the sample weight while wet, a sample was taken from the original beaker of water, and then placed on the suspended basket. Once the scale weight stabilized the weight was recorded along with the temperature of the water.

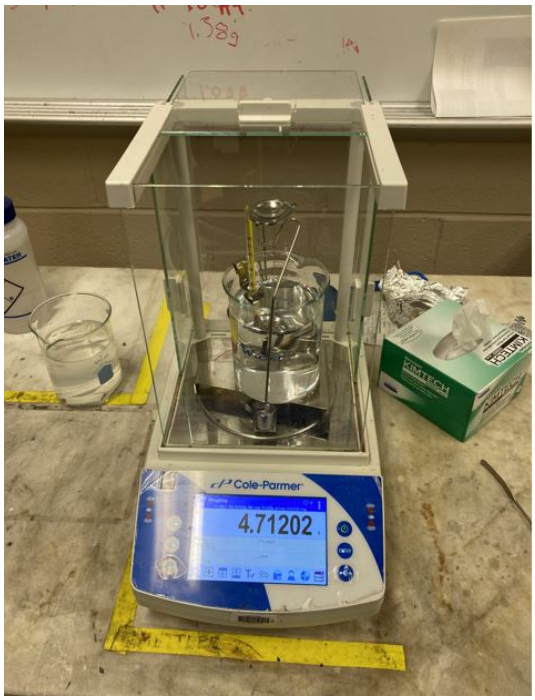

(a) Archimedes Density testing suspended in water.

(b) Archimedes Density testing for saturated and dry weight.

Figure 74. Archimedes Density testing setup.

The second measurement was the saturated weight of the samples. For the set up, shown in Figure 74b, the beaker set up was removed and the regular scale was used to weight just the sample. The scale was zeroed out. To get the saturated weight, the sample was removed from the water beaker, and placed on a towel and lightly dabbed off with a damp towel to remove the excess water on the outer surface. It was then placed on the scale, recording the weight once the scale stabilized.

The final measurement taken was the dry weight of the sample. For this weight, the sample was completely dried by placing it in a dryout oven for at least an hour. Then the sample was removed and placed into a drybox for a minimum of 10 minutes to cool. Using the same set up in Figure 74b, the sample was then weighed on the scale and recorded once stabilized.

The sintered samples actual density (ρ_s) is calculated with Equation 2. The water

density (ρ_w), determined from a chart in ASTM C693-93 based on the water temperature, is multiplied by the sample's dry weight (W_{dry}). This value is then divided by the difference between the sample's suspended weight (W_{susp}) and saturated weight (W_{sat}).

$$\rho_s = \frac{\rho_w \times W_{dry}}{(W_{susp} - W_{sat})} \tag{2}$$

To determine the overall relative density of the sample, the sample's true density, based on the solid loading, is divided by the calculated actual density providing the percentage of densification for the sample.

IV. Results

4.1 Si_3N_4 cast turbine rotor FEA results

4.1.1 AFRL operating requirements.

4.1.1.1 Differing Coefficients of Thermal Expansion in the bore.

The FEA simulation for the thermal stresses imparted on the Si_3N_4 turbine rotor at the bore by the 2507 stainless steel shaft are shown in Figure 75. At 427°C the bore fails near the edge of the shaft at 900 MPa due to the expansion of the shaft. The failure region in the bore is denoted in the yellow and red region in the stress plot in Figure 75a. The factor of safety (FOS) plot, in Figure75b, further shows the failure above 900 MPa outlined in pink. These results indicate the difference in coefficient of thermal expansions need to be taken into account requiring the use of a joining mechanism, such as a tolerance ring, to reduce or eliminate these thermal stresses.

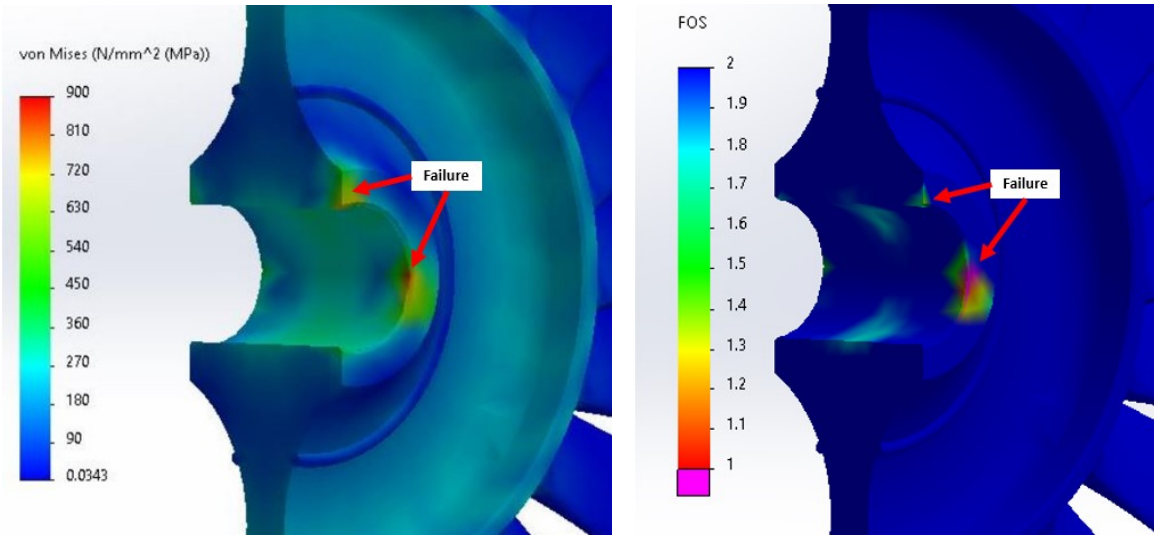

(a) Thermal stress plot of the turbine rotor and shaft assembly with shaft removed.

(b) Factor of Safety plot of the assembly with shaft removed.

Figure 75. Thermal finite element analysis of the 2507 Stainless steel shaft and Si_3N_4 turbine rotor.

4.1.1.2 Centrifugal stress analysis.

Initially the FEA included only centrifugal loads in the three BYU variant turbine rotor hub designs: BYU tapered hub, leading-edge flat hub, and filled hub. For the BYU tapered hub the FEA results produced a peak stress of 528 MPa located on the outer edge of the hub in between the fillets at the blade root, indicated in red in Figure 76a. Figure 76b shows a zoomed in region of the blades. The peak stress region stretches from the leading edge to the trailing edge between the blades, but no failure occurs. Peak stresses in the hub region were 337 MPa.

When mass was added to the hub on the leading-edge side to simplify the design, the peak stresses, denoted in red, between the blade fillets coalesced to the tapered trailing edge side of the turbine rotor, shown in Figure 77. These peak stresses increased to 547 MPa. However, the stresses at the bore were reduced to a peak stress of 316 MPa.

For the final design with the straight walled hub, the stress between fillets was removed and the peak stress shifted to the bore region, shown in Figure 78a. Figure 78b shows the stress plot produced by the simulation with a peak stress of 277 MPa at the center of the hub. When evaluating the shaft region there appears to be red streaks within the bore. These stress increases were positioned below the blades and resulted from additional mass of the blade.

None of the three designs indicated failure under centrifugal loading conditions. As more mass was added to the hub, the stress between fillets was reduced and the overall stresses at the shaft decreased. When increasing mass in a rotating design, it is expected that the stresses will coalesce towards the center of mass. The FEA showed in Figures 76 and 77 for the first two designs that the dominate stresses were higher since the loads were in the outer edge of the hub at the tapered location where there was no mass behind those edges to distribute the centrifugal stresses. As more

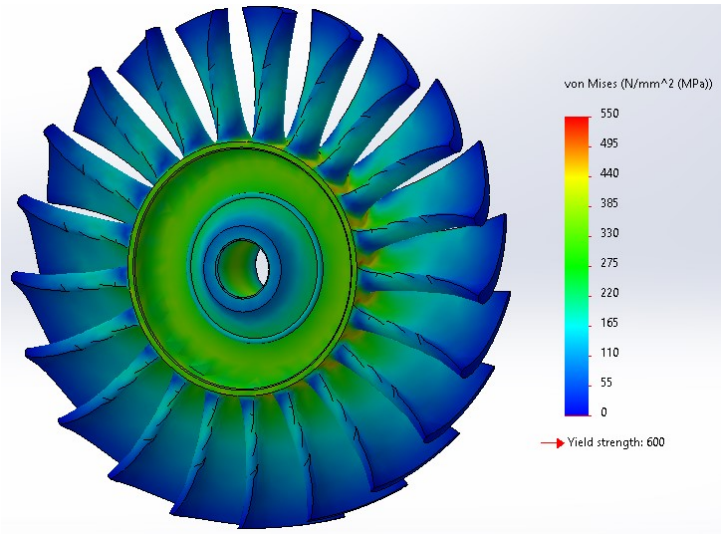

(a) Centrifugal stress analysis of the BYU tapered hub design.

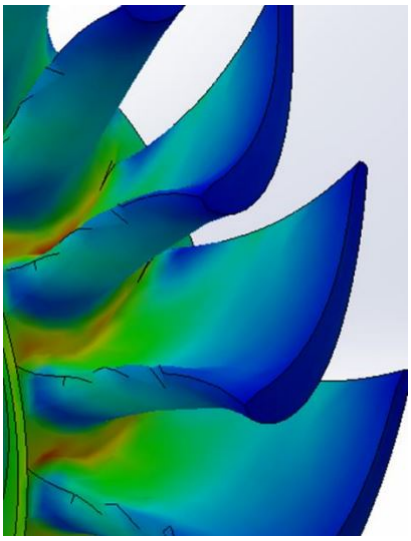

(b) Close up of analysis in the blade region indicating peak stress.

Figure 76. Centrifugal stress analysis of the BYU tapered hub design.

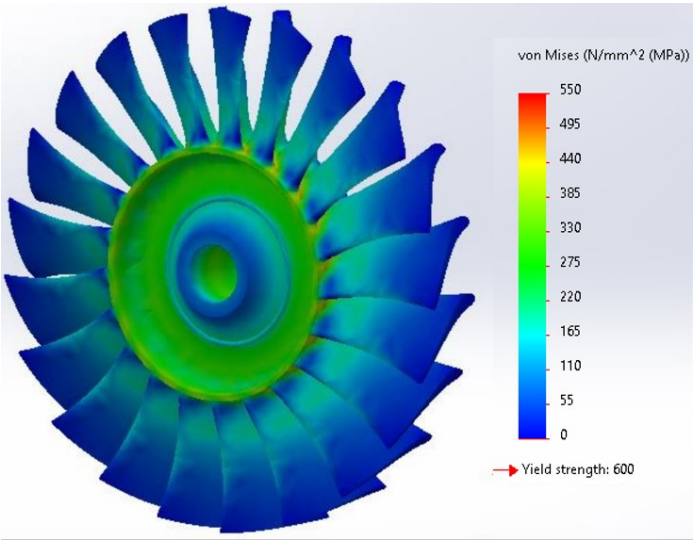

(a) Centrifugal stress analysis of the half filled hub design.

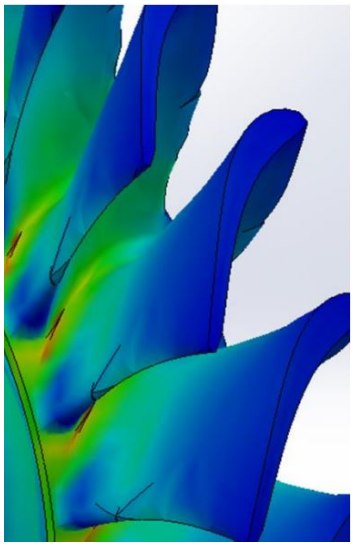

(b) Close up of analysis in the blade region indicating peak stress.

Figure 77. Centrifugal stress analysis of the half filled hub design.

mass in the hub was added, the centrifugal stress was concentrated more on the bore region allowing for the stresses to distribute more easily towards the center of the turbine rotor. This analysis showed a thicker hub region reduced the affects in the

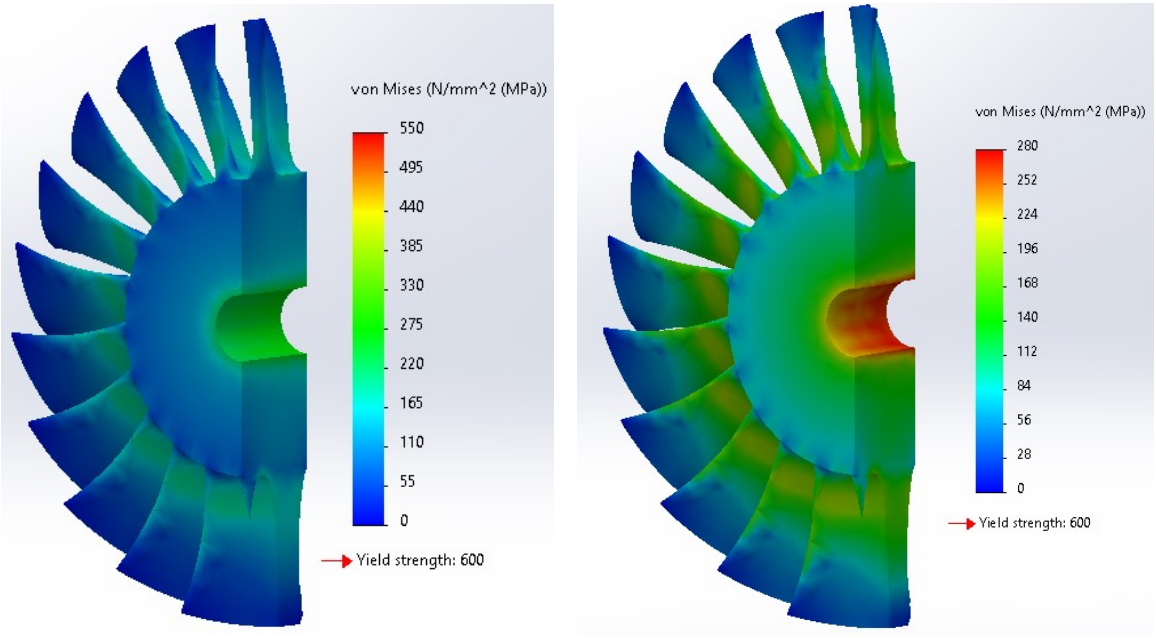

(a) Centrifugal stress analysis of the full filled hub design.

(b) Centrifugal stress analysis of the full filled hub design indicating peak stress.

Figure 78. Centrifugal stress analysis of the filled hub design.

outer radial portion of the hub, while concentrating the stresses in the bore.

4.1.1.3 Thermal stress analysis.

The second FEA evaluated the thermal stresses on the three varying turbine rotor hub designs. The BYU tapered hub showed peak stresses causing failure in the blade root region, denoted in Figure 79. Figure 79b shows the region at the blade fillets where failure is indicated on the leading-edge side circled in red with a peak stress of 612 MPa. This shows a potential for failure due to the thermal expansion of the fillets. In the bore region a peak stress of 391 MPa was found in the center of the bore correlating to the largest region of mass in the hub.

As mass was added to the hub on the other two designs, the peak stress region shifted to the bore. Figure 80a shows the thermal stress analysis for the partially filled hub on the leading edge, with a peak stress of 525 MPa. The peak stresses were

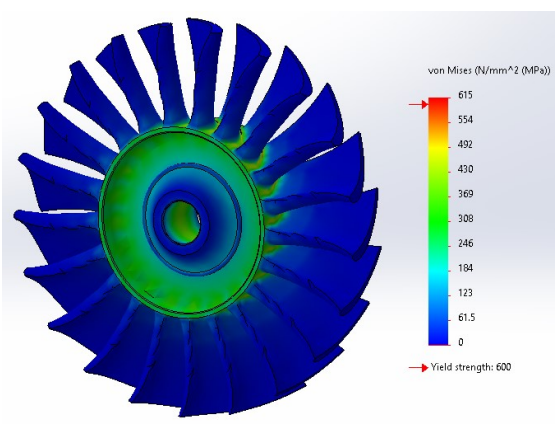

(a) Thermal stress analysis of the BYU tapered hub design.

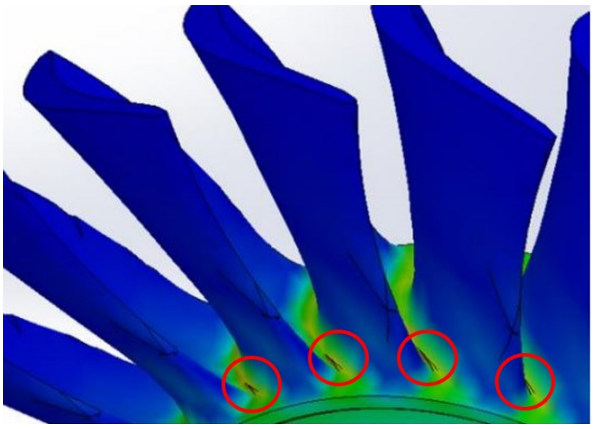

(b) Close up of analysis in the blade region indicating failure due to thermal expansion in the fillets.

Figure 79. Thermal stress analysis of the BYU tapered hub design.

in the bore where the increased mass region of the filled in portion of the hub was located. Figure 80b shows the analysis for the filled hub with a peak stress of 600 MPa. The indicated peak stresses were distributed at the center of the bore and were right at failure levels.

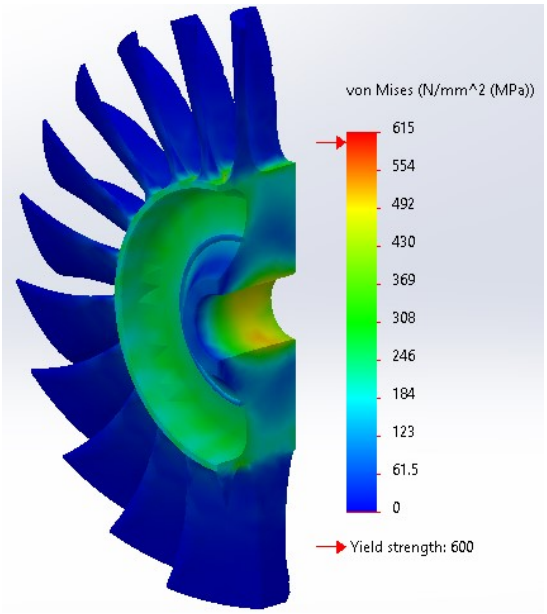

(a) Thermal stress analysis of the partially filled hub design.

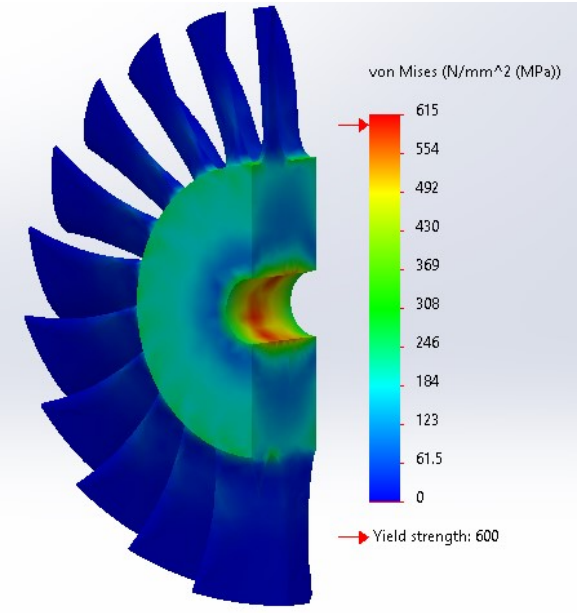

(b) Thermal stress analysis of the filled hub design.

Figure 80. Thermal stress analysis of the partially filled hub and filled hub.

The thermal FEA indicated a dominating effect due to thermal stresses than those from centrifugal stresses. The issue with the fillet expansion causing failure was reduced by adding mass to the outer portion of the hub, allowing for the energy to distribute through more material. However, under the given temperature conditions larger stress was added to the bore as more mass was added, eventually leading to initial failure in the filled hub. This was due to a large temperature difference between the bore and radially outer portion of the hub, the additional mass allowed for more energy to be absorbed and increased the temperature differential between the two regions leading to the increasing stress in the bore.

4.1.1.4 Combined centrifugal and thermal stress analysis.

The combined FEA provided an overall determination on how the turbine rotor would perform under expected operating conditions. The analysis determined failure above 600 MPa under combined loading conditions, shown in Figure 81. The maximum stress in the BYU tapered hub, partially filled hub, and filled hub, was at 757 MPa, 816 MPa, and 857 MPa, respectively. For each hub design, the failure region was located in the center of the bore with the peak stress increasing as mass was added to the hub.

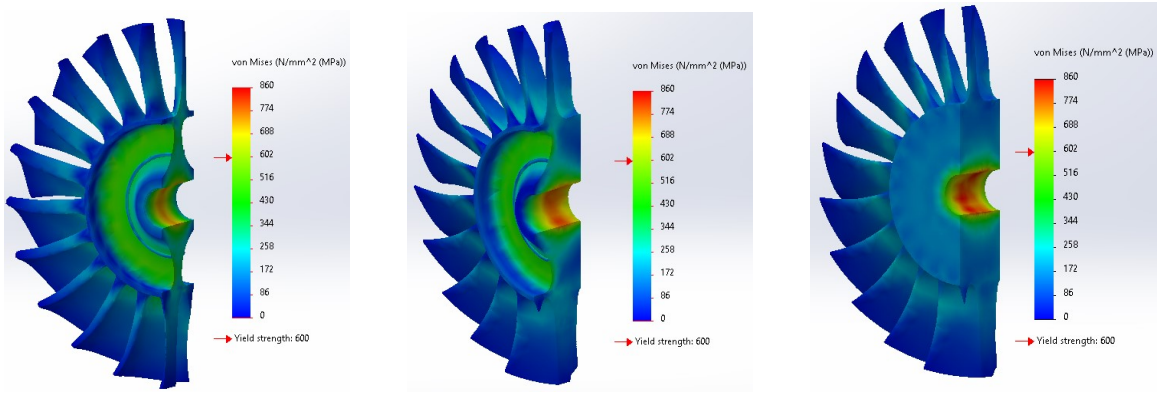

(a) BYU tapered hub. (b) Partially filled hub. (c) Filled hub.

Figure 81. Combined centrifugal and thermal stress analysis.

The full failure regions for each turbine rotor design are shown in the FOS diagram in Figure 82. Failure, denoted in pink, can be seen in the regions in the bore corresponding with the areas of larger mass. The completely filled in hub showed failure throughout the entire bore. Using the given thermal profile from Section 3.2.1 and a speed of 90,000 RPM the designs would not be able to withstand loading conditions.

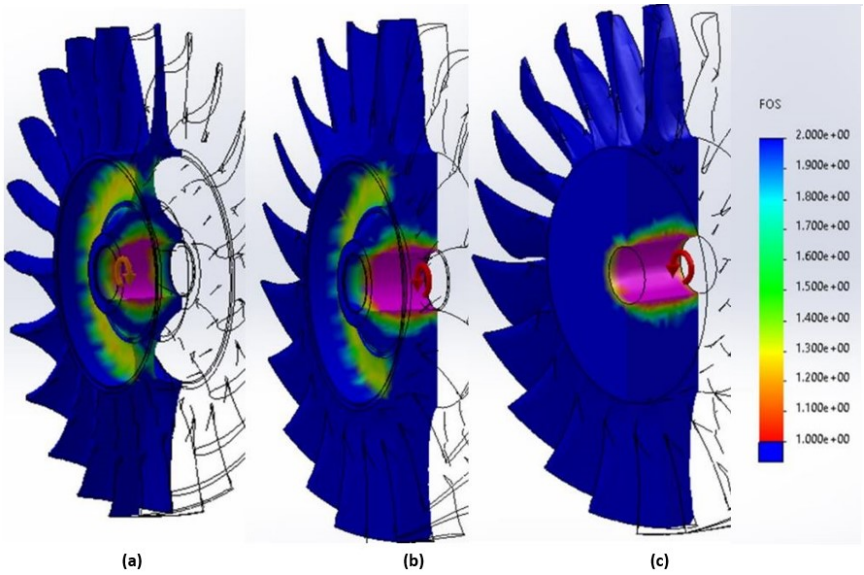

Figure 82. Combined centrifugal and thermal stresses FOS plot: BYU tapered hub (a), half filled hub (b), filled hub (c).

Altering the thermal profile at the bore for the BYU tapered hub and filled hub, in order to decrease the temperature differential, presented a linear decrease in overall peak stress located in the bore. Figure 83 shows a plot of the maximum stresses for the BYU tapered hub, in blue, and filled hub, in green, with the expected material yield stress in red. As the bore temperature was increased, with all other thermal and centrifugal conditions the same, the stress decreased for both hub designs. At a bore temperature of 743°C for the BYU tapered hub and 762°C for the filled hub, the maximum stress, located in the bore, is equivalent to the yield strength. Additionally, the filled hub stress decreased at a faster rate than the BYU tapered design. After 800°C the filled in hub had lower maximum stress values than the BYU design.

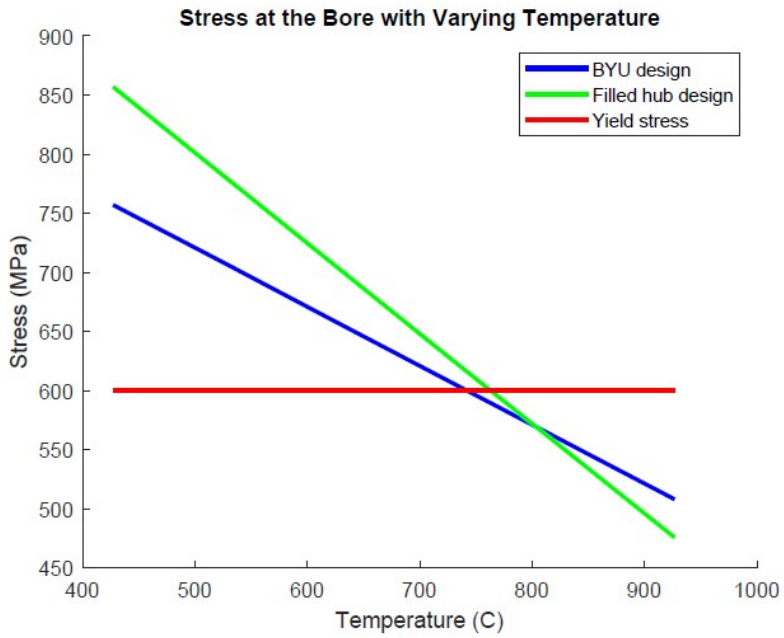

Figure 83. Plot showing peak stress in the bore determined through FEA with increasing bore temperature.

4.1.2 Si_3N_4 cast turbine rotor JetCat P400 operating conditions analysis.

For the three designs analyzed, the FEA showed each cast turbine rotor was able to meet the full power conditions of the JetCat P400 based on the given design criteria outlined in Table 3 of Section 3.2.2. The BYU tapered hub design, in Figure 84, showed peak stresses at 557 MPa located in the bore consistent with earlier analysis. The analysis further showed a second high level of stress around 474 MPa located in the middle of the hub at the base of the taper, shown in orange. This result shows the additional stress carried in the middle of the hub with the reduced mass.

The analysis for the partially filled hub, Figure 85, showed peak stresses located in the bore at 531 MPa. When viewing the hub on the leading edge with the added mass, the stress was significantly reduced throughout the hub. However, when viewing the trailing edge, the tapered hub side shows a secondary peak stress around 425 MPa

located in the center portion of the hub. The addition of mass on the leading edge side caused less stress in the hub and reduced the stress in the bore from the difference in temperature between the outer hub and bore.

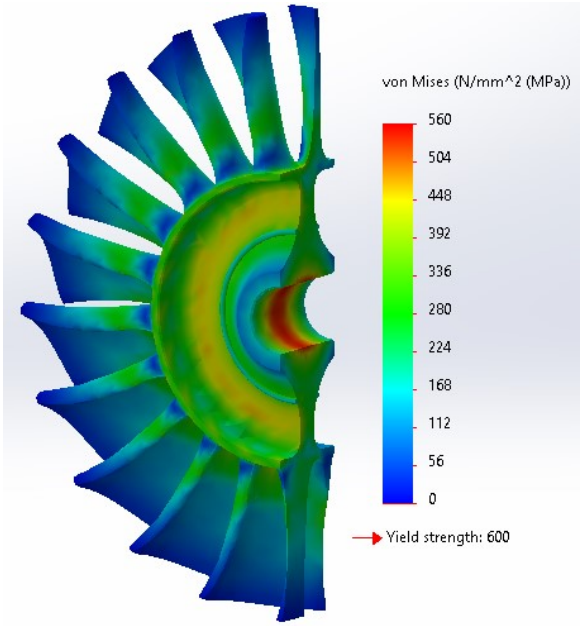

Figure 84. BYU tapered hub design 98,000 RPM full powered JetCat P400 analysis.

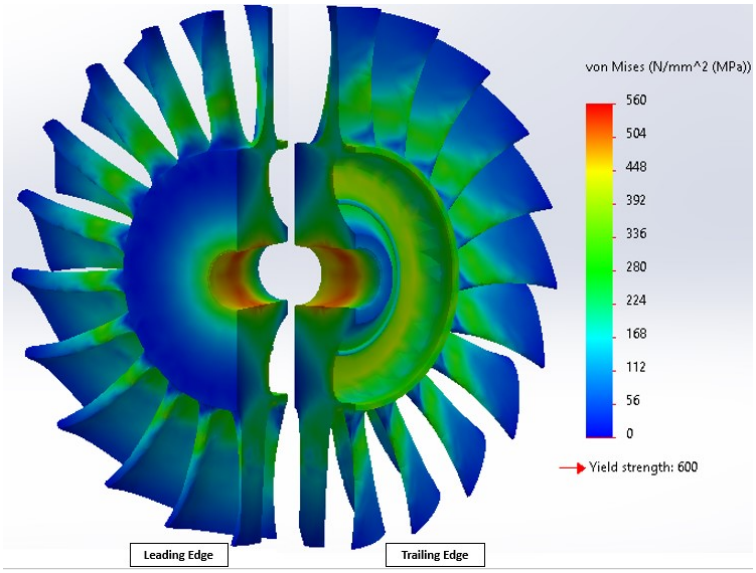

Figure 85. Partially filled hub design 98,000 RPM full powered JetCat P400 analysis.

The analysis for the fully filled hub, Figure 86, showed peak stresses located in the bore at 493 MPa. As shown on the partially filled hub leading edge side, there were additional significant stresses in the middle of the hub due to the added mass. The fully filled hub design held up to the operating conditions the best out of the three designs. This was due to the fact that the temperature gradient across the hub was much lower than the analysis from the first set of operating conditions given by AFRL.

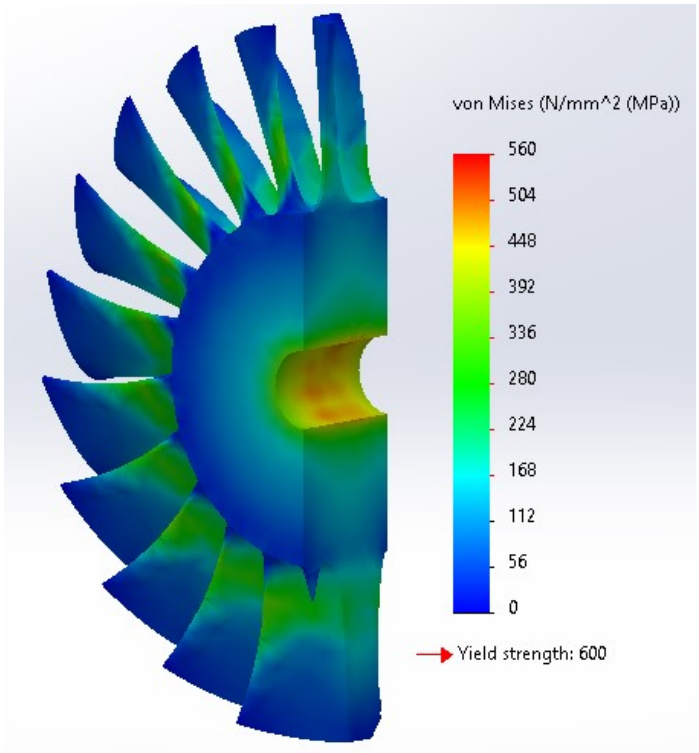

Figure 86. Fully filled hub design 98,000 RPM full powered JetCat P400 analysis.

4.1.3 Key takeaways.

Running the FEA for both the individual and combined loads showed that based on the given parameters thermal stresses dominated. For solely the centrifugal loads, by adding mass to the hub, the loads were concentrated at the bore and reduced the

overall stress of the design. For the temperature profile analysis, as mass increased the energy was absorbed which eliminated the fillet expansion issue seen in the BYU tapered hub. However, the addition of mass also led to an increase in stress at the bore. When analyzed under both centrifugal and thermal conditions, each design showed failure at the bore. The more mass in the hub, the larger the failure stress due to the large temperature difference between the bore and the outer hub.

By adjusting the bore temperature, therefore decreasing the temperature differential, the BYU tapered hub and filled hub were able to be brought below the yield stress and meet the operating conditions of the engine. The temperature increase in the bore could conceivably be increased closer to the limit of the stainless-steel shaft or bearings to accommodate a higher temperature. If taken to 1000°C at the bore, based on the linear correlation, the stress in the bore for the BYU tapered hub and filled hub design would be 472 MPa and 418 MPa, respectively. As shown by the operating conditions in the JetCat P400, utilizing the simpler filled hub design along with a smaller temperature differential provides a stronger turbine rotor design. Additionally by making the design less complex, the manufacturing process had more chance of success and gave more flexibility to the FOS and Si_3N_4 material strength properties required. After the analysis it was determined the simple filled in hub design would be utilized for further casting of the final Si_3N_4 turbine rotor.

4.2 Mold testing and design

4.2.1 Surface Roughness evaluation.

For the surface roughness testing, all the application times and RSa values are shown in Table 4. The table shows the initial samples of VeroClear and Polycast untreated. Then shows the mist treatments followed by the effects of pouring liquid isopropyl alcohol and Rain X treatments.

Table 4. Surface roughness properties

Surface Treatment	Application Time (min)	RSa (μm)
VeroClear No Treatment	NA	4.3
PolyCast No Treatment	NA	12.8
Alcohol aerosol mist	20	1.4
Alcohol aerosol mist	30	2.4
Alcohol	1	2.6
Alcohol	2	1.8
Alcohol	3	1.5

Surface Treatment	Application Time (min)	RSa (μm)
Rain X	1	1.3
Rain X	2	1.3
Rain X	3	1.1
Alcohol and Rain X	1 each	1.3
Alcohol and Rain X	2 each	1.3
Alcohol and Rain X	3 each	1.6

Surface roughness in the untreated Polycast molds can be easily seen when compared to the untreated VeroClear molds in Figure 87. Distinct ridges can be seen in Figure 87a showing the deposited layers from the printing process, where the VeroClear sample, Figure 87b, has some surface roughness but provides a smoother surface finish void of distinct ridges. The difference in the presence of ridges is due to the difference between the two printing methods. The untreated Polycast sample had an RSa value of 12.8 μm, while the VeroClear was one third of the RSa value at 4.3 μm. These scans show the necessity for smoothing out the ridges in the Polycast molds to allow the Si_3N_4 to release more effectively from the mold.

When processing in the alcohol chamber for 20 and 30 minutes, the Polycast mold samples came out very gummy and were initially flexible. The samples had to be left to dry in the open air to dry until they could be handled and moved off the Polysher platform. The 20 minute samples were able to be transferred to another surface after five minutes of dry time, however, the 30 minute molds took about 15 minutes to be able to move without causing any deformation. Manufacturer recommendations

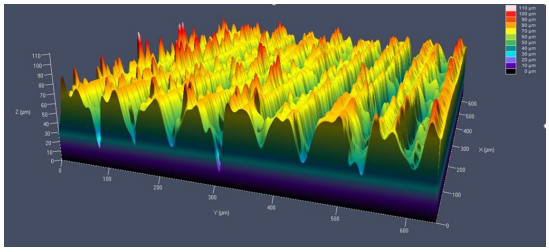

(a) Polycast untreated mold.

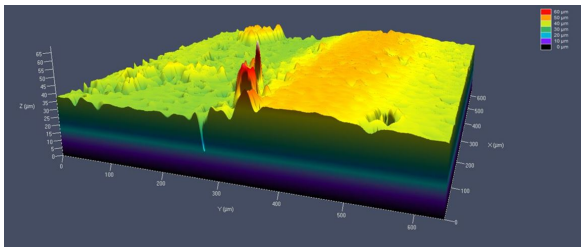

(b) Veroclear untreated mold.

Figure 87. Surface scans at 10X zoom of the untreated Polycast and VeroClear molds.

stated to allow 2 days dry time for the samples, however, after 1 day the 20 minute samples were fully dry and back to their initial rigidity and shape. Even after 2 days the 30 minute dry time samples remained very flexible, became almost rubber like, and did not hold shape as well. Some samples even became permanently warped.

Evaluating the surface finishes of the 20 and 30 minute samples produced RSa values of 1.4 and 2.4 μm. The higher value in the 30 minute sample is due to oversaturation of the Polycast material from the isopropyl alcohol. The surface scans, shown in Figure 88, clearly show a smooth surface on the 20 minute mold sample removing the ridges in Figure 88a. Figure 88b shows the layer ridges removed, but also shows deformation of the sample due to oversaturation. This led to the determination that 20 minutes was the appropriate amount of time in the alcohol chamber to reduce the surface roughness of the Polycast mold sample.

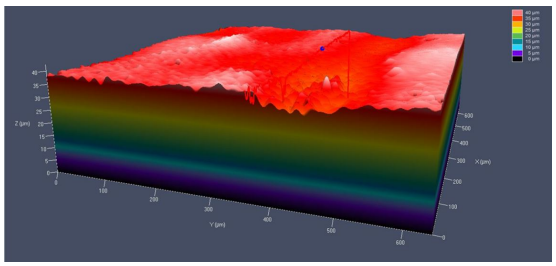

(a) 20 min in the Polysher.

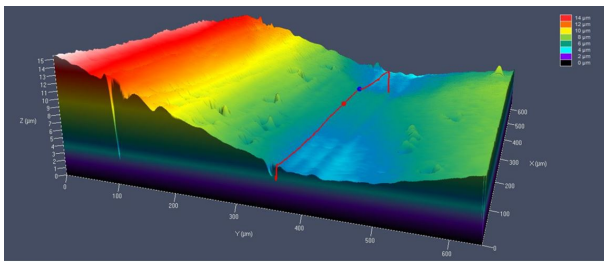

(b) 30 min in the Polysher.

Figure 88. Polycast mold surface scans from the Polysher isopropyl alcohol aerosol bath treatment.

Since the cast turbine mold is a negative, the mist would not be able to easily get into the mold and effectively smooth out all the layers. For this reason liquid isopropyl alcohol poured into the mold was used to get the same effect as the alcohol mist. Since the Polycast material has showed it loses rigidity with liquid isopropyl alcohol, Rain X, a liquid release agent, was also tested to determine if there were any similar effects from other potential liquid sources. The effects of the isopropyl alcohol are shown in Figure 89. Pouring the isopropyl alcohol into the mold and letting it sit in there for one, two, and three minutes produced RSa values of 2.6, 1.8, 1.5 μm, respectively. When viewing the scans, the one minute test, Figure 89a, shows the layers beginning to smooth out, but still partially visible, while the two minute sample, Figure 89b, shows a smooth surface finish. The three minute surface, Figure 89c, produced the lowest RSa of the three samples, but it shows that the extra minute began causing deformation in the surface and an uneven finish.

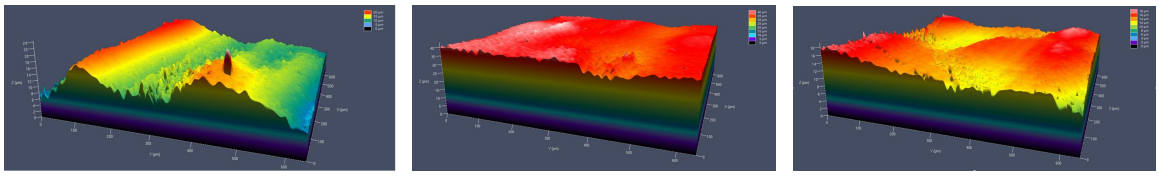

(a) 1 minute trial. (b) 2 minute trial. (c) 3 minute trial.

Figure 89. Surface scans from the liquid isopropyl alcohol trial.

When evaluating the surface roughness effects of the potential mold release agent Rain X, the one, two, and three minute tests yielded RSa values of 1.3, 1.3, and 1.1 μm, respectively. Evaluating the scanned images in Figure 90, the one and two minute scans, Figure 90a and 90b, produced similar results and showed Rain X's potential for reducing the printed layers while still having some uneven surfaces in the sample. The three minute sample, Figure 90c, showed the smoothest surface of the three and demonstrated that Rain X will dissolve the material to some degree meaning it could be used to smooth the mold and act as a mold release. Care needs

to be taken if used in conjunction with the isopropyl alcohol to assure the mold is not dissolved negatively.

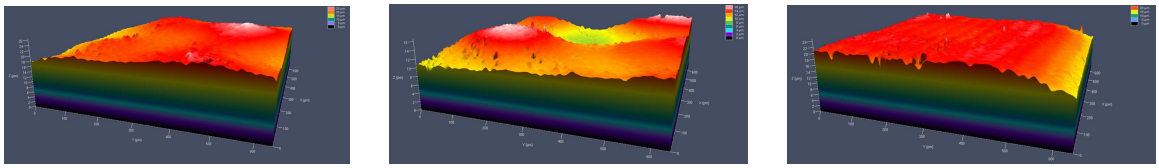

(a) 1 minute trial. (b) 2 minute trial. (c) 3 minute trial.

Figure 90. Surface scans from the liquid Rain X trial.

When applying the isopropyl alcohol followed by the Rain X to simulate application of the smoothing agent followed by release agent, the one, two, three minute tests yielded RSa values of 1.3, 1.3, and 1.6 μm, respectively. The scanned images of the one minute sample in Figure 91a, show the surface finish beginning to fuse but still incomplete. The two minute sample, Figure 91b, showed the best fusion of the layers and flattest surface. The three minute sample, Figure 91c, shows the sample beginning to deform beyond the flat surface of the 2 minute test. All of the three combined treatments follow similar trends to the isopropyl alcohol treatment, leading to the conclusion that the isopropyl alcohol has a larger effect on the Polycast material than the Rain X.

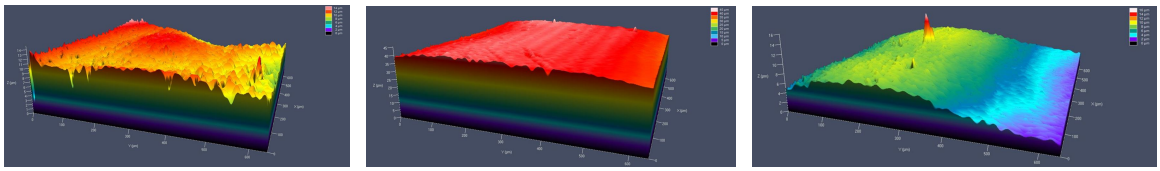

(a) 1 minute trial. (b) 2 minute trial. (c) 3 minute trial.

Figure 91. Surface scans from the liquid isopropyl alcohol and Rain X trial.

When comparing VeroClear and untreated Polycast molds, the VeroClear has a much smoother surface. However, when utilizing the treatments it was determined if the mist chamber is to be utilized, 20 minutes provides the smoothest surface for a mold when able to coat the whole inner surface. When the mold inner surface cannot

be coated through aerosol means then applying liquid isopropyl alcohol into the mold for 2 minutes produced the smoothest surface with results comparable to the mist. This shows that a better surface can be created utilizing the Polycast material than the VeroClear material after treatment.

However, due to the porous nature of Polycast, it is effected by liquid agents. This means if a liquid solvent such as Rain X were further applied for mold release, the mold could potentially be affected further. This was shown when the Rain X provided fusion of layers after sitting in the mold for three minutes. This outcome leads to the determination that if a liquid release agent must be used, it needs to be limited to no more than 2 minutes of use at a time to prevent the mold from dissolving too much. Since the isopropyl alcohol seemed to have the greatest effect on the Polycast sample, it seems the best solution for the molds would be t minutes in liquid isopropyl alcohol and no more than two minutes with a liquid release agent if required.

4.2.2 Mold release testing.

Proper release of material from the mold during drying was critical to prevent cracking of the Si_3N_4 samples due to adherence to the mold surfaces. For both the Polycast and VeroClear materials, four mold release agents were tested including an aerosol Teflon known as Allied Teflon, dry Teflon applied with a brush, liquid Rain X, and Smooth On (an aerosol release). For VeroClear, UV light is typically utilized to fully cure the mold so UV and non-UV treated molds were tested with each mold release. However, this study showed no variation between either the VeroClear or Polycast molds being UV cured or not.

The Polycast samples were split into two trials. The first trial tested all the mold release agents as well as a baseline untreated specimen. For these molds, the Si_3N_4 was pored halfway into the mold due to the amount of slurry available. For the

untreated Polycast molds, in Figure 92a, each sample shows the Si_3N_4 adhered to the sides of the mold while drying causing the sides of the mold to bow inward as the Si_3N_4 dried and began to shrink. This adherence caused stress cracking in the corners of each mold and massive cracking through the non-UV treated mold on the right. For the Polycast molds treated with Allied Teflon, Figure 92b, the molds were less bowed in, but the Si_3N_4 never released from the sides of the mold. There was still enough adherence to the mold that led to cracking in the corners of the UV cured mold and a small amount of cracking in the corners of the non-UV cured mold. However, there were no large cracks thoughout the remainder of the Si_3N_4 sample.

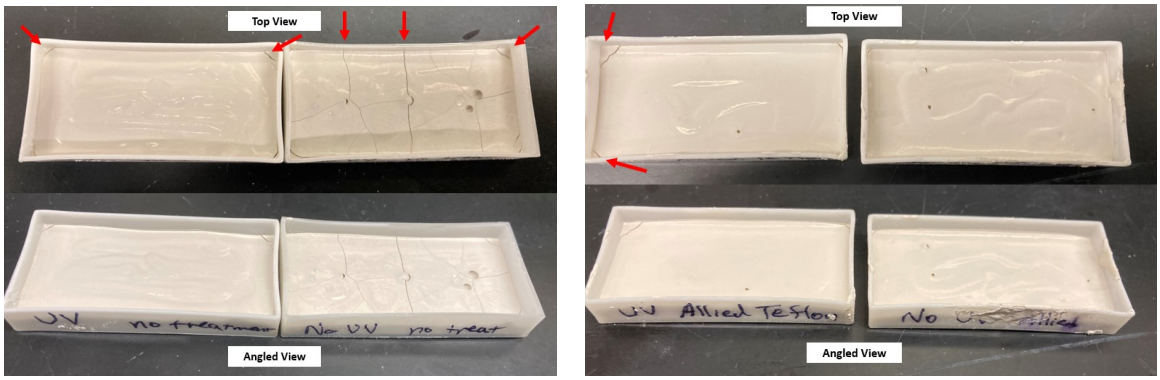

(a) Untreated Polycast samples.

(b) Allied Teflon Polycast samples.

Figure 92. First Polycast mold release trial samples: Untreated and Allied Teflon.

When evaluating the dry Teflon release agent, Figure 93a, there was minimal cracking of the Si_3N_4 in the corners for both samples. This cracking was due to some adherence to the mold walls as the Si_3N_4 did not fully release from the sides. When observing the Rain X samples, Figure 93b, the non-UV cured sample showed the Si_3N_4 releasing from the mold wall, which can be seen in the left angled view. This led to only one small crack in the corner of the sample. However, this was not duplicated in the UV cured sample which adhered to the walls and cracked in the corners.

Both Smooth On samples, in Figure 94, showed the best results overall as the

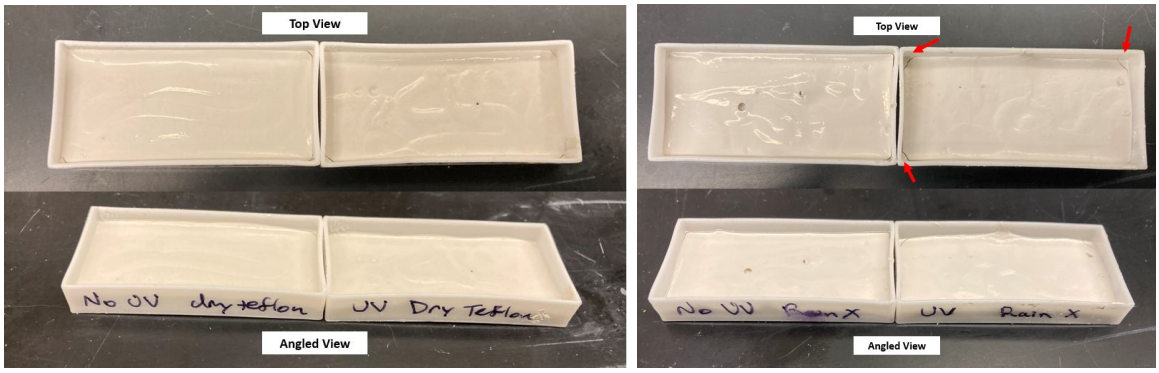

(a) Dry Teflon Polycast samples. (b) Rain X Polycast samples.

Figure 93. First Polycast mold release trial samples: Dry Teflon and Rain X.

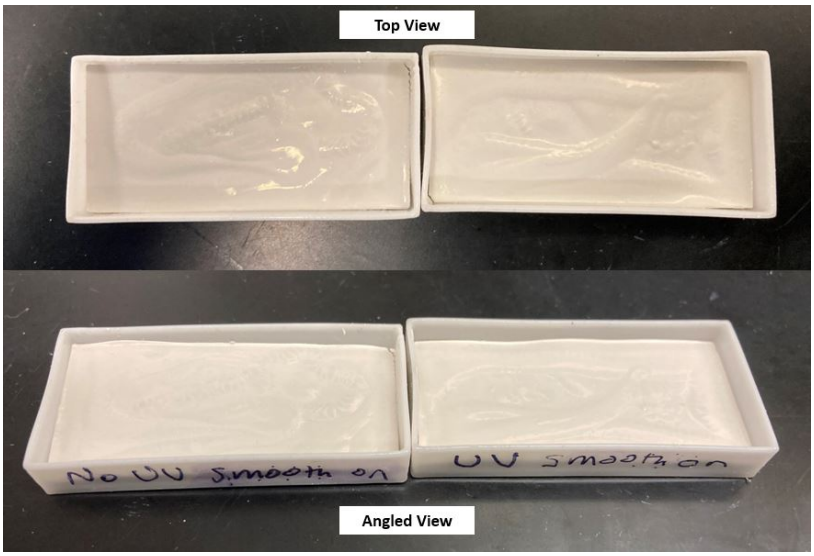

Figure 94. First Polycast mold release trial Smooth On samples.

Si_3N_4 released from the walls. This is evident by looking at the top view and seeing the space between the Si_3N_4 sample and walls. Only one small crack in the corner was noticed in the UV sample on the right.

The results of the first trial appear to show the Smooth On release agent as the best agent to use. It also appeared, that Rain X was a potential alternate that showed some signs of allowing the material to release from the mold. While the dry Teflon had minimal cracking it was deemed unnecessary for further study due to the difficulty of

applying the material with a brush to an enclosed mold. After the first trial, a second trial was conducted with the Polycast material using the same shaped molds, from a second print, completely filled with the Si_3N_4 slurry. As shown in Figure 95 this trial consisted of a baseline untreated sample and the remaining three most promising releases: Rain X, Allied Teflon, and Smooth On.

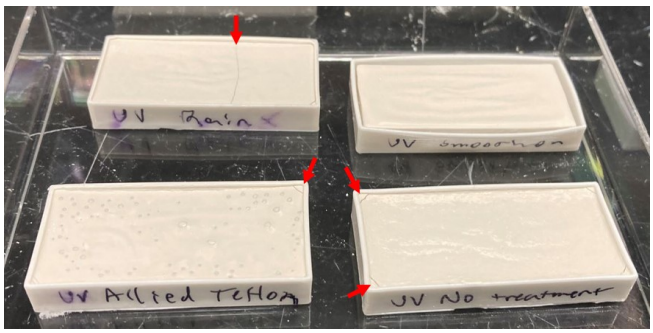

(a) Second Polycast mold release trial samples side view.

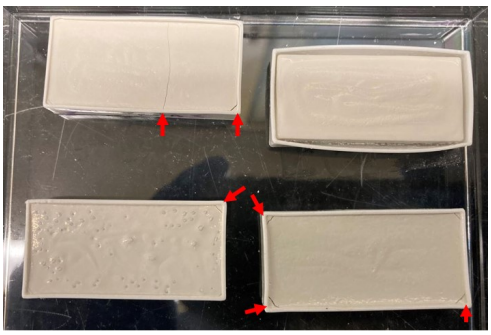

(b) Second Polycast mold release trial samples top view.

Figure 95. Second Polycast mold release trial samples.

The untreated Si_3N_4 sample, in the bottom right of Figure 95, developed cracks in the corners and was unable to release from the walls of the mold. The Rain X sample in the top left, began to release from the top of the mold. This is evident from the top lip of the mold bowing outward which is best seen in Figure 95b. However, the release did not happen from the entire mold and led to a stress crack through the sample and in the bottom right corner. For the Allied Teflon treated mold, in the bottom left, the Si_3N_4 material did not release from the mold and had one crack in the top right corner. Overall, this was minimal cracking but still failed to release from the sides. Since the Allied Teflon was cast last there were some air bubbles that got inserted into the material and escaped during drying. The Smooth On sample, in the top right, showed the best results of all the mold releases. As can be seen in the images the sample completely pulled away from the mold intact and holding shape with no cracking. This further shows that as the Si_3N_4 was pulling away, the mold

bowed outward once the material began drying which assisted with the release.

Similar trials were conducted with the VeroClear, with the addition of Rain X being tested at 5, 10, and 15 minute time intervals to determine if there was a difference. The untreated samples in Figure 96a showed a baseline of massive cracking in the UV treated sample. While there was no visible cracking in the untreated non-UV cured sample, each sample adhered to the mold. When observing the Allied Teflon, in Figure 96a, stress cracks could be seen throughout both samples. Additionally the Si_3N_4 adhered to the mold while drying causing the mold to bow inwards. Similar results were seen with the dry Teflon, Figure 96b, with stress cracking observed throughout both samples. The Si_3N_4 also adhered to both samples during drying causing the mold to bow inwards.

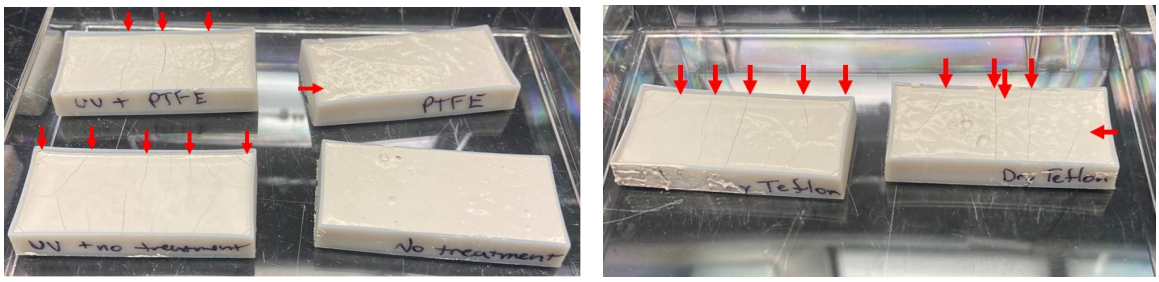

(a) Untreated and Allied Teflon samples.

(b) Dry Teflon samples.

Figure 96. VeroClear mold release trial samples: untreated and Teflons.

Each of the Rain X samples proved ineffective at allowing the Si_3N_4 to release from the VeroClear molds. The five minute samples can be seen on the left along with the ten minute treated samples on the right of Figure 97a. The 15 minute treated Rain X sample can be seen on the left of Figure97b. Each sample was also bowed inward similar to the Teflon samples due to the Si_3N_4 adhering to the walls during drying. The Smooth On samples, on the right side of Figure 97b, were both successful in allowing the Si_3N_4 to release from the mold. There was no cracking observed in either of the samples and the Si_3N_4 samples retained their original shape.

Additionally, the VeroClear molds retained their shape as they are more rigid than the Polycast molds. For both mold materials it was evident that Smooth On was the best mold release agent for the Si_3N_4 material.

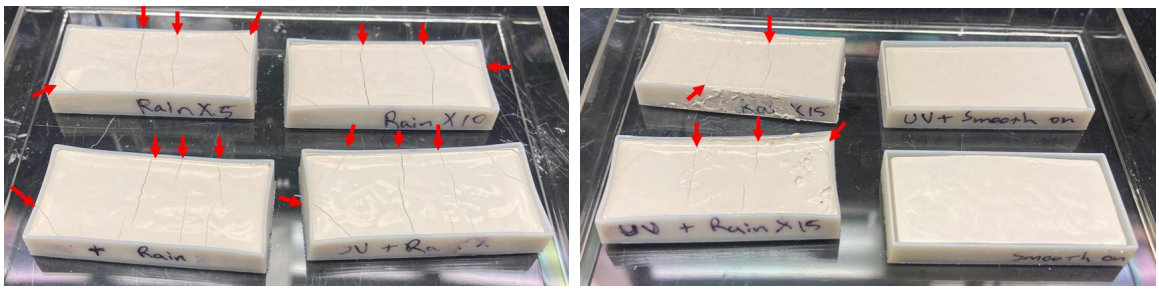

(a) Rain X 5 and 10 minute samples. (b) Rain X 15 minute and Smooth on samples.

Figure 97. VeroClear mold release trial samples: Rain X and Smooth On.

4.2.3 Mold design considerations.

As the casting process was being developed, multiple considerations were taken into account to allow for an effective mold to be designed. Unique characteristics for the molds were observed between each design. For molds produced on the Ultimaker, Figure 98, the Polycast material was opaque and did not allow easy viewing into the blade chambers. However, the slicing software for the Ultimaker allowed for the ability to use only external supports and reduce the amount of infill between the blades, so less material would need to be burned away.

For the Objet printed mold, shown in Figure 99, the VeroClear material was clear and allowed the ability to easily see how the slurry was distributing throughout the mold. However, the Objet printer required the use of internal supports, which had to be removed with a water jet. This led to the roughness that can be seen in the turbine blade regions. Additionally, the Objet printer is not capable of printing a partial infill between the blades leaving more material that needs to burn away.

The mold produced on the Formlabs printer, shown in Figure 100, was quickly

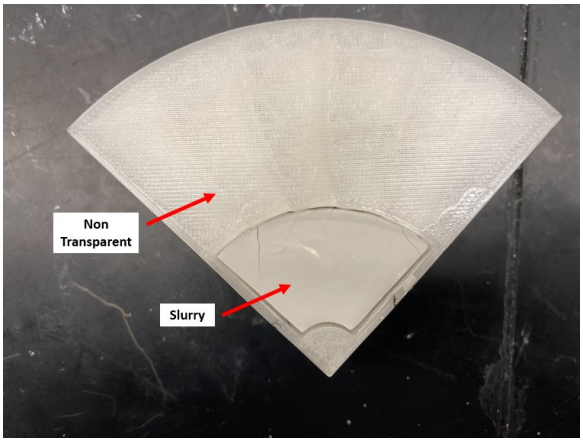

Figure 98. Quarter turbine mold printed in the Ultimaker.

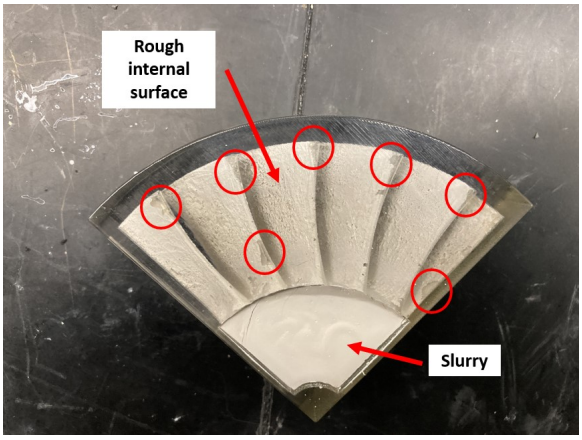

Figure 99. Quarter turbine mold printed in the Objet.

ruled out as a suitable material for a mold. Similar to the VeroClear material, the Standard Clear Resin from Formlabs, allowed the ability to easily see through the mold. However, the material itself when printed was brittle and easily broke if the walls were too thin. Additionally, while there were no internal supports, there was some deformation from printing in the blade region, highlighted in red. While this printer could potentially yield better structural results, one of their engineering resins would need to be tested. The molds created with the Formlabs printer were used to test venting techniques but were not used to make actual parts.

The original molds, from both the Ultimaker and Objet, were cast with the 43%

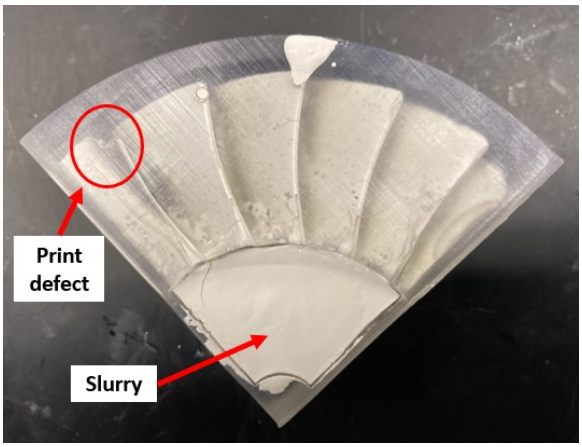

Figure 100. Quarter turbine mold printed in the Formlabs printer.

Si_3N_4 utilizing a Smooth On release agent. When filling the molds, many of the turbine blades were only partially filled. This was due to the inability for air to escape from the blades. As the molds filled with slurry, the air got trapped, forming pockets that were unable to escape even with the vibration tables. These air pockets are highlighted in the Objet printed mold in Figure 99.

To alleviate the issue of air pockets, two configurations were tested to allow for the air to escape using Formlabs printed molds. The first design used holes drilled into the tip of the turbine rotor blade mold on the top surface, shown in Figure 101. For this initial test, these holes were only drilled at the outer tip for two of the turbine blades. These blades filled easily on the vibrating table as the hole allowed air to escape. The other blades all had air pockets, circled in red, that could not be removed from the mold. This led to the determination that air holes were necessary to remove the trapped air from the blades to completely fill the rotor blades with slurry.

The second Formlabs printed design, previously shown in Section 3.1.2.4, created an outer shell that fit tightly around the turbine mold. This turbine mold would have the turbine blades ends exposed allowing for air to be able to vent off and allow

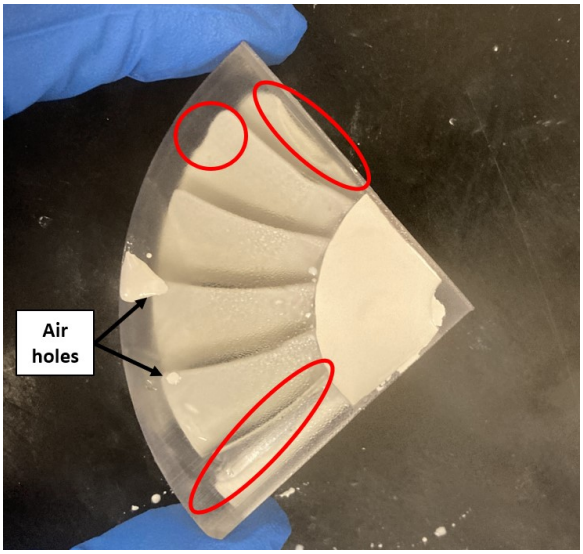

Figure 101. Formlabs quarter turbine mold with air holes.

for easier access to remove the support material from the Objet printed mold for a potentially smoother surface finish. When casting into this two part mold, even with a tight fit, the slight gap between the outer and inner mold allowed the slurry to slowly spill out over time, as shown in Figure 102. Since the slurry began spreading against the outer shell, it was immediately determined this approach would not work and could easily cause deformation and further cracking during drying.

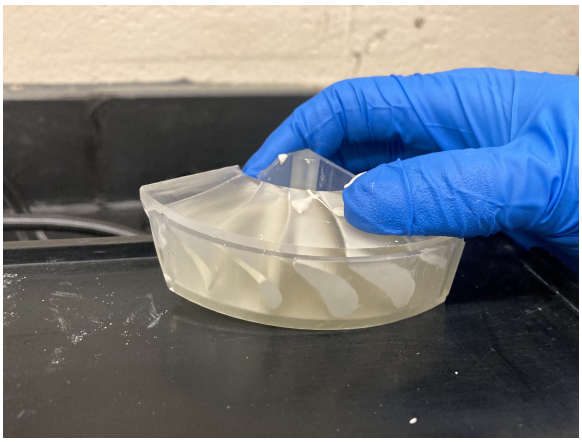

Figure 102. Two part quarter turbine mold showing spreading.

After drying in the humidity chamber, the quarter turbine samples exhibited stress cracking as shown in Figure 103. In the hub region, the Si_3N_4 material seemed to pull away from the walls due to the mold release as desired. When viewing the Polycast mold, in Figure 103a, cracking can be seen in the hub region leading up to the blades and shows initial cracking where the blade root meets the hub. Since the mold was opaque, the turbine blades were not visible. When looking at the Formlabs mold in Figure 103b, the stress cracking in the turbine blades, circled in red, is easily seen. With the drying chamber already at 99%, there could not be any higher humidity level to allow the samples to dry more slowly.

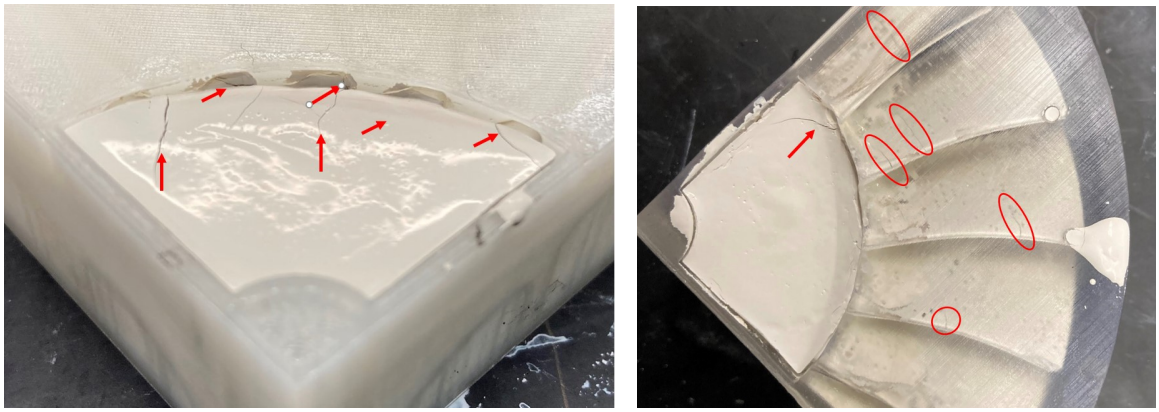

(a) Polycast mold showing stress cracks in the hub and base of the blades.

(b) Formlabs mold showing stress cracking in the blades.

Figure 103. Stress cracking due to drying in quarter molds

To test how the molds burned away, the Polycast and Objet mold samples underwent binder burnout, shown in Figure 104. Even with the mold material between the turbine blades (and 100% infill with VeroClear), the molds burned away completely. While the Polycast mold, on the left, completely burned away with no trace, there was some residual ash left over from the Objet mold seen in Figure 104b. The ash residue, from excess material, did not appear to adhere to any parts of the ceramic. Due to the stress cracks already present in the samples from drying, the turbine blades for both samples disintegrated during binder burnout, while the hubs were still partially

intact. This led to the conclusion that part of the cracking issues could be due to the excess material in the molds causing uneven drying between the non-exposed blades and the exposed hub. Therefore, it was necessary to find a way to allow the blades to be partially exposed to the chamber to assist with drying. Additionally, removing some of the excess material from the mold could allow for some of the water to escape more easily through the porous molds.

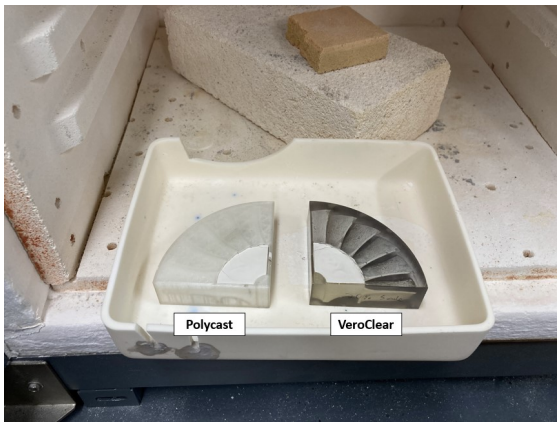

(a) Quarter turbines samples before binder burnout.

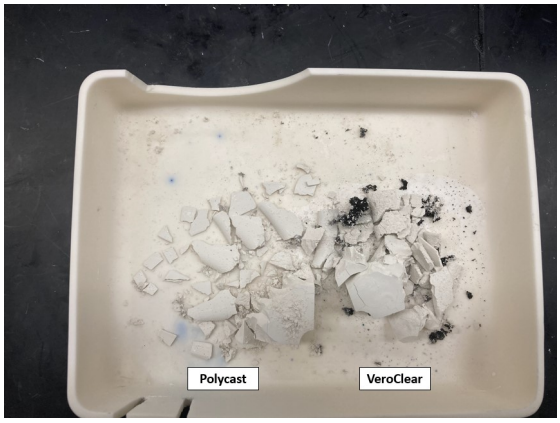

(b) Quarter turbine samples after binder burnout.

Figure 104. Quarter turbine molds undergoing binder burnout: Polycast (right) and Objet (left).

Another issue that was discovered during testing was leftover Si_3N_4 material remaining on the mold after the sample had dried and released from the mold. Figure 105a shows the Si_3N_4 specimen after drying. The Smooth On allowed the specimen to fully release from the mold and actually come out. However, leftover residue of Si_3N_4 can be seen in the bottom of the mold leading to a rougher finish on the bottom. This roughness was seen in other specimens as well as shown in Figure 105b. The two specimens exhibited larger signs of residue leftover on the mold and some pock marks, potentially due to foaming. One solution to solve some of the rough finish would be to incorporate a defoaming agent into the slurry. While this could solve some issues it may change the overall strength properties of the material.

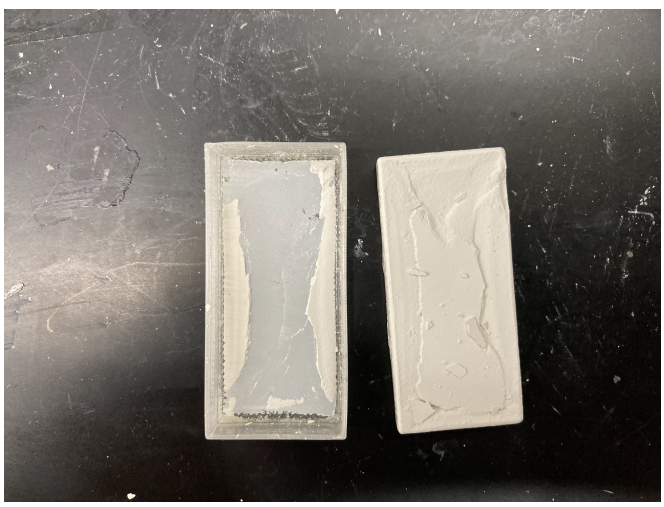

(a) Specimen and its mold showing residue.

(b) The bottom of two specimens showing flaking and pock marking.

Figure 105. Leftover Si_3N_4 material on the mold leading to rougher surface.

4.2.4 Overall design determination.

After reviewing the results, it was determined the Smooth On would act as the best release agent for either mold material option. Since the turbine rotor mold was going to be enclosed, a liquid Smooth On was utilized instead of the aerosol. The Ultimaker printed mold, utilizing Polycast material, was chosen for the final mold over the Objet. This was due to the fact that it could be smoothed down to a much smaller surface roughness value, did not require internal supports, and could easily customize the infill percentage of the mold. To smooth out the layers in the Polycast mold, isopropyl alcohol was poured into the mold and left to sit for two minutes to provide a smoother surface. Once the mold was treated with the isopropyl alcohol it was left to dry for two days to ensure the mold material was fully dry.

For the final mold design, shown in Figure 106, two air holes were added to each blade at the top of the mold. One air hole was located at the tip of the blade and one at the root. Since the Polycast material creates an opaque mold, the material between the blades was removed. While the mold was still mostly opaque, this allowed the

ability to partially view the filling of the blades to ensure a complete fill. Additionally, since the Polycast material was porous, reduced material may assist with drying the blades, potentially helping with the cracking previously observed during drying as well as having less material to burn away during binder burnout.

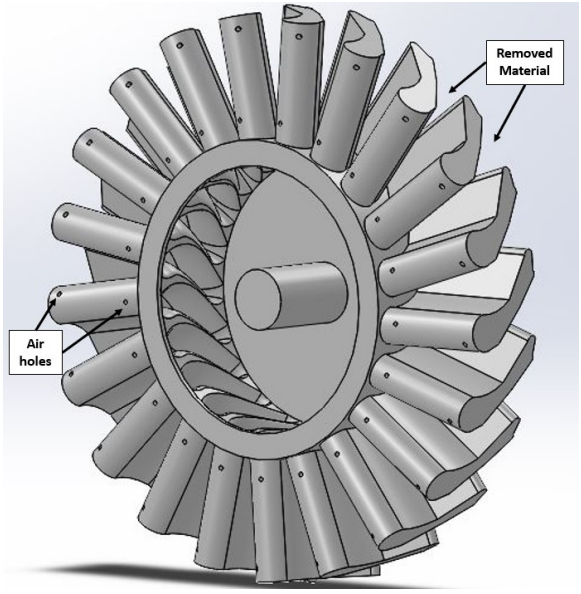

Figure 106. Final turbine rotor mold design after mold testing.

4.3 Turbine Rotor Fabrication Results

4.3.1 Cast turbine rotor results.

When casting the turbine, the addition of air vents allowed the mold to fill completely throughout its entirety to include the blade sections, as shown in Figure 107. The wide gauge needle assisted with a slow steady pour into the mold, as the turbine mold slowly spun around due to the vibration of the table allowing for even distribution of the slurry. The constant humidity applied by an external humidifier kept the slurry from separating and starting to dry throughout the cast.

Two weeks into the drying process in the humidity chamber, the turbine rotor

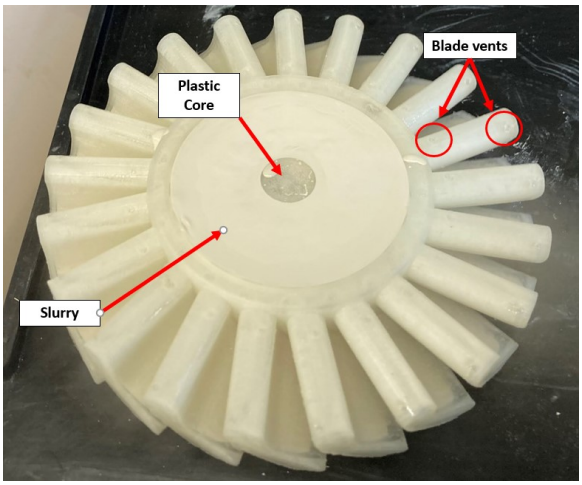

Figure 107. View of the turbine rotor after casting prior to the drying chamber

began developing stress cracks in the hub. Once the full dry time was complete the turbine rotor was removed, shown in Figure 108, for evaluation. Upon initial inspection, the turbine rotor appeared to release from the mold in the hub region shown in Figure 108a. When viewing the trailing edge side of the turbine rotor, Figure 108b, the turbine blades released from the mold in the blade regions as well.

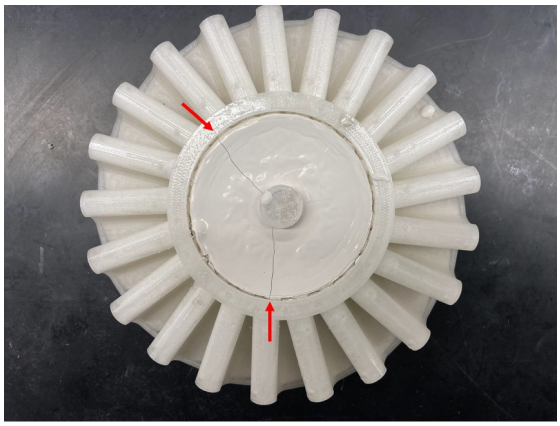

(a) Top view of the cast turbine after the drying process.

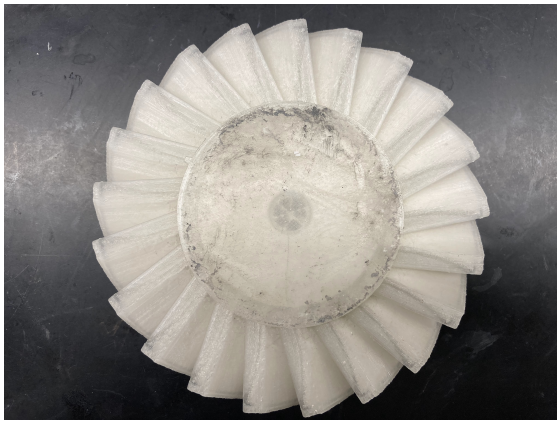

(b) Bottom of the cast turbine after the drying process.

Figure 108. View of the cast turbine after the drying process.

In Figure 108a, a large crack can be seen through the middle of the hub that extends to the trailing edge side. The location where the hub joined the turbine rotor

blades shows further stress cracking, highlighted in Figure 109, leading to a failed turbine rotor.

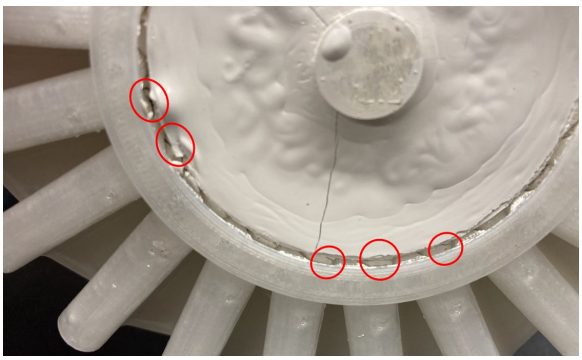

Figure 109. View of the cracking at the blade root and hub.

Figure 110. Cast turbine rotor post binder burnout.

After binder burnout, the turbine rotor failed due to the stress cracking in the hub and blades after drying. Each turbine rotor blade detached from the hub, shown in Figure 110. The blades breaking off was due to uneven drying in the humidity chamber. While the hub was exposed, the turbine blades were not exposed to air, causing the blades to dry at a slower rate leading to stress cracking, To alleviate the uneven drying, there needs to be ventilation built into the mold in the top of the

turbine rotor blades to allow more exposure.

Throughout all of the specimens cast in this research a high consistency of successful samples was difficult to achieve. An initial batch of eight Si_3N_4 rectangular samples were completely failed during processing. The first four failed during the drying stage, followed by the final four failing during binder burnout, shown in Figure 111.

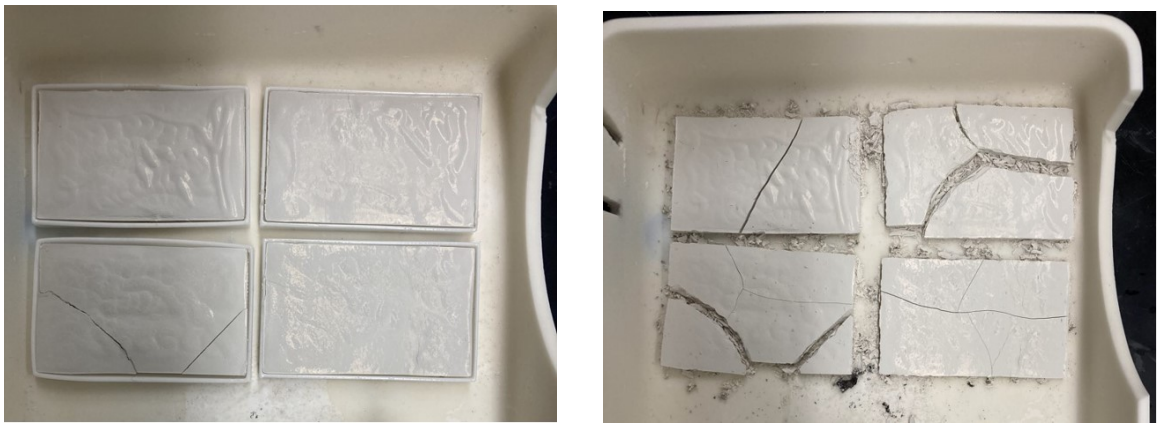

(a) First batch of specimens before binder burnout.

(b) First batch of specimens after binder burnout.

Figure 111. First batch of strength specimens for binder burnout.

A second batch was made, and out of the original eight samples four successfully made it through sintering. The eight samples can be seen in Figure 112. The initial set shows the eight samples with no perceivable defects. After binder burnout, Figure 112b, four of the samples developed cracking and failed. The remaining four samples were sintered and had no further issues, as shown in Figure 113. These final samples were to be used to cut into test samples to determine strength characteristics for the 43% Si_3N_4. Unfortunately, the samples shrunk beyond the ASTM standard and could not be utilized for testing. These inconsistencies through processing present a challenge in providing a scalable manufacturing capability utilizing the casting method.

(a) Second batch of specimens before binder burnout.

(b) Second batch of specimens after binder burnout.

Figure 112. Second batch of strength specimens for binder burnout.

Figure 113. Successful sintered batch of strength specimens.

4.3.2 Printed turbine rotor results.

To practice with the ADMATEC printer, a test print of the filled hub design used for casting was printed utilizing the alumina slurry. The initial print of the filled hub was successful and took three days to get through water debinding. However, after binder burnout, delamination occurred between the layers and the alumina turbine rotor became very fragile. The turbine rotor was further damaged when trying to move it after binder burnout, shown in Figure 114. The delamination and weak state were due to the filled hub design exceeding the thickness limits of 10 mm, unknown at the time, set by the printer manufacturer. The filled hub had an axial thickness of

15 mm and a radial thickness of 17 mm between the outer hub wall and bore. This showed the hub would need to be re-designed to account for the thickness limitations.

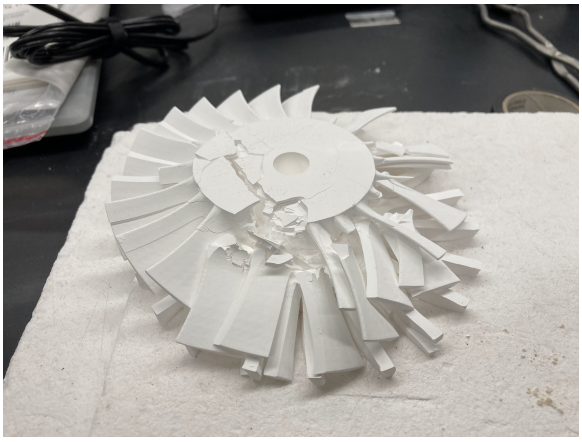

Figure 114. Initial turbine rotor test print on the ADMATEC printer after binder burnout.

To account for the alumina thickness limitations of no more than 10 mm in two directions, the single row honeycomb design was printed. Additionally, supports were added to the bottom of the turbine blades to assist with the structural integrity of the print. The turbine rotor was successfully printed but the design was scaled incorrectly, with the through thickness at 30% scaling in the Z-direction and the layer planes at 30% in the Y-direction and 10% in the X-direction, leading to the oblong shape shown in Figure 115. After printing the turbine rotor, shown on the build plate in Figure 115a, was then submerged in water for debinding for two days. Figure 115b shows the turbine rotor post-water debinding and a color change from yellow to white can be observed. There were no issues with the turbine rotor after water debinding and the supports were then removed from the blades prior to binder burnout.

For support processing and removal ADMATEC initially recommended utilizing a support generator software such as Magics, which is able to produce a .STL or .SLC file. Once the file was created, ADMATEC recommended either underexposing or overexposing the final support layer creating a weak spot where the support would

(a) Single row honeycomb alumina hub design after printing.

(b) Single row honeycomb alumina hub design after water debinding.

Figure 115. Printed single row honeycomb alumina hub design full turbine.

just separate in the green state. To underexpose, a one layer gap is created in the geometry or exposure time for that layer is set to 0 ms, then print with two times the layer height for the next layer to adhere to the support. This would result in minimal adhesion. To overexpose, the last support layer receives 10 to 20 times the normal light source applied to it to ensure there is very little cross linking created between the print. ADMATEC said that it was best to remove the supports in the green state, but also said they could be removed after sintering. Removing supports after sintering could allow for more control, but also is more difficult since the ceramic is more dense.

Initially, Magics was utilized to generate supports for the turbine rotor, however, the software put out the supports as a seperate file from the turbine rotor, using

both file formats, and could not be used in the ADMATEC printer. The same type of supports generated in Magics, were then designed along the blade leading edge utilizing Solidworks, shown in Figure 116. Using this design provided a single .STL file that could be used for printing with the supports added. However, since it was a single file and the support material ended after the hub started, there was no way to distinguish the difference in support layers and turbine layers, so the two exposure methods described above could not be applied, or the hub would separate.

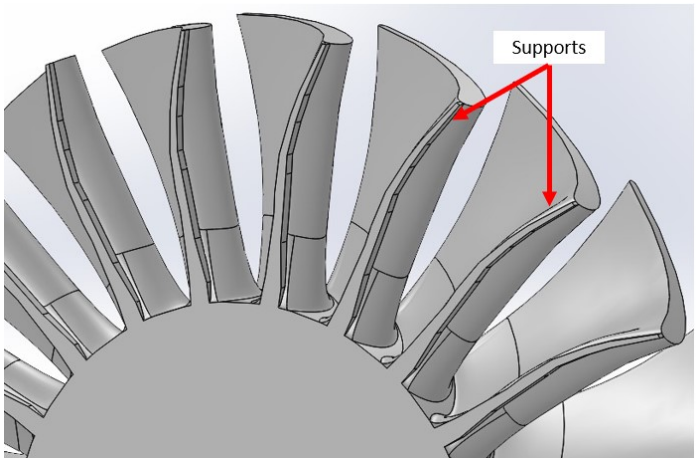

Figure 116. Turbine rotor blade supports design.

Therefore, the supports were removed by hand with a razor blade while the turbine rotor was still in a green state for easier removal. Due to the thin nature of the supports that were added, some of the supports began falling off during water debinding. During removal, the razor blade was easily able to slice through the layers of the turbine rotor blades in the green state. However, as this was done by hand, it was difficult to know the exact location of where the blades began, and the support ended. This led to some of the leading edge of the blades to be squared off during removal which can be seen in Figure 117. When looking at the trailing edge side of the blade, it was noticed that the printed turbine blade layers progressively extended out from the hub as the blade root fillet was built. Due to the gradual increase in

layer length for each consecutive layer, consideration was given to whether supports were needed at all or would removing them partially weaken the turbine rotor blades. For initial printing of the turbine rotors for a successful design, it was decided to leave the supports.

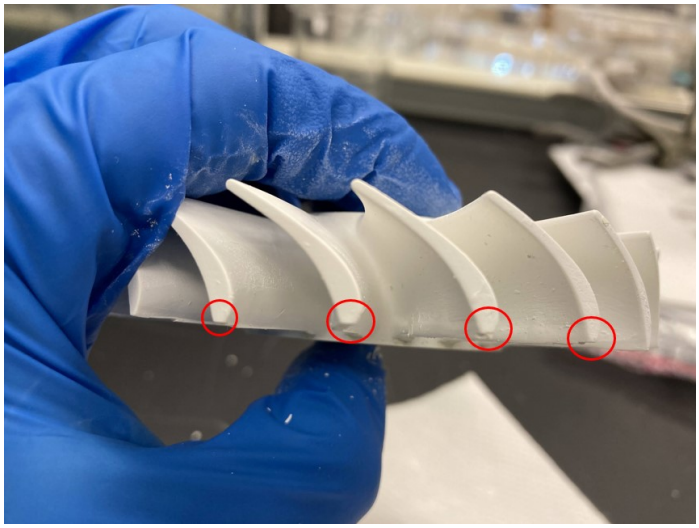

Figure 117. Single row alumina honeycomb hub design after support removal.

Once the supports were removed, the turbine rotor underwent binder burnout. During the process delamination occurred throughout the turbine rotor blades, as shown in Figure 118. The initial delamination appeared to be approximately where the extruded holes in the hub ended and then other layers of delamination occurred below this level. Part of the reason the delamination happened was due to the incorrect scaling. Since the through thickness was scaled 30% instead of 10% the filled portion of the hub was beyong the 10 mm thickness for alumina, leading to portions of the blade closer to the leading edge side to delaminate. It was also observed that the areas near the trailing edge of the blade, on the top side of the image, did not experience delamination due to the material thickness being within limits because of the honeycomb holes.

In addition to the delamination, after sintering, significant radial cracking, circled

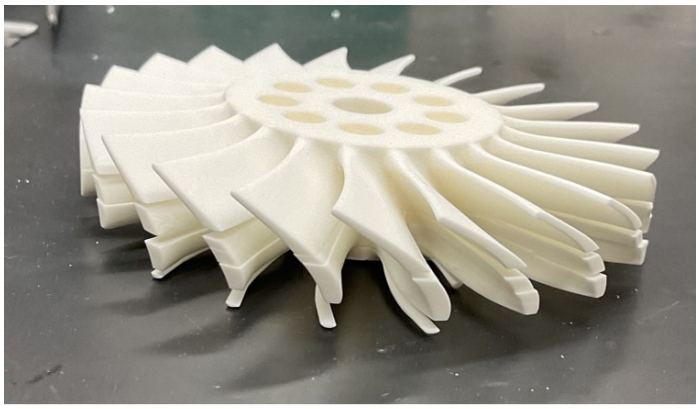

Figure 118. Single row alumina honeycomb hub design after binder burnout.

in Figure 119a, was noticed in the hub on the trailing edge side of the turbine rotor. The radial cracking extended from the top of the hub about midway down to the delamination layer coincident with the bottom of the extruded hole. The radial cracking through the hub was believed to be due to the overall thickness of the material in the top half of the hub. This radial cracking was not seen on the leading edge side of the turbine rotor, shown in Figure 119b.

To further investigate what was occurring in the hub causing the delamination and cracking, the three partial hub prints were created out of alumina. Utilizing correct scaling of 10% in the Z through thickness direction and 30% in the X and Y layer plane, the partial turbine rotors underwent binder burnout and sintering and were analyzed for noticeable defects. The results for the single row honeycomb design are shown in Figure 120. On the exposed hub side, Figure 120a, two cracks across the hub can be seen circled in red. The first crack appears between the holes where the base of the extruded hole meets the remaining filled in hub. The second crack appears approximately halfway below the first crack and the leading edge hub surface. However, no delamination appears to carry from the cracks throughout the blades. When viewing the leading edge hub surface, Figure 120b, several radial surface cracks can be seen in the top portion of the leading edge hub side. The radial cracks appear

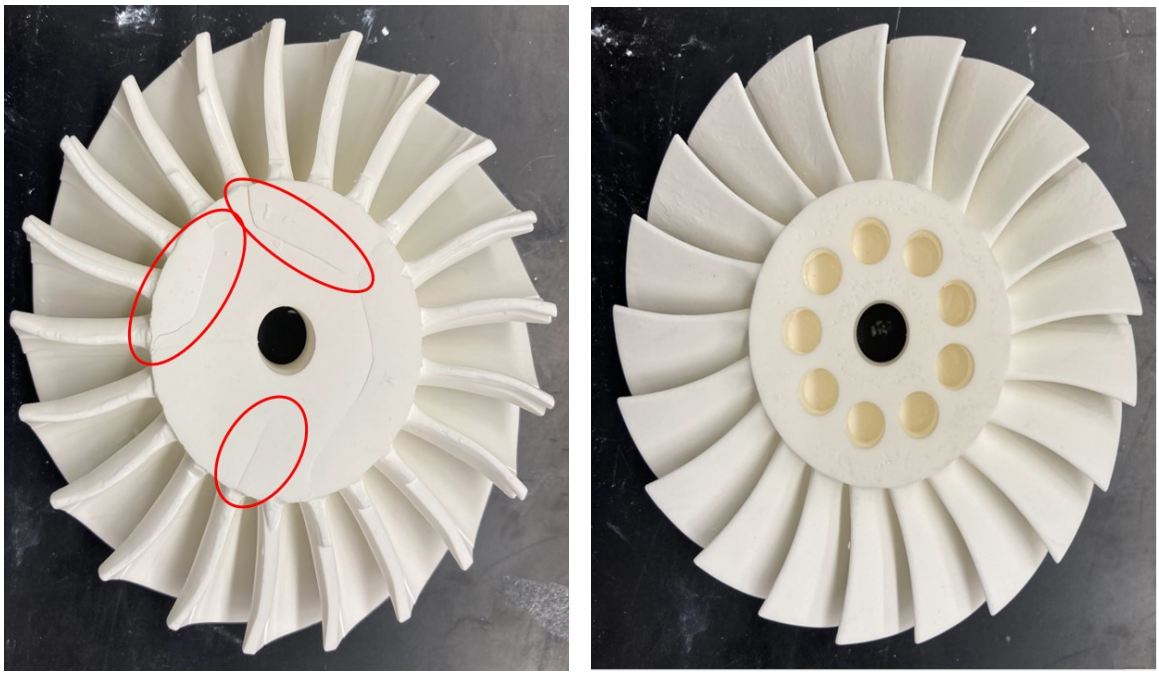

(a) Leading edge side of the oval turbine rotor. (b) Trailing edge side of the oval turbine rotor.

Figure 119. Radial cracking in the hub of the oval turbine rotor.

at the surface level and do not appear to extend beyond 1 mm into the hub. No radial cracking was seen on the trailing edge side of the hub. Additionally, there was some roughness on the hub surface due to excess print material leftover from the build. This would normally be smoothed out during post-processing. Also, support material was left on the blade edges leading to a rougher finish while some of the supports fell off during water debinding.

The results for the multi-row honeycomb design, originally designed for the zirconia thickness limits, is shown in Figure 121. A large crack developed in the hub at the base of the extruded holes, shown in Figure 121a. The cracking between the hole led to delamination that propagated from the center of the hub out through the first two turbine blades. Minor radial cracking, circled in Figure 121b, was seen in the top layer of the leading edge side of the hub similar to the single row design. No additional radial cracking was seen on the trailing edge side of the hub.

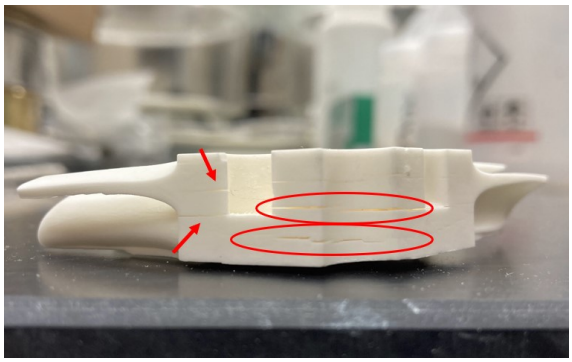

(a) Partial single row honeycomb hub design exposed hub view.

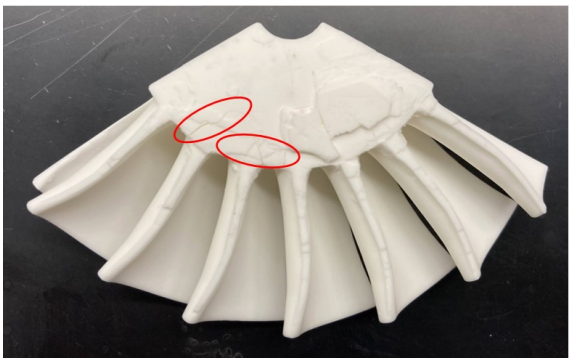

(b) Partial single row honeycomb hub design leading edge surface view.

Figure 120. Partial single row honeycomb hub design results.

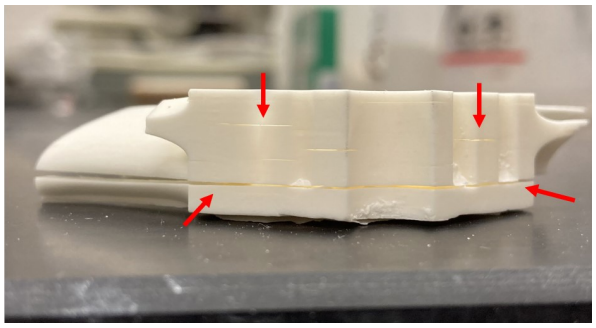

(a) Partial multi-row honeycomb hub design exposed hub view.

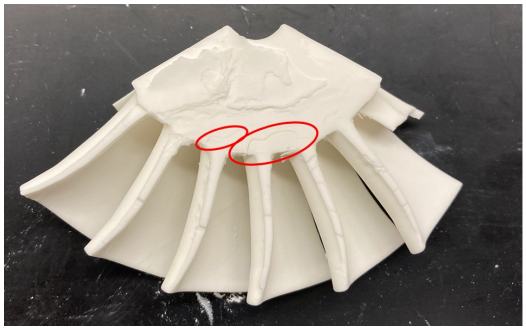

(b) Partial multi-row honeycomb hub design leading edge hub view.

Figure 121. Partial multi-row honeycomb hub design results.

The results for the multi-row design capped on both ends is shown in Figure 122. This design was developed to determine if having internal pockets would be possible and allow appropriate drying and debinding while still meeting the maximum thickness limit. From the exposed hub side, Figure 122a, multiple cracks can be seen propagating throughout the hub along multiple layers. These cracks appear to jump across layers as they move through the hub. There was no evident cracking through the turbine rotor blades, but significant radial cracking was seen on both sides of the hub similar to the cracking shown on the trailing edge side seen in Figure 122b. This cracking protruded half-way through the axial thickness portion of the hub

perpendicular to the other layers, not seen in the other samples.

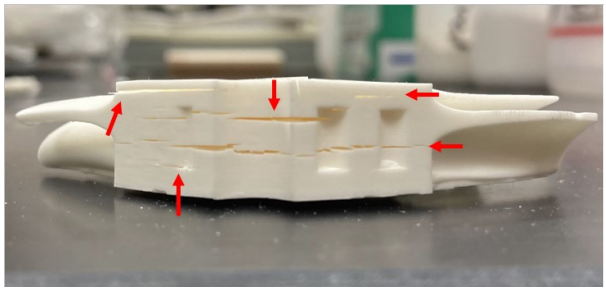

(a) Partial capped end internal honeycomb hub design exposed hub view.

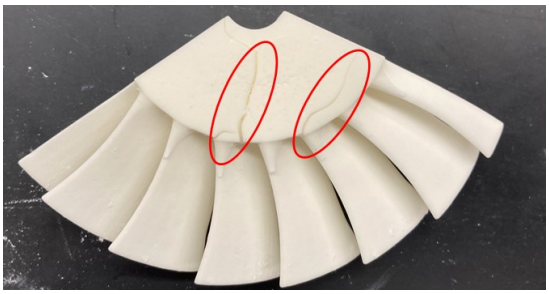

(b) Partial capped end internal honeycomb hub design top hub view.

Figure 122. Partial capped end internal honeycomb hub design results.

After viewing the partial hub specimens, it was determined the cracking at the base of the holes was due to stress concentrations from the edge of the hole and the solid layer underneath. Due to the multi-row sample having many more holes, it is believed this increased the amount of stress concentrations causing the extra delamination and crack to propagate through the blade regions. This concept was tested further by adding a 0.762 mm radial fillet to the base of the holes in the hub study to see if the crack could be eliminated. In the single row hub as well, the second crack that propagated half way down between the base of the hub and the bottom of the hole was due to the thickness of the hub, as this did not occur in the multi-row sample. The overall thickness in the hub led to inadequate water debind and dry time. The sample should have been allowed to water debind for longer and air dry for two days instead of just one to ensure all the water was removed. Finally, the capped design produced significant cracking through its thickness. It is believed that having caps on both ends prevented the water from penetrating the sample to remove the binding agent during water debinding. The lack of penetration and dry time led to more significant cracking throughout the entire hub. The capped ends slowed the exposure of the inside of the hub to water and air, therefore more exposure time is potentially required to allow more thorough debinding removal and

drying prior to binder burnout. The minor radial cracking seen in the single row and multi-row samples was believed to be due to the thickness of the hub on the leading edge side. For both samples, the leading edge side was capped and attached to the base plate while in the water tank, this could have led to the minor radial cracking due to inadequate binder removal in the debinding process. This could potentially be eliminated with the through hole designs, by removing the capped end altogether.

To further examine the delamination and radial cracking, six separate designs were printed. All six hubs had no issues through printing or water debinding. After binder burnout the three hub designs with the through holes, shown in Figure 123, all showed no delamination or radial cracking issues. The other three designs, shown in Figure 124, each showed some potential delamination issues. For the BYU tapered design the thin-walled portion of the outer hub were seen breaking off the hub. Upon inspection of the filleted hub and the non-filleted hub design some larger cracks were seen in the base of the hub around where the hole ends and the cap begins, initially indicating the fillet was not successful.

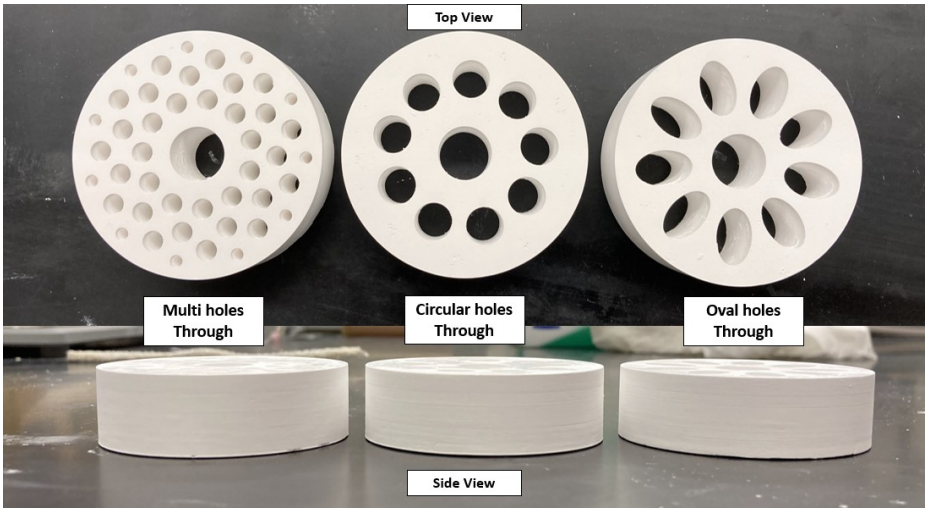

Figure 123. Through hole hub designs post binder burnout.

Once sintered the hubs were inspected again. As seen in Figure 125, the three

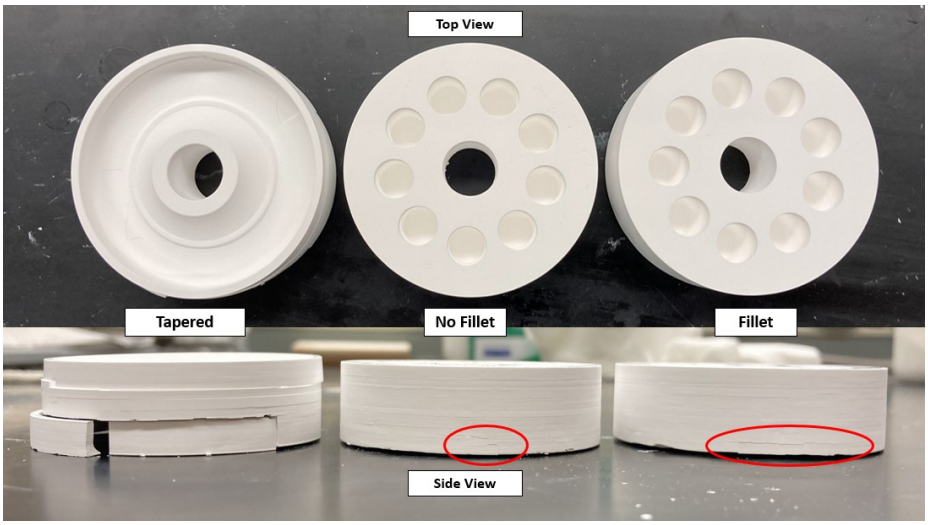

Figure 124. Fillet and tapered hub designs post binder burnout.

hubs with the through hole design all sintered with no visible delamination or radial cracking. The BYU tapered design continued to show the outer hub wall broken away in multiple pieces, shown in Figure 126, leading to a failed design. The failure was due to the lack of supports in the middle of the hub which weakened the thin outer walls during printing. When viewing the filleted and non-filleted hubs, shown in Figure 126, the non-filleted design had multiple layers of delamination seen in the sample. The largest delamination appeared around the entire outer portion of the hub due to the stress concentration where the end of the extruded hole met the cap. The filleted hub yielded similar results to the non-filleted hub with delamination and cracking located in the same locations. In both samples, the crack does not appear to have gone through the center of the hub and remained near the outer portion of the hub. This confirmed that the main delamination seen in previous samples was predominately due to stress concentrations between the holes and cap at the base of the hub. The fillet used in this study was very small, a larger rounded fillet may be required along with printing at a smaller layer height to help reduce the delamination due to stress concentrations. The filleted and non-filleted design also showed a small

amount of radial cracking in the filleted and non-filleted design after sintering. This small radial cracking was on the capped hub side which was connected to the build plate sacrificial layer seen in the previous designs. This appeared to still be due to lack of water exposure and the binder not being fully removed.

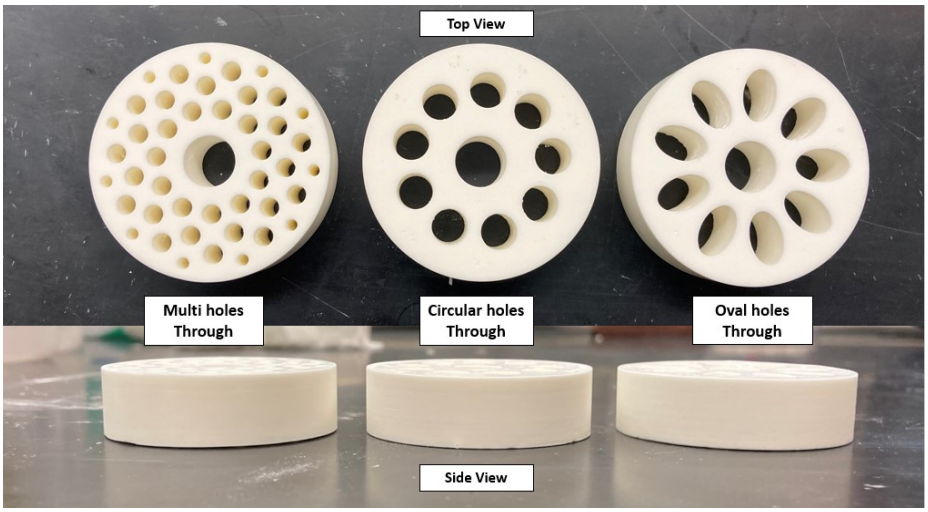

Figure 125. Through hole hub designs post sinter.

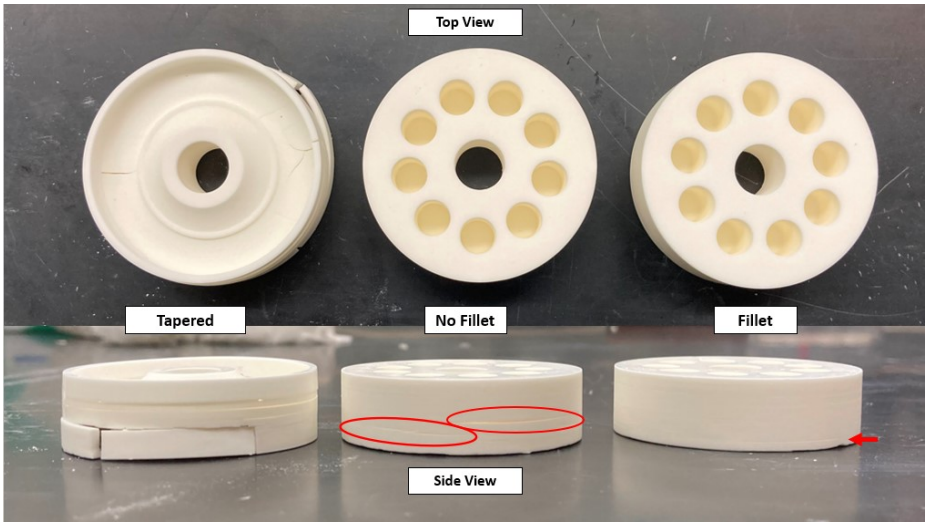

Figure 126. Fillet and tapered hub designs post sinter.

Once the hubs were complete, they were sent to the AFIT model shop to test integration with the tolerance ring. The shop was able to successfully machine the

bore to within a tolerance of ± 0.00508 mm well beyond the required tolerance. Once the bore was machined to size, the tolerance ring was successfully pressed into the hub, as shown in Figure 127. The shop then inserted a 10 mm diameter rod, similar to the JetCat P400 shaft size, to simulate coupling of the bore and shaft. This shows the tolerance ring is feasible for use to integrate the stainless steel shaft and the alumina turbine rotor.

Figure 127. Alumina rotor hub with tolerance ring and shaft inserted.

After the hub study, the alumina design with a single row of holes extruded all the way through the hub was chosen for the final turbine rotor design. Upon initial print and water debinding there were no observed issues. The supports were removed utilizing a razor blade after water debinding, which led to a slightly rougher finish along the blades, shown in Figure 128a. The supports were the most difficult to remove at the tapered portion of the blade root. Consideration was given to altering the supports in later designs, so they extend from the blade tip to the beginning of the fillet. This would allow for the end of the support layer to be easier to distinguish. It was also determined that once the initial supports were removed, sandpaper should

be utilized to smooth out some of the roughness. The trailing edge side of the turbine rotor, shown in Figure 128b, showed a smooth print finish. Other than the roughness from support removal, no immediate defects could be detected.

(a) Leading edge side after water debinding and support removal.

(b) Trailing edge side after water debinding and support removal.

Figure 128. Final turbine rotor after water debinding and support removal.

After binder burnout, the turbine rotor was removed from the ash furnace, shown in Figure 129. No delamination was seen in the blade regions. The leading edge side, shown in Figure 129a, showed signs of possible small radial surface cracking. This radial cracking did not extend deep through the thickness of the hub and seemed to indicate binder had not fully been dissolved during water debinding. Additionally it was believed that since the leading edge side rested on the alumina plate in the furnace, this affected the binder release during binder burnout. The leading edge side of the hub was also rougher from the removal of the base layer and supports. The trailing edge side, shown in Figure 129b, showed signs of significant radial cracking in the hub, which had not been seen in any of the previous samples on the trailing edge side. The cracking in the trailing edge side was larger and protruded through the axial thickness of the hub, similar to cracks caused by stress. Prior to removing

the turbine from the ash furnace, the door was cracked open at 220°C to assist with cooling. It was initially believed this caused rapid cooling and led to thermal shock that led to the cracking on the exposed leading edge hub side, shown in Figure 129b.

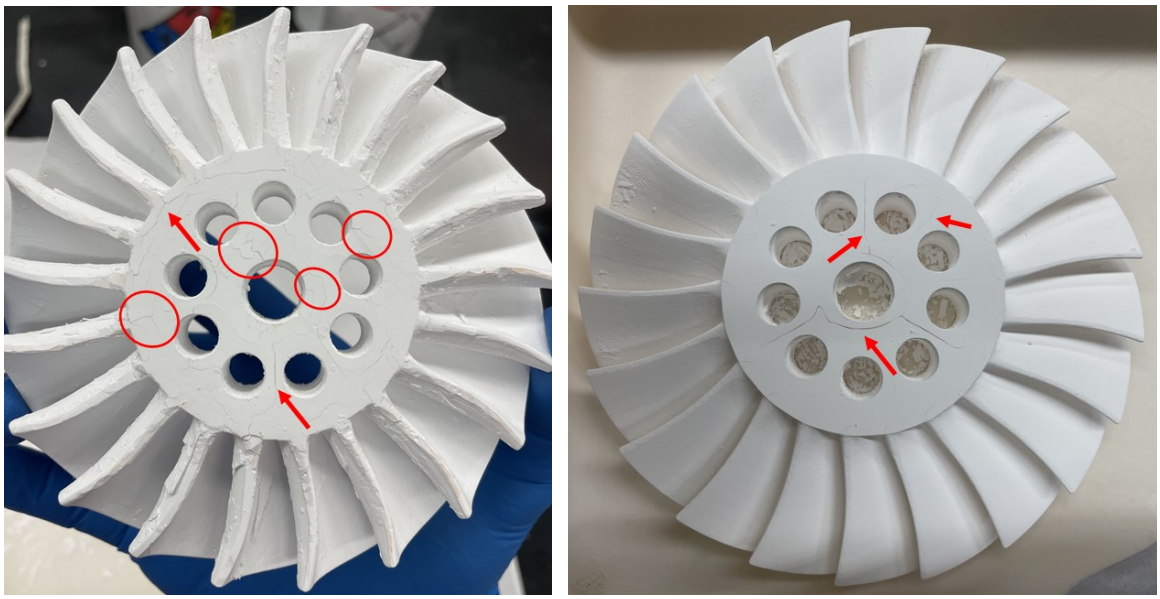

(a) Leading edge side after binder burnout. (b) Trailing edge side after binder burnout.

Figure 129. Final turbine rotor after binder burnout.

Once sintered the final turbine rotor design was inspected, shown in Figure 130. No delamination could be seen throughout the blades. The radial cracking on the leading edge side of the hub, shown in Figure 130a, was only visible on the surface and did not appear to extend down through the hub as in previous specimens. The leading edge side of the turbine rotor also had a rough surface finish left over from processing which would need to be post-processed to smooth out further. The trailing edge side, shown in Figure 130b, still showed significant radial cracking through the hub due to the thermal stress that occurred during binder burnout.

The turbine rotor print successfully removed the delamination that had been seen in the blades and demonstrated the ability to make a ceramic turbine rotor in only1.5 weeks with an overall weight of 118.68 g. However, the large radial cracking from the

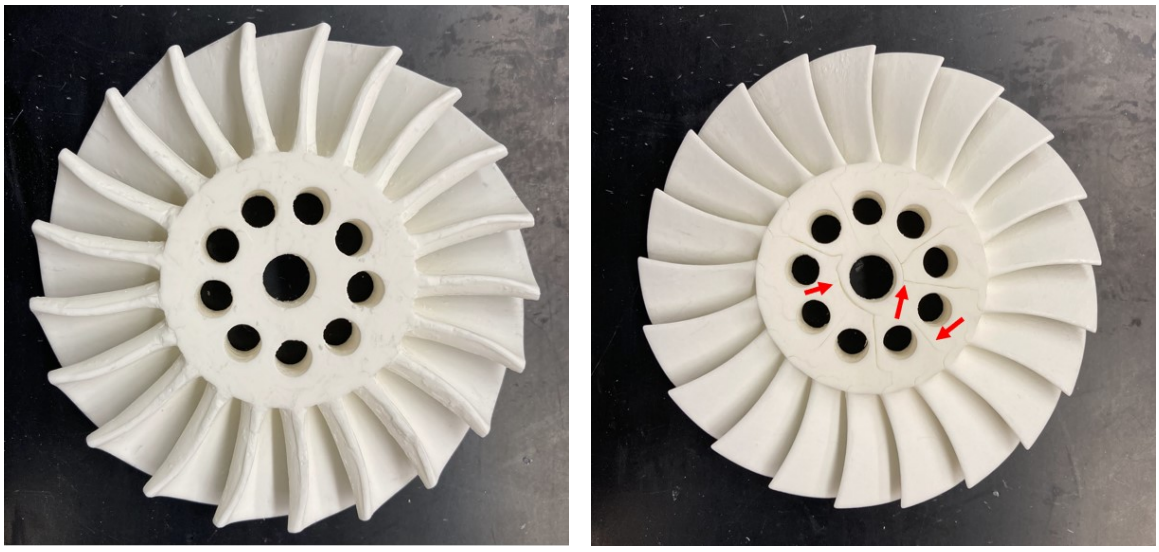

(a) Leading edge side after sintering.

(b) Trailing edge side after sintering.

Figure 130. Final turbine rotor after sintering.

exposed trailing edge side, believed to be due to thermal shock, and the small radial cracking seen on the leading edge side due to issues in the binder removal process had to be removed. The small surface radial cracking appeared to be due to two potential sources. The first source was believed to be due to issues in the binder removal process due to uneven heating from the leading edge hub side resting on the ceramic plate in the oven, preventing the binder from burning off evenly. The through holes did appear to reduce the minor radial cracking in the leading edge side of the hub by allowing the turbine rotor to be exposed to more water and air during water debind and binder burnout, but did not eliminate it. After further discussion about the printing process, it was also found that the first ten layers of the print were set to a different exposure time, as recommended by ADMATEC, to assist with removal from the base layer. When the print was prepped, the first layer was set to duplicate ten times with each layer being underexposed. This led to an additional 0.5 mm thickness being added to the leading edge side of the hub that was potentially not fully removed from the prints. Due to the difference in exposure, any unremoved

underexposed layers could have also aided in the radial cracking seen on the leading edge side of each rotor sample. To account for the affects from the sacrificial layer, two separate prints were produced. The first print was the same final turbine rotor design tested previously, and the second print, shown in Figure 131, had a 0.5 mm thick sacrificial layer on the leading edge side that covered the entire span of the turbine rotor. Additionally in both prints the supports were altered so they extended from the blade tip to the beginning of the fillet to make it easier to see during removal.

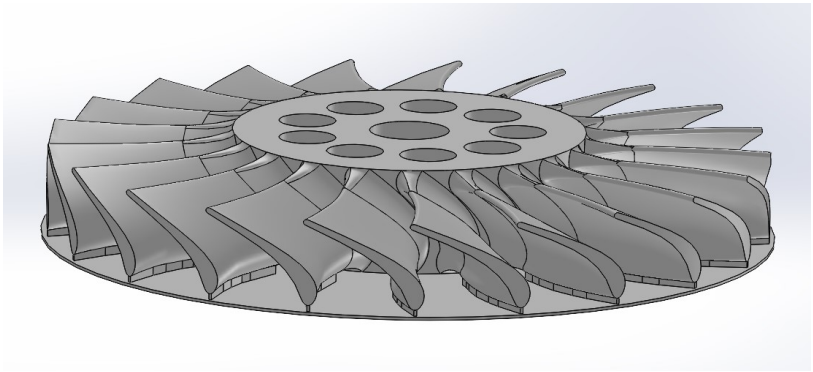

Figure 131. Turbine rotor design with 0.5 mm sacrificial layer.

Both turbine rotors printed successfully and were underwent water debinding. The unaltered print with no sacrificial layer was removed from the base plate after one day of water debinding. The base layer that adhered the turbine rotor to the base plate was easy to remove and the turbine rotor was placed back in the water tank to undergo water debind for one more day. After the 2 days of water debinding it was removed to be post-processed. The second turbine rotor with the new sacrificial layer design from Figure 131, was left on the base plate in the water tank to undergo water debind for 5 days. This allowed for a longer saturation in the water to allow more residual binder to be removed. After 5 days it was removed for post-processing and to air dry. Removing the sacrificial layer from the second turbine rotor print proved difficult. While the sacrificial layer was distinguishable, it proved difficult to remove

due to the underexposure, when compared to the original overexposed base layer. For both turbine rotor prints the blade support removal went a lot smoother than before with the addition of sandpaper, shown in Figure 132. The red section shows the new support structure that was created that stops at the beginning of the fillet. A razor blade was first used to remove the supports, shown in the yellow section, as well as the sacrificial layers in the hub. This left a rougher surface on the blades and hub from the material removal. Then the sandpaper smoothed out the hub and rough portions of the blades back to the original geometry, shown in green. Once post-processed and after a two day air dry time, both turbine rotors were elevated using thin alumina crucibles, shown in Figure 133, to allow for even heat exposure throughout the entire turbine rotor during binder burnout.

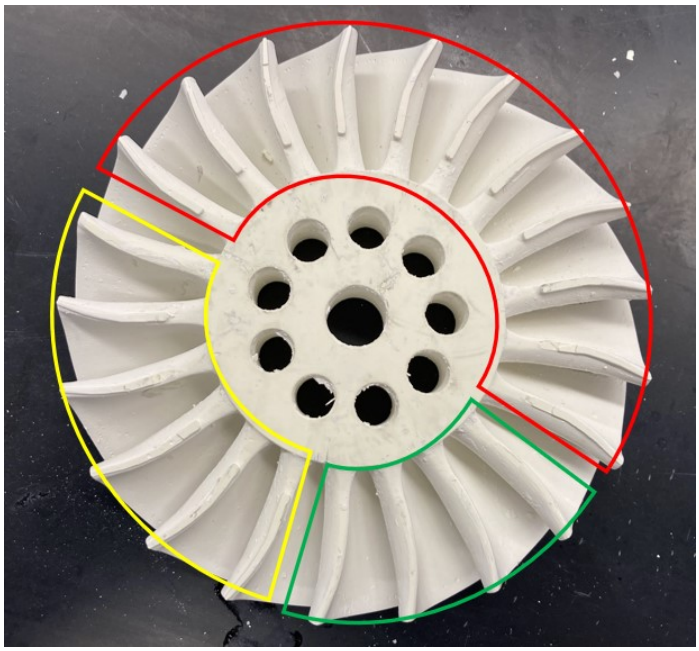

Figure 132. Stages of support removal from the turbine blades: red: original supports, yellow: supports cut off, green: edges sanded.

During binder burnout the turbine rotor samples were allowed to cool to room temperature prior to removal from the furnace. Upon removal, as seen in Figure 134, the 2 day water debind turbine rotor exhibited the same stress cracking in the trailing

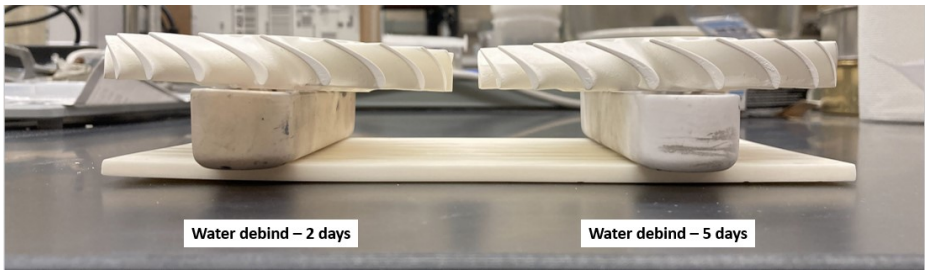

Figure 133. Turbine rotor designs elevated using alumina crucibles.

edge side seen in the last turbine print. However, there was no large cracking evident on the print that underwent 5 days of water debinding. When viewing the leading edge of each of the turbine rotors, the surface cracking from the debinding marks were still evident seen in previous samples. For both samples there was no delamination noticed in the blades. After inspection, the turbine rotors were then sintered for final densification.

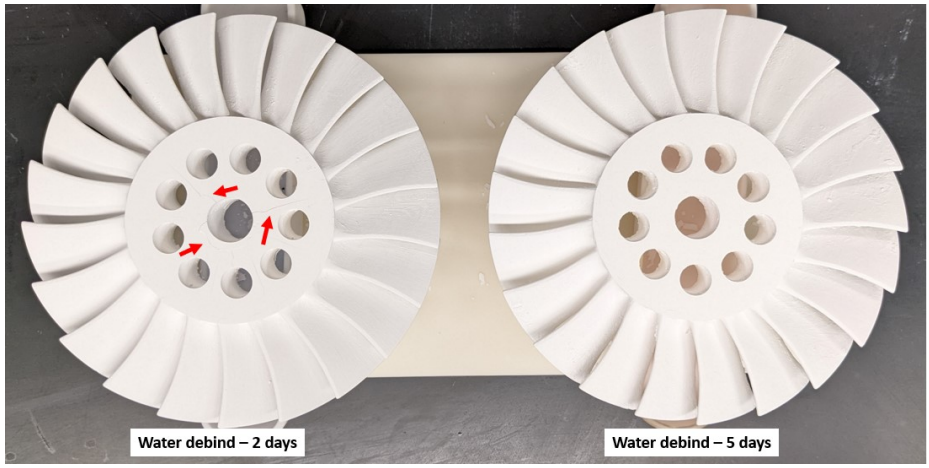

Figure 134. Trailing edge turbine rotor designs after binder burnout.

After sintering, the turbine rotors were removed for final inspection. When evaluating the trailing edge, shown in Figure 135, the 2 day water debind turbine rotor still showed evidence of the large radial cracking, but there was still no cracking in the print that underwent a longer water debind. However, both turbine rotor prints

exhibited small stress cracking in the outer rim of the hub where the blades met the outer wall. When observing the leading edge of each of the turbine rotors, shown in Figure 136, the surface cracking from debinding was still evident, but minimal. For both samples there was no delamination noticed in the blades. One blade in the turbine that underwent the 5 days of binder burnout, was partially broken off. This was done while handling the turbine rotor as it was being transferred to the sintering oven, not due to the actual sintering process.

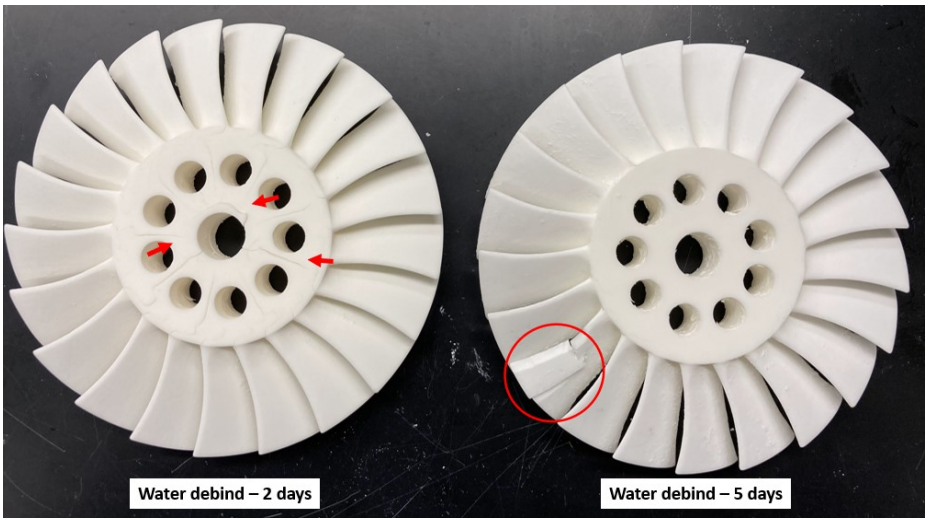

Figure 135. Trailing edge turbine rotor designs after sinter.

After these final two turbine rotor prints, it was determined that most of the cracking in both sides of the hub was due to inadequate time for water debinding. Since the turbine rotors are larger specimens then typically produced, more time was required beyond the manufacturers recommendation. This test showed, the large radial cracking was not due to thermal shock, but was instead due to insufficient binder removal during water debinding. By allowing for 5 days of water debinding, the water had more time to distribute throughout the turbine rotor and dissolve out the binder, leaving very small amounts behind to be completely removed during binder burnout. The small radial cracking was still evident for both rotor samples,

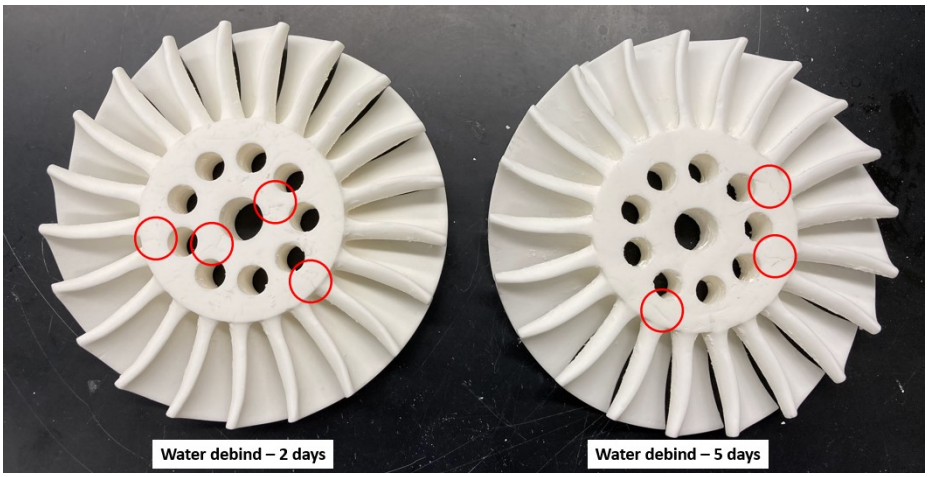

Figure 136. Leading edge turbine rotor designs after sinter.

due to inadequate water exposure for binder removal. The 2 day sample was not removed from the base plate until one day after water debinding, so the leading edge side was only exposed to the water for one day which was not enough time to allow the water to infiltrate the pores in the ceramic and dissolve the binder. The 5 day water debind turbine rotor, while it allowed for more debinding time, it was also left on the base plate the entire time. While water was initially able to infiltrate the turbine rotor and assisted by the extruded holes, the leading edge side of the hub was never exposed to the water preventing the binder on the surface from dissolving. The elevation of the turbine rotors may have helped in some binder release, but the main cause of all cracking issues in the hub was determined to be primarily affected by the amount of time the turbine rotor was exposed to the water.

Overall the turbine rotor delamination and radial cracking issues were solved, leaving minimal debinding marks on the bottom of the rotor. To eliminate the final cracking issues that were observed a turbine rotor support piece and change of procedures is recommended. The support design, shown in Figure 137a consisted of three conical supports that would elevate the hub. Additionally, an outer ring would support the turbine rotor blades after the supports were removed. The small amount

of cracking that was observed near the blades, occurred after the supports were removed and were associated to gravity pulling them downwards creating small stress cracks. The blade ring would allow the turbine rotor blades to be supported and hub elevated, shown in Figure 137b, throughout water debind and binder burnout eliminating the stress until the turbine rotor was ready for densification. This design would easily be printed using the SLCM printer for follow on turbine rotors.

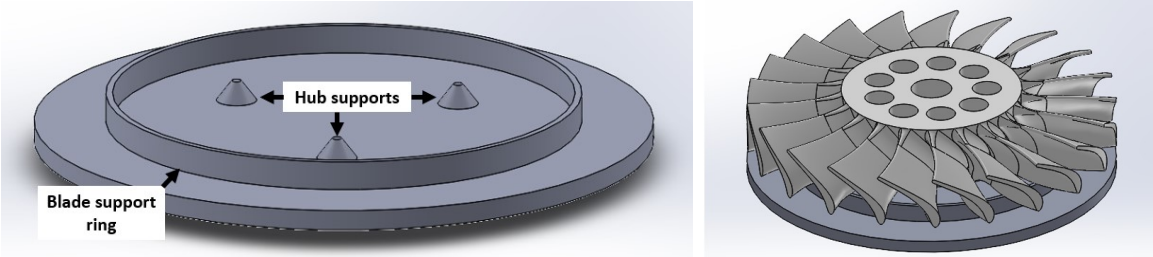

(a) Alumina support design. (b) Support holding the turbine rotor.

Figure 137. Final turbine rotor alumina support design.

To ensure full binder removal during water debind, the turbine rotor would need to undergo water debind for one day while on the base plate. Then the turbine rotor could be removed from the base plate and have the supports and any sacrificial layers removed from the turbine rotor. Once processed, the turbine rotor would then be placed on the support piece and placed back into the water tank to undergo water debinding for four more days. This would allow for water to sufficiently infiltrate the turbine rotor across every surface and dissolve out the binder. After water debinding, the turbine rotor could then undergo the normal dry time and binder burnout while resting on the support piece, which would also ensure even heating throughout the part. Finally, it is recommended to test a powder bed for final sintering to allow for the blades to continue to maintain support throughout the densification process. This would increase the total manufacturing timeline to two weeks, as outlined in Figure 138.

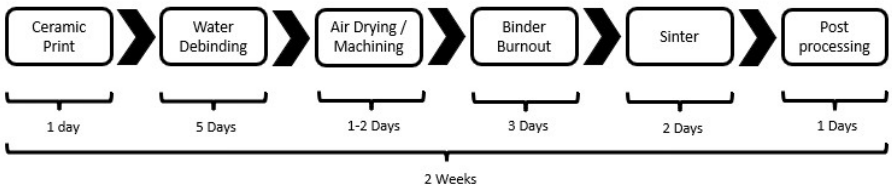

Figure 138. Updated SLCM fabrication timeline.

4.4 Printed turbine rotor JetCat P400 FEA Results

4.4.1 Initial printed design analysis.

Due to the thickness restrictions for zirconia and alumina, different designs were incorporated to allow reduction of material in the hub similar to partial infill in polymer 3D printing. Circles were used to reduce the stress concentrations in the hub designs as much as possible. These two designs were then run in FEA to determine the operating limits for each material at JetCat P400 relevant conditions. For the alumina material, a design with a single row of nine circular holes was analyzed to account for the maximum material thickness of 10 mm. The results for the alumina turbine rotor analysis, shown in Figure 139, show a peak stress of 276 MPa on the leading edge side of the blades located approximately mid-span. The middle of the turbine blades hold the largest amount of stress for the entire turbine rotor. The turbine rotor shows the ability to operate under idle conditions for the JetCat P400 with a 1.5 factor of safety.

When the alumina turbine rotor ran at half power, the yield strength was exceeded with a peak stress in the blade region, shown in Figure 140a in red, on the trailing edge side at 617 MPa. When viewing the FOS plot in Figure 140b, failure regions can be seen more distinctly outlined in pink. Failure was predicted in the middle part of the blade regions, middle of the bore region, and between the circular holes in the hub due to the stress concentrations.

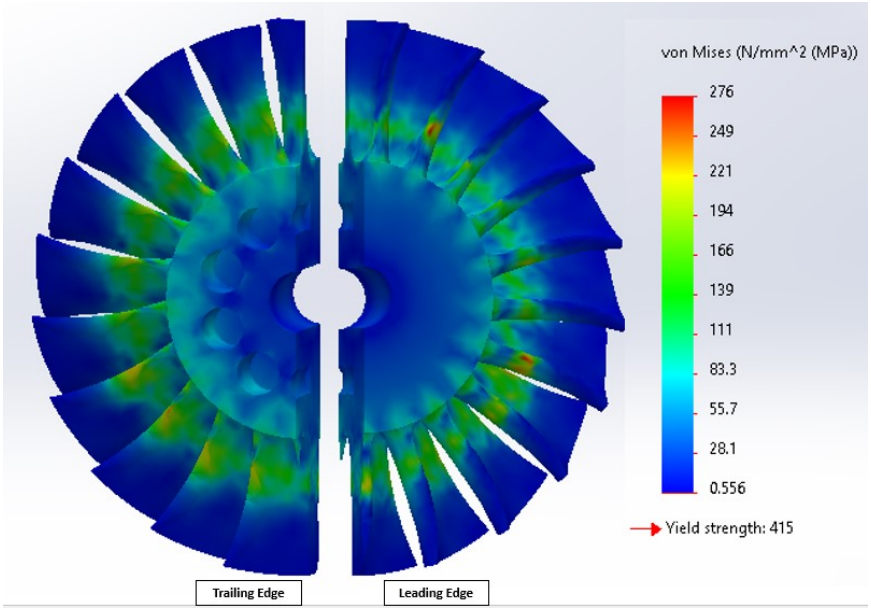

Figure 139. Analysis of the alumina turbine rotor under JetCat P400 idle power conditions.

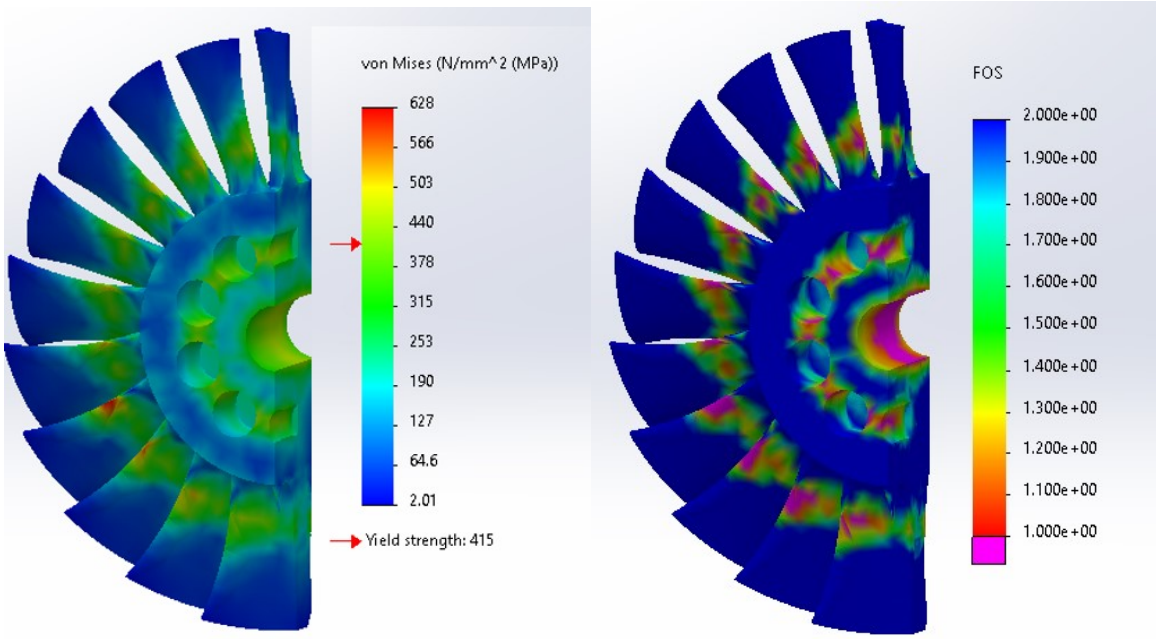

(a) Stress analysis. (b) Factor of safety plot.

Figure 140. Analysis of the alumina turbine rotor under JetCat P400 half power conditions.

For the zirconia material, a hub design with four rows of circular holes was analyzed to account for the maximum allowable material thickness of 5 mm. When the design analysis was conducted at half power, results shown in Figure 141, the zirconia turbine rotor showed peak stresses of 654 MPa located at stress concentration points between the inner row of the circular holes on the trailing edge side and located on the bore on the leading edge side. Due to the stress distribution, it is expected that failure will first occur in either the bore or first set of holes near the bore. The zirconia turbine rotor design is predicted to operate under JetCat P400 half power conditions with a 1.2 factor of safety.

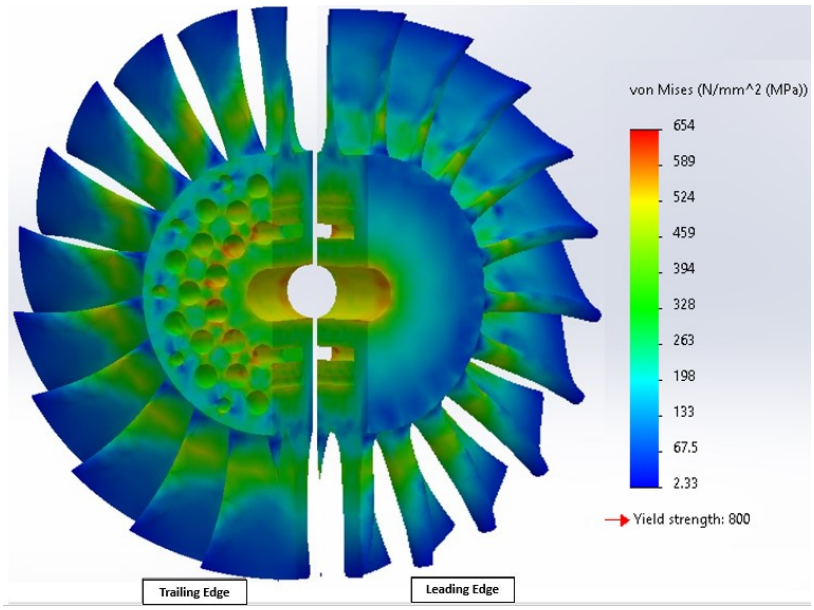

Figure 141. Analysis of the zirconia turbine rotor under JetCat P400 half power conditions.

When viewing the full power results for the zirconia design, shown in Figure 142, the turbine rotor indicates failure in the hub region. A peak stress of 1,054 MPa can be seen, Figure 142a, throughout the bore and between the inner row of circular holes. The FOS plot, in Figure 142b, indicated failure in pink regions in between the first two inner honeycomb rows and through the bore.

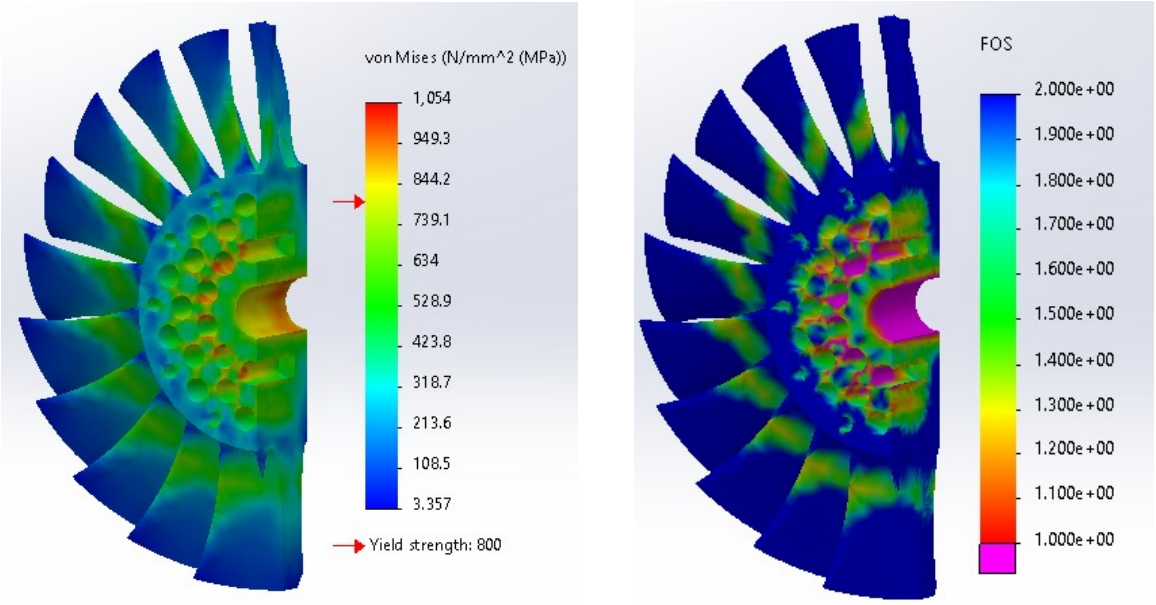

(a) Stress analysis.

(b) Factor of safety plot.

Figure 142. Analysis of the zirconia turbine rotor under JetCat P400 full power conditions.

The FEA results show the alumina design can operate up to idle conditions, and will initially fail in the turbine blade region if operated beyond this limit. The zirconia design can operate up to half power conditions and will fail in the hub region if pushed beyond these conditions. In the designs, the failure region needs to be considered, as failure in the blade region could lead to more damage as the blades brake off and are thrown downstream. Full power JetCat P400 conditions are possible with Si_3N_4, as shown in Section 4.1.2, but this would be dependent on the material properties for the Si_3N_4 photopolymer slurry developed for the ADMATEC printer. Currently a Si_3N_4 photopolymer slurry is in development by Oak Ridge.

4.4.2 Turbine rotor hub design analysis.

The six hub designs were analyzed to determine the JetCat P400 regime each alumina turbine rotor could operate in. The peak stresses, based on idle conditions, were all located in the middle of the turbine blades with the peak calculated stresses

shown in Table 5. The detailed FEA results can be viewed in Appendix 2. The peak stress ranged from 241 MPa for the multi-row through hole hub design to 289 MPa for the single row circular through hole design. While there was a 40 MPa difference between designs, every design showed the capability to easily run at idle conditions. Since this turbine rotor was made with alumina, none of the turbine rotors were able to achieve the mid power regime.

Table 5. Turbine rotor hub design FEA results.

Design	Peak Stress (MPa)
Single row partial fill - no fillet	252
Single row partial fill - fillet	272
Single row through holes - circles	289
Single row through holes - ellipse	252
multi-row through holes	241
BYU tapered design	244

4.4.3 Final turbine rotor printed design analysis.

The results for the final turbine rotor design made out of alumina show similar results to the initial design. When computationally run at idle, Figure 143, a peak stress appears on the leading edge side located in the middle of the turbine blades at 289 MPa. The middle of the turbine blades hold the largest amount of stress for the entire turbine rotor. The turbine rotor analysis shows the ability to operate under idle conditions for the JetCat P400 with a 1.4 factor of safety.

When the final alumina turbine rotor design was analyzed at half power it also failed similar to initial design simulations. The yield strength was exceeded with a peak stress in the blade region, shown in Figure 144a, at 627 MPa. When viewing the FOS plot in Figure 144b, failure regions can be seen more distinctly outlined in pink. Failure occurs in the middle part of the blade regions, middle of the bore region, and between the circular holes in the hub due to the stress concentrations.

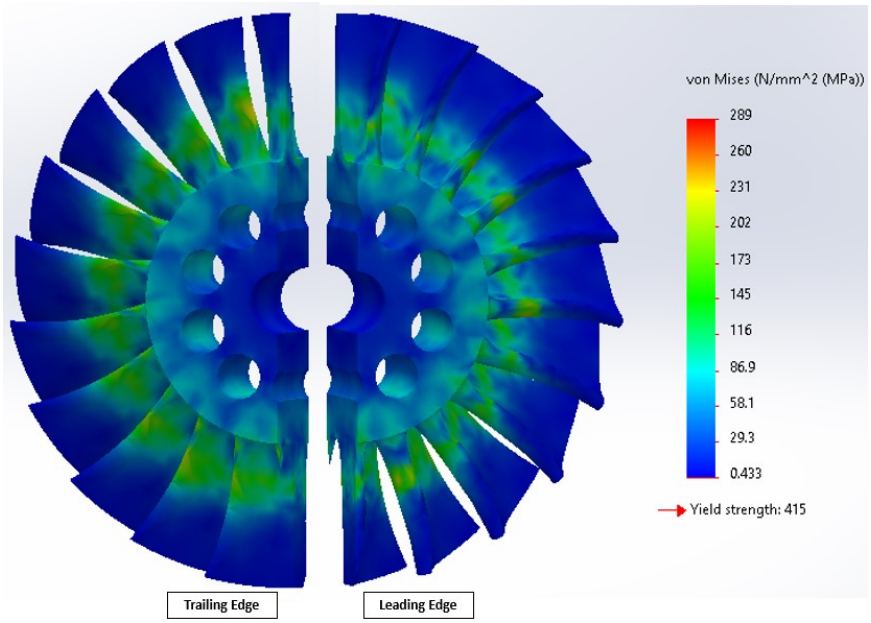

Figure 143. Analysis of the final turbine rotor design under JetCat P400 idle power conditions.

When analyzing the final turbine rotor design for centrifugal loads at room temperature, the analysis predicted failure to occur just prior to 82,750 RPM. The failure occurred in between the holes in the middle of the hub, highlighted in Figure 145. This failure is primarily due to stress concentrations from the holes in the hub.

4.5 Material characteristics

4.5.1 Si_3N_4 shrinkage results.

The shrinkage measurements and results for each stage are shown for the two 43% Si_3N_4 sintered specimens with Sample 1 data in Table 6 and Sample 2 data in Table 7. The samples tested, in Figure 146a, were the two successful samples from the Smooth On test with the VeroClear molds. These two samples were utilized to record shrinkage estimations and density data. The slurry for both samples filled the entire mold length and width, but could not be accurately measured for depth. The

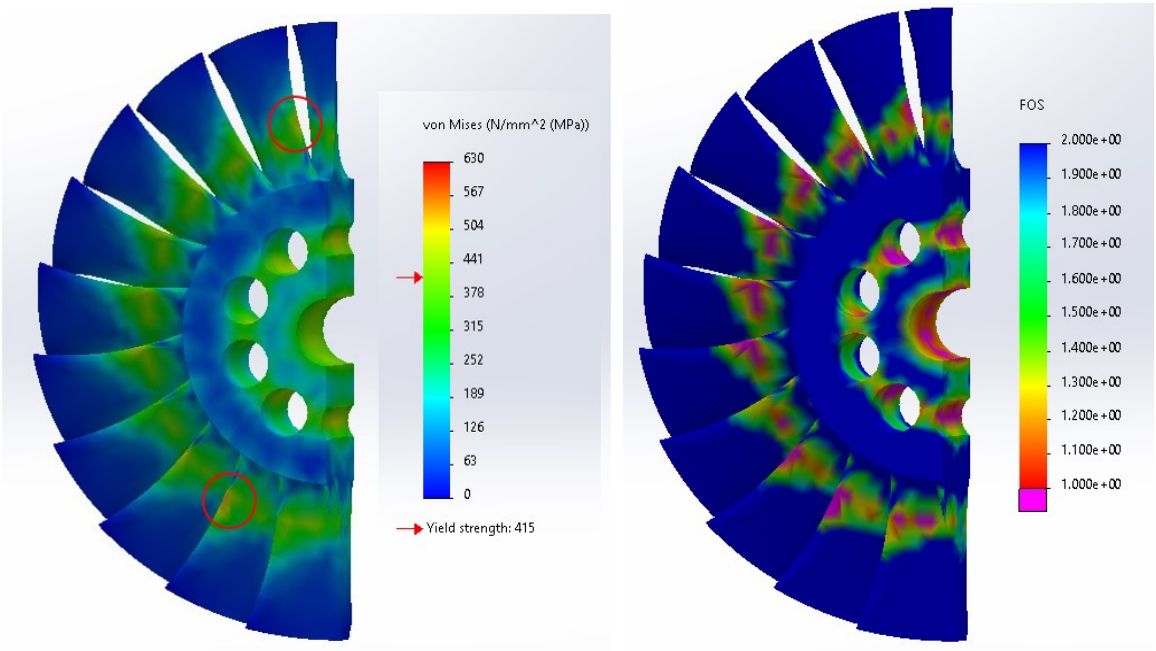

(a) Stress analysis. (b) Factor of safety plot.

Figure 144. Analysis of the final turbine rotor design under JetCat P400 half power conditions.

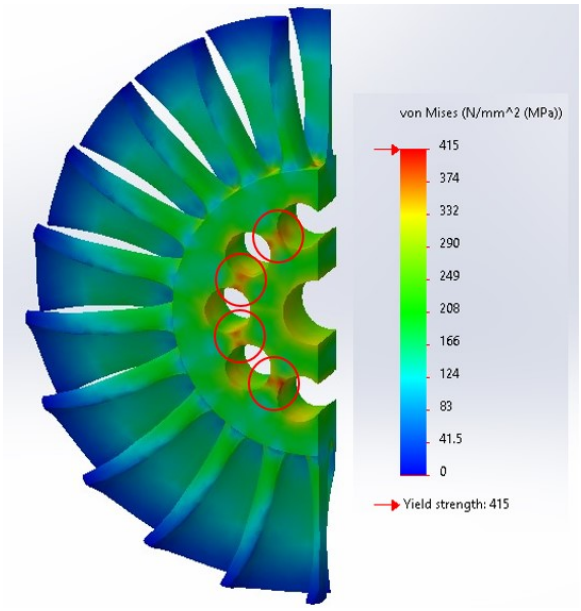

Figure 145. Analysis of the final turbine rotor design at 82,750 RPM.

first sample averaged a shrinkage of approximately 18.1% after sintering. The total overall shrinkage, shown in Figure 146b, including drying and binder burnout, was an overall shrinkage value of 20.4%.

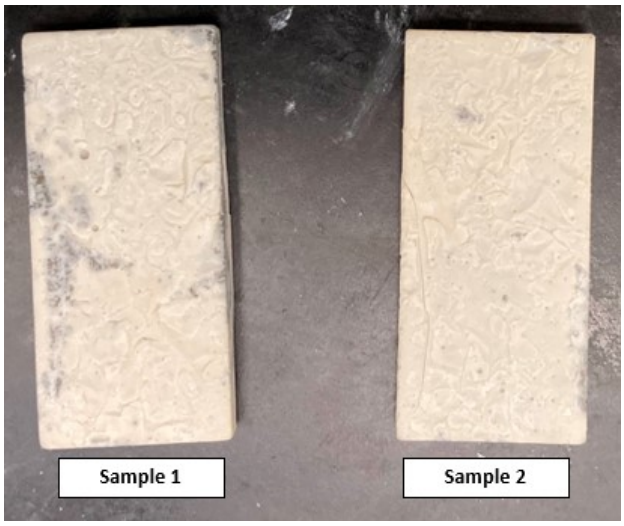

(a) Two 43% Si_3N_4 sintered specimens.

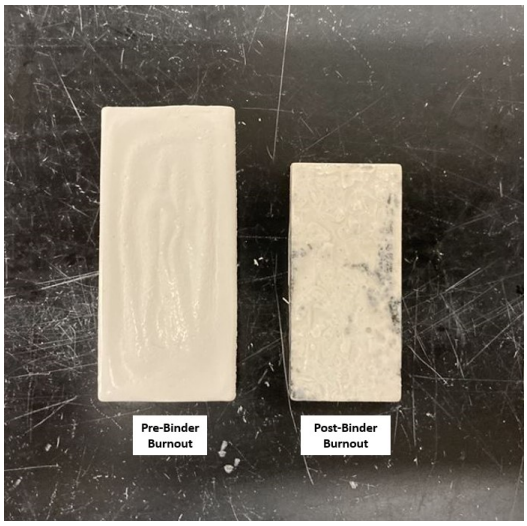

(b) Comparison of overall shrinkage of the 43% Si_3N_4.

Figure 146. 43% Si_3N_4 shrinkage results.

Table 6. Sample 1 shrinkage data.

	Length (mm)	**Width (mm)**	**Depth (mm)**
Initial Size	44.77	20.70	N/A
Post Binder Burnout	43.83	20.24	5.67
Post Sinter	35.60	16.50	4.70
	Lengthwise (%)	**Widthwise (%)**	**Depthwise (%)**
Binder Burnout Shrinkage	2.10	2.22	N/A
Post Sinter	18.78	18.48	17.11
Overall	20.48	20.29	N/A

The second sample averaged a shrinkage of 19.3% after sintering. The total overall shrinkage of the second sample, including drying and binder burnout, was an overall average shrinkage value of 20.5%. Between the two samples the 43% Si_3N_4 initial esti-

mates show the material shrinks during sintering close to 18.5% for a total shrinkage of approximately 20.5%.

Table 7. Sample 2 shrinkage data.

	Length (mm)	**Width (mm)**	**Depth (mm)**
Initial Size	44.77	20.70	N/A
Post Binder Burnout	43.80	20.34	5.01
Post Sinter	35.50	16.50	4.00
	Lengthwise (%)	**Widthwise (%)**	**Depthwise (%)**
Binder Burnout Shrinkage	2.17	1.74	N/A
Post Sinter	18.95	18.88	20.16
Overall	20.71	20.29	N/A

4.5.2 Si_3N_4 density results.

The results for the density testing are displayed in Table 8 using the same two samples from the shrinkage testing. The water temperature was 21.9°C, corresponding to a water density of 0.998 g/cm^3. This led to a density of 3.093 g/cm^3 for sample one and 3.114 g/cm^3 for sample two. This led to an apparent porosity of 0.08% for Sample 1 and 0.05% for Sample 2. The true density for 43% Si_3N_4 was 3.262 g/cm^3 based on the materials added to the slurry. From the true density and sample density the overall relative density was 94.8% for sample one and 95.47% for sample two leading to an average overall densification of the material of 95.14%.

4.5.3 Alumina shrinkage results.

The overall shrinkage results were calculated measuring the diameter and axial thickness of an alumina turbine rotor prior to binder burnout and post sintering, and can be seen in Figure 147. The measurements, shown in Table 9, were compared to the expected scaled and unscaled measurements from the Solidworks design. The pre-

Table 8. Si_3N_4 Density data.

	Sample 1	Sample 2
Water suspension (g)	5.405	4.748
Saturated weight (g)	7.977	6.984
Dry weight (g)	7.970	6.981
Sample Density (g/cm^3)	3.093	3.114
Relative Density (%)	94.8	95.47
Apparent porosity (%)	0.08	0.05

binder burnout measurements yielded a diameter of 118.45 mm and a thickness of 17.4 mm. The post-sintering measurements yielded a diameter of 92.73 mm and thickness of 12.87 mm. This yielded an overall diameter shrinkage of 22%, shown in Figure 147, compared to an expected diameter shrinkage of 23% per scaled dimensions. For the thickness measurement, an overall shrinkage of 26% was calculated, shown in Figure 147b, while the thickness was expected to shrink only 10%. The initial 16% disparity between the thickness shrinkage expectations indicated the hub may need to be re-scaled to achieve the desired results.

Table 9. Alumina turbine rotor shrinkage measurements.

	Expected	Actual
Diameter Post-print (mm)	119.5	118.45
Thickness Post-Print (mm)	17.46	17.4
Diameter Post-Sinter (mm)	91.87	92.73
Thickness Post-Sinter (mm)	15.88	12.87
Diameter shrinkage (%)	23	22
Thickness shrinkage (%)	10	26

4.5.4 Four point bend fixture results.

When machining the four point bend structure for testing, the SiC material was deemed unable to be machined utilizing electrical discharge machining (EDM) tech-

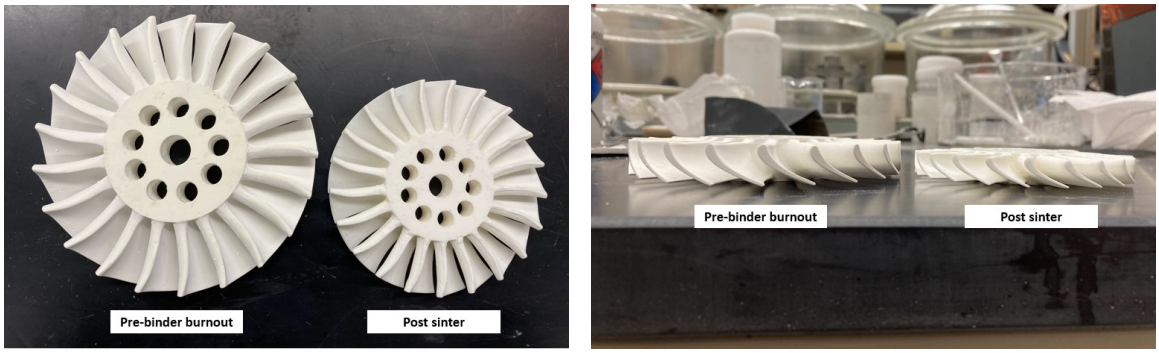

(a) Diameter shrinkage. (b) Thickness shrinkage.

Figure 147. Alumina turbine rotor shrinkage.

niques and required diamond tools or grinders to cut it to shape. This led to a more simplified top and bottom fixture, shown in Figure 148a, than previously designed shown in Figure 69. The top and bottom fixtures were made rectangular to strengthen and simplify the design. The inner grooves, that acted like a basket to catch the sample, were replaced with a simpler U-groove between the point loads. The guide slots from the original design were removed, and stainless steel alignment tools were created to ensure the test specimen was put in the correct place on the bend structure prior to testing. Rounded holes were used to hold the 2 mm ceramic rods, as shown in Figure 148b. If the tools were unable to drill out the holes, they would be replaced with V-grooves cut into the material to still allow the ceramic rods to act as point loads for the fixture. Instead of separate push rods for the top and bottom fixtures, the top and bottom pieces were extended lengthwise, and the total thickness of the material was reduced from 20 mm to 9.5 mm. The extended arms attached to the stainless steel rods that connected it to the MTS machine. While the new design was simplified due to machining concerns on the very hard SiC, the device still allows for articulation during testing with the ceramic rods. The point loads maintained appropriate spacing for three or four point bend testing and the alignment tools ensure proper placement of the specimen prior to testing.

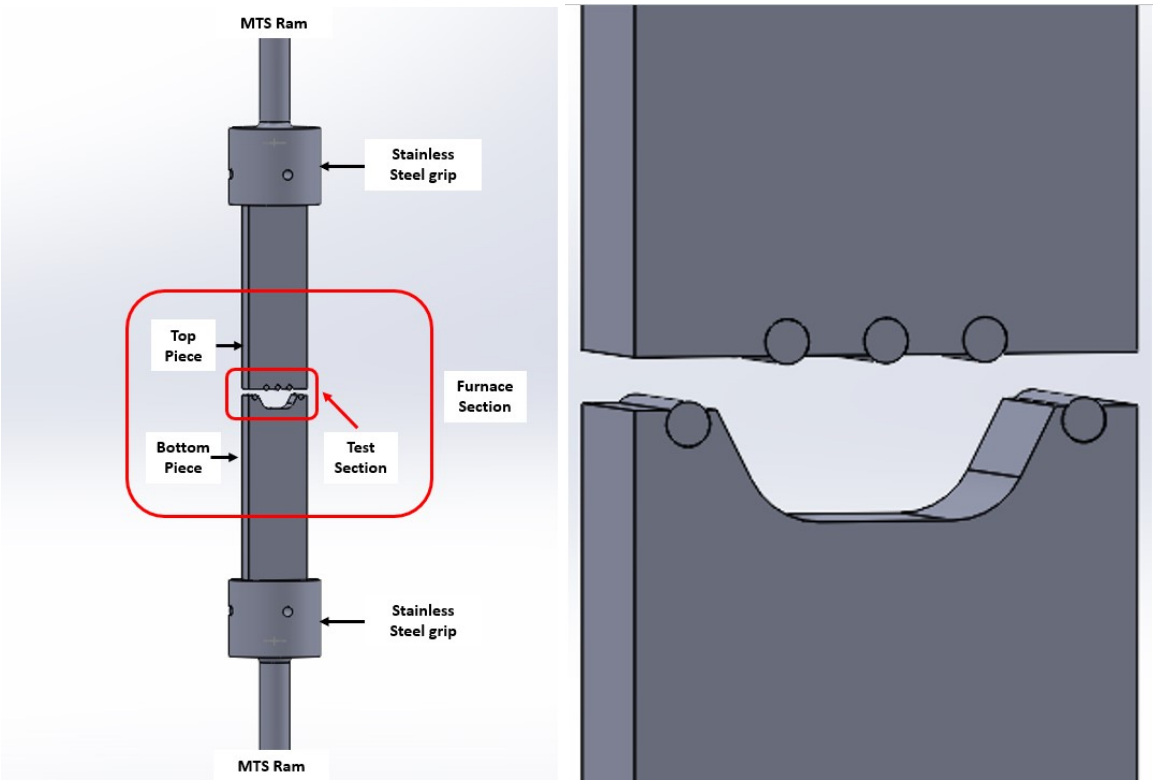

(a) Silicon Carbide four point bend fixture.

(b) Close up view of the test section with 2 mm rods inserted.

Figure 148. AFRL shop simplified four point bend fixture design.

V. Conclusions and Recommendations

5.1 Analysis on preliminary turbine rotor design for AFRL specified operating conditions

For Objective 1, FEA was conducted on a preliminary Si_3N_4 turbine rotor design to determine failure points in the turbine rotor based on design cycle analysis for increased T_4 conditions. This required a thermal study to be completed to determine the stress caused by the difference in coefficient of thermal expansions between the Si_3N_4 turbine rotor bore and the 2507 stainless steel engine shaft. Further analysis was conducted for three turbine rotor designs based on the individual thermal profile and centrifugal profile, followed by the combined thermal and centrifugal profile given by AFRL, assuming the stresses from the bore and shaft were negated with a tolerance ring. The hub design analysis started with the initial BYU tapered design, and increasingly simplified the hub by creating a half tapered/half-filled in, followed by a completely filled in hub.

The first analysis determined there was failure in the bore due to the difference in coefficient of thermal expansion between the shaft and ceramic. A peak stress of 900 MPa was seen at the edge of the bore, exceeding the assumed yield strength of Si_3N_4 of 600 MPa. This analysis confirmed the need for a joining mechanism to eliminate the thermal stresses induced by differing coefficients of thermal expansion.

For the individual centrifugal profile analysis, all three turbine rotor designs were able to meet the 90,000 RPM centrifugal requirement. The BYU tapered hub and partially filled hub had the largest stresses located in the blade region at 528 MPa and 547 MPa, respectively. However, as mass was added to the hub region, the stresses in the bore began to reduce. The filled in hub design removed the peak stresses in the blade regions and reduced the overall bore stress from 337 MPa seen in the BYU

tapered design down to 277 MPa. This indicated that an increase in mass in the hub helped reduce the centrifugal forces in the outer radial portion of the hub, allowing the loads to concentrate more easily on the center bore.

In the individual thermal profile analysis of 1300°C in the middle of the turbine blades and 427°C at the bore, the BYU design failed due to expansion of the fillets in between the blade roots. This failure was not seen with the other two designs as the additional mass allowed for the energy to dissipate throughout the hub. Also, it can be seen between the three designs that as mass was added to the hub, the thermal stresses at the bore increased with the filled hub having the highest stresses at 600 MPa, right at yield stress. The thermal stress appears as the dominating factor in the turbine rotor induced by the large difference in temperature between the bore and turbine blades. The increased mass allowed for more energy absorption increasing the temperature profile difference between the blade and bore regions, thus increasing the stress at the bore.

For the combined temperature and centrifugal force analysis, each Si_3N_4 turbine rotor failed in the bore region, exceeding the yield stress of 600 MPa. The peak stress increased as more mass was added to the hub from the BYU tapered design at 757 MPa to the fully filled hub at 857 MPa. This confirmed that the Si_3N_4 turbine rotors could not meet the operating conditions given by AFRL, due to the thermal stress from the temperature differential of 873°C between the blades and the bore.

To determine the effects of the large temperature differential, the bore temperature for the BYU tapered and fully filled hub designs were increased in increments of 100°C from 427°C to 927°C. As the bore temperature increased, the peak stress for both designs decreased linearly in the bore region. The fully filled hub decreased at a faster rate than the tapered design and by 800°C had a lower maximum stress in the bore than the tapered design. Each design was able to operate below the yield strength of

the material at a temperature of 743°C for the tapered design and 762°C for the filled hub. This shows that a Si_3N_4 turbine rotor is feasible to meet the design criteria from AFRL, however, it requires the bore temperature to be increased, thus reducing the temperature differential. This increase will be dependent on the shaft and bearing temperature limits, which will ultimately lead to new design criteria for a turbine rotor.

5.2 Turbine rotor manufacturing process

For Objective 2, a suitable manufacturing process was identified for producing a turbine rotor by evaluating methods of casting with a sacrificial mold and SLCM 3D printing. A Si_3N_4 turbine rotor was cast using a sacrificial mold and compared to the process of stereolithography based ceramic manufacturing (SLCM) of an alumina turbine rotor using an Admaflex 300 SLCM printer. The entire casting process for the turbine rotor took 7 weeks, while the SLCM turbine rotor process took 1.5 weeks. For the casting method, a mold study was conducted to determine the best mold release agent, evaluate the surface roughness of the mold, and produce the best mold design to assist with casting. The mold study looked at three mold materials: VeroClear printed with an Objet 260 Connex 3 printer, Polycast printed on an Ultimaker FDM printer, and the Standard Resin printed with a Formlabs printer.

For the sacrificial mold study, it was determined that Smooth on Universal mold release agent was the best of the mold release agents tested. Smooth on was the only release agent that allowed the slurry to pull away from the mold wall while it dried with no cracking. All other release agents showed signs of stress cracking due to portions of the slurry adhering to the mold. All mold materials were able to burn away during binder burnout, but Polycast was the only material that did not leave behind any ash.

The VeroClear mold required internal support structures in the blade regions that had to be removed with a water jet and left a rougher surface on the blades because of residual support material that could not be removed. Additionally, there was no ability to create a partial infill in the plastic, reducing the mold porosity and leaving more mold residue that would have to be burned off. The Standard Resin did not require internal supports but had issues with incomplete printing of the blade regions. Additionally, the mold material was brittle, and as with the VeroClear, there was no ability to create a partial infill. The Polycast mold allowed for the flexibility to adjust the infill of the solid portions of the mold as needed and to place support structure on the outside of the mold for printing so the internal portion of the mold would be untouched. The downside to the Polycast material was its opaqueness obstructing the view of the slurry as it was cast in the blade region, a problem that did not exist for the VeroClear and standard resin.

With regard to the surface roughness, the Polycast material untreated was 12.8 μm and the VeroClear was 4.3 μm. When treating the Polycast material with isopropyl alcohol for 2 minutes, the surface roughness was reduced to 1.8 μm which fused the layers to a smooth finish. Any longer of a treatment and the isopropyl alcohol began to degrade the mold surface. Of the three materials tested, Polycast was determined to be the most suitable material for this application due to its ability to melt away with minimal residue, printing flexibility, and surface smoothness after treatment.

The final Polycast mold design was smoothed out with isopropyl alcohol for 2 minutes and treated with a liquid Smooth On mold release to get to all internal cavities. Material between the turbine rotor blades was removed with a partial infill between the walls to allow for some visibility when casting. Each blade also had two vent holes to prevent air from being trapped in the blade region to ensure complete fill.

The casting method utilized a 43% Si_3N_4 slurry to allow the material to easily flow into the enclosed cavities of the mold. The turbine rotor was dried in a humidity chamber for one month and then underwent binder burnout. Upon completion of drying, stress cracks formed in the hub and could be seen at the root of the blades. After binder burnout, the blades broke off the hub due to stress cracking, leading to a failed turbine rotor. The stress cracks were induced in the blades due to uneven drying between the hub and the blades since the hub was exposed to air and the blades were covered by the mold. In addition to the turbine rotor, consistency for cast specimens was an issue. Only 50% of the rectangular samples prepared for testing successfully made it through sintering, showing how delicate the process is even with simple geometries.

While a suitable sacrificial mold was found, the whole casting process proved complex and produced inconsistent results, with multiple stages of the process allowing potential defects to be introduced. During slurry mixing and casting, air bubbles become trapped in the slurry and were not fully removed, even with the vibration table, leading to micro-cracking and voids in the ceramic as it dried. During the drying stage, uneven drying or potentially too fast of a dry time in the humidity chamber induced stress cracks, ultimately leading to a failed specimen. After drying, care had to be taken when moving the samples in the green state from the humidity chamber to the furnace as they were fragile and could easily break. To fix some of these defects, the use of a defoaming agent would be required to help with some of the induced air. Also, the top portion of the blades in the mold would need to be exposed to air to allow for more even drying. This may assist with producing a successful cast turbine, but there will still be issues with producing consistent results for a complex geometry. While the sacrificial mold helps reduce tooling cost and time, the casting process is not suitable for large-scale production of turbine rotors due to the ease at

which defects can be introduced leading to inconsistent results.

The SLCM process utilized an alumina photopolymer to produce a turbine rotor, since a Si_3N_4 photopolymer is still in development and the more capable zirconia slurry was not available during the initial research. The alumina turbine rotor had no issues printing directly from a .STL file and easily held shape during water debinding. Once through water debinding the specimen was easy to handle and process in the green state to remove any supports. During binder burnout and sintering it was determined that the capped portion of the turbine rotor was causing delamination due to stress concentration at the base of the extruded holes. Small surface cracking on the leading edge hub occurred due to slight uneven heating caused by the capped portion resting on a ceramic plate. Additionally, some of the underexposed sacrificial layer may not have been fully removed adding to the radial cracking issues on the leading edge hub side.

This led to a study that examined six hub designs, testing three extruded hole designs all the way through the hub, the BYU tapered design, a filleted hole design, and a non-filleted hole design. For the through hole designs, it was found there were no cracking issues due to thickness or delamination formed by internal stresses assisting in more even heating throughout the hub. The BYU tapered design became weak on the outer rim, due to lack of supports for the tapered portion. The added fillet seemed to reduce some of the delamination, but appeared to be too small to remove it entirely. The hub study led to a final turbine rotor design using a single row of circular holes, acting as a partial infill, extruded through the entire hub. Additionally, the AFIT model shop was able to successfully integrate the tolerance ring into the hub by machining the bore within the required tolerance and inserting the ring with a drill press.

For the final design, an alumina turbine rotor was successfully manufactured.

There was no delamination in the blades seen through any of the final turbine rotors. Radial cracking was observed in the hub on the exposed trailing edge side from incomplete binder removal. Smaller binder marks were noticed on the surface of the leading edge side because it rested on the base plate during water debinding, impeding water saturation. Additionally, small stress cracks were noticed where the blades met the hub, due to stress caused by gravity after the supports were removed. The radial cracking on the leading edge side was removed by extending the water debind time to 5 days, allowing water to penetrate and dissolve the binder. To alleviate the remaining cracking, the turbine rotor was to be removed from the base plate after one day of water debind and then placed onto the support structure, which allowed for water penetration to dissolve off the remaining binder on the leading edge and provide full blade support until sintering.

The SLCM printing method shows a lot of promise in manufacturing. The photocuring of the slurry eliminates the introduction of air bubbles or other defects during the printing process. Due to the slurry being a water-soluble photopolymer, the binding agent is easily removed in water if the thickness limitations are not exceeded. Issues due to stress cracking were due to thickness limitations and stress concentrations introduced by the design of the turbine rotor. Longer than normal water debinding ensured the binder was fully dissolved. The stress concentrations became predictable, and the design was quickly altered through CAD software and then reprinted. The results of the prints were consistent and once the design was altered to remove the induced stress concentrations between layers and adjust the water debind timeline, the print had no issues producing consistent results. The SLCM process removes many of the opportunities to introduce defects that were seen in casting, and removes the need for any mold to hold shape. By directly printing the ceramic turbine rotor, the timeline was reduced to 2 weeks, which is 5 weeks faster than the

cast turbine. The predictability and consistency of results, ease of processing, fast timeline, and low material cost make this process potentially scalable and beneficial for large-scale manufacturing of complex ceramics.

5.3 Analysis for manufactured turbine rotor design for JetCat P400 operating conditions

For Objective 3, the turbine rotors "as manufactured" geometry was analyzed through FEA to determine failure criteria in a JetCat P400 relevant environment for the Si_3N_4, alumina, and zirconia turbine rotors designs. This required multiple combined thermal and centrifugal simulations to determine which JetCat P400 operating regimes (idle, mid-power, and full power) the different turbine rotor designs could operate in. For the cast Si_3N_4 turbine rotor, the BYU tapered hub, partially filled hub, and fully filled hub designs from Objective 1 were analyzed. The printed turbine rotor designs were analyzed based on modifications created to account for the material thickness restrictions of 10 mm for an alumina printed rotor and 5 mm for a zirconia printed rotor. While not used as a material to produce a turbine rotor, zirconia was analyzed to determine the potential operating regime that could be achieved for follow on research. The alumina design featured a single row of extruded holes in the hub to reduce material thickness, and the zirconia design featured multiple rows of small, extruded holes acting as partial infill in the hub. A final printed alumina design was also analyzed to determine the JetCat P400 operating regime it could operate in and determine the highest centrifugal force it could sustain in a room temperature spin test.

The FEA for the Si_3N_4 turbine rotor designs showed the ability for each design to operate in the JetCat P400 full power range, with a peak stress located in the bore for the tapered, partially filled, and fully filled hub designs of 526, 531, and 493 MPa,

respectively. The filled hub was the most suitable design for casting, not only due to the lowest amount of stress, but also because it was the most simplified design which would reduce potential defects in the casting process due to more complex geometries.

The initial alumina turbine rotor design showed the ability to operate in the JetCat P400 idle regime with a peak stress of 276 MPa located in the center blade region. The alumina turbine rotor exceeded its yield strength of 415 MPa throughout the blades, hub, and bore, in the mid-power regime with a maximum stress of 617 MPa located in the blade region. This conclusion showed that most alumina turbine rotors would likely only be able to operate in the idle range with a factor of safety around 1.5.

The initial zirconia turbine rotor design showed the ability to operate in the JetCat P400 mid-power range, showing a peak stress of 654 MPa due to stress concentrations between the circular infill. When the simulation was conducted at full power, the turbine rotor exceeded the yield strength of 800 MPa, with a peak stress of 1,054 MPa though the bore and stress concentrations from the inner rows of infill. This simulation shows that failure is expected to happen in the hub region, and not the blades, and would be able to operate under mid-power conditions with a factor of safety of 1.2.

The final alumina turbine rotor design produced similar results to the initial design. The final design was only able to operate in the idle range with a 1.4 factor of safety, showing a peak stress of 289 MPa in the middle blade region. During the mid-power simulation failure occurred in the blade, hub, and bore region at a peak stress of 627 MPa in the blade region. For a spin test at room temperature, the turbine rotor design analysis showed it would exceed yield strength, just prior to 82,750 RPM, in the hub from stress concentrations due to the holes.

5.4 Material properties and preparation for JetCat P400 testing

For Objective 4, material properties were experimentally quantified for the Si_3N_4 and alumina. The 43% Si_3N_4 shrinkage and density values were characterized using rectangular cast samples. The shrinkage was determined by taking measurements of the specimens from the original cast size, post-binder burnout sample size, and post-sinter sample size to determine the sintering shrinkage and overall shrinkage. The initial sintering shrinkage was found to be 18.5% with an overall shrinkage value of 20.5%. The density was characterized utilizing the Archimedes method. The average overall densification of the Si_3N_4 samples was 95.14% with an average apparent porosity of 0.063%.

For the alumina turbine rotor, the diameter shrunk 22%, which was close to expectations of 23% total reduction. However, the turbine rotor thickness shrunk 26%, compared to expected results of 10%. In order to test the turbine rotor in the JetCat P400, more shrinkage information needs to be recorded to fine tune results to manufacture the expected turbine size as a drop in replacement.

For strength testing a four-point bend structure was designed utilizing SiC. This bend structure can be used for three-point and four-point testing at room temperature and elevated temperatures in a furnace up to 1200°C. At the time of publication, the rig is currently being finished by the AFIT model shop.

To fit the alumina turbine rotor to the shaft of the JetCat P400, tolerance rings were procured from USA Tolerance Ring. These rings were then fit to the turbine rotor in preparation for follow-on testing.

5.5 Recommendations

The following are recommendations for follow-on SLCM research from this study:

1. In order to achieve the operating requirements given by AFRL, it is recommended that the bore temperature be increased to reduce the temperature differential experienced by different regions of the turbine rotor. This also will require further consideration of shaft integration techniques to account for other material limits such as the tolerance ring, stainless steel shaft, and bearings. If a larger redesign is possible, designing the turbine with a shrink fitter, placing the rotor bore in compression, could also be beneficial.

2. An additional print using the new water debinding timeline needs to be conducted to ensure all binder cracking is eliminated. This requires removing the supports and base layer from the turbine rotor after one day. Then placing it on the new support structure so the turbine blades are not weakened. Then the turbine rotor must undergo four days of additional water debind. After drying, the support structure should be utilized during binder burnout, followed by a powder bed for support during sintering.

3. For the printed alumina turbine rotor, the part needs to be successfully integrated onto the shaft. The turbine rotor bore now needs to be machined to size and then fitted with a tolerance ring using the same procedures as a hub. Once this is complete, the turbine rotor must ensure it can be fitted into a JetCat P400. This may require a slight adjustment in the scaling of the turbine rotor to achieve desired dimensions. Once integrated, testing needs to be completed for a room temperature spin test to compare the FEA results to real world results. Once the spin test is complete, further testing in the JetCat P400 needs to be conducted to show that the alumina turbine rotor can operate under idle conditions as predicted in the FEA.

4. An additional study can be conducted about how the print layer effects the

print and densification of the turbine rotor. Utilizing a smaller print layer and a larger rounded fillet in the bore should be studied to see if a capped design is possible in the turbine rotor without cracking or delamination.

5. A Si_3N_4 photopolymer is currently being designed by Oak Ridge National Labs. Once successful, follow-on research should take the methods and lessons learned in this study and begin attempting to produce a Si_3N_4 turbine rotor. Additionally, material classification will need to be conducted to determine the room temperature strength, high-temperature strength, shrinkage, and density properties. Strength testing for both the Si_3N_4 photopolymer and alumina photopolymer can be printed and tested using the SiC 4 point bend fixture created in this study. Once the properties are determined, new designs can be analyzed through FEA to see what regimes the turbine rotor can operate in.

Appendix A. Solidworks simulation setups

The following is a walkthrough on how the FEA was set up for the studies conducted. This material assumes a model was already built and will go over how a simulation was created, temperature profile setup, the coefficient of thermal expansion shaft and hub analysis setup, operating simulation performed, how to view results, and all parameters that were used for the study.

A.1 Create a simulation

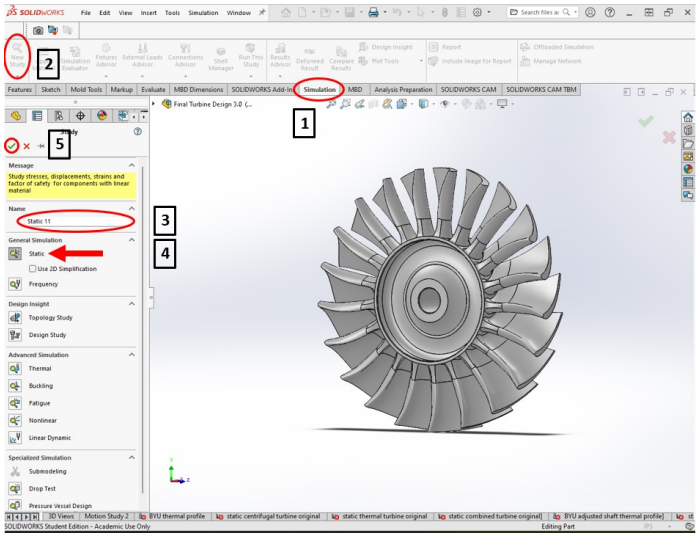

Figure 149. New study start screen.

1. With the completed turbine rotor design or assembly open, click on the "Simulation" tab near the top.

2. Click on the "New Study" tab in the top left.

3. Name the study.

4. Under the "General Simulation" tab click the "Static" icon.

5. Click the green check mark and a study will be started. The initial static simulation will then be created as shown in Figure 150.

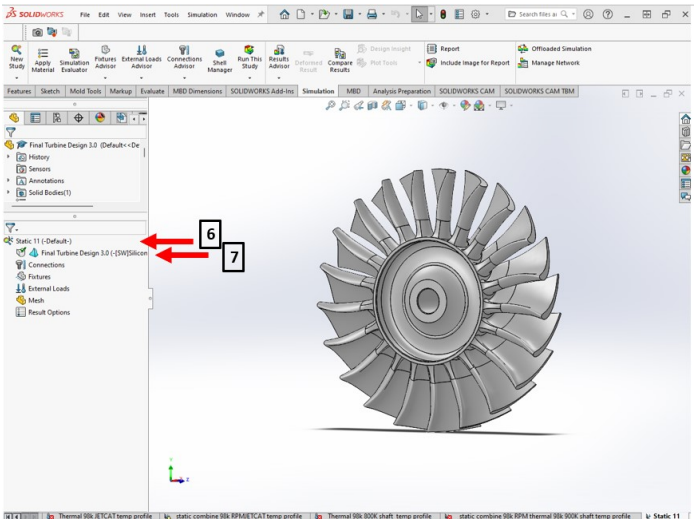

Figure 150. New analysis screen.

6. Right click on the study name and select the "Properties" tab. This will take you to a menu shown in Figure 151. From the "Options" tab ensure "compute free body forces" and "Use inertial relief" is selected. Then click OK.

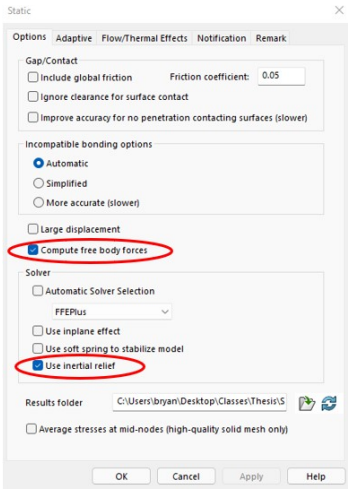

Figure 151. Study properties menu.

7. To establish the material being utilized, right click on the design name in the left column and select “Apply/Edit Material...” from the menu. This will bring up the materials menu shown in Figure 152. If the material being used is not in the database then it will need to be created.

   Note: Many metal materials are listed under the SOLIDWORKS Materials, however, there are currently no ceramics. If the material is in the current database then select it and click “Apply”.

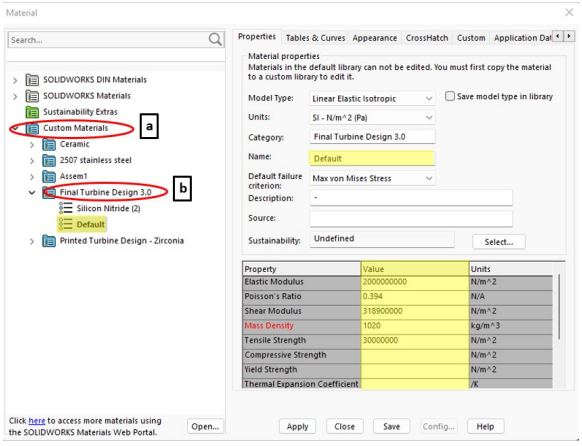

Figure 152. Materials menu.

(a) To create a material, right click on “Custom Materials” and select “New Category’ and name it.

(b) Then right click on the newly named category and select “New Material”. This will create a default material to add information to shown in Figure 152.

(c) From the materials properties box, the new material information can be input. Change the name to the new material and input the values to the appropriate material property boxes. The units can be changed with the “Units” drop down box.

(d) Once the material properties have been inserted, click "Save". Then "apply" and close out of the material menu.

Note: All the property values used in this study can be found in Table 10 and 11.

Table 10. Silicon Nitride and 2507 Stainless Steel Material Properties

Material properties	Silicon Nitride	2507 Stainless Steel
Young's Modulus (E_c) (GPa)	310	200
Poisson's ratio (ν)	0.25	0.3
Density (ρ) (kg/m^3)	3188	7806
Tensile strength (MPa)	600	800
Compressive strength (MPa)	6000	NA
Yield strength (MPa)	600	552
Coefficient of Thermal Expansion (α) ($1/K$)	2.50E-6	1.30E-5
Thermal Conductivity ($W/(mK)$)	20	15

Table 11. Alumina and Zirconia Polymer Ceramic Slurry Properties

Material properties	Alumina	Zirconia
Young's Modulus (E_c) (GPa)	360	210
Poisson's ratio (ν)	0.21	0.22
Density (ρ) (kg/m^3)	3900	6060
Tensile strength(MPa)	415	800
Compressive strength(MPa)	4150	8000
Yield strength(MPa)	415	800
Coefficient of Thermal Expansion(α) ($1/K$)	7.5E-6	1E-5
Thermal Conductivity ($W/(mK)$)	30	10

8. These are the initial study property settings and material settings used for each study. Once established the remaining setup was dependent on the study being created.

A.2 Creating a thermal profile

Before the shaft and hub and turbine rotor simulations were conducted a thermal profile had to first be created. Figure 153, shows how to create a thermal profile after creating a simulation.

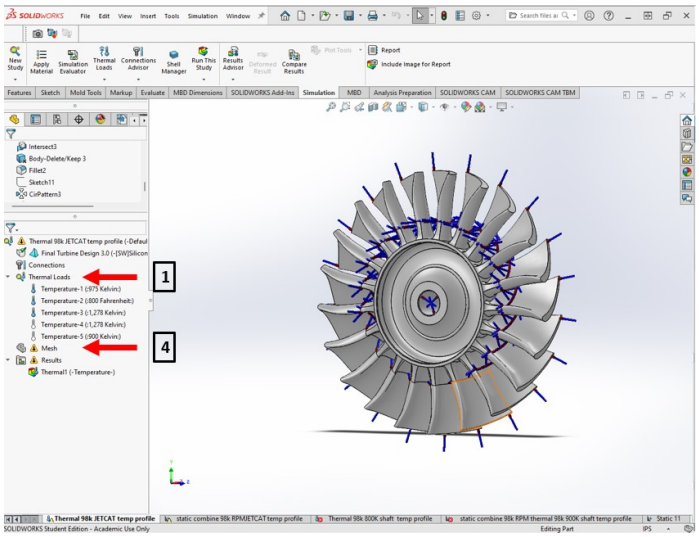

Figure 153. Thermal study setup.

1. After setting up the study properties and material properties, right click on "Thermal Loads" tab and select "Temperature". This will bring up the temperature menu shown in Figure 154

   Note: This action can also be performed from the "Thermal Loads" tab at the top of the screen

2. Ensure that "Temperature" is checked, then select the faces and edges that the specific temperature is for. A blue probe will show up on that face or edge.

3. Once the regions are selected, enter the temperature for that specific thermal load. Then click on the green check mark.

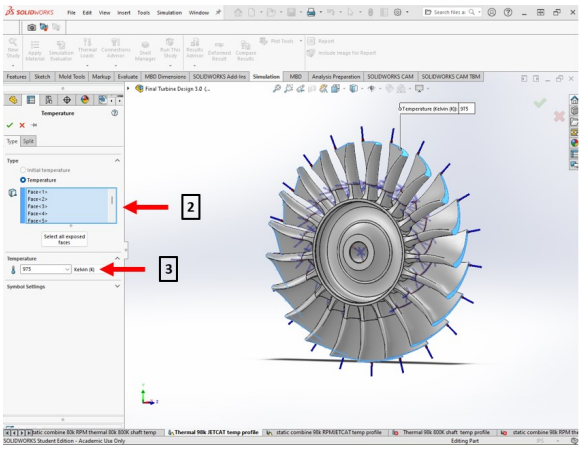

Figure 154. Temperature menu.

Note: Depending on computer processing speed, more then 15 faces or edges may begin to slow down the computer. If this is the case, instead of setting the temperature for every face in one region, consider building multiple thermal loads for that specific temperature regions at only 10 to 15 probes.

Note: Having the blue probes displayed for each thermal load created will also slow down the computer. To hide the probes, right click on the specific load and select "Hide". Do not select "Suppress" as this will take the thermal load out of the analysis.

4. Repeat Steps 1 to 3 until the thermal profile is built. Once the thermal profile is built, right click on "Mesh" and select "Mesh and run". This will create a default mesh and run the thermal profile, which can then be viewed by clicking on the result in the results tab.

   Note: If a different mesh than the default is desired then right click on mesh and hit create mesh. From there the mesh can either be made more fine or more coarse. A finer mesh will create more data points and a more detailed study, but it will also create a larger data file and will take longer to run.

A.3 Shaft and hub analysis setup

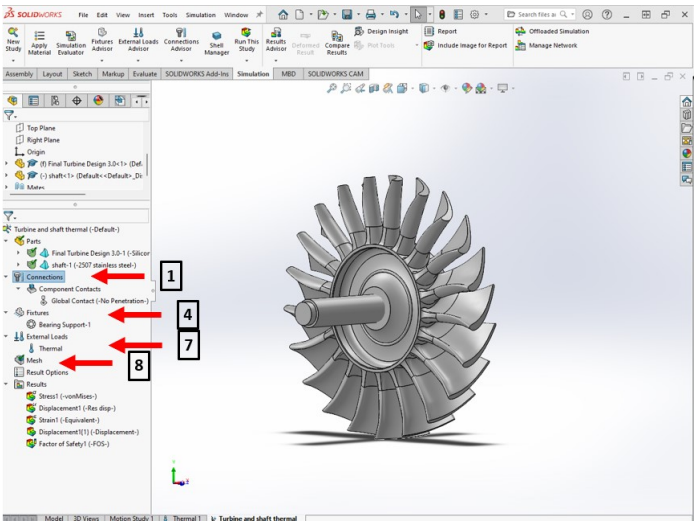

Figure 155. Shaft and hub assembly setup.

1. After applying the study properties and material properties from the initial set up in Section A.1 for the assembly, right click on the "Connections" tab on the left side of the menu, shown in Figure 155, and select "Component contacts". This will populate a components menu shown in Figure 156.

   Note: This option can also be selected from the drop down in the "Connections advisor" button in the top simulation tab.

2. From the component contact menu select "No Penetration" for the contact type.

3. Then under "Components" make sure "Global Contact" is selected and ensure the entire assembly is selected. Once complete, hit the green check mark.

4. Next the bearing fixture will be set up. Right click on the "Fixtures" tab on the left side of the menu in Figure 155. Select "Bearing support" to bring up the fixture menu shown in Figure 157.

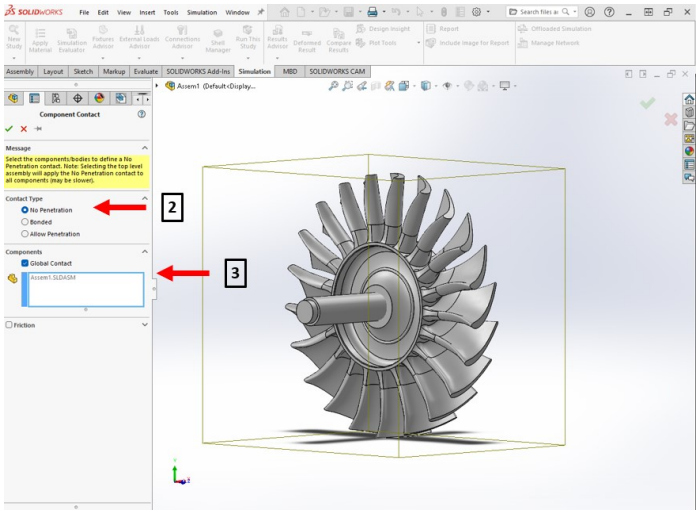

Figure 156. Component contacts menu.

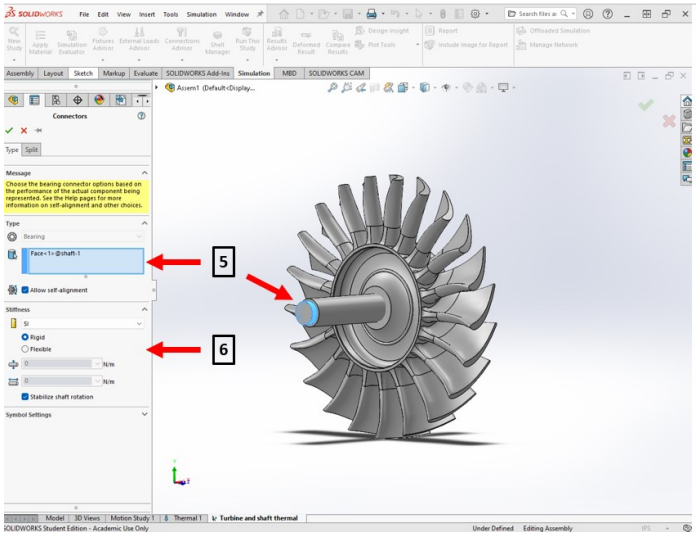

Figure 157. Connectors menu.

Note: This can also be selected from the "Fixtures Advisor" option in the top simulation tab.

5. Under the type section on the left ensure "Allow self-alignment" is checked. Then select the face the bearing is to be placed on. For this assembly a groove had to be created on the shaft for the bearing placement.

6. Under the stiffness section, ensure “Rigid” is selected and the box is checked for “Stabilize shaft rotation”. Then check the green check mark and go back to the original set up menu in Figure 155.

7. Next the thermal load was applied. Right click on “External loads” and select “Thermal Effects” from the menu. This will bring up the static simulation menu with the “Flow/Thermal Effects” tab opened shown in Figure 158.

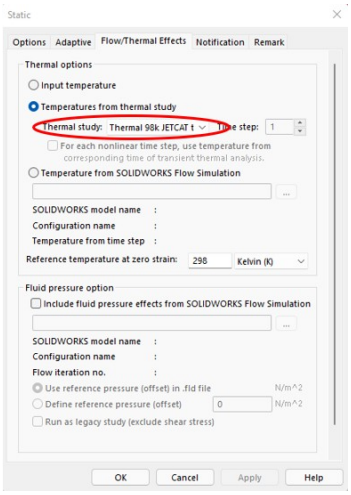

Figure 158. Flow/Thermal Effects menu.

8. From this menu select “Temperatures” from thermal study and in the drop down select the thermal profile you set up in Section A.2. Once selected click “Apply” and “OK”.

   Note: This can also be selected from the “External Loads Advisor” option in the top simulation tab.

9. Once the thermal profile is established Mesh and Run the simulation as shown in Section A.2. This will populate results for the assembly.

   Note: When viewing the assembly, it may be advantageous to remove the shaft to view where the stresses are located. From Figure 159, right click on the shaft

part file on the left hand side and select either “Hide” or “Change transparency” from the menu. Do not select “Suppress” as this could change the simulation results.

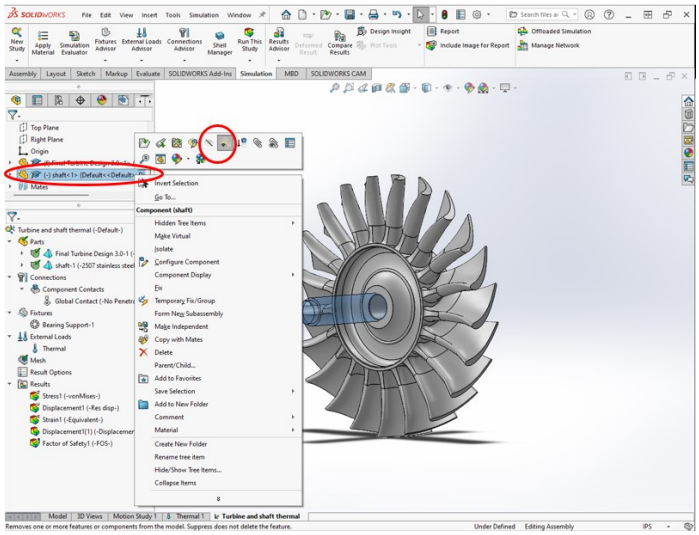

Figure 159. Menu options allowing removing of the shaft from view.

A.4 Turbine rotor operating conditions analysis setup

For the turbine rotor simulations no connections or fixtures were applied. The centrifugal load and thermal profiles were built based on the profiles shown in Table 12.

1. After applying the study properties and material properties from the initial set up in Section A.1 for the turbine rotor design, right click on the “External loads” tab on the left side of the menu, shown in Figure 160, and select “Centrifugal”. This will populate the centrifugal loads menu shown in Figure 161.

   Note: This option can also be selected from the drop down in the “External loads advisor” button in the top simulation tab.

Table 12. Combined thermal and centrifugal analysis regimes.

Operating Profiles	Rotational Velocity (RPM)	Blade tip Temp (°C)	Blade root Temp (°C)	Middle blade Temp (°C)	Bore Temp (°C)
AFRL Profile	90,000	1.200	1,200	1,300	427
JetCat P400 Idle	30,000	342	377	537	427
JetCat P400 Half Power	80,000	632	485	827	427
JetCat P400 Full Power	98,000	700	627	1,005	427

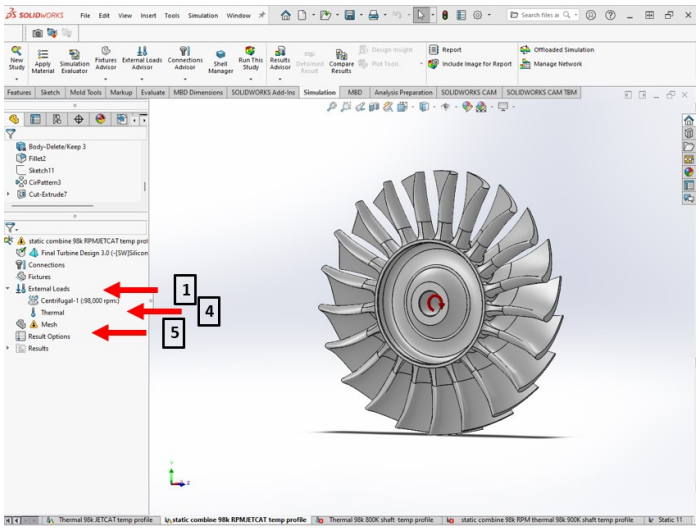

Figure 160. Combined centrifugal and thermal analysis study.

2. In the "Selected Reference" section, select the reference face the turbine rotor will be rotating around. For the turbine rotor the face selected was the bore.

3. Under the "Centrifugal force" section, ensure "Metric" is selected and input the RPM for the simulation. Ensure the simulation is run in the counter-clockwise direction based on the leading edge of the blade as shown in Figure 161. If it is shown facing clockwise, then select the "Reverse direction" button. Once the centrifugal forces are established, select the green check to save the force.

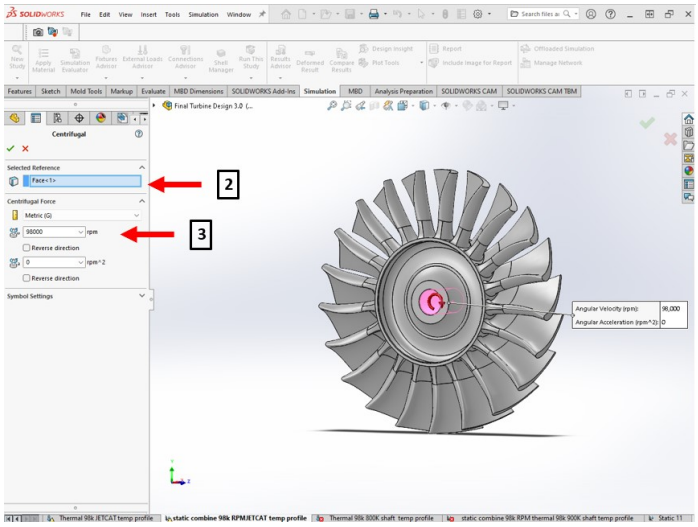

Figure 161. Centrifugal loads menu.

4. Next set the thermal profile for the external loads as shown in Section A.3.

5. Select mesh and run as shown in section A.2 to run the study and produce results.

   Note: If the mesh is applied separately you can run the study by selecting the "Run this study" button on the top of the screen under the simulations tab or by right clicking on results.

A.5 Viewing results

Once the analysis has been run the results will post. For the thermal profile, only the thermal profile analysis results will post. For the assembly analysis and the combined turbine rotor analysis stress, displacement, and strain results will be auto generated as shown in Figure 162. A factor of safety plot will have to be created if wanting to view where the failure occurred. This will be shown below along with other helpful visual tips for presentation purposes.

Caution: If a yellow triangle is displayed by the study, mesh, and results sections

it means a change was made to the design and the results may no longer be valid. The simulation needs to be meshed and run again to clear the caution. If the study relies on a thermal profile, the thermal profile will most likely need to be re-run as well. Re-run the thermal profile study first, then run the second simulation.

Note: If the design appears to be deformed, then the deformed result is most likely selected in the upper "Simulation" tab menu located at the top of the screen in Figure 162. Deselect the deformed results and the original design will reappear.

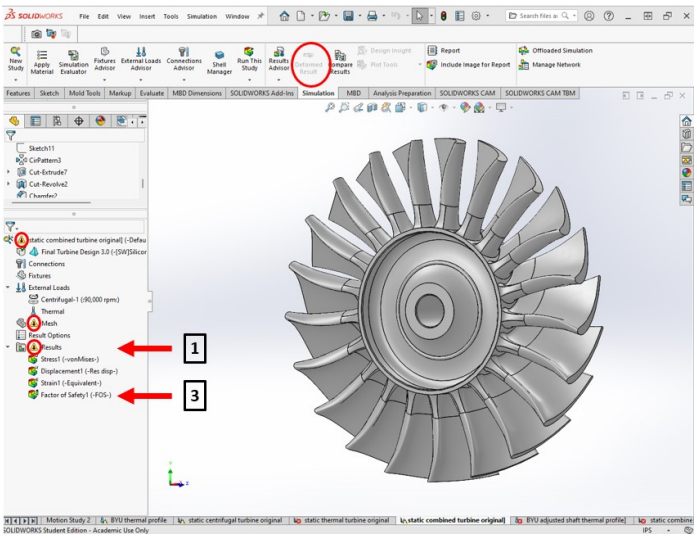

Figure 162. Results display menu.

1. To create a "Factor of Safety" plot right click on "Results" and select "Define Factor of Safety Plot". This will generate the factor of safety plot and pull up the factor of safety menu shown in Figure 163.

2. Select the appropriate failure criteria for the plot from the drop down menu. Then select the green check mark to populate the plot.

3. From the main results menu from Figure 162, double click on the factor of safety plot that was created to pull it up. Then right click on the factor of safety plot under the results section and select "Chart option" or "Settings". This will

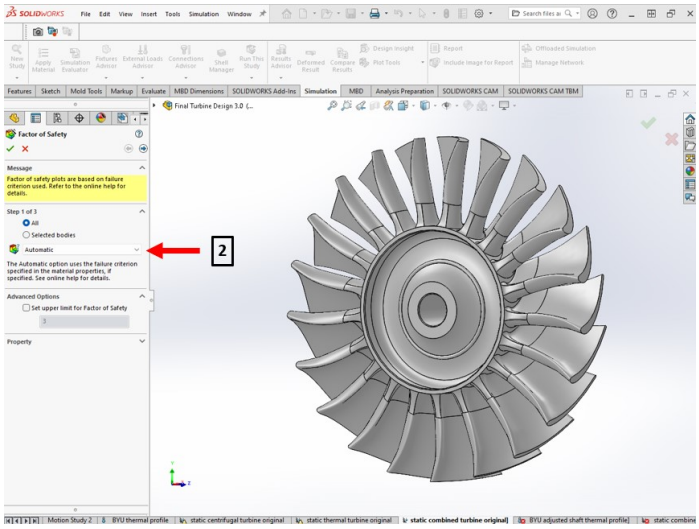

Figure 163. Factor of safety menu.

bring up the menu for the minimum factor of safety values and allow you to adjust the plot as appropriate. The menus that populate are shown below with the settings chart as Figure 164(a) and the chart options as Figure 164(b).

4. From the settings tab in Figure 164(a), select the "Boundary options" to display when viewing the cutaway view. It is recommended to select "None" for picture purposes.

5. When the factor of safety plot is populated it automatically defines the minimum and maximum criteria based on the simulation results. To view the areas of failure, click the "Chart options" tab in Figure 164(b). Deselect "Automatically defined minimum value" and change the value to 1. Then change the failure display color under"Specify color for values below minimum value". The maximum value can also be adjusted to provide a better FOS layout. Once desired settings are selected, click the green box to get to the main menu.

   Note: Pink is the recommended color, due to the fact it contrasts well with other colors in the chart.

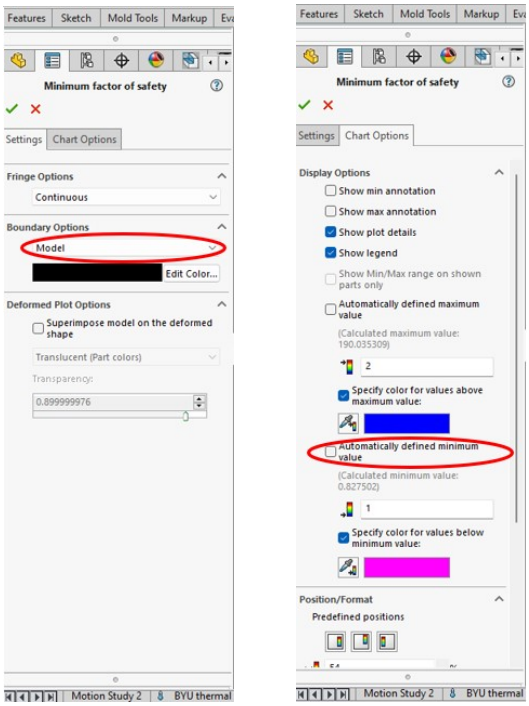

(a) Factor of safety settings tab.

(b) Factor of safety chart options tab.

Figure 164. Minimum factor of safety options menu.

When viewing the plots, a cutaway view, shown in Figure 165, is the most useful view to see how different results are affected throughout the design. The following walkthrough shows how to set the cutaway view for the stress plot, but this can be applied to viewing any of the other plots as well.

1. From Figure 165, select the stress plot under the "Results" tab on the left. Then right click on the "Stress plot" tab and select either "Edit definition", "chart options", or "settings". This will bring up the stress plot display menu shown in Figure 166.

2. From the "Definitions" tab in Figure 166(a), under the display section set the stress criteria wished to be displayed from the drop down menu. Then set the units for the legend to display as well. This study utilized Von Mises Stress and MPa.

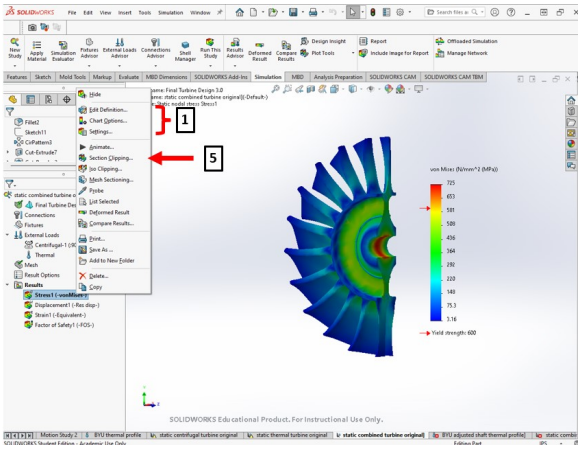

Figure 165. Cutaway stress plot.

3. From the "Chart options" tab, in Figure 166(b), the defined minimum and maximum values can be adjusted similar to when setting the values for the factor of safety plot. For the stress plots, the boxes for "Automatically defined maximum and minimum" values were selected.

4. From the "Settings" tab, in Figure 166(c), under "Boundary options" select what boundaries should be displayed for the cutaway in the dropdown menu. For taking images for results "None" is recommended. Once all options have been set select the green check mark to save the settings.

5. Once 'Settings" have been selected, right click on the "Stress plot" tab on the left under "Results". Select "Section clipping" to pull up the section clipping menu and produce the cutaway, shown in Figure 167.

6. From the "Section clipping" select the "Plane view".

7. Then select which plane to view the section clipping from. Additionally, to choose the direction to clip away from the design toggle the clipping direction button off to the side.

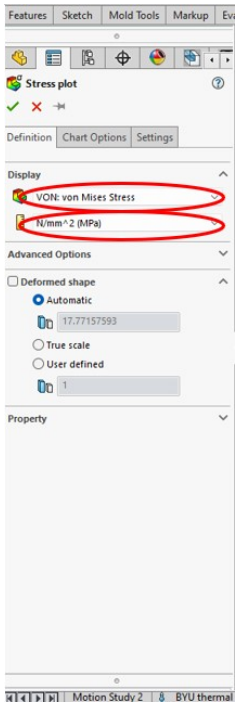

(a) Stress definitions tab.

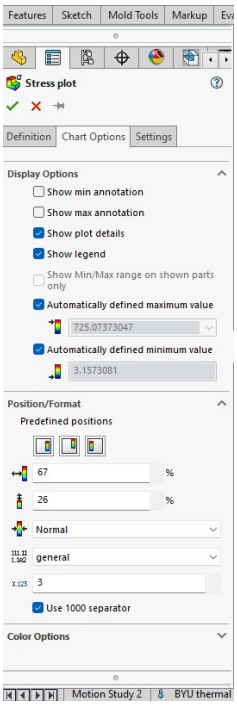

(b) Stress chart options tab.

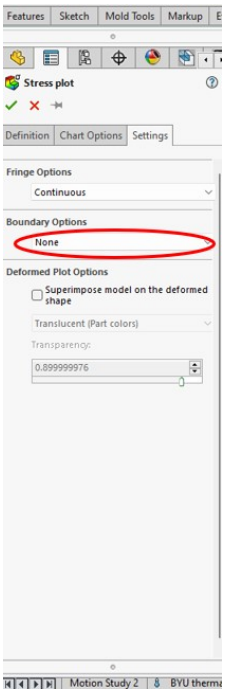

(c) Stress settings tab.

Figure 166. Stress plot display menu.

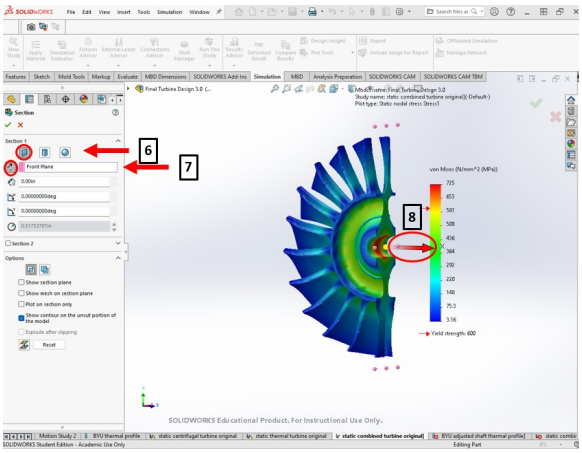

Figure 167. Section clippling menu.

8. Drag the arrow to display the desired portion of the plot. Once set to desired position select the green check. The plot is then ready for viewing.

Appendix B. Turbine rotor hub study FEA results

The following are the FEA results from the turbine rotors in the hub study. The turbines were run under JetCat P400 idle conditions utilizing alumina material.

B.1 FEA of hub designs

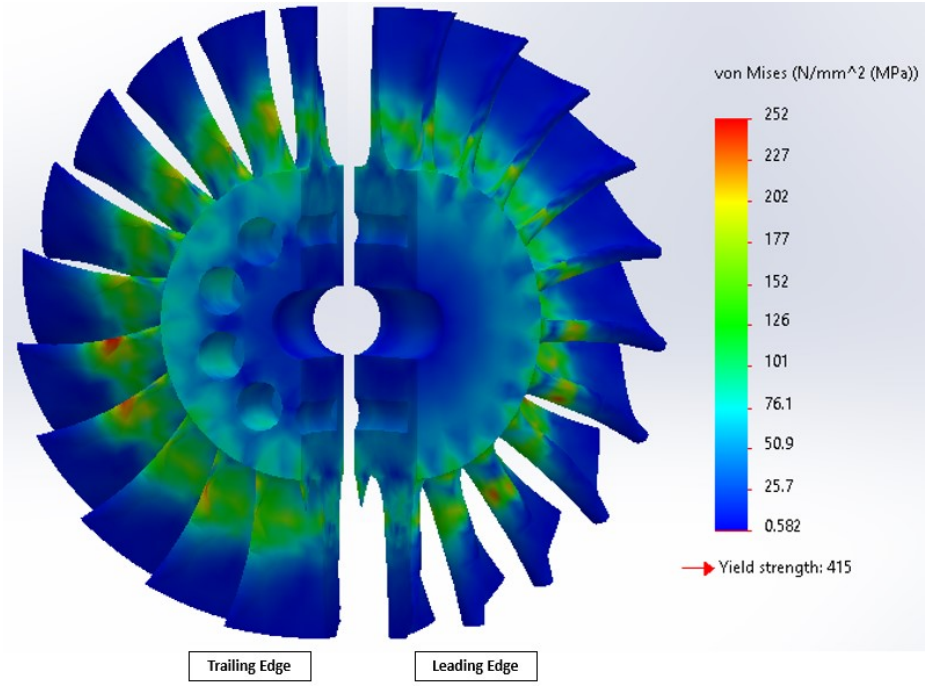

Figure 168. Single row circular hub design with no fillet.

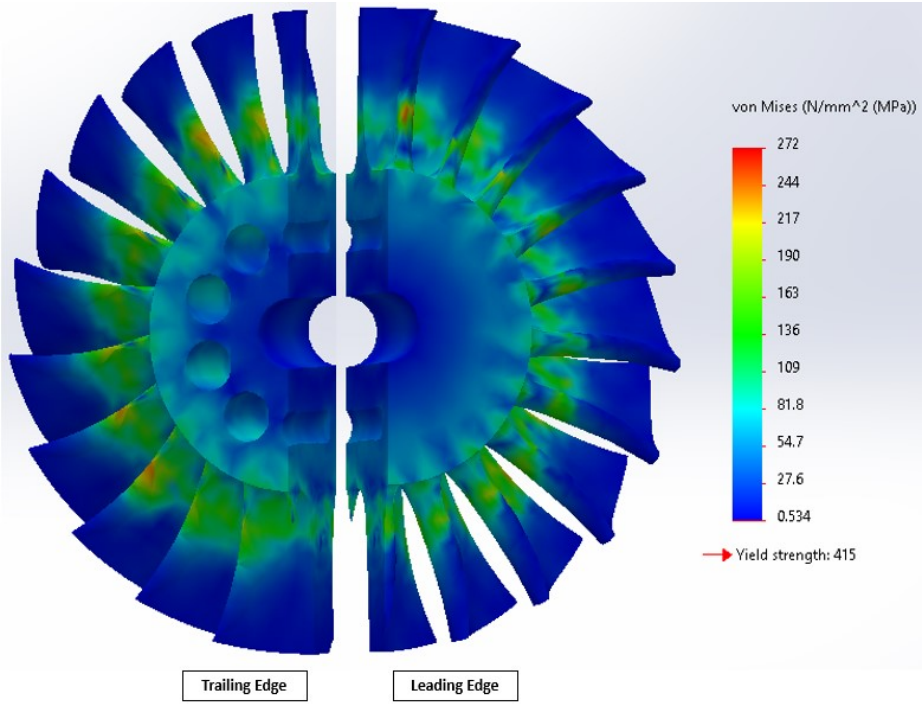

Figure 169. Single row circular hub design with a fillet.

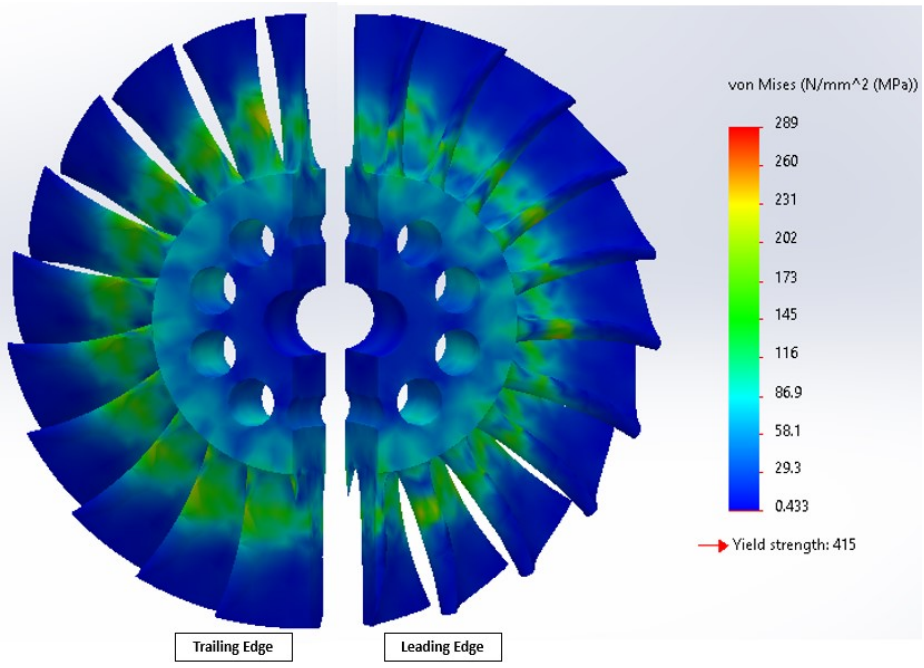

Figure 170. Single row circular hub design with through holes.

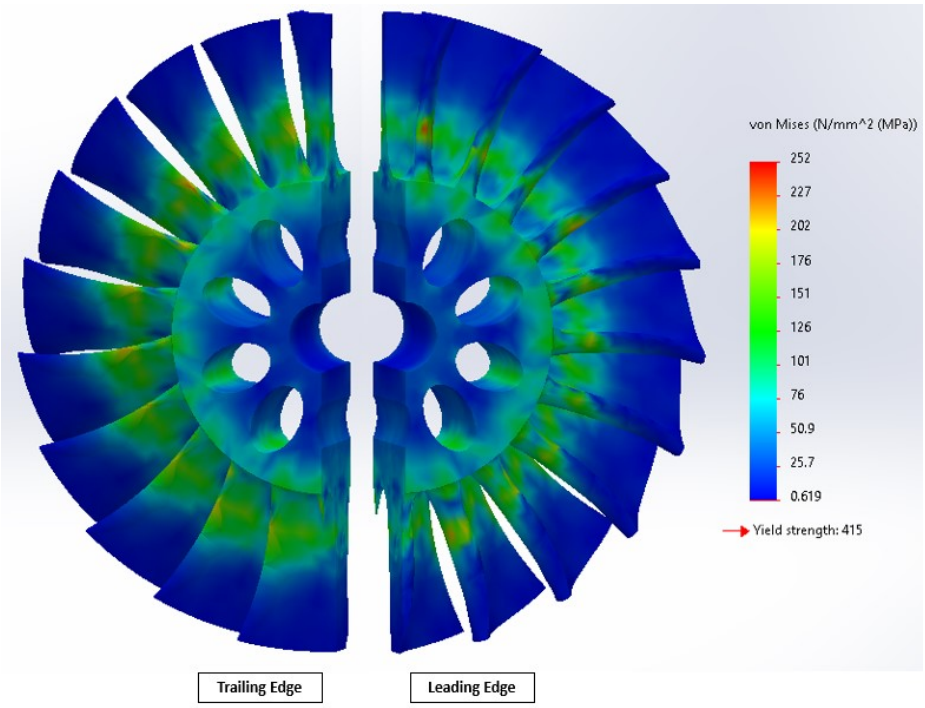

Figure 171. Single row ellipse hub design with through holes.

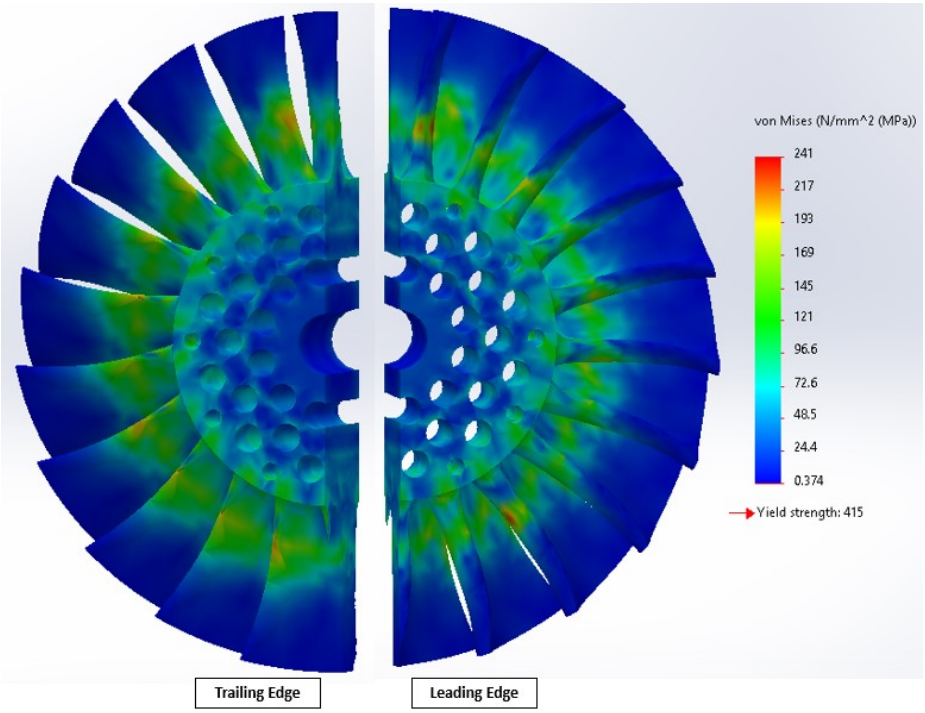

Figure 172. Multi row circular hub design with through holes.

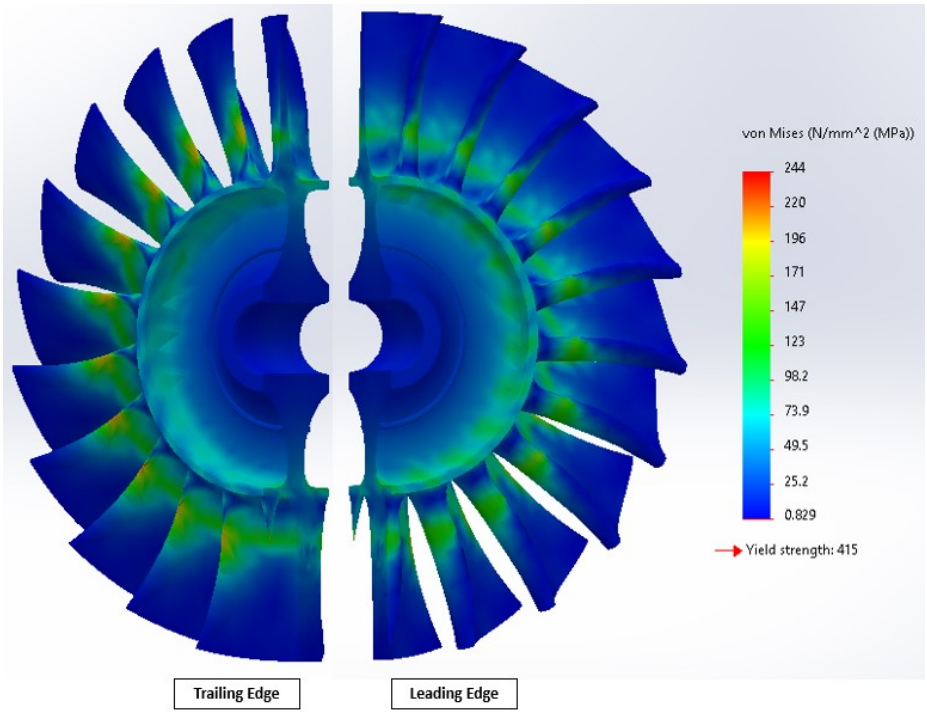

Figure 173. BYU tapered hub design with through holes.

Bibliography

1. "Official Website - JetCat," World Wide Web Page, Available at *https://www.jetcat.de/en*.

2. Douillard, A. and St-Pierre, J.-M., "How It's Made - Model RC Turbines - YouTube," 10 2012.

3. Bedke, A., Deveraux, D., Johnson, B., Halliday, J., Smithson, C., Green, E., and Cable, M., "Ceramic Turbine Integration: Winter Semester Design Report," 4 2021.

4. Cheah, C. M., Chua, C. K., Lee, C. W., Feng, C., and Totong, K., "Rapid prototyping and tooling techniques: A review of applications for rapid investment casting," 2 2005.

5. Huang, M., He, P., Yang, J., Duan, F., Lim, S. C., and Yip, M. S., "Fabrication and characterization of mini alumina ceramic turbine rotor using a tailored gelcasting process," *Ceramics International*, Vol. 40, 2014, pp. 7711–7722.

6. "Rapid fabrication of alumina-based ceramic cores for gas turbine blades by stereolithography and gelcasting," *Journal of Materials Processing Technology*, Vol. 209, 9 2009, pp. 5886–5891.

7. Rueschhoff, L. M., Trice, R. W., and Youngblood, J. P., "Near-net shaping of silicon nitride via aqueous room-temperature injection molding and pressureless sintering," *Ceramics International*, Vol. 43, 10 2017, pp. 10791–10798.

8. Rueschhoff, L., Costakis, W., Michie, M., Youngblood, J., and Trice, R., "Additive Manufacturing of Dense Ceramic Parts via Direct Ink Writing of Aqueous Alumina Suspensions," *International Journal of Applied Ceramic Technology*, Vol. 13, 9 2016, pp. 821–830.

9. Ashby, M. F., *Materials Selection in Mechanical Design*, Butterworth-Heinemann, Oxford, 4th ed., 2011.

10. Bocanegra-Bernal, M. H. and Matovic, B., "Mechanical properties of silicon nitride-based ceramics and its use in structural applications at high temperatures," *Materials Science and Engineering A*, Vol. 527, 3 2010, pp. 1314–1338.

11. Stienstra, D., "Introduction to Design of Structural Ceramics," 2003.

12. Richerson, D. W. and Lee, W. E., *Modern Ceramic Engineering Properties, Processing, and Use in Design*, CRC Press, Boca Raton, FL, 4th ed., 2018.

13. Zeng, W., Gan, X., Li, Z., and Zhou, K., "The preparation of silicon nitride ceramics by gelcasting and pressureless sintering," *Ceramics International*, Vol. 42, 8 2016, pp. 11593–11597.

14. Ye, C., Jiang, Y., Yue, X., Ru, H., Jia, H., E, Y., Ren, Q., Sun, S., Wang, W., and Zhang, C., "Effect of temperature and pre-sintering on phase transformation, texture and mechanical properties of silicon nitride ceramics," *Materials Science and Engineering A*, Vol. 731, 7 2018, pp. 140–148.

15. Allison Engine Company, Indianapolis, IN, *Hybrid Vehicle Turbine Engine Design Considerations and Technology Support*, 10 1997.

16. Mattingly, J. D., *Elements of Propulsion : Gas Turbines and Rockets*, American Institute of Aeronautics and Astronautics, Reston, VA, 2006.

17. Picard, B., Blais, A. L., Picard, M., and Rancourt, D., "Power-Density vs Efficiency Trade-off for a Recuperated Inside-Out Ceramic Turbine (ICT))," 2019.

18. Landry, C., Dubois, P. K., Courtois, N., Charron, F., Picard, M., and Plante, J.-S., "Development of an Inside-Out Ceramic Turbine," 2016.

19. Boyle, R. J., Parikh, A. H., and Nagpal, V. K., "Design Considerations for Ceramic Matrix Composite High Pressure Turbine Blades," 2019.

20. Haas, J. E. and Kofskey, M. G., "Effect of Rotor Tip Clearance and Configuration on Overall Performance of a 12.77-Centimeter Tip Diameter Axial-Flow Turbine," 1979.

21. "Current Issues and Problems in the Joining of Ceramic to Metal," 9 2016.

22. Lemus, J. and Drew, R., "Diffusion bonding of silicon nitride to titanium," *British Ceramic Transactions*, Vol. 99, No. 5, 2000, pp. 200–205.

23. Zhou, Y. N., *Microjoining and nanojoining*, Elsevier Science, United Kingdom, 2008.

24. Heinrich, U., Pucher, H., Schenk, B., Reimers, W., and Schmackers, T., "Ceramic/Metal-Shaft/Hub Connection for Applications in Small High Temperature Ceramic Gas Turbine Rotors," 5 2000.

25. Wasson, E. A., Wiedmann, G., Lewis, P., and Reid, N., "Structural materials," *Advanced Materials*, Vol. 3, 1991, pp. 520–521.

26. Cai, K., Guo, D., Huang, Y., and Yang, J., "Solid freeform fabrication of alumina ceramic parts through a lost mould method," *Journal of the European Ceramic Society*, Vol. 23, 12 2003, pp. 921–925.

27. "The Admaflex Technology - Stereolithography / Digital Light Processing," World Wide Web Page, Available at *https://www.admateceurope.com/admaflex-technology.html*.

28. Hampshire, S., "Silicon Nitride Ceramics - Review of Structure, Processing and Properties," *Journal of Achievements in Materials and Manufacturing Engineering*, Vol. 24, 9 2007, pp. 43–50.

29. Zheng, Y. S., Knowles, K. M., Vieira, J. M., Lopes, A. B., and Oliveira, F. J., "Microstructure, toughness and flexural strength of self-reinforced silicon nitride ceramics doped with yttrium oxide and ytterbium oxide," *Journal of microscopy*, Vol. 201, 2001, pp. 238–249.

30. Knutson-Wedel, E. M., Falk, L. K., Björklund, H., and Ekström, T., "Si3N4 ceramics formed by HIP using different oxide additions — relation between microstructure and properties," *Journal of Materials Science 1991 26:20*, Vol. 26, 1991, pp. 5575–5584.

31. Meléndez-Martínez, J. J. and Domínguez-Rodríguez, A., "Creep of silicon nitride," *Progress in Materials Science*, Vol. 49, 2004, pp. 19–107.

32. Weibull, W., "A Statistical Distribution Function of Wide Applicability," *Journal of Applied Mechanics*, 9 1951, pp. 293–297.

33. ASTM, "Standard Practice for Reporting Uniaxial Strength Data and Estimating Weibull Distribution Parameters for Advanced Ceramics 1," *American Society for Testing and Materials*, Vol. C1239-13R18, 2018.

34. "Quick fabrication of aeronautical complicated structural parts based on stereolithography," *Propulsion and Power Research*, Vol. 4, 6 2015, pp. 63–71.

35. ASTM, "Standard Test Method for Flexural Strength of Advanced Ceramics at Ambient Temperature 1," *American Society for Testing and Materials*, Vol. C-1161-18, 2018.

36. ASTM, "Standard Test Method for Density of Glass by Buoyancy," *American Society for Testing and Materials*, Vol. C0693-93, 2013.

REPORT DOCUMENTATION PAGE

Form Approved
OMB No. 0704–0188

1. REPORT DATE *(DD–MM–YYYY)*	2. REPORT TYPE	3. DATES COVERED *(From — To)*
24-03-2022	Master's Thesis	Sept 2021 — Mar 2022

4. TITLE AND SUBTITLE

MANUFACTURING OF A CERAMIC TURBINE ROTOR FOR A COMPACT JET ENGINE

5a. CONTRACT NUMBER

5b. GRANT NUMBER

5c. PROGRAM ELEMENT NUMBER

6. AUTHOR(S)

Capt Bryan T. Leicht, USMC

5d. PROJECT NUMBER

5e. TASK NUMBER

5f. WORK UNIT NUMBER

7. PERFORMING ORGANIZATION NAME(S) AND ADDRESS(ES)

Air Force Institute of Technology
Graduate School of Engineering and Management (AFIT/EN)
2950 Hobson Way
WPAFB OH 45433-7765

8. PERFORMING ORGANIZATION REPORT NUMBER

AFIT-ENY-MS-22-M-304

9. SPONSORING / MONITORING AGENCY NAME(S) AND ADDRESS(ES)

Air Force Research Laboratory
8th St. Bldg 71B
WPAFB OH 45433-7765
COMM 937-713-0047
Email: mark.fernelius.2@us.af.mil

10. SPONSOR/MONITOR'S ACRONYM(S)

AFRL, RQTC

11. SPONSOR/MONITOR'S REPORT NUMBER(S)

12. DISTRIBUTION / AVAILABILITY STATEMENT

DISTRIBUTION STATEMENT A:
APPROVED FOR PUBLIC RELEASE; DISTRIBUTION UNLIMITED.

13. SUPPLEMENTARY NOTES

14. ABSTRACT

The primary goal of this study was to develop a low-cost, timely, scalable manufacturing method that produced a ceramic turbine that can be tested as a drop-in replacement on a JetCat P400 small scale gas turbine engine. This research compared two processes for manufacturing a ceramic turbine utilizing a pour casting method and 3D printing using stereolithography ceramic manufacturing (SLCM). The pour casting method used Silicon Nitride to create a cast turbine using a sacrificial 3D printed mold. The SLCM method evaluated producing an alumina turbine using an ADMATEC Admaflex 300 SLCM printer to directly print a ceramic turbine. This study covers the finite element analysis of multiple designs and detailed overview of the varying manufacturing processes as well as lessons learned. It also covers how the turbines would be tested and incorporated into JetCat P400.

15. SUBJECT TERMS

Ceramic manufacturing, Thesis, small scale engine, ceramic turbine rotor

16. SECURITY CLASSIFICATION OF:			17. LIMITATION OF ABSTRACT	18. NUMBER OF PAGES	19a. NAME OF RESPONSIBLE PERSON
a. REPORT	b. ABSTRACT	c. THIS PAGE			Lt Col Brian Bohan, AFIT/ENY
U	U	U	U	208	19b. TELEPHONE NUMBER *(include area code)* (937) 255-3636, x4773; Brian.Bohan@afit.edu